UNIVERSITY OF GENOA

POLYTECHNIC SCHOOL

DIME - Department of Mechanical, Energy, Management, and Transportation Engineering

Ph.D. in Robotics and Mechatronics

XXXV Cycle

"Locomotion system for ground mobile robots in uneven and unstructured environments"

Supervisor:

Prof. Luca Bruzzone

Candidate:

Shahabedin Nodehi

January 2023

Acknowledgment

I would like to thank everyone who contributed to the work described in this thesis.
First and foremost, I would like to express my deepest gratitude to my supervisor, Professor Luca Bruzzone, for his enthusiasm for the projects, for his support, encouragement, and patience, for his insight and knowledge into the subject matter that steered me through this research and helps me in many aspects of life and my academic research.

My deepest gratitude also goes to Professor Mahdi Bodaghi, who gave me the opportunity to join his research group at Nottingham Trent University in the UK. He has been extremely kind and supportive since the first day, Although my stay in Nottingham was short, it was one of the best periods of my Ph.D.

Many thanks also to Professor Vittorio Belotti and Dr. Marco Sartore for their helpful work and suggestions on many aspects of this thesis.

Finally, I would like to acknowledge my family, who supported me during my life. First and foremost, I would like to thank Mom, Dad, Anahita, and Mehrab for their constant love and support. They have given me the strength to hold on even in the most challenging times and have constantly encouraged me to believe in myself. We shared every moment of this Ph.D. journey from the beginning, and now that it is coming to an end, my greatest hope is that it provided us with the awareness and the tools to face a much more challenging journey called life. Hand by hand, always together.

Table of contents

1 ABSTRACT 10

2 INTRODUCTION 12

2.1 AERIAL ROBOTS 14
2.2 UNDER-WATER ROBOTS 17
2.2.1 Background of underwater robotics 19
2.3 GROUND MOBILE ROBOTS 20
2.3.1 Classification of ground mobile robot locomotion systems and comparison methodology 21
2.3.2 Locomotion system for Ground Mobile Robots 24
2.3.2.1 Wheeled Robots 24
2.3.2.1.1 Mobility of Wheeled Robots 24
2.3.2.1.2 Different types of wheels 24
2.3.2.1.3 Kinematic Constraints 27
2.3.2.1.4 Conventional Wheels 28
2.3.2.1.5 Pure Rolling Condition 28
2.3.2.1.6 Nonslip Condition 29
2.3.2.1.7 Swedish wheel 29
2.3.2.1.8 Robot Configuration Variables 29
2.3.2.1.9 Restriction on Robot Mobility 30
2.3.2.1.10 Characterization of Robot Mobility 31
2.3.2.1.11 Five Classes of Wheeled Mobile Robots 33
2.3.2.1.12 Wheeled Robotic Structures 34
2.3.2.1.13 Robots with Four Wheels 38
2.3.2.1.14 Special Applications of Wheeled Robots 39
2.3.2.2 Legged Robots 40
2.3.2.3 Gait Locomotion 43
2.3.2.3.1 One-legged robot 45
2.3.2.3.2 Two-legged or Biped Robot 45
2.3.2.3.3 Three-Legged or Tripod Robot 46
2.3.2.3.4 Four-Legged or Quadrupedal 47
2.3.2.3.5 Hexapod or Six-Legged robots 48
2.3.2.3.6 Control of walking robots 48
2.3.2.4 Tracked Robots 50
2.3.2.4.1 Classifications of tracked locomotion systems 50
2.3.2.4.2 Classification of frame architectures of tracked robots 51
2.3.2.4.3 Ground mobile robots with tracks, non-articulated frame 51
2.3.2.4.4 Ground mobile robots with tracks, articulated frame 52
2.3.2.4.5 Classification of track profiles 55
2.3.2.4.6 Classification of track types 57
2.3.2.5 Design methodologies for tracked ground mobile robots 60
2.3.2.5.1 Modeling and simulation of the dynamic behavior of TGMRs 60
2.3.2.5.2 Motion resistance of tracks 61
2.3.2.5.3 Motion resistance due to the internal friction of the tracks 62
2.3.2.5.4 Motion resistance due to the external forces 62
2.3.2.5.5 Overall robot motion resistance 63
2.3.3 Hybrid Robots 65
2.3.3.1 Leg-wheel hybrid locomotion systems 65
2.3.3.2 Leg-track hybrid locomotion systems 67
2.3.3.3 Wheel-track hybrid locomotion systems 68
2.3.3.4 Leg-wheel-track hybrid locomotion systems 69
2.3.4 Comparison of locomotion system features 69

3 THE WHETLHLOC ROBOT 74

3.1 FUNCTIONAL DESIGN OF THE WHETLHLOC ROBOT 76
3.1.1 Design methodology for hybrid locomotion robots with the obstacle-climbing capability 76
3.1.2 The WheTLHLoc conceptual design 79

3.2 STEP CLIMBING ANALYSIS 81
3.2.1 Definition and kinematics of the step climbing phases 81
3.2.2 Stability analysis 90
3.2.3 Non-slipping conditions 97
3.3 SELECTION OF THE STEP CLIMBING KINEMATICS AS A FUNCTION OF THE STEP HEIGHT 99
3.4 EXPERIMENTAL TESTS ON PROTOTYPE 104
3.4.1 Control Architecture 106
3.5 CONCLUSION 108

4 SNAKETRACK 109

4.1 SINGLE TRACK ROBOT 110
4.1.1 FMT (Flexible Mono-tread mobile Track) robot 110
4.1.2 The RCTR (Reconfigurable Continous Track Robot) robot 112
4.2 THE SNAKETRACK MOBILE ROBOT 115
4.2.1 Functional designing of the SnakeTrack robot 115
4.2.2 3D printing process and materials 118
4.2.2.1 The PLA plus material 119
4.2.2.2 The TPU material 120
4.2.3 The spinal column of the robot 121
4.2.4 The motorized end modules 123
4.2.5 The geometry of track 125
4.2.5.1 Summary of track geometry 125
4.2.5.2 The positioning of the centers of the joints 129
4.2.6 Static analysis of the thrust exerted by the actuators when it moves on a 60 ° inclined plane 130
4.3 DETAILED DESIGN 134
4.3.1 Design of the joints 134
4.3.1.1 The connection joints for the vertebral elements 134
4.3.2 The modules of tracks 136
4.3.3 FEM analysis of stresses and displacements that occur at the connection end of module 138
4.3.4 Constructive design of the vertebral joints 143
4.3.5 The motorized end modules 146
4.3.6 The robot Sprockets 148
4.3.7 Sizing of the actuators 151
4.3.7.1 The gearmotors 151
4.3.7.2 Steering Actuators (SA) 151
4.3.7.3 Track Actuator (TA) 152
4.4 KINEMATICS OF THE UNDERACTUATED STEERING 155
4.4.1 Prototyping 159
4.4.1.1 The preliminary prototype of the SnakeTrack robot 159
4.4.2 Conclusion 163

5 PORCOSPINO 164

5.1 SUMMARY 165
5.2 FUNCTIONAL DESIGN OF PORCOSPINO 166
5.3 PROTOTYPING AND EXPERIMENTAL TESTS 169
5.4 CONCLUSIONS AND FUTURE DEVELOPMENTS 171

6 CONCLUSION 172

6.1 LIST OF PUBLICATIONS: 174

7 REFERENCES 175

List of Figures

FIGURE 2-1 EXAMPLES OF FIVE CATEGORIES OF UAVS. A): A ROTARY WINGS UAV, IN PARTICULAR, A HEXACOPTER FROM; A CONVERTIBLE UAV, B) A QUADROTOR WITH TILTING ROTORS FROM TILT RACING DRONE [25]; C) A BIO-INSPIRED UAV, IN PARTICULAR, A ROBOTIC FLYING INSECT [26]; D) A FIXED-WING UAV [14], IN PARTICULAR, AN ELECTRIC GLIDER; E) A LIGHTER-THAN-AIR UAV, IN PARTICULAR, A BLIMP [27], [16]. 16
FIGURE 2-2 THE ROV JASON 2 (COURTESY OF THE WOODS HOLE OCEANOGRAPHIC INSTITUTE, HTTP://WWW.WHOI.EDU) 17
FIGURE 2-3 MOBILITY IN UNSTRUCTURED ENVIRONMENTS VS. SPEED AND ENERGY EFFICIENCY OF THE POSSIBLE HYBRID LOCOMOTION SYSTEMS [32] 21
FIGURE 2-4 GROUND MOBILE ROBOT CLASSIFICATIONS 22
FIGURE 2-5 THE GENERAL DESIGN OF A STANDARD WHEEL. (A) SIDE VIEW, (B) FRONT VIEW, AND (C) TOP VIEW 25
FIGURE 2-6 STRUCTURES OF STANDARD WHEELS. (A) PASSIVE FIXED WHEEL, (B) PASSIVE OR ACTIVE, OFF-CENTERED ORIENTABLE WHEEL, AND (C) ACTIVE ORIENTABLE WHEEL WITHOUT OFFSETS 26
FIGURE 2-7 (A) SWEDISH WHEEL, (B) ATTACHMENT OF A SWEDISH WHEEL 27
FIGURE 2-8 THE INSTANTANEOUS CENTER OF ROTATION. (A) CAR-LIKE ROBOT; (B) THREE-STEERING-WHEELS ROBOT 31
FIGURE 2-9 (A) BICYCLE-TYPE ROBOT AND (B) INVERTED-PENDULUM- TYPE ROBOT 35
FIGURE 2-10 (A) TWO-WHEEL DIFFERENTIAL DRIVE, (B) SYNCHRONOUS DRIVE, (C) OMNI-MOBILE ROBOT WITH SWEDISH WHEELS, (D) OMNI-MOBILE ROBOT WITH ACTIVE CASTER WHEELS, AND (E) OMNIDIRECTIONAL ROBOT WITH ACTIVE STEERABLE WHEELS 36
FIGURE 2-11 A) LEGGED ROBOTS: BIGDOG [63], B) RHEX [35], C) TITAN XI [65]. 42
FIGURE 2-12 ONE LEGGED MULTI-JOINT HOPPER [73] 45
FIGURE 2-13 (A) HONDA ASIMO[74], (B) TOPIO 3.0 [75], (C) ALDEBARAN NAO [76], (D) FUJITSU ENON [77] 46
FIGURE 2-14 (A) SONY AIBO [82] (B) SPOT [83] (C) TITAN VIII [84] 47
FIGURE 2-15 ROBOTS IN SCANSORIAL ENVIRONMENTS (RISE) [86] 48
FIGURE 2-16 TAXONOMY OF TRACKED GROUND MOBILE ROBOTS BASED ON FRAME ARCHITECTURE [33]. (A)[90] - (B)[91] - (C)[92] - (D)[13] - (E)[93] - (F)[94] - (G)[95] - (H)[96] - (I)[97] - (J)[98]. 51
FIGURE 2-17 DYJOB ROBOT [99], TGMRS-NA WITH A MOVABLE CENTER OF GRAVITY (LEFT); LATERAL VIEW (CENTER), AND FRONT VIEW (RIGHT) OF THE TQTMR ROBOT [100] [33]. 52
FIGURE 2-18 SNAKE-LIKE TRACKED ROBOT WITH MODULES IN SERIES [102] (LEFT); QUINCE ROBOTS, WITH FRONT AND REAR ACTIVE FLIPPERS [103] (CENTER); TALBOT, QUADRUPED ROBOT WITH 3-DOF LEGS [104] (RIGHT) [33] 53
FIGURE 2-19 TAXONOMY OF TRACKED GROUND MOBILE ROBOTS BASED ON TRACK PROFILE [33]. A)[114] B)[109] C)[110] D)[111] E)[113] 57
FIGURE 2-20 TAXONOMY OF TRACKED GROUND MOBILE ROBOTS BASED ON TRACK TYPE [33]. A)[93] B)[115] C)[116] D)[117] E)[118] 57
FIGURE 2-21 TGMR-CT WITH FLAT TRACKS FOR FLAX RAW MATERIAL COMPACTING [119] (LEFT); TGMR FOR PIPE INSPECTION WITH MAGNETIC LOCOMOTION [120] (RIGHT) [33]. 58
FIGURE 2-22 TERZAGHI'S MODIFIED BEARING CAPACITY FACTORS [33]. 62
FIGURE 2-23 TRACK SINKAGE (z_0, LEFT [M]) AND SUM OF COMPACTION AND BULLDOZING RESISTANCES (R_B+R_C, RIGHT [N]) AS FUNCTION OF THE TRACK WIDTH B [M] AND LENGTH L [M] [33]. 64
FIGURE 2-24 LEG-WHEEL HYBRID ROBOT WITH RETRACTABLE LOCOMOTION MODULES: LEGGED MODE (A) AND WHEELED MODE (B) [137] 65
FIGURE 2-25 THE LEG-WHEEL HYBRID OCTOPUS ROBOT [138]. 66
FIGURE 2-26 STEPPING TRIPLE WHEEL HYBRID ROBOTS [37]: A) SPACECAT [139]; B) EPI.Q. [140] 67
FIGURE 2-27 LEG-TRACK HYBRID ROBOTS [37]: A) IROBOT SUGV [141] AND B) TITAN X [142]. 68
FIGURE 2-28 WHEEL-TRACK HYBRID ROBOTS: A) WITH VARIABLE-SHAPE TRACKS [113]; B) HELIOS VI [144]; C) WITH GALILEO WHEEL [145] 68
FIGURE 2-29 THE HYBRID LEG-WHEEL-TRACK AZIMUTH ROBOT [146], [37] 69
FIGURE 3-1 THE WHETLHLOC ROBOT: FRONT VIEW (A), REAR VIEW (B). 80
FIGURE 3-2 WHETLHLOC LOCOMOTION MODES: WHEELED LOCOMOTION (A), TRACKED LOCOMOTION (B), HYBRID LEG-WHEEL-TRACK LOCOMOTION (C). 80

FIGURE 3-3 STEP CLIMBING SEQUENCE, DIVIDED IN NINE PHASES: STEP APPROACH (1), LEG LOWERING (2), TRACK RAISING (3), EDGE APPROACH (4), LEG RETREAT (5), LIFT COMPLETION (6), EDGE OVERCOMING (7), LEG RAISING (8), AND STEP DEPART (9).....82
FIGURE 3-4 MAIN GEOMETRICAL PARAMETERS OF THE WHETLHLOC ROBOT.....84
FIGURE 3-5 FINAL POSITIONS OF PHASE 2, STEP APPROACH ($T = T_5$). 85
FIGURE 3-6 GENERIC POSITION IN PHASE 3, TRACK RAISING ($T_5 \leq T \leq T_8$) [169]. 85
FIGURE 3-7 FINAL POSITIONS OF PHASE 4, EDGE APPROACH ($T = T_{11}$) [169].....87
FIGURE 3-8 FINAL POSITIONS OF PHASE 5, LEG RETREAT ($T = T_{17}$) [169].....88
FIGURE 3-9 GENERIC POSITION IN PHASE 6, LIFT COMPLETION ($T_{17} \leq T \leq T_{20}$) [169]. 89
FIGURE 3-10 FRONT AND REAR TIPPING ANGLES IN THE WORST STABILITY CONDITIONS IN PHASE 5, LEG RETREAT (A: SIMULTANEOUS LEG ROTATION, B: SEQUENTIAL LEG ROTATION), AND IN PHASE 8, LEG RAISING (C: SIMULTANEOUS LEG ROTATION, D: SEQUENTIAL LEG ROTATION).....93
FIGURE 3-11 SCHEMATIC DIAGRAM OF STABILITY CONE.....94
FIGURE 3-12 ROTATION OF THE TRACK SPROCKETS RELATIVE TO THE MAIN BODY (θ_T), OF WHEELS RELATIVE TO THE LEGS (θ_W), OF THE LEFT AND RIGHT LEG RELATIVE TO THE MAIN BODY (θ'_L AND θ'_R); PHASES ARE NUMBERED IN GREEN. 95
FIGURE 3-13 ANGLES OF LEFT AND RIGHT LEG (θ_L AND θ_R) AND MAIN BODY PITCH ANGLE (θ_B) WITH RESPECT TO THE FIXED REFERENCE FRAME O(X,Y,Z); PHASES ARE NUMBERED IN GREEN.....96
FIGURE 3-14 ABSOLUTE X AND Z COORDINATES OF THE MAIN BODY REFERENCE FRAME (O') AND OF THE OVERALL C.O.G. (G); PHASES ARE NUMBERED IN GREEN.....96
FIGURE 3-15 FRONT AND REAR TIPPING ANGLES (γ_F AND γ_R); PHASES ARE NUMBERED IN GREEN. THE GREY ZONE INDICATES INSUFFICIENT TIPPING ANGLES.....97
FIGURE 3-16 STATIC CONDITIONS AT THE BEGINNING OF PHASE 6, LIFT COMPLETION ($T = T_{17}$). 98
FIGURE 3-17 INFLUENCE OF STEP HEIGHT H AND MAXIMUM PITCH ANGLE $\theta_{B,MAX}$ ON THE ROBOT STABILITY; $\gamma_{F,MIN}$: MINIMUM FRONT TIPPING ANGLE; $\gamma_{R,MIN5}$: MINIMUM REAR TIPPING ANGLE IN PHASE 5; $\gamma_{R,MIN8}$: MINIMUM REAR TIPPING ANGLE IN PHASE 8. THE YELLOW PLANE REPRESENTS THE NULL SURFACE, AND THE CYAN PLANE REPRESENTS THE MOTION PLANNING RELATIONSHIP IMPOSED BY EQ. (51).....100
FIGURE 3-18 INFLUENCE OF STEP HEIGHT H AND MAXIMUM PITCH ANGLE $\theta_{B,MAX}$ ON THE NON-SLIPPING CONDITION ($X_{S1} - X_G > 0$), FOR DIFFERENT STATIC FRICTION COEFFICIENTS: $F_W = F_T = 0.5$ (BLUE), 0.7 (VIOLET), 0.9 (GREEN), 1.1 (RED); THE STABILITY CONDITION IS VERIFIED IN THE REGIONS WHERE THE SURFACES ARE HIGHER THAN THE NULL SURFACE (YELLOW). THE CYAN PLANE REPRESENTS THE MOTION PLANNING RELATIONSHIP IMPOSED BY EQ. (51). 101
FIGURE 3-19 STABILITY AND NON-SLIPPING CONDITIONS AS A FUNCTION OF THE STEP HEIGHT H WITH THE PROPOSED MAXIMUM PITCH ANGLE LAW $\theta_{B,MAX}(H)$. LEFT: MINIMUM FRONT AND REAR TIPPING ANGLES $\gamma_{F,MIN}$ (RED), $\gamma_{R,MIN5}$ (GREEN), AND $\gamma_{R,MIN8}$ (BLUE) [°]. RIGHT: $X_{S1} - X_G$ [M] FOR DIFFERENT STATIC FRICTION COEFFICIENTS: $F_W = F_T = 0.5$ (BLUE), 0.7 (CYAN), 0.9 (GREEN), 1.1 (RED). CONTINUOUS LINES REFER TO THE ABSENCE OF PAYLOAD AND DASHED LINES TO THE MAXIMUM PAYLOAD (0.5 KG).....102
FIGURE 3-20 NON-SLIPPING CONDITION AS A FUNCTION OF STEP HEIGHT H AND OF THE STATIC FRICTION COEFFICIENT $F_W = F_T$. LEFT: $X_{S1} - X_G$ WITHOUT PAYLOAD; THE CONDITION IS VERIFIED IN THE REGION WHERE $X_{S1} - X_G$ (BLUE SURFACE) IS HIGHER THAN 0 (YELLOW PLANE). RIGHT: THE DIFFERENCE BETWEEN ($X_{S1} - X_G$) WITH 0.5 KG PAYLOAD AND ($X_{S1} - X_G$) WITHOUT PAYLOAD. 103
FIGURE 3-21 INTERNAL LAYOUT OF THE ROBOT: UPPER LAYER (A), LOWER LAYER (B), INTERNAL VIEW OF THE PROTOTYPE (C).....104
FIGURE 3-22 STEP CLIMBING SEQUENCE (H = 165 MM).....105
FIGURE 3-23 COMPARISON OF SIMULATION AND EXPERIMENTAL RESULTS: $X_{O'}$ (LEFT), $Z_{O'}$ (CENTER), θ_B (RIGHT). CONTINUOUS LINES: EXPERIMENTAL TESTS; DASHED LINES: SIMULATION. BLUE LINES: H = 142 MM; RED LINES: H = 165 MM. 105
FIGURE 3-24 EXPERIMENTAL TESTS IN VARIOUS OPERATIVE CONDITIONS: CLIMBING OF A MARBLE STAIR (A) AND OF A STAIR WITH STEEL EDGE (B), LOCOMOTION ON WHEELS AND OMNI WHEELS ON FLAT AND EVEN TERRAIN (C), MIXED LEG-WHEEL-TRACK LOCOMOTION TO CLIMB IRREGULAR OBSTACLES (D), TRACKED LOCOMOTION ON SOFT AND YIELDING TERRAIN (E) AND ON IRREGULAR TERRAIN (F).....106
FIGURE 3-25 LABVIEW MAIN VIRTUAL INSTRUMENT FOR MOTION CONTROL 107
FIGURE 4-1 ROBOT FTM [101]. 111
FIGURE 4-2 FLEXIBLE TRACK OF THE FTM ROBOT [101].....112
FIGURE 4-3 RCTR ROBOT TRACK LOCKING SYSTEM [174].....113
FIGURE 4-4 RCTR ROBOT TRACK RELEASE SYSTEM [174].....113
FIGURE 4-5 THE THREE EXAMPLES SHOWN OF MOBILE ROBOTS COMPARED: FROM LEFT TO RIGHT THE FTM ROBOT, THE SNAKE TRACK AND THE RCTR ROBOT [3,4] 115

FIGURE 4-6 3D MODEL OF THE SNAKETRACK ROBOT 116
FIGURE 4-7 3D VIEW OF THE VERTEBRAL COLUMN 117
FIGURE 4-8 3D VIEW OF THE EXTERNAL TRACK 118
FIGURE 4-9 HOW THE APPEARANCE OF THE MATERIAL VARIES WITH THE PERCENTAGE OF INFILL [177] 119
FIGURE 4-10 3D VIEW OF THE VERTEBRAL COLUMN. 122
FIGURE 4-11 3D MODELS WHEN TURNING TO THE RIGHT WITH A MINIMUM RADIUS 123
FIGURE 4-12 GEOMETRIC DIAGRAM WITH THE MINIMUM TURNING RADIUS 123
FIGURE 4-13 TOP VIEWS OF THE END MODULES 124
FIGURE 4-14 END MODULES OF SNAKETRACK 124
FIGURE 4-15 FRONT VIEW OF THE SNAKETRACK IN FULL STEERING CONFIGURATION 125
FIGURE 4-16 3D MODEL OF THE TRACK 126
FIGURE 4-17 INITIAL GEOMETRY OF THE MODULE 126
FIGURE 4-18 TOP VIEWS OF TRACK-CONNECTED MODULES 127
FIGURE 4-19 REAR VIEWS OF SNAKETRACK 128
FIGURE 4-20 SECTIONED VIEW OF SNAKETRACK 128
FIGURE 4-21 BOTTOM VIEWS OF A SINGLE MODULE OF TRACK 129
FIGURE 4-22 3D MODEL OF A SINGLE TRACK MODULE 129
FIGURE 4-23 SIDE VIEW OF THREE CONNECTED MODULES 130
FIGURE 4-24 SNAKETRACK PROTOTYPE REACHING A RAMP 131
FIGURE 4-25 TOP VIEWS OF THE ROBOT SPINE, SHOWING THE INTERNAL STRUCTURE OF THE VERTEBRAL ELEMENTS 134
FIGURE 4-26 TOP VIEW OF THE SPINAL COLUMN WHEN THE ROBOT TURNS 90° 135
FIGURE 4-27 MALE ENDS OF THE CONNECTION JOINTS BETWEEN THE TRACK MODULES 136
FIGURE 4-28 FEMALE ENDS OF THE CONNECTION JOINTS BETWEEN THE TRACK MODULES 136
FIGURE 4-29 SCALE DRAWING OF THE TOP VIEW OF TWO CONNECTED MODULES 137
FIGURE 4-30 TOP VIEWS OF THE MODULE; THE FOUR HOLES AT THE LATERAL ENDS ALLOW THE COUPLING OF THE TRACK WITH THE SPROCKET TEETH 137
FIGURE 4-31 SIDE SECTION VIEW OF THE TRACK MODULE 138
FIGURE 4-32 FEM ANALYSIS OF SINGLE MODULE 139
FIGURE 4-33 DETAIL OF THE FEM MESH MADE AT THE CONNECTION END OF THE TRACK MODULE 139
FIGURE 4-34 VON MISES STRESSES (TRACK TRACTION) 140
FIGURE 4-35 DETAIL ZOOM OF THE VON MISES TENSION 141
FIGURE 4-36 DISPLACEMENTS RECORDED FOR THE TRACK MODULE 141
FIGURE 4-37 DETAIL ZOOM OF THE AREAS MOST SUBJECT TO MOVEMENT 142
FIGURE 4-38 POSSIBLE REALIZATIONS OF COMPLIANT UNIVERSAL JOINTS: TWO-AXIS FLEXURE JOINT (A) AND COMPLIANT CARDAN U JOINT (B); REVOLUTE JOINT WITH SUPERELASTIC INSERT (C). 143
FIGURE 4-39 DESIGN OF THE COMPLIANT VERTEBRAL JOINTS: CORE (C), EXTERNAL PLATES (P), LATERAL SUPPORTS 144
FIGURE 4-40 TOP VIEW OF THE SPINAL COLUMN OF THE ROBOT 145
FIGURE 4-41 TOP VIEWS OF ONE OF THE TWO MOTORIZED MODULES PLACED AT THE ENDS OF THE ROBOT 146
FIGURE 4-42 FRONT VIEWS OF ONE OF THE FOUR SPROCKETS IN THE ROBOT 148
FIGURE 4-43 2D CAD OF ONE SIDE OF THE POLYGON 149
FIGURE 4-44 3D VIEW OF THE GEAR INTERPOSED BETWEEN THE GEARMOTOR SHAFT AND SPROCKETS AXIS 150
FIGURE 4-45 RELATIVE ORIENTATIONS OF ADJACENT VERTEBRAE IN A STRAIGHT POSITION (LEFT) AND STEERED POSITION (RIGHT) OF THE VERTEBRAL COLUMN. 155
FIGURE 4-46 VARIATIONS OF THE ROPE LENGTHS AS FUNCTIONS OF THE YAW ANGLE OF THE VERTEBRAL JOINTS. 157
FIGURE 4-47 DIFFERENCES BETWEEN THE VARIATIONS OF THE ROPE LENGTHS AND THEIR LINEAR APPROXIMATIONS AS FUNCTIONS OF THE YAW ANGLE OF THE VERTEBRAL JOINTS. 158
FIGURE 4-48 TURNING RADIUS AS A FUNCTION OF THE YAW ANGLE OF THE VERTEBRAL JOINTS 158
FIGURE 4-49 THE SNAKETRACK ROBOT AND ITS REMOTE CONTROL 159
FIGURE 4-50 LEFT: THE TOP VIEW OF THE SPINAL COLUMN OF THE ROBOT WITH THE RADIO CONTROL, RIGHT: ELECTRONIC COMPONENTS POSITIONED IN THE SPACES BETWEEN THE ROBOT'S VERTEBRAE. 160
FIGURE 4-51 LEFT: VIEW OF THE LATERAL PROFILES OF THE VERTEBRAL ELEMENTS; RIGHT: ROBOT TRACK MODULES 161
FIGURE 4-52 TOP VIEW OF TWO CENTRAL ELEMENTS OF THE VERTEBRAE CONNECTED BY TPU JOINTS 161
FIGURE 4-53 VIEWS OF THE SNAKETRACK ROBOT WHEN IT ASSUMES THE STEERING CONFIGURATION 162

FIGURE 4-54 PRELIMINARY EXPERIMENTAL TESTS ON THE SNAKETRACK PROTOTYPE: STEERING (LEFT) AND LOCOMOTION ON UNEVEN GROUNDS (RIGHT). 162
FIGURE 5-1 EXTERNAL VIEW OF PORCOSPINO: STRAIGHT POSITION (LEFT) AND STEERING POSITION WITH MINIMUM TURNING RADIUS (RIGHT). 167
FIGURE 5-2 VERTEBRAL COLUMN OF PORCOSPINO. 167
FIGURE 5-3 DETAIL OF THE TRACK MODULES WITH A CENTRAL OPENING (O) FOR CAMERA VISION (LEFT); TRANSVERSAL SECTION OF THE TRACK GUIDANCE SYSTEM (RIGHT). 168
FIGURE 5-7 EXPERIMENTAL TESTS: LOCOMOTION ON UNEVEN GRASSY TERRAIN (LEFT) AND INSPECTION OF A PIPE WITH DIAMETER OF 300 MM (RIGHT). 169
FIGURE 5-8 EXPERIMENTAL TESTS: QUICK CHANGE OF DIRECTION ON UNEVEN TERRAIN (FRAME SEQUENCE 1); PASSIVE ADAPTABILITY OF THE VERTEBRAL COLUMN ON TERRAIN IRREGULARITIES (RIGHT). 170
FIGURE 5-9 EXPERIMENTAL TESTS: RECOVERY MANEUVER AFTER A CAPSIZE ON A FLANK 170

List of tables

TABLE 2-1 ROVS FOR SCIENTIFIC USE 18
TABLE 2-2 DESCRIPTION OF THE FEATURES CONSIDERED IN THE COMPARISON OF LOCOMOTION SYSTEMS. [34] 23
TABLE 2-3 SYNTHETIC COMPARISON OF LOCOMOTION SYSTEM FEATURES.[32] 71
TABLE 2-4 EVALUATION CRITERIA. [32] 73
TABLE 3-1 MAIN GEOMETRICAL PARAMETERS AND VARIABLES AND CORRESPONDING DIMENSIONLESS RATIOS. 83
TABLE 3-2 COORDINATES THE CONTACT POINTS WITH THE GROUND FOR THE NINE-STEP CLIMBING PHASES. 92
TABLE 3-3 KINEMATIC PARAMETERS CONSIDERED IN THE SIMULATIONS. 95
TABLE 4-1 COMPARISON OF THE MAIN CHARACTERISTICS THAT HAVE BEEN IDENTIFIED IN THE THREE TYPES OF ROBOTS TAKEN AS AN EXAMPLE. 114
TABLE 4-2 MAIN CHARACTERISTICS OF SNAKETRACK 117
TABLE 4-3 MECHANICAL PROPERTIES OF PLA 120
TABLE 4-4 TPU FEATURES [180] 121
TABLE 4-5 COMPONENTS INDICATED IN FIGURE 4-10 122
TABLE 4-6 VALUES OBTAINED, AND QUANTITIES USED TO CARRY OUT THE CALCULATIONS 133
TABLE 4-7 RESULTS OBTAINED FROM THE CALCULATIONS CARRIED OUT 140
TABLE 4-8 COMPONENTS PRESENT IN THE ROBOT END MODULES 147
TABLE 4-9 GEARMOTOR TECHNICAL DATA 151
TABLE 4-10 CHARACTERISTIC QUANTITIES OF THE GEARMOTOR AND USEFUL DATA FOR SIZING 152
TABLE 4-11 TECHNICAL CHARACTERISTICS OF THE TRACTION GEARMOTOR 152
TABLE 4-12 CHARACTERISTIC QUANTITIES OF THE GEARMOTOR AND USEFUL DATA FOR SIZING 153

1 Abstract

One of the technology domains with the greatest growth rates nowadays is service robots. The extensive use of ground mobile robots in environments that are unstructured or structured for humans is a promising challenge for the coming years, even though Automated Guided Vehicles (AGV) moving on flat and compact grounds are already commercially available and widely utilized to move components and products inside indoor industrial buildings. Agriculture, planetary exploration, military operations, demining, intervention in case of terrorist attacks, surveillance, and reconnaissance in hazardous conditions are important application domains.

Due to the fact that it integrates the disciplines of locomotion, vision, cognition, and navigation, the design of a ground mobile robot is extremely interdisciplinary. In terms of mechanics, ground mobile robots, with the exception of those designed for particular surroundings and surfaces (such as slithering or sticky robots), can move on wheels (W), legs (L), tracks (T), or hybrids of these concepts (LW, LT, WT, LWT). In terms of maximum speed, obstacle crossing ability, step/stair climbing ability, slope climbing ability, walking capability on soft terrain, walking capability on uneven terrain, energy efficiency, mechanical complexity, control complexity, and technology readiness, a systematic comparison of these locomotion systems is provided in [1].

Based on the above-mentioned classification, in this thesis, we first introduce a small-scale hybrid locomotion robot for surveillance and inspection, WheTLHLoc, with two tracks, two revolving legs, two active wheels, and two passive omni wheels. The robot can move in several different ways, including using wheels on the flat, compact ground,[1] tracks on soft, yielding terrain, and a combination of tracks, legs, and wheels to navigate obstacles. In particular, static stability and non-slipping characteristics are considered while analyzing the process of climbing steps and stairs. The experimental test on the first prototype has proven the planned climbing maneuver's efficacy and the WheTLHLoc robot's operational flexibility. Later we present another development of WheTLHLoc and introduce WheTLHLoc 2.0 with newly designed legs, enabling the robot to deal with bigger obstacles.

Subsequently, a single-track bio-inspired ground mobile robot's conceptual and embodiment designs are presented. This robot is called SnakeTrack. It is designed for surveillance and inspection activities in unstructured environments with constrained areas. The vertebral column has two end modules and a variable number of vertebrae linked by compliant joints, and the surrounding track is its essential component. Four motors drive the robot: two control the track motion and two regulate the lateral flexion of the vertebral column for steering. The compliant joints enable limited passive torsion and retroflection of the vertebral column, which the robot can use to adapt to uneven terrain and increase traction. Eventually, the new version of SnakeTrack, called 'Porcospino', is introduced with the aim of allowing the robot to move in a wider variety of terrains.

The novelty of this thesis lies in the development and presentation of three novel designs of small-scale mobile robots for surveillance and inspection in unstructured environments, and they employ hybrid locomotion systems that allow them to traverse a variety of terrains, including soft, yielding terrain and high obstacles.

This thesis contributes to the field of mobile robotics by introducing new design concepts for hybrid locomotion systems that enable robots to navigate challenging environments. The robots presented in this thesis employ modular designs that allow their lengths to be adapted to suit specific tasks, and they are capable of restoring their correct position after falling over, making them highly adaptable and versatile.

Furthermore, this thesis presents a detailed analysis of the robots' capabilities, including their step-climbing and motion planning abilities. In this thesis we also discuss possible refinements for the robots' designs to improve their performance and reliability.

Overall, this thesis's contributions lie in the design and development of innovative mobile robots that address the challenges of surveillance and inspection in unstructured environments, and the analysis and evaluation of these robots' capabilities. The research presented in this thesis provides a foundation for further work in this field, and it may be of interest to researchers and practitioners in the areas of robotics, automation, and inspection.

As a general note, the first robot, WheTLHLoc, is a hybrid locomotion robot capable of combining tracked locomotion on soft terrains, wheeled locomotion on flat and compact grounds, and high obstacle crossing capability. The second robot, SnakeTrack, is a small-size mono-track robot with a modular structure composed of a vertebral column and a single peripherical track revolving around it. The third robot, Porcospino, is an evolution of SnakeTrack and includes flexible spines on the track modules for improved traction on uneven but firm terrains, and refinements of the shape of the track guidance system. This thesis provides detailed descriptions of the design and prototyping of these robots and presents analytical and experimental results to verify their capabilities.

2 Introduction

Currently, one of the technology domains which has the greatest growth is service robotics [2]. Even yet, the significant use of ground mobile robots in situations that are unstructured or structured for humans is a potential challenge in the upcoming years [3]. Automated Guided Vehicles (AGV) traveling on flat and compact grounds are now commercially available and widely utilized to transport components and products inside industrial structures. Agriculture [4], [5], planetary exploration[6][7], reconnaissance in hazardous conditions, such as radioactive or chemical contamination[8], homeland security and military operations [9], demining [10], intervention in the event of terrorist strikes [11], and surveillance [12] are also significant application sectors.

Many kinds of calamities stem from natural and man-made causes: earthquakes, floods, hurricanes, fires, etc. They cause disruptions and rubles in disaster areas like collapsed buildings, landslides, or volcano eruptions. In many countries, natural disasters leading to casualties are frequently encountered as a result of geological structure and climate patterns. It is very important to reach the victims within the first 48 hours after the disaster to save their lives [13].

However, the difficult physical conditions after natural disasters usually make it hard, difficult, and dangerous to reach the victims. For the purpose of overcoming these difficulties, especially on the international scene, scientific and technological studies are concentrated on the development of search and rescue mobile robots. The biggest contribution of these robots will be keeping the search and rescue personnel out of the disaster region and gathering and processing more information from the site via various sensors and hence preventing further casualties and losses of lives.

During these emergency situations, especially in urban disasters, many different people are deployed such as policemen, firefighters, and personnel of medical assistance. Search and rescue mobile robots need to cooperate to save lives and evacuate victims to safe areas. In such situations, they must act quickly and take abrupt decisions and actions to detection of victims. They must determine the location and status of victims and the stability of the structures as quickly as possible so that first-aid personnel such as medical personnel and firefighters can enter the disaster area and save victims.

All of these tasks used to be performed by humans and trained dogs in very hazardous and risky situations are increasingly undertaken by Search and Rescue Mobile Robots. Three main types of mobile robots can be distinguished:

1. Unmanned Aerial Vehicles (UAVs)- UAVs work without any contact with the ground surface and can help in transporting medical aid to victims and presenting a rough scenario of the accident site to the rescue team [14].

2. Unmanned Underwater Vehicles (UUVs)- UUVs have the ability to search through water and identify fatalities, hazardous subjects, or materials [15].
3. Unmanned Ground Vehicles (UGVs)- UGVs work on the ground surface and can assist rescuers to find and interact with trapped victims, in areas where it is dangerous or difficult for rescue personnel to enter [1].

2.1 Aerial Robots

Over the past ten years, interest in unmanned aerial vehicles (UAVs) has steadily increased among scientific communities, commercial enterprises, and the general public. Consider the possibility that one of the world's most well-known e-commerce platforms intends to use hexacopters to transport products to customers' hands in thirty minutes or less [16].

The National Science Foundation (NSF) has been given $35 million in research funding by the White House in 2016 to expedite the design and control of unmanned aerial vehicles (UAVs), particularly for civilian uses like the monitoring and inspection of physical infrastructures, quick disaster response, agricultural, and meteorological domains [17].

As a result, the number of applications for UAVs is constantly growing. In reality, UAVs are used to investigate seismic risks and earthquake-prone regions. [16] In a small town in southern Italy called Cerreto Sannita, archaeologists are also using UAVs to digitally restore the medieval portion of the town [18]. Some businesses have begun to consider creating a type of personal UAV with a camera to capture self-movies [19], particularly indicated for a sportsman. The information and examples shown above all point to the fact that aerial robotics is experiencing its golden age. UAVs must transition from passive duties, such as inspection, surveillance, monitoring, remote sensing, and so on, to active tasks, like grasping and manipulation This is exactly in line with what the European Robotics Strategic Research Agenda (eSRA), which was introduced in Brussels in 2009 and renewed in 2014, specified [20].

The eSRA states that robotic employees and coworkers, logistic robots, and robots for exploration and inspection are all envisioned uses for aerial and space robotics. To carry out the necessary duties, UAVs must be equipped with manipulation capabilities. Therefore, from a broad perspective, aerial manipulation refers to the actions of using UAVs to grasp, carry, position, assemble, and disassemble mechanical components, measuring devices, and other items. Particularly in certain industrial and service applications that are thought to be extremely risky for a human operator, the introduction of aerial manipulation in the situations outlined by the eSRA can be useful. Aerial vehicles that can do simple manipulation tasks might in fact help humans with these tasks, or at the very least in the most dangerous and important circumstances. Mobile ground platforms [1], underwater [21], and space robots [22] can be taken as examples of this scenario. Consequently, a UAM might be a useful option for giving an aerial vehicle the capacity to carry out deft manipulation duties.

First and foremost, UAVs need to be outfitted with the right equipment to perform aerial manipulation operations. The two approaches that are most frequently used are either mounting a gripper or a multi-fingered hand directly on the aerial vehicle, such as a flying hand (FH), or outfitting the UAV with one or more robotic arms, such as an unmanned aerial manipulator (UAM). In the first scenario, the item can be held and locally adjusted while in flight. However, a

single gripper is insufficient to achieve a full evolution of the UAVs from passive to active duties; mechanical structures attached to the UAVs are then required to carry out more complicated functions.

Robots with the level of mobility provided by flying have a wide range of possible uses. The military applications of aerial robotics have been recognized ever since the beginnings of powered flight, and they have already been realized to have sometimes spectacular effects in surveillance, targeting, and even strike missions. Even more civilian applications exist, such as those for remote sensing, disaster relief, image capture, monitoring, and the delivery of products.

The challenges faced by aerial robots span several distinct fields, including state regulations, man-machine interface design issues, navigation, safety/reliability, collision prevention, and take-off/landing techniques. The size of aerial robots can considerably influence their flight dynamics, and small aerial robots can end up looking considerably different from their larger counterparts. Comparable with their manned counterparts, aerial robots may enjoy diverse propulsion systems and operate over large speed ranges.

Aerial robots must be equipped with reliable position and actuation equipment so as to be capable of controlled flight, and this constitutes a nontrivial requirement prior to doing research or development in this field. However, many universities, research centers, and industries have now met this requirement and are actively working on the challenges presented above. The largest obstacle to the commercial development of aerial robots is, however, the necessity to comply with and support a regulatory environment that is only beginning to address these rapidly developing systems. [16]

There are many applications for Aerial robots; some of the most important are considered for civilian uses like monitoring and inspection of physical infrastructures, smart response to disasters, and agricultural and meteorological domains. [23]

It is challenging to do an exact taxonomy of UAVs due to the variety of applications for aerial vehicles since there are many devices on the market with various dimensions, mechanical configurations, actuators, and other characteristics. The classification of aerial robotics is more complicated than that of manned aviation because the term currently covers a very diverse range of systems with various scales, mechanical configurations, and actuation principles. Aerial robots are essentially miniature reproductions of manned aircraft designs in the great majority of cases. [12] Following what was shown in [24], grouping the UAVs according to their low maneuverability and high endurance toward their high maneuverability yields: i) rotary wings unmanned aerial vehicles (RW-UAVs), such as multirotor (including quadcopters and hexacopters), small-scale helicopter-based unmanned aerial vehicles (HUAVs), coaxial helicopters, and ducted fan unmanned aerial vehicles; ii) convertible unmanned aerial vehicles (UAVs), which have interchangeable designs such as tilting rotors or cruise-flight-enabled ducted fans unmanned aerial vehicles, tail. The vertical take-off and landing (VToL) UAVs are one of the above-mentioned vehicles that can detach

from and land on the ground without using a runway. Multirotor UAVs are less expensive and easier to control than conventional aircraft. They are adept at hovering, but their best characteristic isn't endurance.[16].

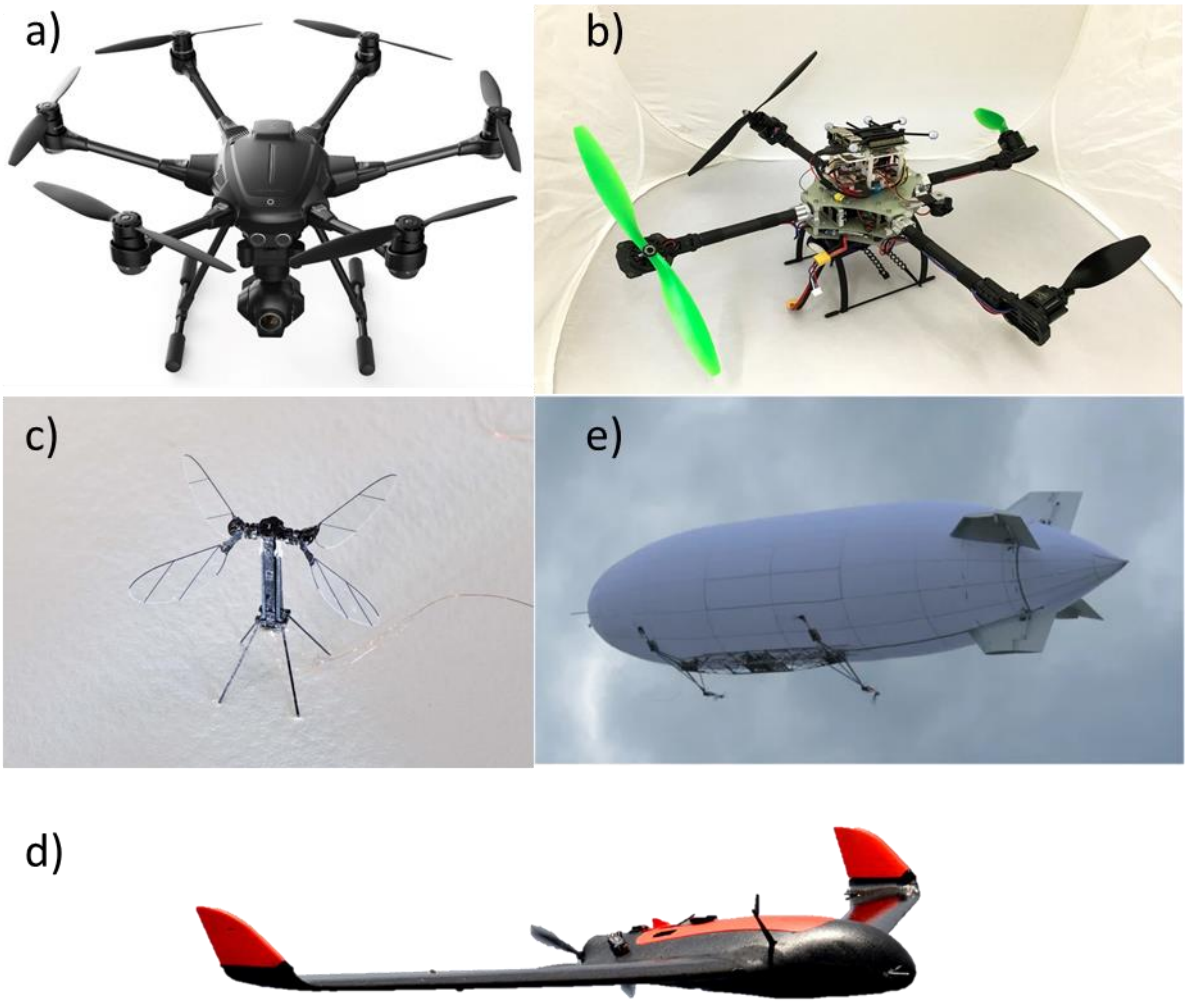

Figure 2-1 Examples of five categories of UAVs. a): a rotary wings UAV, in particular, a hexacopter from; a convertible UAV, b) a quadrotor with tilting rotors from TILT Racing Drone [25]*; c) a bio-inspired UAV, in particular, a robotic flying insect* [26]*; d) a fixed-wing UAV* [14]*, in particular, an electric glider; e) a lighter-than-air UAV, in particular a blimp* [27], [16].

2.2 Under-water Robots

Underwater robotics has seen a lot of research and development over the past ten years, particularly in the area of autonomous underwater vehicles (AUVs). The necessity for the application of underwater robotic systems has grown as the ocean draws significant attention to environmental concerns, resources, and scientific and military endeavors. AUVs have undergone extensive development to solve difficult engineering and scientific issues brought on by the dangerous and unstructured ocean environment. Around 30 new AUVs were produced globally in the 1990s, and many more have been produced until this date. R&D activities in the AUV community have increased as a result of the creation of novel materials, cutting-edge computing, and sensory technologies, as well as theoretical developments. However, this is just the start of more sophisticated yet useful and dependable AUVs [21].

Oceans make up two-thirds of the surface of the planet and have historically had a significant role in determining human wellbeing. They make it possible to carry products across countries, much as in the past. The oceans are now important suppliers of food and other commodities like oil and gas. In the near future, it's possible that gas hydrate extraction and offshore metal mining may both become commonplace. On the other hand, natural events like hurricanes and tsunamis pose a danger to human safety and cause infrastructural damage due to the ocean.

Figure 2-2 The ROV Jason 2 (courtesy of the Woods Hole Oceanographic Institute, http://www.whoi.edu)

Using a range of tools, our scientific knowledge of deep water is quickly growing. Diverse additional technologies, including towed or lowered equipment, trawls, dredges, autonomous seabed instrumentation, and deep-sea drilling, were used in conjunction with diving and human-occupied submersibles to perform the first scientific investigations. Recently, remotely controlled and self-driving vehicles have started to change seabed investigation, often providing better data at lower prices. Seafloor observatories connected by satellites and fiber-optic cables will soon return enormous volumes of data from coastal and deep-sea locations. These observations will supplement those from more traditional expeditionary studies, and their installation and maintenance will both need

teleoperated or robotic assistance. The Jason 2 vehicle created at the Woods Hole Oceanographic Institution is an example of a remotely operated vehicle designed for the scientific study of the seafloor (shown in Figure 2-2), and a list of remotely operated vehicles for scientific exploration can be found in Table 2-1 (the last vehicle in the table, Kaiko, was lost several years ago).

Table 2-1 ROVs for scientific use

Vehicle	Depth (m)	Institution	Manufacturer
Hyperdolphin	3000	JAMSTEC	ISE
Dolphin 3K	3000	JAMSTEC	JAMSTEC
Quest	4000	MARUM	Shilling
Tiburon	4000	MBARI	MBARI
ROPOS	5000	CSSF	ISE
Victor	6000	IFREMER	IFREMER
Jason	6500	WHOI	WHOI
ISIS	6500	NOC	WHOI
UROV 7K	7000	JAMSTEC	JAMSTEC
Kaiko	11000	JAMSTEC	JAMSTEC

Currently, remotely operated vehicles (ROVs) that are physically attached through a tether to receive power and data are used almost exclusively to service offshore oil and gas infrastructure, with human divers only being utilized for the shallowest installations. In order to support drilling operations, activate valves, repair or replace subsea components, and carry out a number of other duties necessary to maintain production rates and product quality, subsea systems need substantial work capacity throughout the installation. As offshore oil and gas production goes into deeper seas and economic concerns force important production stages from surface platforms to the seabed, the trend toward robotic and teleoperated subsea intervention seems unavoidable. These systems can carry out difficult operations including clearing away dirt, cleaning with abrasive instruments, and employing a range of nondestructive testing equipment thanks to remotely driven manipulators. The cost rise and the challenges of controlling the lengthy tether are the major reasons why ROV efficacy diminishes with depth.

Autonomous underwater vehicles (AUVs) are unmanned, free-swimming underwater vehicles that can perform various tasks without being constrained by ROV tethers. Such vehicles carry their own energy sources (now batteries, maybe fuel cells in the future) and solely communicate through acoustics and, in the near future, optical communications. These vehicles must function independently from ongoing human supervision; in many circumstances, they operate totally autonomously due to limited communications. Currently, AUVs are utilized for

under-ice surveying, underwater archeology, oceanographic sampling, and scientific surveying. More ambitious uses, such as long-term subsea surveillance, are in the technical development stage. Military applications, like mine detection and landing site survey, are now operational. Currently, AUVs are unable to perform normal ROV activities like sampling or manipulation because these situations may be difficult for even experienced human pilots to navigate [21].

There are around 200 AUVs in use, many of them experimental. Nevertheless, they are developing quickly. Recently, several businesses have started using AUVs for commercial services. As an example, the cost savings of a survey carried out using an AUV instead of a towed vehicle for the oil and gas business is up to 30%, and the data quality is often greater. Likewise, complete AUV systems for particular, predetermined missions are currently offered by commercial producers in a number of nations. Currently, most ROVs are equipped with remotely controlled manipulators as standard equipment, but autonomous manipulation remains a research difficulty; two programs, SAUVIM [28] and ALIVE [29], were committed to examining this control issue.

2.2.1 Background of underwater robotics

Humans have utilized boats from the beginning of recorded history, but submerged vehicles are relatively modern inventions. The legend has it that Aristotle invented the skapheandros (boat-man), which allowed Alexander the Great (Alexander III of Macedonia, 356-323 BC) to remain underwater for at least half a day during the Tiro War in 325 BC. This invention is thought to be the first known instance of an underwater device. If accurate, this would predate Archimedes' rule, which was originally stated about 250 BC, hence it is definitely implausible. The first underwater vehicle may have been created by Leonardo Da Vinci. The Codice Atlantico (Codex Atlanticus), which was composed between 1480 and 1518, has a description of his endeavors. According to legend, Leonardo experimented with the notion of an underwater military machine but destroyed the findings because he thought they were too hazardous. The North-seeking apparatus, which was granted a patent in 1908 and employed gyroscopic principles to create the first autopilot, was likely the first maritime control system to use feedback theory [30]. It is noteworthy to note that the proportional-integral-derivative (PID) control, which is often used today in many industrial applications, was first fully evaluated in 1929 by Minorsky [31]. From that point on, the usage of feedback theory in maritime control increased steadily. In 1953, POODLE, the first remotely controlled underwater vehicle, was created. The ROV developed during the 1960s and 1970s, mostly for military applications. The commercial offshore sector began to employ ROVs in the 1980s, and they also started to appear for research purposes. In the 1970s, the first tetherless, autonomous cars were created for testing. AUVs are now used more often for scientific, military, and commercial purposes. Commercial suppliers provide turnkey AUV systems for a variety of purposes, and a number of businesses offer AUV services [15].

2.3 Ground Mobile Robots

In the next 20 years, the global market for mobile robots is anticipated to grow significantly, exceeding the market for industrial robotics in terms of sales and units. These robots gained a lot of attention in recent decades, mainly due to their vast usage in uneven, multi-structured environments. Homeland security, surveillance, demining, reconnaissance in risky situations, and agriculture are significant application areas. In general, designing mobile robot locomotion systems for unstructured environments is difficult, especially when the robots must navigate rough or soft terrain or overcome obstacles.[32]

Since the robotics field integrates the disciplines of locomotion, vision, cognition, and navigation, the design of a ground mobile robot is extremely interdisciplinary. In terms of mechanics, ground mobile robots, except those designed for particular surroundings and surfaces (such as slithering or sticky robots), can move on wheels (W), legs (L), tracks (T), or hybrids of these principles (LW, LT, WT, LWT). [33] provides a detailed analysis of different locomotion systems, comparing them in terms of their maximum speed, obstacle-crossing ability, step/stair climbing ability, slope climbing ability, capacity to walk on soft ground, ability to walk on uneven ground, energy efficiency, mechanical complexity, control complexity, and technological readiness [34].

In summary, wheeled robots maximize speed and energy efficiency, while legged robots have higher mobility in unstructured situations. Tracked robots fall somewhere in the center and are especially well-suited to navigating soft and yielding terrain because of the huge contact surface with the ground. The chart of Figure 2-3 [32] illustrates a fairly synthetic and qualitative sketch of the characteristics of locomotion systems, with the horizontal axis denoting mobility in unstructured situations and the vertical axis denoting speed and energy efficiency. L, T, and W systems are diagonally positioned in the graph, indicating that mobility in unstructured environments is inversely proportional to speed and energetic efficiency. Hybrid combinations aim to fill the right upper zone with a combination of benefits but are constrained by the rise in mechanical complexity, which consequently results in performance trade-offs.

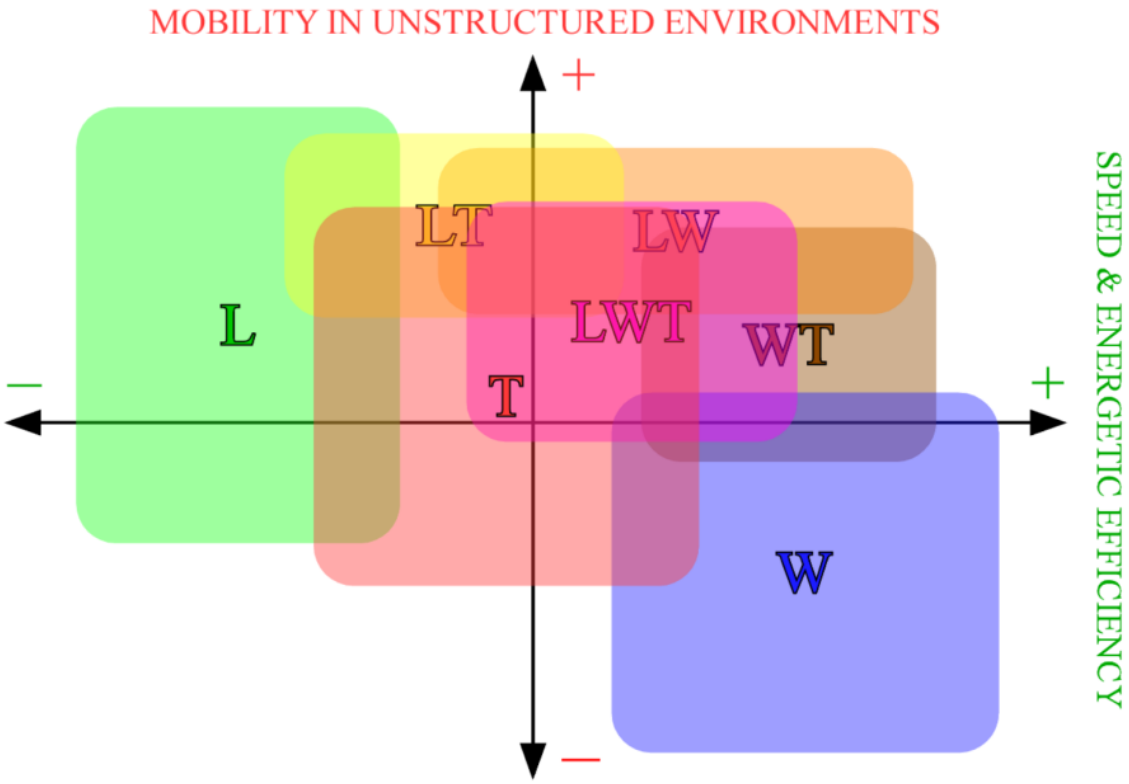

Figure 2-3 Mobility in unstructured environments vs. speed and energy efficiency of the possible hybrid locomotion systems [32].

2.3.1 Classification of ground mobile robot locomotion systems and comparison methodology

Even though certain robots in this study can travel briefly on water, this dissertation discusses locomotion techniques for robots that move mostly on land.[35]. Additionally, because they are used for extremely specialized purposes, special-purpose locomotion principles (such as jumping robots, snake-like slithering robots, and wall-adhering robots) won't be covered. Furthermore, some researchers have proposed sophisticated locomotion strategies that utilize two or more cooperative mobile robots [36]. These cooperative approaches to robot mobility, however, will not be taken into consideration because they call for elaborate supervision systems and are infrequently used; instead, only the principles of locomotion for autonomous ground robots that do not interact with other vehicles or fixed devices will be covered [32].

Based on these criteria, ground mobile robots can be divided into three major categories:

- robots with wheels (W),
- robots with tracks (T),
- and robots with legs (L).

Additionally, the combination of these locomotion principles results in a class of robots named hybrid robots. Examples of the four possible combinations that

result in hybrid locomotion systems may be found in the scientific and industrial areas. These combinations are legs-wheels (LW), legs-tracks (LT), wheels tracks (WT), and legs-wheels-tracks (LWT). Figure 2-4 summarizes the four hybrid categories as well as the three primary categories of ground mobile robots.

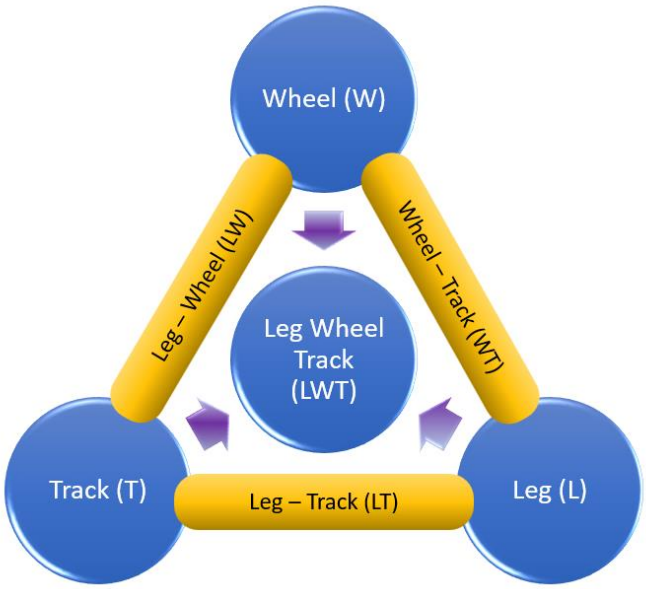

Figure 2-4 Ground mobile robot classifications

A set of features that may be objectively studied must be developed to compare locomotion systems in detail; Table 2-2 proposes a set of 10 features together with their related definitions. The remaining three features (mechanical complexity, control complexity, and technology readiness) describe system complexity and have an impact on other features, such as reliability. The first seven features (maximum speed, obstacle crossing capability, step/stair climbing capability, slope climbing capability, walking capability on soft terrains, and energy efficiency) are related to pure mobility performance and are quantitatively measurable. Since autonomy depends on energy efficiency, it is not explicitly taken into consideration.

Table 2-2 Description of the features considered in the comparison of locomotion systems. [34]

Feature	Definition
speed	maximum speed on flat and compact surfaces in the absence of obstacles
obstacle crossing	capability of crossing obstacles with random shapes in unstructured environments (e.g. rocks)
step climbing	capability of climbing up single steps and stairs in environments structured for humans
slope climbing	capability of climbing compact slopes with a sufficient friction coefficient (> 0.5)
walking capability on soft terrains	capability of walking on soft and yielding terrains (e.g. sand)
walking capability on uneven terrains	capability of walking on uneven terrains (e.g. grassy ground, rocky ground)
energy efficiency	energy efficiency in normal operating conditions, on flat and compact terrains
mechanical complexity	level of complexity of the mechanical architecture
control complexity	level of complexity of the control system (hardware and software)
technology readiness	level of maturity of the necessary enabling technologies

2.3.2 Locomotion system for Ground Mobile Robots

In this section, With reference to the criteria listed in Table 2-2, the key aspects of the various mobile robot locomotion system categories are summarized and reviewed.

2.3.2.1 Wheeled Robots

Robots with wheels are frequently employed to achieve mobility because they have a number of benefits, including a straightforward structure, high energy efficiency, quick speed, low manufacturing cost, and others. This section's goals are to give a broad overview of wheeled mobile robots, explore their mobility-related characteristics, describe the most prevalent examples of such robots, and explain wheel-terrain interaction models and suspension systems. [37]

In this manner, the section is structured: the description of the restriction to robot mobility brought on by these pure rolling situations is covered in section 2.3.2.1.1. We first discuss several wheel designs that are employed in mobile robot development and then extract the relevant kinematic restrictions. As a result, we are able to describe a robot's mobility and demonstrate that these robots can only be divided into five groups, each of which corresponds to two mobility indices.

We show several examples of wheeled mobile robot realizations using various wheel types in Section 2.3.2.1.12. The composition and characteristics of common wheel mechanics are described. The ability of omnidirectional movement, manufacturing costs, controllability, and ability to traverse different types of terrain are all design considerations for wheeled robots [38].

2.3.2.1.1 Mobility of Wheeled Robots

We discuss many types of wheels and wheel implementations in mobile robots in this section. We talk about how using these wheels restricts robot movement and come up with a classification of robot mobility that makes it possible to completely describe robot mobility regardless of the number and kind of wheels.

2.3.2.1.2 Different types of wheels

Wheeled mobile robots are commonly employed in numerous applications to achieve robot locomotion. In general, wheeled robots move more quickly and use less energy than other types of vehicles (such as tracked or legged robots). Because of their straightforward procedures and fewer stability issues, controlling them requires less work. Wheeled mobile robots are suited for a broad variety of target locations in practical applications, notwithstanding the difficulty in navigating rough terrain or uneven ground conditions. There are two options when considering a single-wheel design: a regular wheel or a unique wheel. A typical tire can be thought of as a typical wheel. Special wheels have distinctive mechanical components like rollers or spheres. Figure 2-5 depicts a typical wheel's general layout. A typical wheel design should meet the following three requirements:

1- the two offsets d and b are determined;
2- whether a mechanical design allows for steering action (i. e., to fix the wheel orientation or not);
3- choosing the appropriate steering and driving actuation (i. e., active or passive drive).

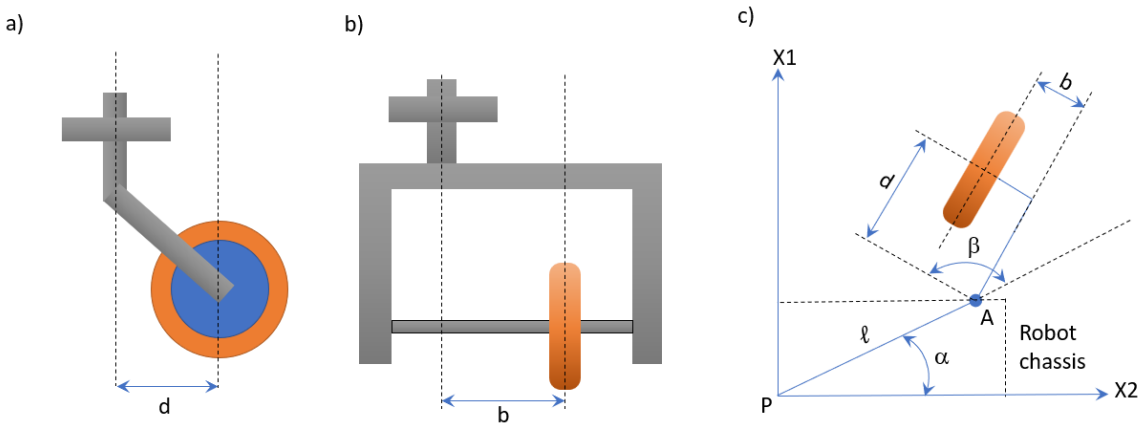

Figure 2-5 The general design of a standard wheel. (a) side view, (b) front view, and (c) top view

The kinematic parameter design issue for a single standard wheel is condition 1. 0 or a positive constant are both acceptable values for the parameter d. The wheel's lateral offset, or parameter b, is often set to zero. To provide pure rolling contact between the wheel and the ground without creating rotational slip at the contact point, a nonzero b may be chosen in a specific design. This is little utilized, and we mainly take the scenario of zero lateral offset b into consideration.

Whether or not the wheel orientation can be adjusted is a design issue with condition 2. The wheel provides a velocity constraint on the driving direction if the steering axis is fixed. The third condition involves the design dilemma of choosing whether to passively drive steering or motion or to activate it with actuators. In kinematic modeling, the offset d is crucial if steering motion is permitted. There is a nonzero offset d for a typical caster wheel, often known as an off-centered orientable wheel. The junction joining the wheel module to the robot chassis is shown as Point A in Figure 2-5. Using the steering and driving motions of the wheel module, a caster wheel creates two orthogonal linear velocity components at point A. This indicates that the motion of the robot is not further restricted in velocity by a passive caster wheel. Because any desired velocity at point A may be generated by solving the inverse kinematics problem, holonomic omnidirectional movement can be accomplished if a caster wheel is outfitted with two actuators that drive steering and driving motions independently [38].

The permitted velocity direction at point A is constrained to the wheel orientation if the offset d is set to zero. Because the wheel orientation cannot be adjusted passively in this situation, the steering motion shouldn't be passive. However, the actuation of other wheels can passively determine the driving speed. Due to the nonholonomic velocity limitation, wheel orientation is to be actively

directed in the desired velocity direction. This suggests that prior to movement, the wheel orientation should be aligned.

In conclusion, there are four main categories of standard wheels. The first is a wheel that is passively powered and has a fixed steering axis. A passive caster wheel with offset d comes in second. The third type of wheel uses an active caster wheel with an offset d, where actuators regulate the driving and steering movements. The fourth wheel is an active orientable wheel with zero offset d, where actuators are used to power steering and driving motions. Figure 2-6 depicts the architecture of each wheel type.

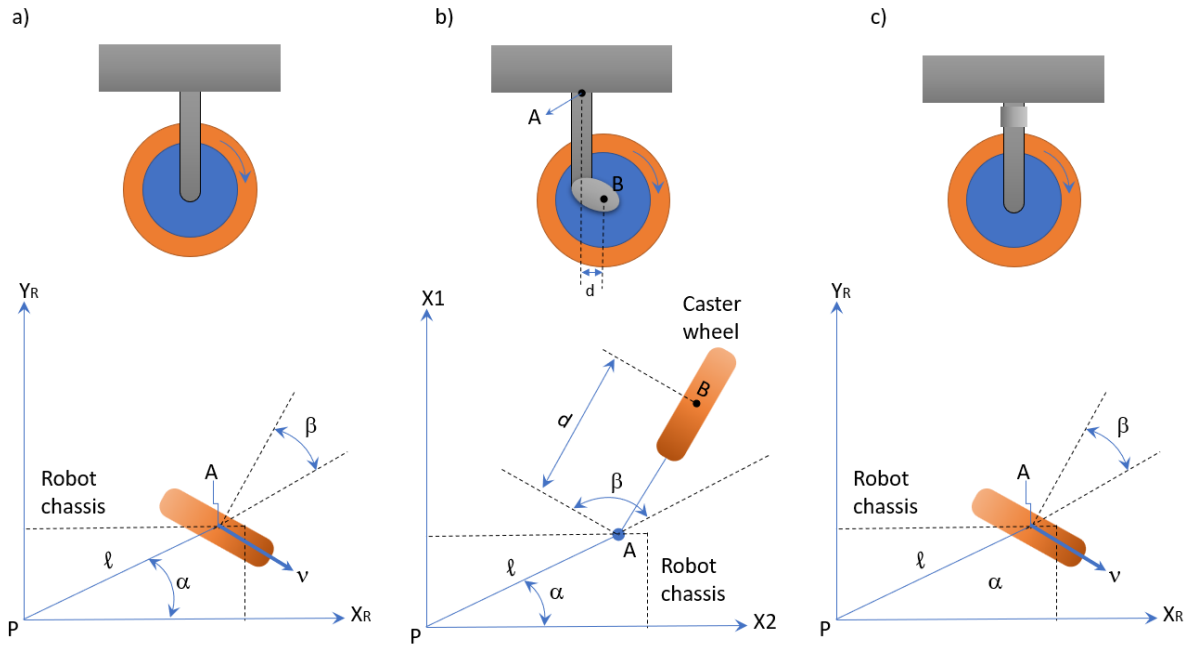

Figure 2-6 Structures of standard wheels. (a) passive fixed wheel, (b) passive or active, off-centered orientable wheel, and (c) active orientable wheel without offsets

Standard wheels are useful because of their straightforward design and high level of dependability, although robot motion is constrained by the nonholonomic velocity constraint (i.e., no sideslip condition). However, special wheels can be used to give a mobile robot omnidirectional motion, ensuring three degrees of freedom for plane travel. We look at the Swedish wheel and the spherical wheel as two examples of common special wheel designs [38].

Figure 5 shows the Swedish wheel. The outer rim of the wheel is lined with tiny passive free rollers. The nonholonomic velocity limitation is removed by using free rollers. The wheel moves laterally because passive rollers are free to rotate around the axis of rotation. As a result, the driving velocity should be managed, and the lateral velocity should be passively determined by the other wheels' actuation.

In Figure 2-7, a spherical wheel is seen. Rollers that make rolling contact with the sphere limit its ability to rotate. Driving rollers and supporting rollers are two categories for the rollers. The rolling contacts operate as nonholonomic limitations

while the driving rollers actuate the sphere, causing the motion of the sphere module to become holonomic. This suggests that the robot can be moved at any time at any desired linear or angular velocities. A holonomic omnidirectional mobile robot can be created by using the spherical wheel, and the robot establishes smooth and continuous contact between the sphere and the ground. The sphere-supporting mechanism's design is challenging, and because of the point contact, the payload must be extremely light. Another disadvantage is that when moving over the unclean ground, the sphere's surface may become polluted, and uneven ground is challenging to navigate. The practical use of the spherical wheel is constrained by these shortcomings. An example of the use of spherical wheels can be found in [39] and [40]. The nonholonomic manipulator in [41] and the passive haptic system in [42] are two examples of how the spherical structure can be used for specialized robotic transmissions.

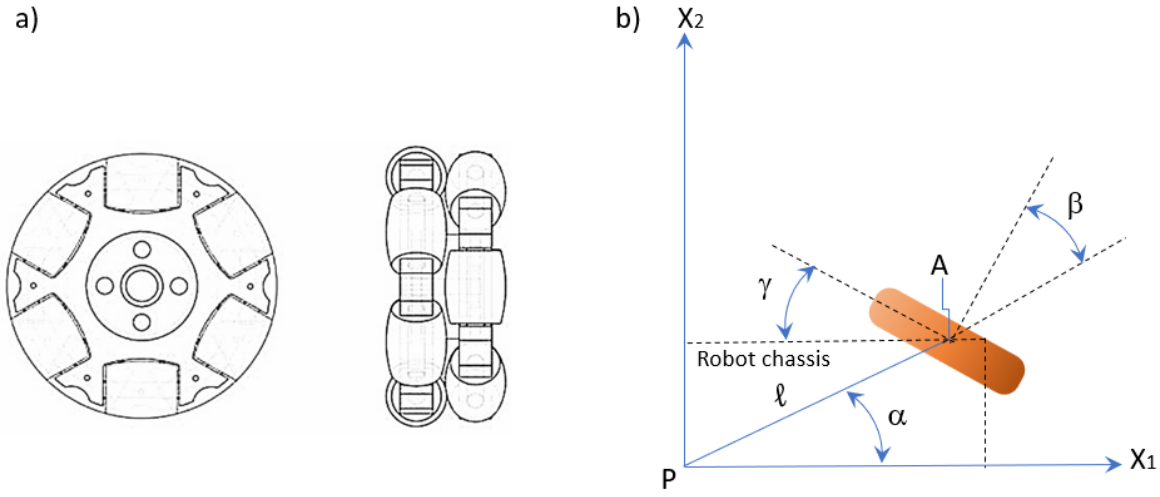

Figure 2-7 (a) Swedish wheel, (b) attachment of a Swedish wheel

2.3.2.1.3 Kinematic Constraints

As a first stage, we suppose that the mobile robot under investigation consists of a rigid cart with nondeformable wheels and is traveling horizontally. The posture vector $\xi = (x\ y\ \theta)^T$, where x and y are the coordinates of a reference point P on the robot cart and θ is the orientation of a mobile frame linked to the robot with respect to the inertial frame, representing the position of the robot on the plane (Figure 2-8).

We assume that each wheel's plane remains vertical while it is in motion and that it revolves around its horizontal axle, whose orientation in relation to the cart might be either constant or variable. We make a distinction between the conventional and Swedish wheels, two fundamental types of idealized wheels.

Each time, it is assumed that there is just one point of contact between the wheel and the ground. The fact that the velocity of the material point of the wheel in contact with the ground is equal to zero leads to kinematic limitations. The kinematic constraints for a standard wheel suggest that the center's velocity is

proportional to the wheel rotation velocity and parallel to the wheel plane (nonslip condition) (pure rolling condition). Each time, it is assumed that there is just one point of contact between the wheel and the ground. The fact that the velocity of the material point of the wheel in contact with the ground is equal to zero leads to kinematic limitations. The kinematic constraints for a standard wheel suggest that the center's velocity is proportional to the wheel rotation velocity and parallel to the wheel plane (nonslip condition, pure rolling condition) [38].

2.3.2.1.4 Conventional Wheels

Now, we determine the fundamental shape of the kinematic constraint for a conventional wheel. The conventional wheel design comes in a number of modifications, as seen in Figure 2-6. We first concentrate on the orientable wheel in Figure 2-6b that is not centered. A stiff rod from A (a fixed location on the cart) to B, aligned with the wheel plane, connects the cart to the wheel center, B. The rod can revolve around a fixed vertical axle at point A, whose length is indicated by the symbol d. In relation to the reference point P, the location of A is described by two constant polar coordinates, l and α. The angle β represents the rotation of the rod with respect to the cart.

The wheel's radius is represented by the letter r, while its angle of rotation on its horizontal axle is represented by the letter φ. As a result, the description includes two variables, φ(t) and β(t), as well as four constant parameters, α, l, r, and d. The kinematic constraints are generated using these notations in the manner shown below. We explicitly provide the derivation for the broader scenario related to a caster wheel (Figure 2-6 b). One only has to take into account the scenario of d = 0 and constant β (fixed wheels) or d=0 and variable β (steering wheels) for fixed or steering wheels (steering wheels) [38].

The following vector expression, $\frac{d}{dt}OB = \frac{d}{dt}OP + \frac{d}{dt}PA + \frac{d}{dt}AB$, gives us the velocity of the center of the wheel, which we first assess. The two parts together as:

$$\dot{x}cos\theta + \dot{y}sin\theta + l\dot{\theta}sin\alpha + (\dot{\theta} + \dot{\beta})dcos(\alpha + \beta) \quad (1)$$

and

$$-\dot{x}sin\theta + \dot{y}cos\theta + l\dot{\theta}cos\alpha + (\dot{\theta} + \dot{\beta})dsin(\alpha + \beta) \quad (2)$$

$r\dot{\varphi}$ and 0, which represent the pure rolling and nonslip situations, are the projections of this vector into the direction of the wheel plane, that is, onto the vectors $(\cos(\alpha + \beta - \pi/2)$, $\sin(\alpha + \beta - {}^{\pi}/_{2})$ and the vector of the wheel axle $\cos(\alpha + \beta)$, $\sin(\alpha + \beta)$. These criteria can be restated in the following compact form after some adjustments.

2.3.2.1.5 Pure Rolling Condition

$$(-\sin(\alpha + \beta) \;\; \cos(\alpha + \beta) \;\; lcos\beta)\mathcal{R}(\theta)\dot{\xi} + r\dot{\varphi} = 0 \quad (3)$$

2.3.2.1.6 Nonslip Condition

$$(-\cos(\alpha+\beta) \;\; \sin(\alpha+\beta)\, d + l sin\beta)\, \mathcal{R}(\theta)\dot{\xi} + r\dot{\beta} = 0 \qquad 4$$

R(θ) is the orthogonal rotation matrix representing the orientation of the robot with respect to the inertial frame in the earlier supplied expressions, i.e.

$$R(t) = \begin{pmatrix} cos\theta & sin\theta & 0 \\ -sin\theta & cos\theta & 0 \\ 0 & 0 & 1 \end{pmatrix} \qquad 5$$

These general expressions can be made simpler for many sorts of conventional wheels, as was previously stated. When a wheel is fixed, its center is fixed in relation to the cart and its orientation is constant. This is equivalent to a constant β and d = 0 value (Figure 2-6 a). After that, the nonslip equation becomes:

$$(\cos(\alpha+\beta) \;\; \sin(\alpha+\beta) \;\; l sin\beta)\, \mathcal{R}(\theta)\dot{\xi} = 0 \qquad 6$$

The nonslip equation for steering wheels has the following form because the center of the wheel is also fixed in relation to the cart (i.e., d = 0), with β time-varying nonslip condition equation. In Figure 2-6c, this structure was already described. With a nonzero length rod AB and a time-varying orientation angle β, the scenario given by equations nonslip condition and Pure Rolling Condition is comparable to caster wheels.

2.3.2.1.7 Swedish wheel

Similar to fixed wheels, the location of a Swedish wheel in relation to the cart is characterized by three constant parameters: α, β, and l. Characterizing the direction of the zero component of the velocity at the wheel's contact point with respect to the wheel plane requires the addition of another parameter. The angle between the rollers' axle and the wheel plane, or γ, is this parameter (Figure 2-7b).

The kinematic constraints now impose only one condition

$$[-\sin(\alpha+\beta+\gamma) \;\; \cos(\alpha+\beta+\gamma) \;\; lcos(\beta+\gamma)] \times \mathcal{R}(\theta)\dot{\xi} + rcos\gamma\dot{\varphi} = 0 \qquad 7$$

2.3.2.1.8 Robot Configuration Variables

We now take a look at a wheeled robot with N wheels of the types that were previously discussed. To distinguish variables associated with these four categories, we use the following subscripts: f for fixed wheels, s for steering wheels, c for caster wheels, and sw for Swedish wheels. N_f, N_s, N_c, and N_{sw} are used to indicate how many wheels of each type there are, where $N = N_f + N_s + N_c + N_{sw}$.

The generalized coordinate vector shown below perfectly describes the robot's configuration:

1. Posture coordinates: The posture vector is $\xi(t) = (x(t)\; y(t)\; \theta(t))^T$.

2. Orientation coordinates: the steering and caster wheels' N_s+N_c orientation angles, expressed $\beta(t) = (\beta_s(t)\beta_c(t))^T$.
3. Wheel rotation coordinates, or $\varphi(t) = (\varphi_f(t)\ \varphi_s(t)\ \varphi_c(t)\ \varphi_{sw}(t))^T$, are the N rotation angles of the wheels.

The term "set of configuration coordinates" refers to the entire set of coordinates. $N_f + 2N_s + 2N_c + N_{sw} + 3$ is the total number of configuration coordinates.

2.3.2.1.9 Restriction on Robot Mobility

The following concise form can be used to express the pure rolling conditions for fixed, steering, and caster wheels as well as the restrictions pertaining to Swedish wheels.

$$J_1(\beta_s, \beta_c)R(\theta)\dot{\xi} + J_2\dot{\varphi} = 0 \quad (8)$$

with

$$J_1(\beta_s, \beta_c) = \begin{pmatrix} J_{1f} \\ J_{1s}(\beta_s) \\ J_{1c}(\beta_c) \\ J_{1sw} \end{pmatrix} \quad (9)$$

where J_{1f}, $J_{1s}(\beta_s)$, $J_{1c}(\beta_c)$, and J_{1sw} are, respectively, $(N_f \times 3)$, $(N_s \times 3)$, $(N_c \times 3)$, and $(N_{sw} \times 3)$ matrices, whose forms directly result from the kinematic restrictions, whereas J_2 is a constant. The radii of the wheels, with the exception of the Swedish wheels, whose radii are multiplied by cosγ is in the (N×N) diagonal matrix.

$$C_{1c}(\beta_c)R(\theta)\dot{\xi} + C_{2c}\dot{\beta}_c = 0 \quad (10)$$

where $C_{1c}(\beta_c)$ is a constant diagonal nonsingular matrix with entries equal to d, and C_{2c} is a constant diagonal nonsingular matrix with elements deriving from the nonslip constraints.

The last restrictions concern the non-slip requirements for fixed and steering wheels. They are best described as:

$$C_1^*(\beta_s)R(\theta)\dot{\xi} = 0 \quad (11)$$

Where

$$C_1^*(\beta_s) = \begin{pmatrix} C_{1f} \\ C_{1s}(\beta_s) \end{pmatrix} \quad (12)$$

In equation 12 C_{1f} and $C_{1s}.(\beta_s)$ are matrices $(N_f \times 3)$ and $(N_s \times 3)$, respectively.

It's crucial to note that the requirements (equation 11) affecting the fixed and steering wheels are the sole ones responsible for the limitations on robot movement.

These circumstances suggest that the vector $R(\theta)\dot{\xi}$ is a member of $N[C_1^*(\beta_s)]$, the null space of the matrix $C_1^*(\beta_s)$. Because J_2 and C_{2c} are nonsingular matrices, there exists a vector $\dot{\varphi}$ and a vector $\dot{\beta}_c$ for each $R(\theta)\dot{\xi}$ meeting this condition, and they both satisfy requirements (equation 8) and (equation 9), respectively.

Clearly rank $C_1^*(\beta_s) \leq 3$. It is impossible for the plane to move in any direction if it equals 3, which results in the equation $R(\theta)\dot{\xi} = 0$. More generally, limitations on robot mobility are associated with the rank of $C_1^*(\beta_s)$, as will be covered in more depth in the sections that follow.

Noting that condition (11) has a clear geometrical meaning is important. The robot's mobility may be understood as an instantaneous rotation around the instantaneous center of rotation (ICR), whose location in relation to the cart may change over time. Any location on the cart has a velocity that is always orthogonal to the line between that point and the ICR. This is especially true for the fixed positions on the steering wheel and fixed places on the fixed wheels of the cart. The nonslip criterion, on the other hand, denotes that the wheel center's velocity is parallel to the wheel plane. These two facts suggest that the ICR is where the fixed and steering wheels' horizontal rotation axles cross (Figure 2-8). This is the same as the requirement that rank $C_1^*(\beta_s) \leq 3$ [38].

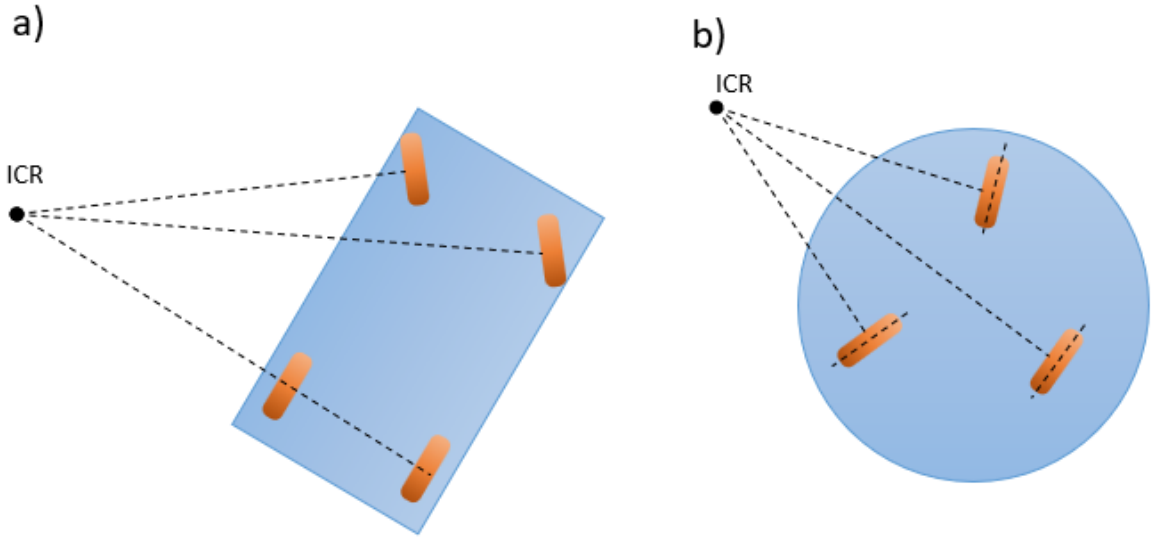

Figure 2-8 The instantaneous center of rotation. (a) car-like robot; (b) three-steering-wheels robot

2.3.2.1.10 Characterization of Robot Mobility

As previously stated, the rank of $C_1^*(\beta_s)$, which relies on the robot design, directly affects the robot's mobility. The degree of mobility δ_m is defined as:

$$\delta_m = 3 - rank\,[C_1^*(\beta_s)] \qquad 13$$

Let's investigate the case rank first. The robot is believed to have at least two fixed wheels based on the symbol $C_{1f} = 2$. The ICR, whose location in relation to the cart is set in such a manner that the only motion allowed is a rotation of the cart around this fixed ICR, is formed when there are more than two fixed wheels. Obviously, such a design is unacceptable from the user's perspective. Therefore, we take that position. $C_{1f} \leq 1$.

Moreover, we assume that:

$$rank\,[C_1^*(\beta_s)] = rank\,C_{1f} + rank\,[C_{1f}(\beta_s)] \leq 2 \qquad 14$$

According to the following set of circumstances, these two hypotheses are equivalent:

1. All of the robot's fixed wheels, if there are any, are mounted to a single common axle.
2. The steering wheel centers are not a part of the fixed wheels' common axle.
3. The number of steering wheels that may be independently orientated to maneuver the robot is equal to rank $[C_{1s}.(\beta_s)]$.

This figure is referred to as the steerability level.

$$\delta_s = rank\,[C_{1s}(\beta_s)] \qquad 15$$

When a robot has more than δ_s steering wheel, the motion of the additional wheels must be synchronized in order to ensure that the ICR is present at all times.

We get to the conclusion that the two specified indices, δ_m and δ_s, meet the following criteria for wheeled mobile robots of practical interest:

1. The degree of motion meets the $1 \leq \delta_m \leq 3$. The lower limit requires that we only take into account scenarios where motion is feasible, whereas the higher bound is clear.
2. The amount of steerability satisfies $0 \leq \delta_m \leq 3$. Only robots without fixed wheels may reach the top limit, whereas robots without steering wheels fall under the lower bound.
3. The following conditions are met: $2 \leq \delta_m + \delta_s \leq 3$.

The instance $\delta_m + \delta_s = 1$ is unacceptable because it involves the robot rotating around a fixed ICR. Due to the assumptions, the examples $\delta_m \geq 2$ and $\delta_s = 2$ are not included since $\delta_s = 2$ implies $\delta_m = 1$. According to the following array, these constraints suggest that only five structures corresponding to the five pairings (δ_m,δ_s) matching the aforementioned inequalities are of practical importance.

$$\delta_m = 3\ \ 2\ \ 2\ \ 1\ \ 1 \qquad 16$$

$$\delta_s = 0\ \ 0\ \ 1\ \ 1\ \ 2 \qquad 17$$

The form type (δ_m,δ_s) robot will be used to denote each sort of structure in the sentences that follow.

2.3.2.1.11 Five Classes of Wheeled Mobile Robots

The five kinds of wheeled robot constructions are now briefly described, together with the mobility limitations that are specific to each class. next Section includes details and examples [24].

2.3.2.1.11.1 Type (3,0) Robots

These robots just have Swedish or caster wheels instead of fixed or steering wheels. These robots are known as omni-mobile because they have complete planar mobility, or the ability to travel in any direction without having to reorient.

2.3.2.1.11.2 Type (2,0) Robots

These robots lack steering wheels in favor of one, two, or more fixed wheels that share an axle. Mobility is bound in the sense that the velocity $\dot{\xi}(t)$ at a given posture $\xi(t)$ is required to fall within a two-dimensional distribution covered by the vector fields $R^T(\theta)s_1$ and $R^T(\theta)s_2$, where s1 and s2 are two constant vectors covering $N(C_{1f})$ The wheelchair is a common illustration of one of these robots.

2.3.2.1.11.3 Type (2,1) Robots

These robots feature at least one steering wheel and no fixed wheels. If there are many steering wheels, the orientations of each one must be synchronized in order for $\text{rank}[C_{1s}.(\beta_s)] = \delta_s = 1$ The velocity $\dot{\xi}(t)$ must fall into a two-dimensional distribution that is covered by the vector fields $R^T(\theta)s_1(\beta_s)$ and $R^T(\theta)s_2(\beta_s)$, where $s_1(\beta_s)$ and $s_2(\beta_s)$ are two vectors that span $N(C_{1s}(\beta_s))$.

2.3.2.1.11.4 Type (1,1) Robots

These robots feature one or more steering wheels with centers that are not on the common axle of the fixed wheels and coordinated orientations. They also have one or more fixed wheels on a single common axle. The orientation angle of one randomly selected steering wheel serves as a parameter for a one-dimensional distribution that the velocity $\xi(t)$ must fit within. This category includes mobile robots designed to resemble conventional cars (often referred to as "car-like robots").

2.3.2.1.11.5 Type (1,2) Robots

These machines feature two or more steering wheels but no fixed wheels. In order to meet the requirement $\text{rank}[C_{1s}.(\beta_s)] = \delta_s = 2$, the alignment of any additional steering wheels must be synchronized. The velocity $\dot{\xi}(t)$ must fit into a one-dimensional distribution with parameters determined by the orientation angles of two randomly selected steering wheels [24].

2.3.2.1.12 Wheeled Robotic Structures

Wheeled mobile robots have a wide range of design configurations. The choice of wheel types, the positioning of wheels, and the choice of the kinematic parameters are design issues for a single-body mobile robot. Design goals should be defined in relation to the specific environments and duties, as well as the robot's initial and ongoing operating expenses. After a classification of robot architectures by the number of wheels in this section, features will be introduced with an emphasis on widely used models.

2.3.2.1.12.1 One Wheeled Robot

Without dynamic control to keep its body balanced, a robot with just one wheel is essentially unbalanced. A unicycle is an example of this. In order to increase stability in the lateral direction, a robot with a rugby-ball-shaped wheel can be utilized as a version of a unicycle, as investigated in [43].

A single-wheel robot can alternatively be considered a spherical robot. For dynamic stability, a balancing mechanism like a spinning wheel is used. The excellent maneuverability and minimal rolling resistance of this method are benefits. However, due to the need for extra balancing devices, the difficulty of control, and the lack of pure dead reckoning position estimate, single-wheel robots are rarely employed in practical applications. A spherical robot illustration can be seen in [44].

2.3.2.1.12.2 Two Wheeled Robots

Two broad categories of two-wheel robots are depicted in Figure 2-9. Robot of the bicycle type is shown in Figure 2-9a. It is typical to drive a rear wheel while steering the front. A balancing mechanism isn't always necessary for bicycle-type robots because their dynamic stability improves with speed. The benefit of this strategy is that the width of the robot can be decreased. A bicycle type, on the other hand, is rarely employed because it loses its position when the robot is motionless. An inverted-pendulum-style robot is seen in Figure 2-9 b. It is a robot with a two-wheel differential drive.

By precisely locating the center of gravity on the wheel axle, static stability can be attained. However, dynamic balancing control, which is comparable to the typical control problem for an inverted pendulum, is frequently used. Comparing two-wheel robots to those with more than three wheels, one can lower the size of a robot. A popular use for a pendulum-type robot is to construct a four-wheel robot out of two of them coupled together. When it reaches the stair, the robot can then climb it by elevating its front wheels. The fact that control effort is constantly needed for dynamic balancing is a significant drawback. Robots of the inverted-pendulum type are exemplified in [45] and [46].

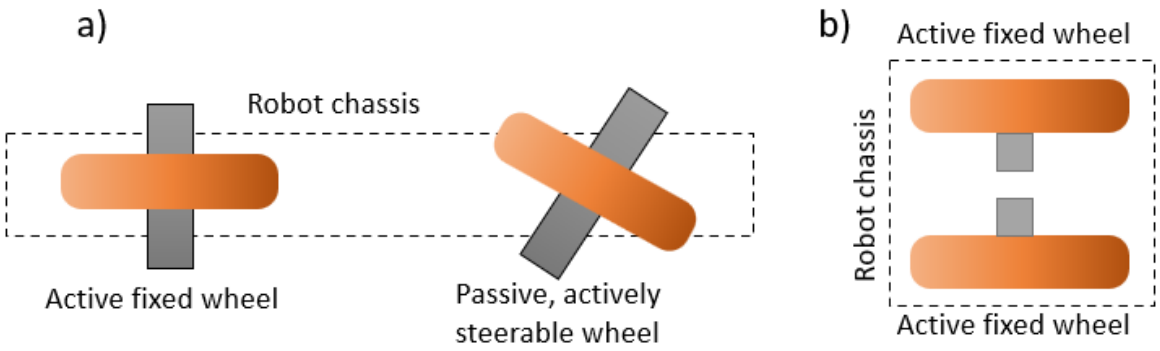

Figure 2-9 (a) Bicycle-type robot and (b) inverted-pendulum- type robot

2.3.2.1.12.3 Three Wheeled Robots

The most popular structure for wheeled robots is one with three wheels since it is structurally stable and has a straightforward design. Depending on the choice of specific wheel types, there are numerous designs. Three-wheel robots can be built using any wheel introduced in this Section. Five well-known design examples are discussed in this section (Figure 2-10):

1. two-wheel differential drive,
2. synchronous drive,
3. omni-mobile robot with Swedish wheels,
4. omni-mobile robot with active caster wheels,
5. omnidirectional robot with steerable wheels.

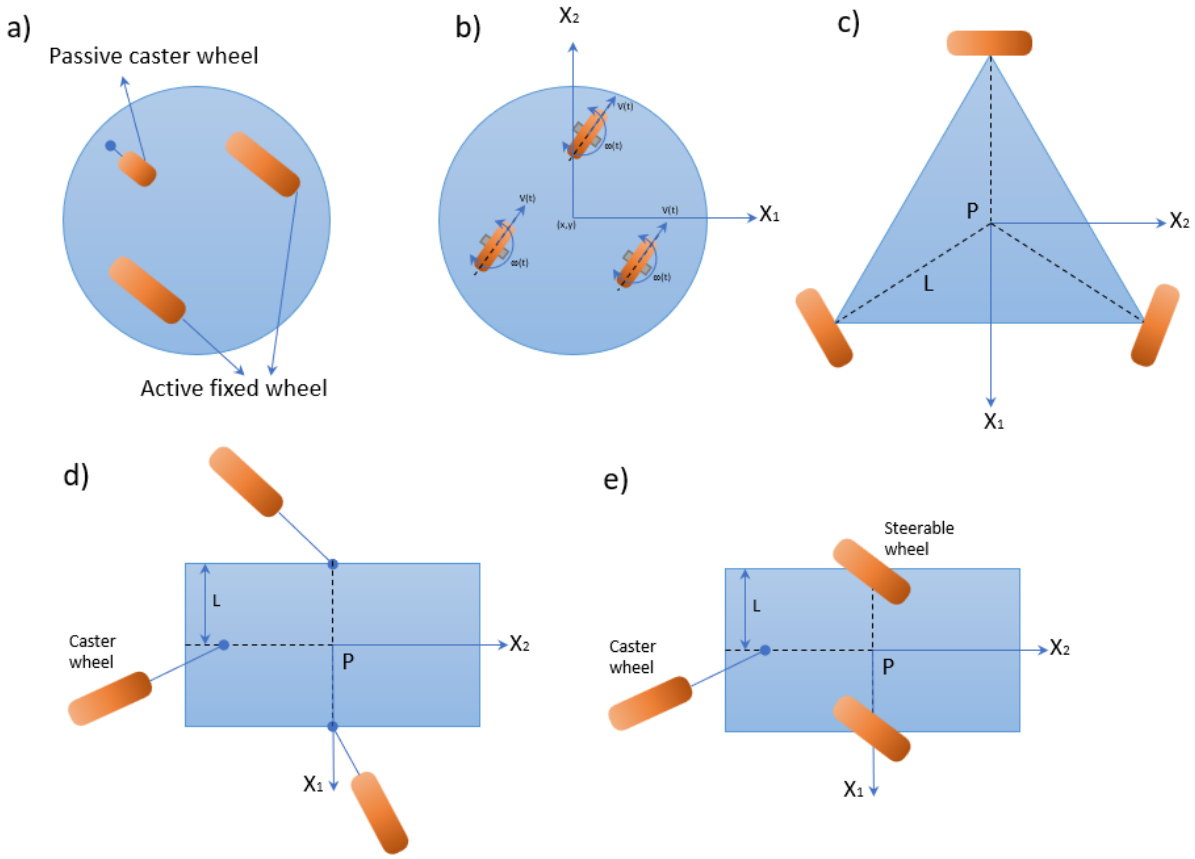

Figure 2-10 (a) Two-wheel differential drive, (b) synchronous drive, (c) omni-mobile robot with Swedish wheels, (d) omni-mobile robot with active caster wheels, and (e) omnidirectional robot with active steerable wheels

2.3.2.1.12.4 Two-Wheel Differential-Drive Robot

One of the most common designs is a two-wheel differential-drive robot, which has two active fixed wheels and one passive caster wheel. The robot may be classified as a type (2,0) robot. By adding passive caster wheels, the robot may be made into a four-wheeled device. The robot's main benefits may be summed up as follows:

- a straightforward mechanical design, a straightforward kinematic model, and inexpensive production.
- There is a turning radius of zero. Expanding obstacle limits by the robot radius r makes it simple to calculate the obstacle-free region for a cylinder.
- Errors in systems are simple to calibrate.

However, it has the following drawbacks:

- Moving uneven surfaces is difficult. In the event that one of the active wheels loses touch with the ground while the robot is traversing rough terrain, its orientation may abruptly shift.
- There is only two-way movement possible.

2.3.2.1.12.5 Synchronous-Drive Robot

Orientable wheels that are either centered or off-centered can be used to build synchronous-drive robots. Each wheel's steering and driving movements are mechanically connected by belts or chains and operated simultaneously, ensuring that the wheel orientations are constant. A synchronous drive robot's kinematic model is the same as that of a robot of type (1,1), the unicycle. In light of this, omnidirectional motion, i. e., motion in any direction may be produced by turning the steering wheels in the direction of the desired velocity. The robot chassis' orientation, however, cannot be altered. A turret may be used sometimes to alter the body's orientation. The fact that the synchronous-drive robot can move in all directions with just two actuators is by far its greatest benefit. Motion control requires less effort since the mechanical construction ensures synchronized steering and driving actions. The fact that odometry data is generally precise and driving forces are equally distributed among all the wheels are further benefits. The disadvantages of this strategy are as follows:

- complex mechanical design.
- Wheels may move at different speeds if the chain transmission has backlash or a loose link.
- Due to nonholonomic velocity restrictions, omnidirectional mobility requires that the wheel orientations be aligned to the desired velocity direction before moving.

2.3.2.1.12.6 Omnimobile Robot with Swedish Wheels

According to the Five classes of wheeled mobile robots' nomenclature, the omni-mobile robot with Swedish wheels falls under type (3,0). A holonomic omnidirectional robot must have at least three Swedish wheels. The ease of building omnidirectional mobile robots is a significant benefit of the Swedish wheel. A holonomic omnidirectional robot must have at least three Swedish wheels. Since active steering or wheel modules are not necessary for the construction of omnidirectional robots, the mechanical architectures of the actuating elements may be kept simple. However, a wheel's mechanical construction gets a little more intricate. The Swedish wheel has the disadvantage of vertical vibration due to discontinuous motion-induced connections. A number of mechanical designs have been put out to address this issue; examples may be seen in [47] and [48]. It's comparatively low durability as compared to traditional tires is another disadvantage. [49] gives an illustration of a robot employing Swedish wheels.

2.3.2.1.12.7 Omnimobile Robot with Active Caster Wheels

Using at least two active caster wheels, a holonomic omnidirectional robot may be built, and the robot also belongs to type (3,0). Regardless of the wheel orientations, the robot may be programmed to produce any linear or angular velocity. The downsides of Swedish wheels, such as vertical vibrations or longevity

issues, may be overcome since the robot employs normal tires. In [50], an example is given. The following list of drawbacks for this robot may be summed up:

- When the space between the wheels is too close together, instability may occur because the footprint's placement shifts in relation to the robot's chassis.
- A sudden shift in wheel orientations might occur if the robot abruptly changes its direction of motion to the opposite one. This phenomenon, known as the "shopping-cart effect," may cause sudden, high steering velocities.
- If a driving motor is mounted directly on the wheel, steering movements will cause the motor's wires to wind up. A gear train should be used to convey the input angular velocity from the driving motor, which is coupled to the robot chassis, in order to prevent this. The mechanical system here gets fairly intricate.
- More than four actuators are utilized if a robot has more than two active caster wheel modules. It takes three actuators at the very least to produce holonomic omnidirectional motion, hence this system is overactuated. As a result, actuators need to be precisely regulated in a synchronized manner.

2.3.2.1.12.8 Omnidirectional Robot with Active Steerable Wheels

Omnidirectional robots may also be constructed using centered orientable wheels; at least two modules are needed. The active caster wheel and the centered orientable wheel vary significantly in that the wheel orientation must always coincide with the intended direction of motion, as determined by inverse kinematics. Given that it is a robot of type (1,2), this fact suggests that it is nonholonomic and omnidirectional. In [51], the control issue is addressed. The mechanical disadvantages resemble those associated with employing active caster wheels (i. e., many actuators, and complicated mechanical structures). Allowable steering angles are constrained to prevent wiring issues since, in many situations, the driving motor is directly connected to the driving axis. Additional to the five types mentioned previously, there are many other design options for three-wheel robots. To increase stability, the aforementioned ideas can be used for four-wheel robots. Additional wheels can be passive wheels without imposing further kinematic restrictions. The inverse kinematics problem needs to be solved in order to add active wheels and control them. Robots with four wheels need suspension to stay in contact with the ground and keep their wheels from floating over uneven surfaces.

2.3.2.1.13 Robots with Four Wheels

Our attention is drawn to the car-like construction among the numerous four-wheel robots. The Ackermann steering geometry, which has a car-like construction, is seen in Figure 2-8a. To maintain the same instantaneous center of rotation, the front two wheels should be guided simultaneously. The slightly varying rotational curvatures make it obvious that the orientations of the two

front wheels are different. Since this solution is kinematically identical to having one orientable wheel, the robot falls within the category of robot type (1,1). A car-like robot has the significant benefit of being stable when moving at high speeds. However, a little complex steering system is needed. A differential gear is necessary to provide pure rolling of the rear wheels during the turning action if the rear wheels are powered. The turning radius becomes non-zero if the front wheel's steering angle is less than 90 degrees. Parking motion control in a crowded area is so challenging.

2.3.2.1.14 Special Applications of Wheeled Robots

2.3.2.1.14.1 Articulated Robots

A robot can be upgraded to an articulated robot, made up of trailers and a robot. The luggage-transporting trailer system at supermarket shops is a common illustration. A mobile robot can benefit in several ways by utilizing trailers. Robots that are modular and reconfigurable, for instance, may adapt their design to different service duties. The most basic design of an articulated robot is that of a vehicle with several passive trailers. A proof of controllability and the creation of open and closed-loop controllers employing canonical forms, such as the chained form, have both become obvious from the perspective of control. The choice of wheel types and choices about the link characteristics are design considerations for trailer systems. It is helpful for real-world applications if trailers can follow the towing robot's course. By utilizing a unique design of passive steering mechanism for trailers, passive trailers may follow the direction of a towing robot within a tiny error; for example, see [52].

Active trailers, on the other hand, are an option. Active trailers come in two different varieties. The initial strategy is to activate the trailers' wheels. Two-wheel differential-drive robots can be utilized as active trailers, and the connecting joints are passive. Accurate path-following control is possible with this kind of active trailer. The second strategy involves acting on the connecting joints. The trailer's wheels are passively propelled. The robot may travel in snake-like motions without the need for wheels by properly actuating the connecting joints. An active prismatic joint can be used as an alternate design to attach two trailers and elevate the one next to them. A trailer system can climb stairs and travel across tough terrain by permitting vertical mobility. [53]

2.3.2.2 Legged Robots

Robots with legs may move about more freely than other types of machines, which makes them useful in a variety of applications on both smooth and rocky surfaces. They need a significant amount of energy and are, nevertheless, quite slow. Legged robots often have several actuators and a sophisticated control architecture.

There are robots with two legs (influenced by humans), four legs (inspired by quadrupeds), and more than four legs (inspired by more than four-legged animals), all of which were developed as mobile, legged machines (inspired by insects). Despite the fact that the number of legs is the most obvious way to categorize legged robots, the gait pattern which can be either static or dynamic is what matters most.

Similar to sluggish insects, robots with a static gait are always balanced because their gait is designed so that the robot's center of gravity's vertical projection always stays within the polygon created by the locations at which the legs make contact with the ground. Using the appropriate stability indices, the gait is constructed after the stability of the robot is evaluated [54].

The robot, however, is not always balanced while moving with a dynamic gait, much like fast-moving, jogging, trotting, or galloping animals [55]. This form of mobility obviously demands a far more sophisticated control system:

- while the dynamic gait design must also be based on the dynamic model, the static gait design may solely be based on the kinematic model;
- while with the dynamic gait, leg trajectories must be adjusted as a function of the robot's speed, varied robot speeds may be obtained with the same leg motions executed at varying rates;
- in contrast to the dynamic gait, which requires correct movement to reach a rest position, the static gait allows the robot to stop in any posture and maintain equilibrium;
- the dynamic gait makes it difficult to account for outside disturbance factors and necessitates thorough motion planning.

Additionally, the mechanical design has a role in the increased complexity of the dynamic gait. For example, each robot leg needs to have multiple degrees of actuated flexibility and, ideally, force sensors on its feet in order to walk dynamically.

Dynamic walking, on the other hand, offers a host of benefits. The energy efficiency is greater, to start with: with the static gait, the robot continually utilizes power to modify its configuration, but kinetic energy is lost with each step, but with the dynamic gait, the majority of kinetic energy is preserved. Additionally, the dynamic gait effectively shields the body from the uneven ground and counteracts outside disturbance effects.

Model-based dynamic gait control techniques may be divided into two primary categories: those based on the zero-moment point (ZMP) concept and those based on passive dynamic walking and limit cycle walking. [56] [57] [58]

The pressure center of the ZMP method is supposed to stay inside the polygon of the foot that is in contact with the ground. The motions are cautious and steady, yet neither they seem natural nor are they really energy-efficient. As gravity and inertial effects play a significant role in the creation of motion, passive-dynamic and limit-cycle walkers, in contrast, are more realistic and energy-efficient.

Additionally, rigorous ZMP walking does not allow for the flight phase that underlies many dynamic actions like sprinting and hopping. Numerous experts believe that ZMP walking is a quasi-static gait due to all of these factors. On the other hand, walkers with limit cycles and passive dynamics can execute movements with flying phases. In reality, they might be seen as bipedal or quadrupedal evolutions of the one-legged hopping robots developed by Raibert and his colleagues in 1986 and afterward (1984).

The explanation of these control strategies is outside the purview of this work, however, it is significant to highlight that the fundamental barrier to the development of legged robots with dynamic gaits is the real-time implementation of these strategies. However, during the past ten years, legged mobile robots with enhanced dynamic walking capabilities, agility, and balance equivalent to humans and animals have been produced owing to advancements in microprocessor technology.

In terms of biped locomotion, the most sophisticated humanoid robots use their arms and upper bodies to help them move, resulting in a dynamic gait that is similar to a human's with extended legs, as opposed to the unnatural stride of the earliest biped robots with bent legs. Additionally, these robots have the ability to absorb blows and get up on their own in the event of falls caused by powerful unanticipated external forces or slick surfaces [59]. They are also capable of sophisticated activities like dancing. [60]

These cutting-edge humanoid biped robots have mostly been created and tested up to now for research purposes, and their high cost restricts the spectrum of potential uses. A rising number of small-scale humanoid robots are now being sold commercially. Two examples are Nao by Aldebaran Robotics and Robonova by Hitec [61] [62]. However, these robots are made for inside entertainment rather than outside use. Contrarily, quadruped robots capable of extremely unstructured situations and with superior dynamic walking skills are currently on the market. Bigdog is a quadruped robot made by Boston Dynamics that is 1 meter tall, 1 meter long, and 90 kg heavy. It is propelled by a diesel engine that powers a hydraulic actuation system (Figure 2-11a). Three active degrees of freedom are included in each leg, and the lower leg also has passive linear pneumatic compliance. BigDog can move on uneven ground and up to 35-degree slopes at speeds up to 0.8ms-1 while pulling 50 kg cargo. [63]

Robot size can be reduced for applications with minimal payloads, such as surveillance. On this lower scale, it is possible to minimize control complexity while maintaining adequate motion performance without increasing the complexity of the leg design. For instance, RHex, a hexapod robot with compliant legs and a self-stabilizing gait that was created by a team of six American and Canadian institutions, is inspired by cockroaches (Figure 2-11b). Despite having only one actuator on each leg and a straightforward mechanical architecture, RHex is capable of a range of actions like walking, sprinting, leaping over obstacles, and climbing stairs. [35] Whegs, created by Case Western Reserve University, is another biologically inspired legged robot with a more straightforward leg design. It is equipped with three-spoke locomotion components [64].

On the other hand, in order to lessen the structural strains brought on by inertial effects, large-legged robots with high payloads are often operated using static gaits and move slowly. The quadruped is the most common type of mechanical design in this situation. For consolidating rocky slopes, the Hirose-Fukushima Robotics Lab created Titan XI (Figure 2-11c), which has a mass of 7000 kg and hydraulically operated legs that are 3.7 meters long. [65]

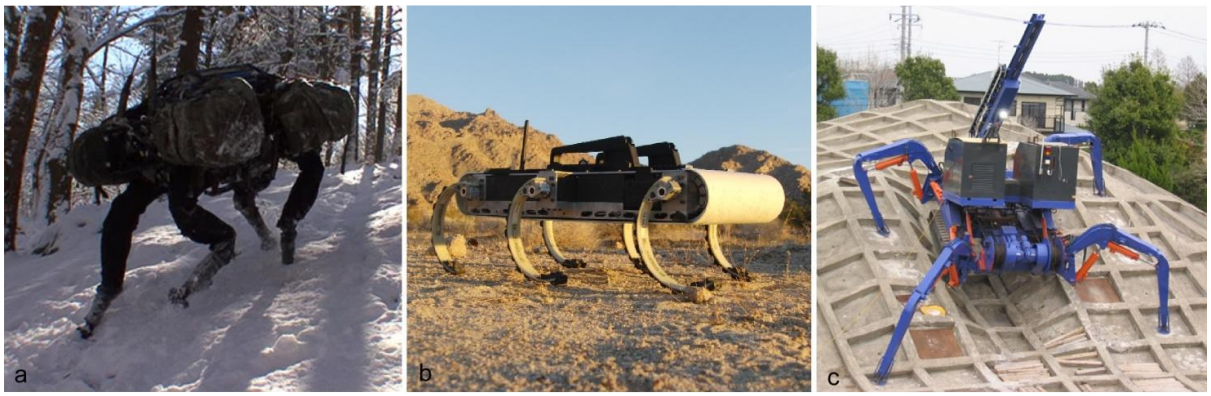

Figure 2-11 a) Legged robots: BigDog [63]*, b) Rhex* [35]*, c) Titan XI* [65].

2.3.2.3 Gait Locomotion

Gait movement is similar to the human walking stance in autonomous biped, quadruped, and hexapod insects, among other creatures. Since maintaining a humanoid robot's posture while it is moving is difficult, legged robots with Gait locomotion can be used instead. Legged robots can move in a more stable and balanced way thanks to Gait, which is a stance that is similar to how humans walk. McKenna et. al in [66] used a dynamic locomotion simulator to illustrate the coupled oscillator concept of GAIT coordination. The simulator's stepping and stance motor routines created the limbs' lifelike motion. A. Sprowitz et. al in [67] introduced a novel approach in which the leg arrangement is designed on a multi-segment, spring-loaded pantograph system. These researchers demonstrated high-speed mobility on a flat surface with the use of simulation software and tests on a four-legged, trotting, quadruped robot.

The spine plays a crucial role in Gait movement, much as it does in human anatomy.

The human spine is significantly more flexible, and it is exceedingly challenging to replicate it in an artificial spine. In his research, Khoramshahiet. al. [68] has demonstrated the impact of a dynamic spine vs a fixed spine. The Gait postures of the actively controlled and stiff spine configurations were compared by their team. Their research demonstrated that actively controlled spines had more different flying phases and double-leg postures than passively controlled spines. The sliding of the feet on the ground and directional stability are the general Gait characteristics that need to be watched for. In contrast to the stiff spine, which had the greatest speed of 0.68 m/s, the best active spine displayed a speed of 0.78 m/s. The robot's spine maintains the weight of its entire body and aids with limb coordination. The precise Gait pattern, directional stability, and body posture arrangement are all products of this limb coordination.

CPGs (Central Pattern Generators) are crucial for limb coordination. Paul and Jacques in [69] assert that the tripartite system that underlies biped movement in humans, for example, consists of supraspinal input, the spinal central pattern generating circuit, and sensory feedback. CPGs have a significant impact because they control sensory modulation. Gary and Gregory in [70] employed the Cyclic Genetic Algorithm, a unique method designed for the Gait coordination in hexapods. They tested their method on Stiquito, a six-legged robot created by Mills [71], which led to an ideal tripod gait and increased speed, with a quick learning and competent algorithm. There are two types of stability: static and dynamic. The stability when the robot is not moving at a specific time is known as static stability. A robot needs its center of gravity to lie between its footprints for static stability. Three points of contact with the ground are necessary for a stable robot, and its center of gravity must be situated halfway between the polygon created by the robot's footprint on the surface. A stable walking robot needs four footprints so that, at any given moment during walking, the polygon may be moved between the other three legs when one leg is in the air. Similar to humans, two-legged walking robots are dynamically stable because the spine, the Central Pattern Generator (CPG), and the synchronization of the limbs sustain the motion. The

intricacy of the robot's limb coordination depends on how many legs are included in the design. The number of legs the robot has determines the potential GAIT pattern. For instance, the potential number of events, or "*N*" will be [72] if the robot has *k* legs.

$$N = (2k-1)! \qquad 18$$

For a bipedal robot, there are six alternative outcomes, therefore the more legs a robot has, the more difficult it is to coordinate its limbs. In the parts that follow, the leg arrangement is covered in more detail.

2.3.2.3.1 One-legged robot

One leg is the bare minimum that a robot can have for legs. It is also known as a "hopper" since the robot can only hop because its foot only makes contact with the ground at one location. By getting off to a steady start, the hopper can navigate uneven terrain and obstacles with ease. The key issue is the hopper's dynamic stability because the robot must actively transfer its bulk to maintain a stable center of gravity. A one-legged, multi-jointed, active hopping robot's trajectory planning was researched by Zhaohong Xu and others [73]. To design a track based on the joint angle trajectory, they created a 6th-order polynomial function over the 5th-order, as illustrated in Figure 2-12.

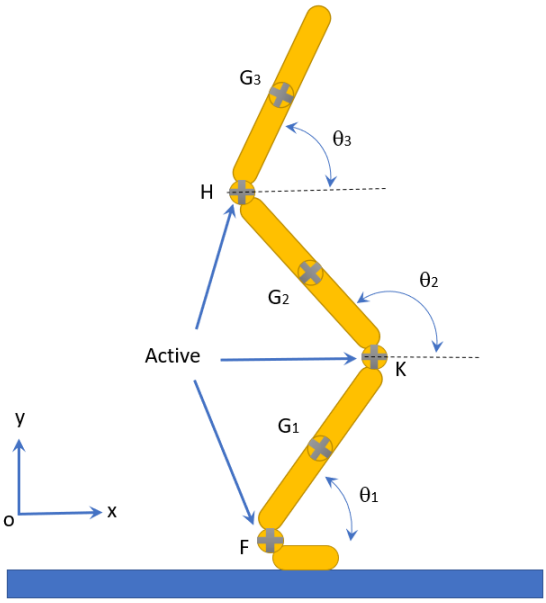

Figure 2-12 One legged multi-joint hopper [73]

Four rigid bodies and a three DOF (Degrees of Freedom) rotating joint were used in the experiment. No elastic components, such as dampers, springs, hydraulic actuators, or pneumatic actuators, were used. The construction of a correction factor under the same boundary restriction conditions was determined by plotting numerous variables against time, including vertical position, joint torque, and joint angle.

2.3.2.3.2 Two-legged or Biped Robot

The most prevalent robots in the past 10 years have been two-legged creatures known as Humanoids. There are many examples available, with the HONDA ASIMO being the most well-known and successful. It is a 130 cm tall, 50 kg–weighted humanoid robot [74]. It can sprint at a speed of 7 kph and can stroll at a speed of 2.7 kph. Its 57 DOFs are dispersed across the body. Head has three degrees of freedom, arms have eighteen, and so forth. A ping pong-playing robot named TOPIO 3.0 [75] was on display at the International Robot Exhibition in

Tokyo. It is a humanoid robot created by TOSY, a Vietnamese business. For its operation, TOPIO 3.0 combines a 200 fps camera with a processor and artificial neural networks. In addition to these, there are numerous additional instances of humanoids, including Nao, a robot that participated in the "Robocup" soccer competition, the Enona personal assistant, and self-guiding robots.

Figure 2-13 (a) Honda ASIMO[74]*, (b) TOPIO 3.0* [75]*, (c) Aldebaran Nao* [76]*, (d) Fujitsu Enon* [77]

A biped robot is capable of moving up and down stairs, running, dancing, and jumping. However, dynamic stability is still a problem for such bipeds. It was established by F. Plestan and others [78] that the theoretical control law was workable. In an underactuated planar, five-link biped robot with a stiff contact model, where the swing leg strikes the ground and an instantaneous double support phase occurs, they verified a method to demonstrate asymptotically stable walking. The ground's Zero Moment Point [56], or ZMP for short, is the location where the total of all the moments of the active forces will be zero. K. Mitobeet. al. [79] applied the ZMP control rule to two distinct biped robots in order to produce a smooth and clear motion in real-time and empirically validate it. They came to the conclusion that by giving the trunk position a reference trajectory, effective walking control was made feasible. By preview control of ZMP, S. Kajita and colleagues [80] proposed a new technique for biped walking and showed its efficacy through a simulation of climbing spiral stairs. The ZMP controller was modeled using a cart table. To correct the inaccuracy caused by the disparity between the accurate multi-body model and the simplistic cart-table model, a preview controller was created. One of the key characteristics of bipedal design is that it can have proportions similar to humans, which piques researchers' curiosity, especially in the context of human-machine interaction.

2.3.2.3.3 Three Legged or Tripod Robot

Tripod or three-legged movement is not a typical technique of mobility since they lack biological equivalents. Self-excited tripedal dynamic experimental robot STriDER was created by scientists at Romela Lab [81]. A step in this robot means that two legs are serving as a stance and the third leg is swinging. The robot moves by moving its center of gravity outside its frame and balancing itself across the gap. The robot's unique idea of actuated passive dynamic locomotion gives it stability, and it can also vary its walking orientation.

2.3.2.3.4 Four Legged or Quadrupedal

The first four-legged dog robot, AIBO, was created by Sony in the middle of 1998 [82]. In Japanese, AIBO is a word for pal or partner. Up to 2005, models from the AIBO robotic pet line were introduced annually in three generations. The robot's microphone, which could record sounds in the immediate area, was one of its key components. Additionally, it included head sensors and lights that could change to reflect its feelings. For the study of human-machine interaction, further four-legged robots that resemble animals have been created. For enjoyment, they can also be handled as pets. Research on how they react to human interaction can also benefit from the development of an emotional attachment.

Figure 2-14 (a) Sony AIBO [82] *(b) Spot* [83] *(c) TITAN VIII* [84]

Spot is a more sophisticated quadruped robot created by Boston Dynamics, is an engine-powered multi-terrain robot. Spot is an agile mobile robot that navigates terrain with unprecedented mobility, allowing you to automate routine inspection tasks and data capture safely, accurately, and frequently in different environments. Spot can carry and power up to 14kg of inspection equipment. Spot features more than 50 sensors, including joint sensors, inertial sensors, acceleration sensors, altitude sensors, an on-board CPU, and 360° camera to autonomously capture 360° images and video indoors or on challenging exterior sites. It walks with the dynamically balanced trot gait and balances itself by estimating its lateral velocity and acceleration from the detected behavior of the legs [83].

The Tokyo Institute of Technology produced Titan VIII. Another illustration of a four-legged robot is this one. Additionally, it moves with a dynamically stable trot gait pattern in which two diagonal legs are raised at the moment of motion. Arikawa and Hirose [84] experimented with a one-leg model to explore the evolution of the robot, particularly the leg mechanism. Regarding its characteristics like velocity, force, and energy consumption, they have made comments.

Being the most dynamically stable robots, quadrupeds' dynamic stability has never been a problem. According to C. Queiroz et al. [85], the quadruped's three legs must always be on the ground for static gait to be stable. They investigated the four-legged robot's static stability using a 2D+1 model that makes use of a robot description that places certain severe constraints. For the same, they created

a number of elaborate gaits. The toe's relationship to the body is described by the model. This model omitted information on the body's alignment, and the leg(s) were also lifted above the floor in height. The authors had thoroughly explained a method for applying the 2D+1 model to discover the robot's stable sequence.

2.3.2.3.5 Hexapod or Six Legged robots

The most reliable and well-liked idea for legged mobility in robots is six legs. Hexapods adopt the tripod gait, in which at least three legs are always in touch with the ground, to maintain their static stability. As the number of leg configurations is provided by N =(2k-1) [72], a vast amount - the control complexity is decreased, but the coordination of the limbs is the key issue with hexapods. A six-legged robot developed at Boston Dynamics with help from other technological colleges and funding from DARPA is called RiSE (Robots in Scansorial Environments) [86]. It is made to climb artificial objects like walls, trees, and other things, both vertically and horizontally. With biological inspiration from insects, the control and foot arrangement was created to climb steep or almost vertical walls.

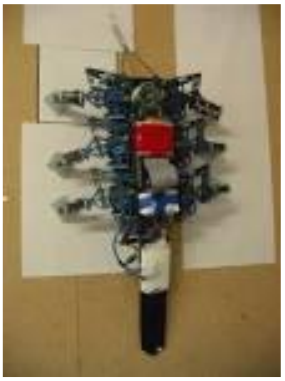

Figure 2-15 Robots in Scansorial Environments (RiSE) [86]

The central control of the legged robots may be relocated locally to each leg in order to govern movement, hence reducing the complexity of limb coordination. By ascertaining the joint rotation angle of each joint, the joint controllers [87] may separately regulate the joints. The separate joint controllers' output is combined by the leg controllers, who also establish the footprint in accordance with the input. The output of the individual leg controller is then sent on to the gait controller. Thus, breaking the complicated control problem down into manageable components facilitates the system's overall functioning.

2.3.2.3.6 Control of walking robots

For researchers, learning how a legged robot walk is never an easy feat. Robots that have been preprogrammed cannot effectively interact with the world on their own since they need to be reprogrammed for each setting. In order to enable the robot to learn things based on its interactions with the outside world, a self-learning approach must be used. At MIT in the late 1990s, Rodney A. Brooks created Genghis [88], a robot with a reinforcement learning system for walking.

By adjusting the movement of its legs, it may learn the coordinates. Positive effects come from moving ahead, whereas negative effects come from crashes. Genghis picks up new information via reinforcement signals from several sensors, including touch sensors and cameras. In their study, Kimura and colleagues [89] explain the actor-critic reinforcement learning method, which entails an actor with a stochastic policy and a critic that calculates the evaluation function for the current policy. By effectively reinforcing the time difference of the critic, the actor enhances the policy.

2.3.2.4 Tracked Robots

In the fast-growing and quickly evolving scenario of service robotics, tracked ground mobile robots are attracting the attention of many researchers in the industrial and academic worlds. Tracked locomotion is particularly suited in presence of soft and yielding terrains, but by adopting hybrid solutions the range of profitable applicability of crawlers greatly extends.

It should be pointed out that there is a vast amount of scientific literature concerning tracked mobile robots, which cannot be exhaustively quoted or included in the references for reasons of space. Selected works cited here were chosen to synthetically represent and compare the main locomotion system architectures involving tracks proposed in the research and industrial scenarios.

2.3.2.4.1 Classifications of tracked locomotion systems

Tracked locomotion systems can be classified in many different ways. Considering the functional features, the most evident classifications can be based on:

- frame architecture: non-articulated/articulated, type of articulation.
- track profile: constant profile, passively or actively deformable profile.
- track type: continuous, mechanical, Omni-tracks.

In principle, these classifications are independent, and it is possible to associate any type of frame with any type of track. This suggests using different taxonomies in parallel instead of a single taxonomy with one root node. Nevertheless, analyzing the state-of-the-art of tracked robots, it is possible to observe that usually more complex frames are associated with simpler tracks, while more complex tracks are associated with simpler frames, since the operative flexibility is generally obtained by only one design aspect, to avoid excessive mechanical complexity [33].

2.3.2.4.2 Classification of frame architectures of tracked robots

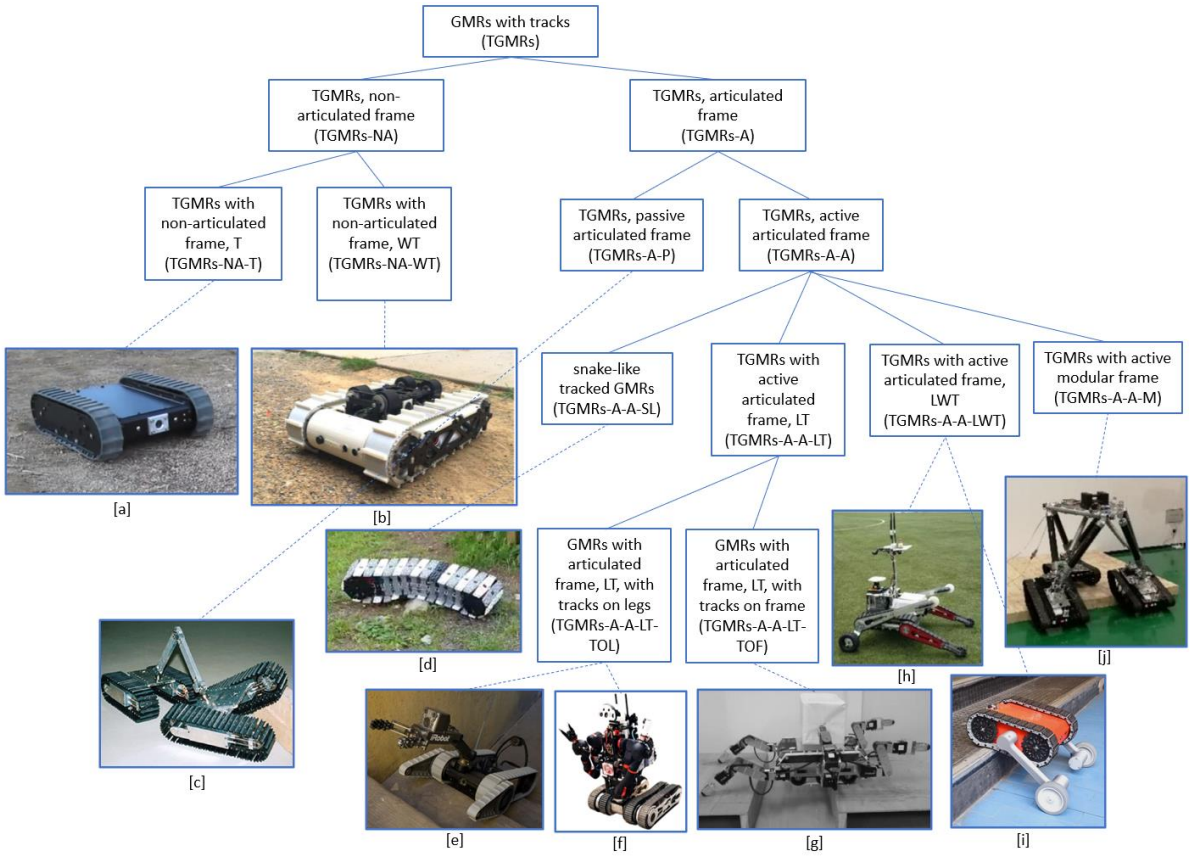

Figure 2-16 Taxonomy of tracked ground mobile robots based on frame architecture [33]. *(a)*[90] - *(b)*[91] - *(c)*[92] - *(d)*[13] - *(e)*[93] - *(f)*[94] - *(g)*[95] - *(h)*[96] - *(i)*[97] - *(j)*[98].

2.3.2.4.3 Ground mobile robots with tracks, non-articulated frame

Tracked ground mobile robots (TGMRs) can have a non-articulated frame (TGMRs-NA) or an articulated frame (TGMRs-A) (Figure 2-16). The first category is very widespread: many small-scale TGMRs equipped with two tracks performing differential steering are available on the market for surveillance and inspection tasks; an example is the Trackbot by Inspectorbots [90] (Figure 2-16). The benefits of this architecture are the extreme mechanical simplicity, and the subsequent reliability and control easiness. Moreover, if the robot is symmetric with the tracks thicker than the robot body (as for the Trackbot), and has no payload mounted externally, it can operate even after a capsize. The main limitation of TGMRs-NA is their limited capability of overcoming high obstacles, steps, and stairs: to start the climbing maneuver, the height of the obstacle at the initial contact point must be lower than the track radius, even if this condition is not strictly mandatory, depending on the friction conditions and on the position of the robot center of gravity. Therefore, some researchers have proposed an internal mechanism to shift the longitudinal position of the robot's center of gravity, improving the step climbing capabilities [99] (Figure 2-17); the obvious drawback

is the weight increase and the reduction of the internal room for hosting the payload.

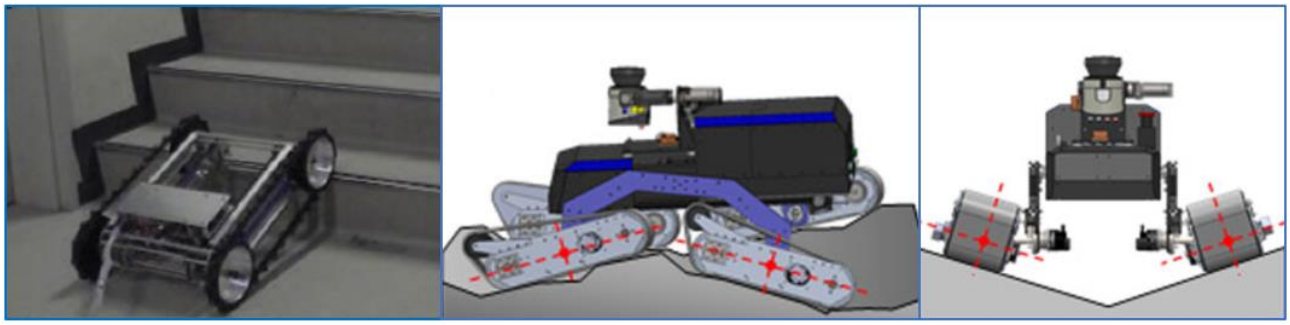

Figure 2-17 Dyjob robot [99]*, TGMRs-NA with a movable center of gravity (left); lateral view (center), and front view (right) of the TQTMR robot* [100] [33].

The TGMRs-NA scheme can be modified with the addition of retractable wheels, giving rise to hybrid wheel-track architectures (TGRMs-NA-WT), capable of a faster-wheeled locomotion whenever tracks are not required. An example is proposed in [91] (Figure 2-16); this symmetric robot can switch locomotion mode by extracting four wheels on both sides of its body thanks to an actuated slider, achieving full operativity after a capsize and maximum maneuverability, with yaw axis mobility, on flat and compact grounds.

2.3.2.4.4 Ground mobile robots with tracks, articulated frame

As regards robots with an articulated frame, we can distinguish between robots with passive articulated frames (TGMRs-A-P) or with active articulated frames (TGMRs-A-A). An interesting example of the first category is Gunryu [92] (Figure 2-16), characterized by two tracked modules connected by an arm mechanism. The arm mechanism is composed of two links connected by a revolute joint with elastic return force, and joined to the two tracked modules respectively by one spherical and one universal joint, for a total of six passive degrees of freedom between the two module bodies. Moreover, the two tracks of each module can be actively tilted with respect to the module body in opposite directions by means of a wired system, for a total of six actuated degrees of freedom (two track motors and one track tilting motor for each module). Experimental tests show that the stability and climbing capability over irregularities and obstacles increase with respect to a single module, but sacrificing maneuverability. Moreover, this design is modular, with many possible passive articulations between the tracked modules, for example in serpentine or quadruped configurations [92].

TQTMR (Tiltable Quad-Tracked Mobile Robot, Figure 2-17) is another example of TGMR with a passively articulated frame [100]; this robot consists of four driving tracks, connected to two rocker links (left and right, Figure 2-17, center) by two-degrees-of-freedom (pitch-roll) passive joints (Figure 2-17, right). This configuration shows advantages in terms of traction, maneuverability, and adaptability to terrain unevenness, while maintaining a low control complexity.

The active articulation of the frames (TGMRs-A-A) can be obtained by different approaches. A possible biologically inspired design leads to snake-like tracked robots (TGMRs-A-A-SL), suitable for inspection in narrow spaces. Some researchers have proposed snakelike tracked robots endowed with a single peripheral track rotating around a vertebral column, which can bend actively in the horizontal plane for steering and actively or passively in the vertical plane to adapt to ground unevenness. Examples are the FMT (Flexible Mono-Track) [101] and SnakeTrack [13] (Figure 2-16). The main hindrances to the development of this design concept are the reliability of the guidance of the track when the vertebral column is steered and the difficult placement of cameras for vision and navigation. To solve the last issue, in the SnakeTrack the track modules are characterized by central holes which allow intermittent vision while the track rotates.

Another possible approach for composing snake-like robots is to put tracked modules in series. For example, the modular robot proposed in [102] (Figure 2-18) is characterized by a high number of actuated degrees of freedom to allow a flexible adaptation to a given terrain, but it requires a very complex control. Moreover, a general limitation of snake-like tracked robots is their inability to perform yaw rotations and follow trajectories with sharp edges.

Figure 2-18 Snake-like tracked robot with modules in series [102] *(left); Quince robots, with front and rear active flippers* [103] *(center); TALBOT, quadruped robot with 3-DOF legs* [104] *(right)* [33].

Besides, snake-like tracked robots, which are relatively rare, TGMRs with active articulated frames (TGMRs-A-A) can be divided in:

- hybrid leg-track robots (TGMRs-A-A-LT);
- hybrid leg-wheel-track robots (TGMRs-A-A-LWT);
- TGMRs with active modular frame (TGMRs-A-A-M).

In the first case, the legs can be tracked extensions of the robot body (TGMRs-A-A-LT-TOL, Tracks On Legs) or non-tracked and connected to the main frame (TGMRs-A-A-LT-TOF, Tracks On Frame). The TGMRs-A-A-LT-TOL category includes many commercial realizations for the homeland, military, or surveillance applications. Examples are the PackBot, with two tracked swing extensions (flippers) on the front [93] (Figure 2-16), or other general-purpose tracked platforms with double (front and rear) flippers [105] [106]. For instance, the Quince GMRs (Figure 2-18, center) are characterized by four front and rear-tracked rotating legs (double flippers) and have been adopted for unmanned exploration missions inside the buildings of the Fukushima nuclear power plants

[103]. Architectures with active flippers are widely used due to their relatively simple mechanics, with higher obstacle crossing capability and operative flexibility and without a significant increase of control complexity with respect to TGMRs-NA, thus allowing an easy man-in-the-loop navigation.

Differently from most common TGMRs-A-A-LT-TOL with front flippers like PackBot, which have two tracks on each side (main track and flipper track), the architecture proposed in [107] for stair climbing has a single track on each side even if the robot body is divided into two parts connected by a revolute joint, therefore the contact between tracks and sprockets must be maintained by an upper guidance system, thus losing symmetry for full operativity after a capsize. This solution has no particular advantage with respect to other architectures and is not widespread.

In other more complex TGMRs-A-A-LT-TOL configurations, the tracks are placed on the end links of articulated legs with more than one degree of freedom. For instance, the quadruped robot TALBOT [104] (Figure 2-18, right) is characterized by four legs with three degrees of freedom each (hip, knee, ankle) and tracked end links, for a total of 16 active degrees of freedom, thus allowing static walking capabilities for obstacle crossing.

In some other examples of TGMRs-A-A-LT-TOL, the active articulated frame has not only locomotion purposes but realizes a simple retractable robotic arm that can be used both to help the robot in overcoming obstacles and to grasp objects [108]. In other more sophisticated humanoid robots belonging to the TGMRs-A-A-LT-TOL category, the tracked legs can be used to vary the vertical position of the trunk, increasing the workspace of the arms [94] (Figure 2-16).

As already said, the second subcategory of TGMRs-A-A-LT is represented by tracked robots in which the operative flexibility is augmented by means of additional legs connected to the main body (TGMRs-A-A-LT-TOF). For example, the hexapod robot presented in [95] (Figure 2-16) is equipped with six four-degrees of freedom legs and two differential steering tracks and is designed to traverse wide gaps, moreover, a quadruped gait involving only the front and rear legs can be adopted, while using the two middle legs to pick and carry objects under the robot body.

When also wheels are added to the hybrid locomotion system, giving rise to the TGMRs-A-A-LWT category, the design objective is to exploit the speed, energetic efficiency, and maneuverability of wheeled locomotion on flat and compact grounds. An example is the Kylin robot (Figure 2-16), derived from a double flipper robot with the addition of idle wheels at the four flipper ends and of two actuated wheels whose axes are fixed to the two front flippers [96]; depending on the flipper angles, the robot can be suspended on the tracks or on four wheels (two actuated and two idle, for differential steering). Also, the WheTLHLoc robot [97] (Figure 2-16) belongs to the TGMRs-A-A-LWT category, having two tracks for differential steering and two rotating legs with actuated wheels at their ends; moreover, two idle Omni wheels are placed on the robot's rear; the robot has three locomotion modes: purely wheeled, remaining suspended on the actuated wheels

and one Omni-wheel, for higher speed and range, purely tracked, and, finally, a mixed mode in which, combining the motion of legs, wheels, and tracks, the robot can climb obstacles, steps and stairs higher than the robot itself. Moreover, the robot is fully symmetric and can continue operating after a capsize.

The fourth subcategory of TGMRs-A-A is represented by tracked modules connected by a mechanism comprising actuated and passive joints, realizing a parallel kinematics system (TGMRs-A-A-M). In [98] a multi-robot system, composed of tracked modules connected by a parallel manipulator capable of carrying a payload is proposed (Figure 2-16). Even if interesting from a scientific point of view, such solutions don't seem to have real advantages compared to simpler and more compact architectures in terms of operative flexibility.

2.3.2.4.5 Classification of track profiles

Considering the track profile, TGMRs can be divided into three categories (Figure 2-19):

- TGMRs with a constant profile of the track (TGMRs-CP);
- TGMRs with a passively deformable profile of the tracks (TGMRs-PDP);
- TGMRs with an actively deformable profile of the tracks (TGMRs-ADP).

Let us note that even the track profile of robots belonging to the first category (TGMRs-CP) is not exactly constant, due to the unavoidable deformations of the tracks subject to gravity, contact forces with the terrain, and internal reactions (contacts with sprockets, idler, and carrier rollers). Nevertheless, the track supporting structure is designed to keep its shape constant, maintaining invariant the gross track profile. On the contrary, in the other two categories, the large variations of the track profiles, based on deformations in the geometry of the track-supporting structure, are functional features planned in the design phase. Most tracked robots belong to the TGMRs-CP category; for example, all the robots shown in Figure 2-16 are TGMRs-CP.

An example of TGMRs with passively deformable tracks (TGMRs-PDP) is discussed in [109]; in this robot (Figure 2-19) the carrier rollers are held by bio-inspired mechanisms, giving rise to compliance of the track profile, with benefits in terms of traction, obstacle climbing capabilities, and shock absorption; a similar solution is proposed in [110] (Figure 2-19), adopting slightly different suspension mechanisms.

While in TGMRs-PDP the deformation of the track is determined by the distribution of the interaction forces between tracks and terrain, in TGMRs with actively deformable tracks (TGMRs-ADP) the shape change is commanded by actuators. There are two possible approaches to vary the track shape: with the first approach (TGMRs-ADP-E) the length of the track varies thanks to its elasticity; with the second approach (TGMRs-ADP-NE), the track profile varies but the track doesn't undergo macroscopic elongations.

An example of TGMR-ADP-E is discussed in [111]. This robot is characterized by two wheels with a peripheral elastic track; in wheeled locomotion mode, the tracks adhere to the wheels; each wheel has an internal four-link mechanism, actuated by self-locking worm gear motors, carrying two carrier rollers; when it is required to enable tracked locomotion, the two four-bar mechanisms move the carrier rollers outside the wheel profile, lengthening the elastic track; moreover, both the track profile and the position of a rotating tail can be tuned depending on the obstacles to be climbed (Figure 2-19). This hybrid locomotion architecture has been demonstrated to be effective and reliable and has practical military and inspection applications.

Another TGMR-ADP-E is presented in [112]; this robot is characterized by two differential-steering tracks, and each track is equipped with a rotating flipper that carries an idle wheel. The flippers are variable-length, elastically loaded, and keep the tracks properly tensioned independently of the flipper angle. The flipper angle is controlled in order to change the track shape: flat and longer to maximize the contact surface on soft terrains, triangular with a variable front angle to face different obstacles.

On the contrary, the hybrid wheel-track robot proposed in [113] is an example of TGMR-AD-NE (Figure 2-19). It is characterized by two wheels and one track on each flank. Each track is supported by sprockets carried by a foldable articulated mechanism with a parallelogram outer shape. Acting on this articulated mechanism, the tracks can be folded, enabling wheeled locomotion, or unfolded for climbing obstacles, steps, and stairs.

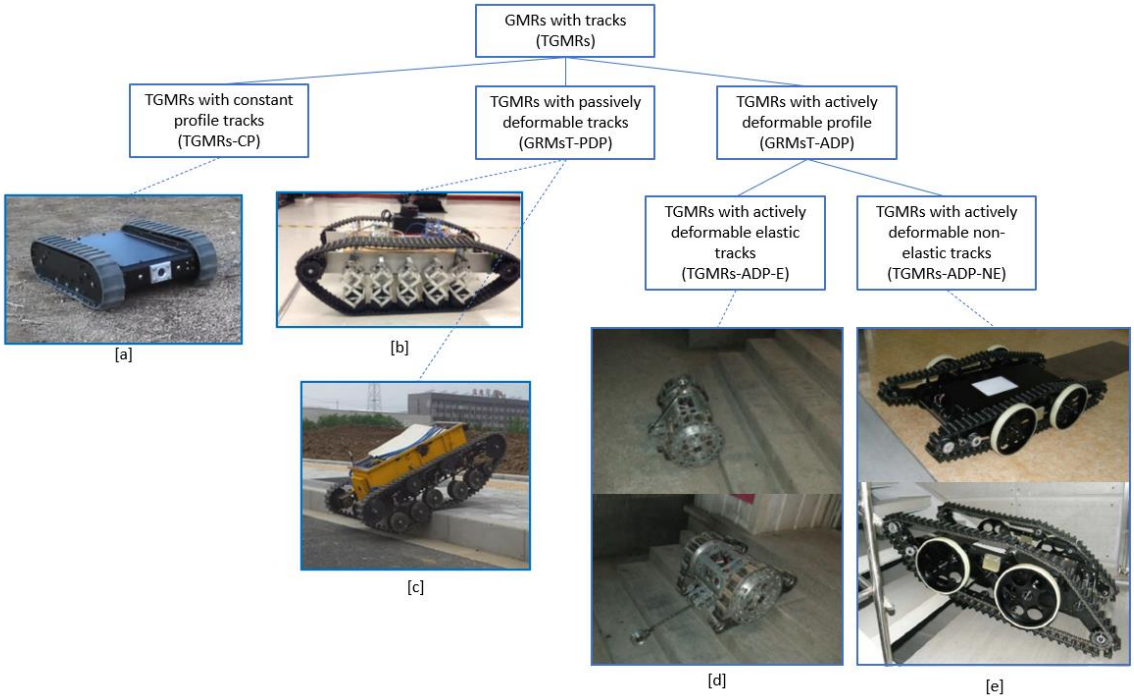

Figure 2-19 Taxonomy of tracked ground mobile robots based on track profile [33]. *a)*[114] *b)*[109] *c)*[110] *d)*[111] *e)*[113]

2.3.2.4.6 Classification of track types

On the basis of the track realization, TGMRs can be classified as (Figure 2-20):

- TGMRs with continuous tracks (TGMRs-CT);
- TGMRs with mechanical tracks (TGMRs-MT);
- TGMRs with Omni tracks (TGMRs-OT).

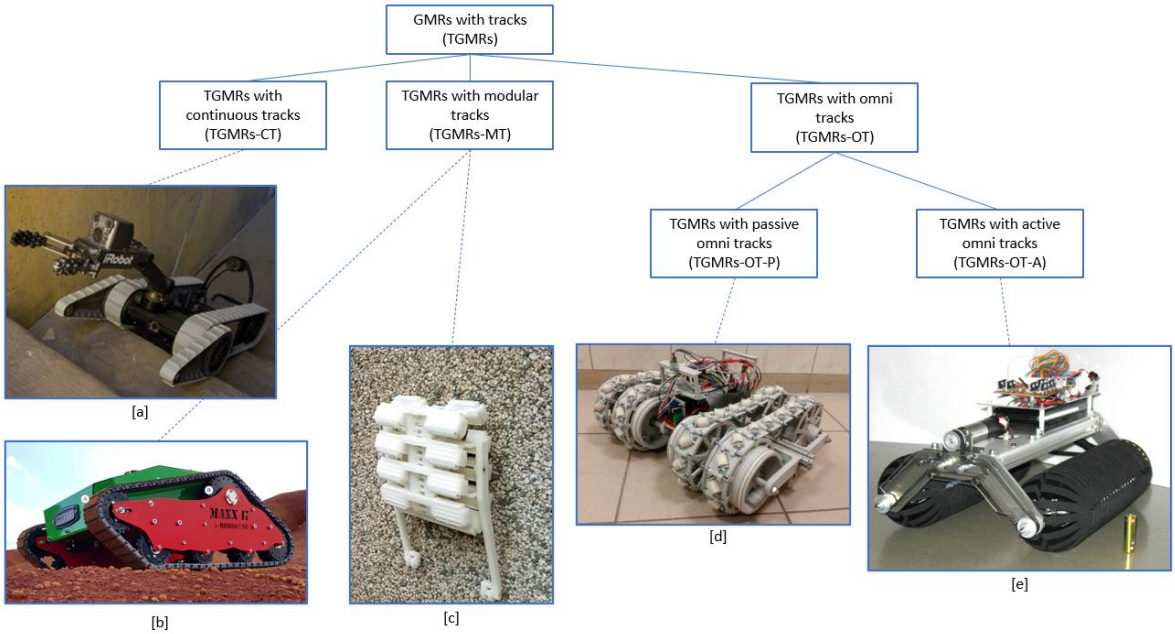

Figure 2-20 Taxonomy of tracked ground mobile robots based on track type [33]. *a)*[93] *b)*[115] *c)*[116] *d)*[117] *e)*[118]

Rubber continuous tracks are indeed the most widespread for robotic applications; for small-scale TGMRs, rubber continuous tracks without internal braiding are acceptable since the longitudinal structural stresses are small; moreover, their application is mandatory for TGMRs with actively deformable elastic tracks (TGMRs-ADP-E). For heavier TGMRs rubber tracks with textile or steel internal braiding are adopted, technologically similar to the tracks of small excavators and tracked vehicles. Continuous tracks have several advantages: extreme robustness to shocks and impacts, very good traction on soft and yielding terrains, and optimum capability of operating on sandy and muddy grounds.

Rubber continuous tracks are usually characterized by protrusions to increase traction on soft and irregular terrains; sometimes flat continuous tracks are adopted to joint two functions: locomotion and compacting of bulk materials. For instance, in [119] a special-purpose service tracked robot is presented, capable of moving inside a truck container, rolling over flax raw material to compress it, increasing its bulk density (Figure 2-21, left).

Figure 2-21 TGMR-CT with flat tracks for flax raw material compacting [119] *(left); TGMR for pipe inspection with magnetic locomotion* [120] *(right)* [33].

As regards mechanical (modular) tracks, composed of modules connected by revolute joints, heavy vehicles usually adopt steel tracks, while for small robots the most common realization is based on high-strength plastic materials. Compared to rubber continuous tracks, the robustness to shocks and impacts is lower and there is a higher risk of locking on sandy and muddy terrains; on the other hand, the motion resistance due to the internal friction of the tracks is usually lower, and mounting and dismounting for maintenance is easier. Therefore, plastic modular tracks are usually adopted for small-size and lightweight TGMRs, as [97], in which the structural resistance is not critical, to maximize the energetic efficiency. Nevertheless, there are examples of applications of mechanical tracks to larger TGMRs, such as MAXXII, a middle-size robot (length: 1m, width: 0.7 m, mass: 40 kg, Figure 2-20), used for soil characterization through its passive suspension system, which is used as sensing device [115].

Sometimes, the modular realization allows the development of special-purpose tracks, tailored for particular applications. For instance, in [116] a small

lightweight robot (186×125×51 mm, 200 g) with biologically inspired spined track modules is proposed (Figure 2-20); to detach the spines from the surface, a mechanism is introduced to imitate the foot attaching and detaching movements of insects. The experimental tests have shown that the robot is capable of climbing on sand, rock, brick, gravel, scree and pebble walls. Also, the robot proposed in [121] is small and lightweight (330×170×80 mm, 860 g) and has been designed using a biomimetic approach. It can climb concrete and brick walls using tracked-spines arrays located around the tracks. The robot uses a combination of the crank-link mechanism and gear transmission to control the tracked spines on both sides of the robot to grasp the asperities, climbing almost vertical walls.

Another very specific application of tracked robots with modular tracks is internal pipe climbing and inspection. For instance, in [122] a robot with three parallel track modules placed at 120° with axial symmetry around the robot's longitudinal axis is discussed. During operation, an adequate contact force between the tracks and the internal pipe surface is granted by radial springs carrying the track modules. The operativity of this robot is evidently limited to a strict range of pipe diameters. On the contrary, other robots for pipe inspection, equipped with magnetic modular tracks, can operate in larger pipes with different diameters, but obviously only in ferromagnetic material. For instance, the robot presented in [120] is equipped with two parallel tracks properly articulated to adapt to different pipe diameters and to improve maneuverability (Figure 2-21, right). In any case, pipe inspection robots are usually designed for this particular environment, and even if they can walk over different terrains they cannot be considered general-purpose inspection platforms.

The third category based on track type is represented by TGMRs with omnidirectional tracks (TGMRs-OT), which can be furtherly divided into robots with passive (TGMRs-OT-P) or active (TGMRs-OT-A) omnidirectional tracks. The functioning principle of omnidirectional tracks is similar to the one of omnidirectional wheels of Mecanum wheels [123]. A robot equipped with Mecanum wheels is holonomic, therefore the number of controlled degrees of freedom is equal to the number of degrees of mobility in the plane. This is particularly useful when the robot is required to operate in very limited spaces, moving in any direction. For instance, forklifts and transport robots with Mecanum wheels are adopted in storage facilities and production halls in which the organization of the spaces is of fundamental importance. On the other hand, Mecanum wheels also have considerable drawbacks: first of all, they have to operate preferably on flat, even, and clean surfaces. Moreover, their resistance to shocks and impacts is limited. Some researchers have proposed hybrid combinations of Mecanum wheels and tracks [117] (Figure 2-20), realizing multidirectional tracks which have the same maneuverability advantages of Mecanum wheels robot and better traction on uneven terrains, shock resistance, and capability of carrying loads, thanks to the higher number of rollers in contact with the terrain and to the elasticity of the tracks. Nevertheless, due to the presence of rollers, the TGMRs-OT-P have still operative limitations in harsh environments.

An example of TGMRs-OT-A is discussed in [118] (Figure 2-20). Its architecture is characterized by two crawlers with circular sections; these crawlers have active rolling axes aligned with the longitudinal axis of the robot, to perform sideling motion whenever necessary while maintaining a large contact surface for motion on soft and yielding terrains. Even in there are no rollers directly in contact with the terrain as in TGMRs-OT-P, this locomotion system still suffers limitations due to the complex mechanical design of the crawlers.

2.3.2.5 Design methodologies for tracked ground mobile robots

2.3.2.5.1 Modeling and simulation of the dynamic behavior of TGMRs

The design of a tracked ground mobile robot has some peculiar aspects related to the functioning principle of the tracks, which are deformable bodies for TGMRs-CT or composed of a closed chain of several rigid links connected by joints for TGMRs-MT and TGMRs-OT, and are in contact with the ground, which can have a wide range of properties, from firm surfaces to soft and yielding terrains.

In the scientific literature, there are many works about the dynamic modeling of the track-terrain interaction, oriented to the prediction of the motion of TGMRs given the terrain properties and the track velocities, which can be profitably exploited in the early design phases. While for wheeled robots the contact areas with the ground are relatively small with respect to the robot dimensions, for TGMRs the contact surface with the ground is remarkable, and macroscopic skidding is unavoidable during steering (skid steering). The mechanics of skid steering has attracted great interest over the last decades, with the pioneering works of Steeds [124] and the subsequent studies by Weiss [125], Crosheck [126], Kitano and Jyozaki [127], Ehlert et al. [128], which provided the analytical models used as the basis for the numerical simulations of the turning behavior of tracked vehicles.

In [129] a general theory for skid steering on firm ground is discussed, which shows a close agreement with experimental results. In [130] a simulation methodology for tracked vehicles on sandy terrain is discussed, capable of predicting sinkage, slip ratios, and turning radius.

When it is required to simulate the motion of a TGMR with a complex arrangement of the tracks and/or operate on irregular grounds and obstacles, it is unavoidable to adopt a numerical multibody approach. Recurdyn is often used as a multi-body package for the simulation of tracked vehicles and robots due to the availability of dedicated tools [131], [132]. Another possible simulation approach, discussed in [133], exploits a high number of virtual wheels in the Gazebo environment to approximate the track's behavior.

The discussion of these modeling and simulation techniques, capable of assessing the motion capabilities of tracked robots in order to reduce the number of physical prototypes necessary to converge to the final design, is out of the scope of this thesis. However, the next Section summarizes the most widespread

empirical models and methods used in the preliminary design of tracks to evaluate their motion resistance.

2.3.2.5.2 Motion resistance of tracks

The sizing of tracks (length, width) and of their motors on the basis of vehicle mass and desired performance is the most peculiar issue in the design of a tracked vehicle. This sizing must consider the features of the range of terrains on which the vehicle has to operate, adopting a proper terramechanics model.

The total motion resistance of a tracked vehicle, which has to be overcome by the actuators, is the sum of three terms:

- the resistance R_t due to the interaction between tracks and terrain;
- the resistance R_{in} due to the internal friction of the tracks;
- the resistance R_e due to the external forces acting on the vehicle.

2.3.2.5.2.1Motion resistance due to the track-terrain interaction

The most widespread method to evaluate the interaction forces between tracks and ground is the Bekker model [134]. According to this approach, the track-terrain contact is assumed to be similar to a rigid footing; the deriving pressure-sinkage relationship allows us to estimate the track sinkage and subsequently the motion resistance. For a track with uniform contact pressure, the sinkage z_0 is given by:

$$z_0 = \left(\frac{p}{k_c/b + k_\phi} \right)^{1/n} = \left(\frac{W/bl}{k_c/b + k_\phi} \right)^{1/n} \qquad 19$$

where: p is the normal pressure; W is the normal load on the track (usually the portion of robot weight supported by the considered track); b and l are the width and length of the track; k_c, k_ϕ, and n are characteristic parameters of the yielding terrain, available in the scientific literature [135]. Using equation 19, it is possible to calculate the work necessary to compact the terrain while the robot goes forward, obtaining the compaction resistance R_c:

$$R_c = b\left(\frac{k_c}{b} + k_\phi \right) \frac{z_0^{n+1}}{(n+1)} \qquad 20$$

Another component of the motion resistance is the so-called bulldozing resistance, due to the presence of yielding terrain in front of the track; the bulldozing resistance R_b can be calculated employing the following expression [136]:

$$R_b = b\left(0.67 \cdot c \cdot z_0 \cdot \left(N_c' - \tan\phi' \right) \cos^2\phi' + 0.5 \cdot z_0^2 \cdot \gamma_s \cdot \left(\frac{2N_\gamma'}{\tan\phi'} + 1 \right) \cos^2\phi' \right) \qquad 21$$

where: c is the terrain cohesion [P_a]; γ_s is the specific weight of the terrain [N/m^3], N'c and N'γ are the Terzaghi's modified bearing capacity factors, which are

functions of the internal friction angle of the terrain ϕ according to the empirical relationships represented in Figure 2-22; the angle ϕ' can be obtained by the following formula [136]:

$$\tan(\phi') = \frac{2}{3}\tan(\phi) \qquad 22$$

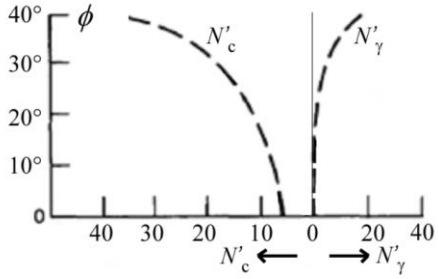

Figure 2-22 Terzaghi's modified bearing capacity factors [33].

Finally, the overall motion resistance due to the track-terrain interaction for a robot with n tracks can be obtained by summing the compaction and bulldozing resistances of each track:

$$R_t = \sum_1^n \left(R_{c,i} + R_{b,i} \right) \qquad 23$$

2.3.2.5.3 Motion resistance due to the internal friction of the tracks

The internal friction effects of the tracks obviously depend on the detailed design of tracks, drive sprockets, idler sprockets, upper and lower rollers (if present), and bearings. As a consequence, an accurate evaluation of this resistance term requires a complex mechanical modeling or an experimental evaluation, if a preliminary prototype is available. For example, it is possible to perform tests on the flat and compact ground, in order to have negligible R_t. Another option, suitable only for rough estimation, is the empirical formula proposed by Bekker [134]:

$$R_{in} = m(0.222 + 0.0108 \cdot v) \qquad 24$$

where R_{in} is the motion resistance [N] due to the internal friction of the tracks, m is the vehicle mass [kg] and v is the vehicle speed [m/s].

2.3.2.5.4 Motion resistance due to the external forces

If the robot is not interacting with the environment during locomotion, for example by means of a robot arm, the motion resistance due to the external forces can be computed as the sum of the component of the weight acting in the motion direction and of the inertial forces:

$$R_e = mg \cdot sen(\alpha) + m_{eq} a \qquad 25$$

where α is the terrain slope and a is the robot acceleration; the equivalent mass m_{eq} is the sum of the robot mass m and of the equivalent mass of the robot rotating bodies, obtained by kinetic energy equivalence. The equivalent mass m_{eq} is usually very close to m and can be approximated to it.

2.3.2.5.5 Overall robot motion resistance

Using the previously discussed equations it is possible to select the main dimensions of the tracks (b, l) and to estimate the required torque and power of the track motors. Obviously, the detailed design of the tracks directly influences R_c and R_b, but also the internal friction resistance R_{in} and the vehicle mass m. Consequently, also resistance R_e is indirectly influenced by b and l. Overall, these mutual relations among the vehicle characteristic parameters imply the need for a recursive design approach.

The two resistance components which are directly related to the track dimensions and to the terrain features are R_c and R_b. Figure 2-23 shows the sinkage z_0 and the track-terrain motion resistance R_t, which is the sum of the compaction and bulldozing resistance, as functions of b and l, for one track of a two-tracked symmetrical robot with overall mass m = 40 kg. The considered terrain is dry sand characterized by the following parameters: kc = 0,99 kN/mn+1, kϕ = 1528 kN/mn+2, n = 1.1, c = 1.04 kPa, N'c = 16.5, N'γ = 5, ϕ = 28°, γ_s = 17800 N/m3.

It is possible to note that, as intuitive and evident from equation 19, the sinkage decreases when the track width and length increase, and consequently also the terrain resistance decreases. The sensitivity to l is higher than the sensitivity to b. On the other hand, increasing too much b and l can be not convenient for the overall vehicle dimensions; moreover, this increases the vehicle mass and consequently the resistance R_e. Therefore, it is necessary to find a proper design trade-off, reaching a suitable compromise among these conflicting requirements.

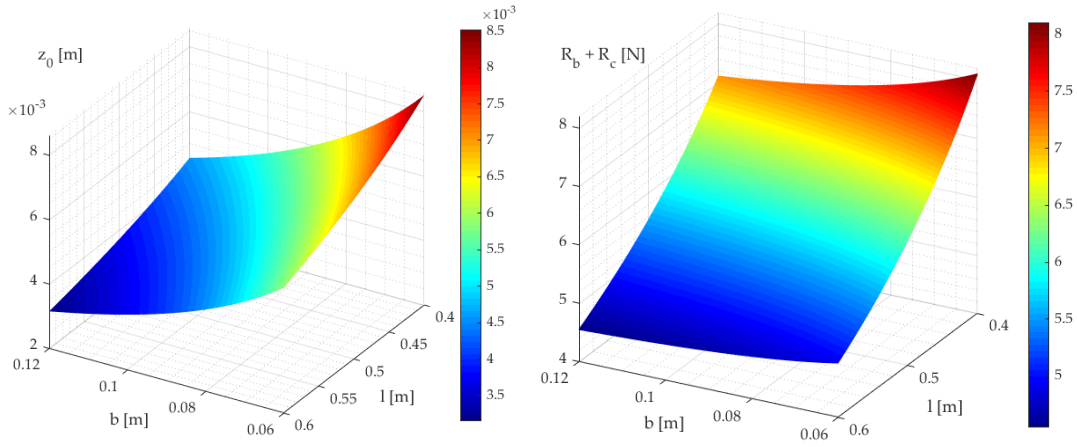

Figure 2-23 Track sinkage (z_0, left [m]) and sum of compaction and bulldozing resistances (R_b+R_c, right [N]) as function of the track width b [m] and length l [m] [33].

2.3.3 Hybrid Robots

Due to its ability to combine the benefits of the different classes while aiming to minimize their disadvantages, hybrid locomotion systems are perhaps the most intriguing options for mobile robots.

In reality, in unstructured areas or in surroundings designed for humans, legged mobility is the best option (in presence of stairs, for example). Humans, on the other hand, often utilize tracked or wheeled extensions to boost their speed and efficiency. In contrast to nature, a mobile robot's design allows for the unfettered integration of legs, wheels, and tracks. We will now talk about the four types of hybrid mobile robots (LT, LW, WT, and LWT).

2.3.3.1 Leg-wheel hybrid locomotion systems

Robots with legs and wheels combine the operating flexibility of legs with the energy economy of wheels. According to [137], there are basically three ways to combine legs and wheels:

- adding extra legs to a wheeled robot that are connected to the robot body;
- using retractable modules that can serve as either wheels or legs; and
- mounting the wheels on the leg links (typically, but not always, at the ends of the legs).

Rarely is the first strategy used. If legs and wheels are utilized alternately, depending on the terrain, robot construction is theoretically straightforward. The biggest disadvantage is that the robot often weighs a lot since the vehicle has two different locomotion systems installed. Additionally, the advantage of wheels in terms of energy efficiency is much diminished if legs and wheels are utilized together. The second strategy is quite intriguing. For instance, a mobile robot with retractable leg wheel modules is presented in [137]. (Figure 2-24).

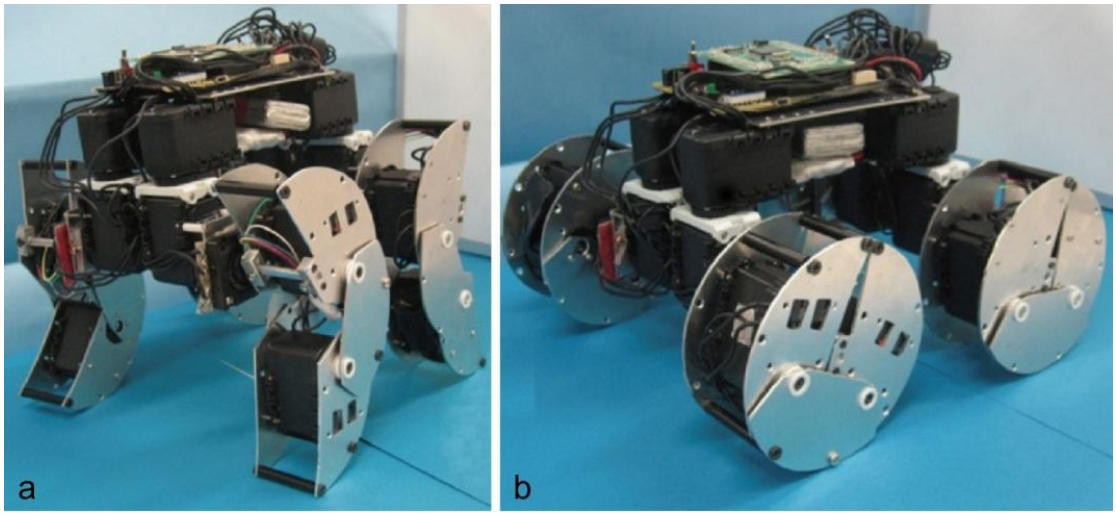

Figure 2-24 Leg-wheel hybrid robot with retractable locomotion modules: legged mode (a) and wheeled mode (b) [137]

The mechanical complexity of the retractable modules and their inadequate durability in soiled conditions or in the event of shocks are the primary shortcomings of this design. Probably the most successful approach to combine legs and wheels is the third method. Octopus (Figure 2-25), a hybrid leg-wheel robot designed by Ecole Polytechnique Federale de Lausanne (EPFL), is one example [138]. It includes tactile wheels and tilt sensors, and its advanced locomotion system comprises 8 motorized wheels with a total of 15 degrees.

Figure 2-25 The leg-wheel hybrid Octopus robot [138].

Another illustration of the third strategy is the stepping triple wheel concept, which EPFL first used in the Spacecat micro-rover [139] the rover can actively lift one wheel to climb obstacles thanks to two three-wheeled locomotion modules that can rotate independently of one another (Figure 2-26 a). Motion control requires eight separate actuators: two for the locomotion modules and six for the wheels.

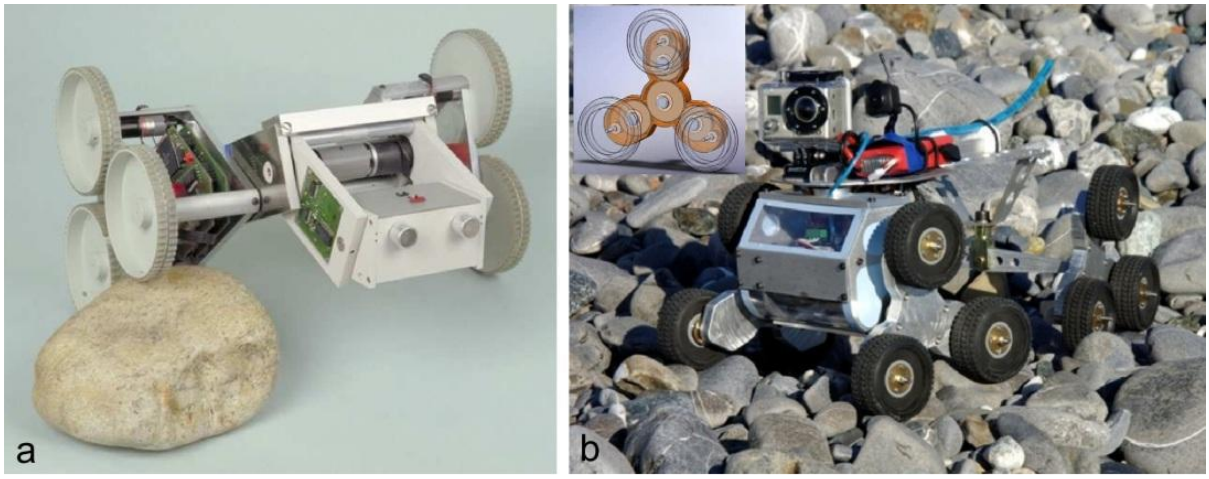

Figure 2-26 Stepping triple wheel hybrid robots [37]*: a) Spacecat* [139]*; b) Epi.q.* [140].

Another illustration of the third strategy is the stepping triple wheel concept, which EPFL first used in the Spacecat micro-rover [139]: the rover can actively lift one wheel to climb obstacles thanks to two three-wheeled locomotion modules that can rotate independently of one another (Figure 2-26 a). Motion control requires eight separate actuators: two for the locomotion modules and six for the wheels.

The Epi.q mobile robots family, created in collaboration between the Polytechnic of Turin and the University of Genoa, has the same three-wheeled locomotion unit shape, ensuring excellent motion performance on uneven terrains and obstacle-climbing capacity (Figure 2-26 b). Each Epi.q locomotion unit is underactuated by a single Gearmotor using an epicyclical mechanism that, depending on dynamic and friction circumstances, transitions between legged and wheeled locomotion automatically and without control input. As a result, the control system's complexity is greatly reduced [140].

2.3.3.2 Leg-track hybrid locomotion systems

For challenging locations, hybrid mobile robots with legs and tracks are often used—as long as speed and energy economy are not priorities. Legs and tracks may be combined in a variety of ways. To achieve legged movement, the easiest method is to employ more than two tracks (often four), which are in relative mobility with regard to the robot frame. Commercially accessible mobile robots created by iRobot for homeland security, surveillance, inspection, and explosive detection are examples of this strategy (Figure 2-27 a). The mobility performance of these robots is comparable to tracked robots, but they are far more capable of overcoming obstacles. They are very strong and dependable [141].

On the other hand, hybrid leg-track robots with more intricate leg structures have a wider range of gait and mobility properties. The Titan X mobile robot from the Hirose-Fukushima Robotics Lab (Figure 2-27 b) has three degrees of freedom in each of its four legs and four belts that serve as both tracks and mechanical transmission for the knee joints while the robot is moving along on its legs [142]. The hybrid leg-track robot created by a research team under the direction of Yokota et al. is another example (2006) [143].

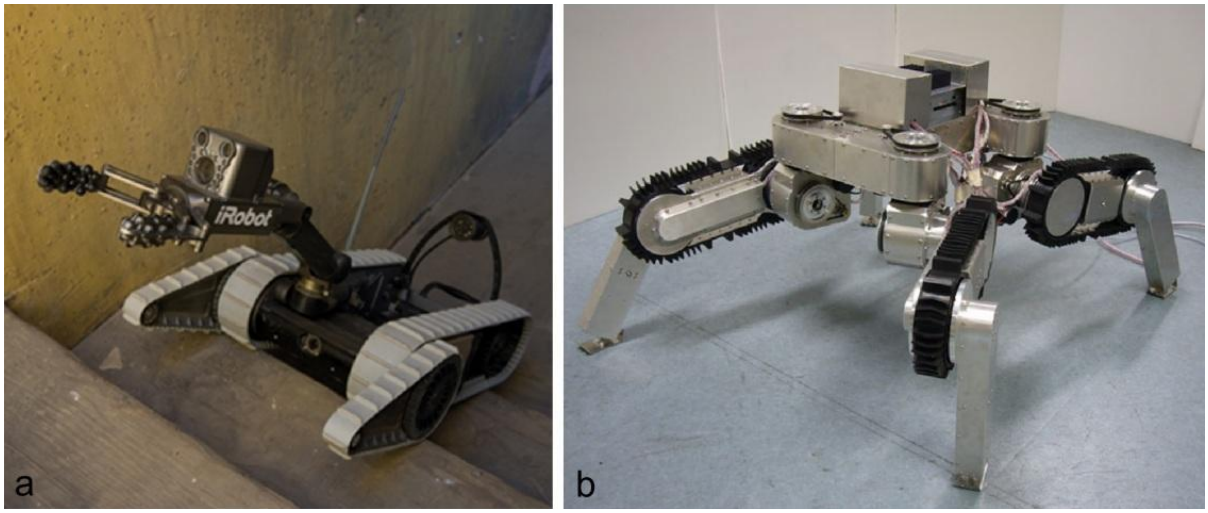

Figure 2-27 Leg-track hybrid robots [37]*: a) iRobot SUGV* [141] *and b) Titan X* [142].

2.3.3.3 Wheel-track hybrid locomotion systems

When it's necessary to combine energy economy on the flat, compact artificial ground with high motion performance on soft, uneven terrains, wheels and tracks work quite well. Wheel contact with the ground may often be enabled or disabled in wheel-track hybrid robots by adjusting the relative location of the tracks and wheels or the form of the tracks. One such hybrid robot was created by the Daegu Gyeongbuk Institute of Science & Technology and features changing form tracks (Figure 2-28) [113]. In the arrangement seen in Figure 2-28, the rails provide movement. On flat, compact terrain, the tracks may be folded, allowing the wheels to provide locomotion.

On the other hand, with the Hirose-Fukushima Robotics Lab's Helios VI tracked carrier (Figure 2-28), movement is never solely carried out by the wheels; the two front wheels are instead included to enhance the carrier's ability to climb stairs [144]. Another intriguing method is the Galileo wheel patented technology, which, for instance, is used in the VIPeR, a mobile platform created by Elbit Systems for surveillance activities (Figure 2-28). The Galileo wheel unites wheels and rails into a single group thanks to extendable crawlers.

Figure 2-28 Wheel-track hybrid robots: a) with variable-shape tracks [113]*; b) Helios VI* [144]*; c) with Galileo wheel* [145].

2.3.3.4 Leg-wheel-track hybrid locomotion systems

The robotic platform Azimuth, which has four independent leg-track-wheel articulations and can produce a broad range of locomotion modes (including holonomic and Omni-directional movements, scaling of obstacles and stairs), is an example of one that incorporates all three forms of locomotion (Figure 2-29). [146]. Although the notion of Azimuth may be applied to outdoor situations, it was primarily created to function in interior settings. Its considerable mechanical complexity is the key flaw.[146]

Figure 2-29 The hybrid leg-wheel-track Azimuth robot [146], [37]

2.3.4 Comparison of locomotion system features

A very synthetic outline of the characteristics of locomotion systems is shown in Figure 2-4, which qualitatively graphs mobility in unstructured environments (y) vs. speed and energy efficiency (x) with reference to the three primary categories and the four hybrid categories of locomotion systems (Figure 2-3). Legged robots are in the left upper zone (worst y, better x), tracked robots are in the center, and hybrid combinations tend to be in the right upper zone. Wheeled robots are in the right lower zone (better x, worst y) (combination of the benefits).

- Robots with legs are in the left zone along the x-axis because their mode of mobility necessitates foot-to-ground collisions. Additionally, torque delivery is necessary for the actuated joints even when they are in a static state (unless non-reversible gearboxes or elastic preload components are utilized to counteract the effects of gravity).
- Due to the fact that interactions with the ground are less severe but nevertheless present, tracked robots are in the center. Additionally,

there are a number of revolute joints connecting the track components, which have basic structures and medium to low energy efficiency.

- Robots with wheels are in the correct place in the Figure 2-4 because they have few revolute joints (one on each wheel), are often implemented with ball bearings, and have good energy efficiency.
- Robots with one wheel are in the lower zone along the y-axis because a wheel cannot overcome obstacles on its own if the first contact point with the obstacle profile is not much lower than the wheel axis.
- Tracked robots are positioned in the center because the broad ground contact area filters out terrain irregularities and lowers contact pressure.
- Robots with legs are in the top zone because their locomotion allows for a high degree of flexibility while moving through unstructured settings since it lets them choose where their feet will make contact with the ground and obstacles.

Generally speaking, hybrid locomotion systems need to include the advantages of the many categories from which they arise. As a result, in the graph shown in Figure 2-3, each hybrid category should be placed in a region defined by the original categories' maximum values along each axis. A nonactive locomotion device is a non-negligible payload, therefore this does not entirely happen (and the graph is created appropriately), as the combination of several locomotion devices reduces total performance. From this perspective, hybrid solutions that combine two separate locomotion systems into a single unit are preferable to hybrid solutions that never combine two locomotion systems, such as the wheel-track robot in Figure 2-28, which is based on the stepping triple-wheel idea. The 10 characteristics outlined in the Section comparison methodology and classification of mobile robots are used to compare the different locomotion systems in Table 2-3. The latter three characteristics represent system complexity whereas the first seven features describe mobility performance and are qualitatively quantifiable. Table 2-4 displays the suggested criteria for ranking the first seven attributes along with ranges that correlate to the various rankings. In Table 2-3, these standards have been used. Some attributes (maximum speed, obstacle-crossing ability, step/stair climbing capability, and walking capacity on uneven terrain) have been standardized with regard to the robot dimensions since mobile robots may come in a variety of sizes.

Table 2-3 Synthetic comparison of locomotion system features.[32]

Locomotion Features	Wheel	Track	Leg	LW	LT	WT	LWT
Maximum Speed	high	medium / high	low/ medium	medium/ high	medium	medium/ high	medium/ high
Obstacle crossing capability	low	medium /high	high	medium/ high	high	medium	high
step climbing capability	low	medium	high	high	high	medium	high
slope climbing capability	low/ medium	high	medium / high	medium/ high	high	medium/ high	high
walking capability on soft terrains	low	high	low/ medium	low/ medium	medium/ high	high	medium/ high
walking capability on uneven terrains	low	medium / high	high	high	high	medium/ high	high
Energy efficiency	high	medium	low/ medium	medium/ high	medium	medium/ high	medium/ high
Mechanical complexity	low	low	high	medium/ high	medium/ high	low/ medium	high
control complexity	low	low	high	medium/ high	medium/ high	medium	high
Technology readiness	full	full	full	full	full	full	full

The capacity to navigate obstacles in unstructured situations and cross ones with arbitrary forms is known as the obstacle-crossing capability (Table 2-2). But the form chosen for quantitative comparison was semicircular. Wheel-based locomotion systems, among others, benefit from the great speed and energy efficiency, as was already noted. These qualities are particularly maximized by wheeled robots developed from automotive technology, equipped with car-like suspensions and Ackermann steering. Wheels and legs may be effectively merged in hybrid systems if it turns out that obstacle-crossing and climbing skills are also essential. On the other hand, as tracks have a greater contact area than legs, they are preferred to increase robot mobility when job requirements are centered on soft and yielding terrains. Legs are more effective for hard barriers with complicated forms. Note that one of the key barriers to robot mobility, slippage in the presence of yielding terrains, slopes, or obstructions, is a complicated process that is noticeably impacted by the control technique [147]. Wheeled and tracked systems' mobility performance may be improved by using appropriate visual-based

and/or adaptive control algorithms [148]; [149]. With relation to legged locomotion, cutting-edge robots with dynamic gaits, like Spot [83], are able to maintain balance in the midst of slippage. Mechanical complexity and control complexity is fundamental design selection factors [150].

Particularly in terms of mean time between failure and mean time to repair, mechanical complexity has a significant impact on the dependability of robot operation. In this respect, pure tracked and wheeled robots are unquestionably straightforward and durable, but robots with complicated mechanical designs, particularly with regard to the linkages in touch with the ground (such as the leg-wheel robot in Figure 2-24), should be avoided in heavy-duty applications. Due to the need for gait planning, control complexity is undoubtedly greater for systems including legs. However, only these designs, particularly when guided by dynamic model-based algorithms, can provide the best performance in climbing and navigating obstacles in unstructured settings. The right combination of locomotion systems for hybrid solutions may be chosen based on the demands of a given job starting with these broad principles.

Table 2-4 Evaluation criteria. [32]

Feature	Evaluation criteria	Ranges		
		Low	Medium	High
Maximum speed	the ratio between the maximum speed and overall length of the robot	< 0.5 s^{-1}	0.5 - 3 s^{-1}	> 3 s^{-1}
Obstacle crossing capability	the ratio between the maximum height of an obstacle with a semi-circular lateral profile that can be crossed and the height of the robot	< 0.25	0.25 – 0.5	> 0.5
Step/stair climbing capability	the ratio between the maximum height of the square step which can be crossed and the height of the robot	< 0.15	0.15-0.35	>0.35
Slope climbing capability	the maximum slope that can be climbed (compact surface, friction coefficient > 0.5)	< 15°	15°-30°	>30°
Walking capability on soft terrains	the capability of walking on:	Compact soil	medium to soft soil	Soft sand
Walking capability on uneven terrains	the ratio between the maximum ground roughness that can be crossed (rocky ground with a random profile) and the height of the robot	<0.1	0.1-0.2	>0.2
Energy efficiency	the ratio between the final gravitational potential energy acquired while climbing a slope at low speed and the energy supplied to the actuators	<0.1	0.1-0.35	>0.35

3 The WheTLHLoc robot

Wheeled Tracked Legged Hybrid Locomotion robot

The goal of this work is the development of a small-scale hybrid locomotion robot for surveillance and inspection, capable of combining tracked locomotion on soft terrains, wheeled locomotion on flat and compact grounds, and high obstacle crossing capability (ratio between the maximum climbable step and the robot height higher than one). The limits on the robot size (track length of 300 mm and width of 350 mm) have been selected as a compromise between two conflicting requirements: sufficient compactness to explore narrow spaces and to stand on the tread of a standard indoor stair, and the capability to climb a standard stair using tracks, legs, and wheels.

These features allow facing a wide range of possible operative conditions, both in outdoor and indoor environments, also in presence of stairs. Fulfilling this entire set of requirements leads indeed to a more complex mechanical and control layout with respect to commercial tracked or wheeled robots with differential steering [151], [114].

In the scientific literature, there are several examples of small-scale robots comprising tracks. Besides the already mentioned basic architecture with two non-articulated tracks and differential steering, robots can be equipped with articulated frames to increase adaptability to terrain unevenness [92], [100]. Another option is connecting tracked units in series, thus composing snake-like robots [152]. A commercially widespread solution to increase the obstacle climbing capability is to add two tracked and rotating swing extensions (flippers) on the front [93]. This solution helps to face the first step, but for continuing the stair ascent the robot must be sufficiently long to touch always at least two step edges. The patented solution [153] is similar, but it combines triangular main tracks and flippers, while the patent [154] adopts non-tracked flippers for lifting up the robot body to climb a step. All these solutions with flippers have a limited ratio between the maximum climbable step and the robot size.

Considering hybrid solutions, there are many ways to combine tracks and legs. The simpler approach is to use them in parallel, as proposed in [155], [156]. An alternative solution is to equip leg links with peripheral tracks[142], also in combination with wheels [157]. The tracked robot proposed in the patent [158] is characterized by a central arm with a tracked link, which can be used both to climb obstacles and to manipulate payloads.

Wheels are introduced in hybrid locomotion systems when speed and large operative range on the flat and compact ground are required. In order to activate and deactivate the wheels, switching on/off their contact with the ground for different locomotion modes, it is possible to use retractable wheels[91], [159], to adopt variable-shape tracks[113] or to change the position of the legs [157], [146], [144]. Some researchers have proposed systems to transform tracks into wheels by means of tensioning systems or articulated supports [160], [161], but their mechanical complexity can reduce reliability, resistance to shocks, and operativity in dirty environments.

Interesting hybrid locomotion systems for service and assistive robots and wheelchairs have been proposed in the scientific literature and are available on

the market, based on stepping triple wheels [162], combinations of wheels and tracks[163], or legs and tracks [164], but in these applications, the size of the vehicle is much larger than the step size, so the robot can climb the stair touching at least two step edges.

Starting from the outlined state-of-the-art, the WheTLHLoc robot (*Wheel-Track-Leg Hybrid Locomotion*) has been proposed [97]. Wheels and tracks are combined by augmenting a differential steering tracked robot with two rotating legs with active wheels placed at their ends. This solution is similar to the mechanical architectures proposed in [144], [157], and in the patent [165], but with functional differences discussed in section 3.1.1. The novelties of this robot with respect to [97] are the analytical evaluation of the step climbing feasibility depending on the operative conditions and the discussion of the experimental tests.

The remaining of the chapter is organized as follows:

- Section 3.1.1 summarizes the design methodology for hybrid locomotion robots with obstacle climbing capability and the functional design of the WheTLHLoc robot (section 3.1.1);
- section 3 analyses the step climbing maneuver, first defining its phases and kinematic relationships (section 3.2.1), and then evaluating the stability and non-slipping conditions (sections 3.2.2 and 3.2.3);
- in section 3.3, starting from the kinematic relationships and conditions discussed in section 3.2, a criterium for planning the step climbing motion as a function of the step height is proposed and analytically assessed;
- section 3.4 discusses the experimental campaign on the first prototype, with the validation of the proposed step/stair climbing motion planning and of the other locomotion modes;
- section 3.5 is the conclusion section.

3.1 Functional design of the WheTLHLoc robot

3.1.1 Design methodology for hybrid locomotion robots with the obstacle-climbing capability

The main phases of the development of a small-scale hybrid locomotion robot with obstacle-climbing capability are here summarized.

Conceptual design. Once defined the functional requirements, the starting point is the intuition and experience of the designer, who invents a completely novel architecture or an evolution of an existing one. Even if it is almost impossible to systematize this phase, some hints can be recalled.

To limit the overall mechanical complexity, hybrid systems should not be the addition of different locomotion devices on the same robot body, but they should comprise members usable in different modes.

For small-scale hybrid locomotion robots, it is generally accepted to have good speed on flat and compact grounds, usually by wheels, but lower speed during obstacle climbing, performed by a sequence of statically stable positions. This allows simplifying the architecture of the legs, if present, thus reducing control complexity. Dynamic gait indeed maximizes the obstacle climbing performance [58], but it needs a much more complex and expensive mechatronic architecture since the stability of dynamic obstacle climbing depends not only on the planned trajectory but also on the speed at which it is executed.

In real operative conditions, an overturn of a small robot is frequent, and the capability of restoring operativity by proper maneuvers or keeping it thanks to the robot symmetry greatly enhances the reliability in accomplishing the mission. Moreover, for use in harsh environments, compact outer shapes without appendages are highly preferable for resistance to shocks.

Geometrical synthesis of obstacle climbing. Once defined the simplified topology of the robot and the corresponding minimum set of geometrical parameters are, the motion sequence for obstacle climbing is synthesized considering only kinematic constraints: the trajectory of the main body, tangency of wheels, and tracks with the obstacle, absence of interferences. A dimensionless approach can be used, with ratios between the dimensions and a significant robot size (e.g., the robot wheelbase or wheel/track radius). Using dimensionless ratios is more general, since most features, such as stability and non-slipping conditions, are independent of the robot scale. For example, for the WheTLHLoc architecture, a medium-size realization can be considered, with around 1 m of length, more oriented to outdoor exploration. The kinematic synthesis must be carried out for any obstacle shape considered in the functional requirements, but the variety of obstacles that can be present in outdoor missions is difficult to classify through a limited number of profile classes. Consequently, the climbing of steps and stairs is primarily studied, firstly since they are present in almost all indoor environments, and secondarily because climbing a vertical step represents a severe test with respect to most obstacle shapes.

Analysis of the obstacle climbing feasibility. After the kinematic definition of the maneuver, stability and non-slipping conditions must be assessed.

Regarding stability, a static analysis is sufficient in the case of static gait, with negligible inertial effects. With static gait, all positions of the planned trajectory are statically stable with the robot subject only to gravity forces and ground reactions. To take into account inertial effects and other disturbances, a proper stability margin must be imposed, for example, a minimum value of the tipping angles (section 3.2.2). Let us note that the inertial effects can be reduced for the same statically stable trajectory by performing it with lower speed and acceleration. Therefore, for any statically stable trajectory, it is always possible to find proper motion planning for which the inertial effects are sufficiently small with respect to the selected stability margin.

For the non-slipping condition, which is influenced by the surfaces of the ground and obstacles, the minimum values of friction coefficients generally depend

on the obstacle's geometry (for example the step height). This feasibility assessment can be performed by multibody simulation or by analytical approach, which is preferable since it leads to a deeper understanding of the robot's behavior and of the sensitivity to geometrical and motion planning parameters. In this phase, the member masses are approximated since the embodiment design is not yet available. This analysis is iterated, leading to modifications of the main robot's geometrical dimensions and motion planning. For example, in section 3.3 the step climbing motion law is defined as a function of the step height based on the analytical evaluation of stability and non-slipping conditions.

Embodiment design. The detailed mechatronic design of the prototype (structural parts, internal layout, motors, gearheads, control architecture) is obtained starting from the main geometrical parameters. The selection of the actuators and transmission components is based on the required velocity, obtainable from the kinematic motion planning, and on the required torque/force, obtainable from the static analysis. Proper safety coefficients must be used to consider friction in transmissions and dynamic stresses due to impacts. At the end of this phase, the real mass properties are available and must be used to update the assessment of the step climbing feasibility.

Experimental campaign. The tests on the prototype are the last validation before final production and commercialization. For the obstacle profiles for which the motion laws have been defined and tested by multibody simulation or analytically, the experiments can be performed by controlling the robot axes in position. On the contrary, the robot can be remotely controlled by a human to test its effectiveness in other operative conditions, for example on random unevenness and yielding terrains. Impact forces, e.g. in case of a fall, are difficult to be theoretically evaluated since they depend on the compliance of ground and robot members. Consequently, an embodiment redesign must be performed based on the failures that occurred during the tests, leading to the final product through an iterative process.

3.1.2 The WheTLHLoc conceptual design

The conceptual design of the WheTLHLoc starts from the following requirements:

- small-scale ground mobile robot for indoor and outdoor inspection and surveillance, with a maximum track length of 300 mm and an overall size of around 450×350×130 mm;
- payload up to 0.5 kg (typically cameras, microphones, and environmental sensors);
- tracked locomotion on outdoor yielding terrains (maximum speed 0.1 m/s);
- wheeled locomotion on indoor compact grounds (maximum speed 0.9 m/s);
- the capability of climbing standard stairs with 300 mm of tread and 160 mm of the riser.

The WheTLHLoc robot is shown in Figure 3-1. It is characterized by two tracks (T), two legs (L), and two wheels (W), all independently actuated by six-gear motors. While the gearmotors of tracks and legs are placed inside the main body (MB), the gearmotors of the wheels (WM) are located at the leg tips, to avoid mechanical transmissions along the legs. Two Omni wheels (OW) are placed on the rear. The robot is equipped with a front camera (FC) and a rear camera (RC). The internal layout of the robot is discussed in detail in [97].

Let us consider the main body reference frame O'(x',y',z'), shown in white in Figure 3-1. The pitch axis y' coincides with the axes of the two revolute joints connecting the legs to the main body, x' is the longitudinal roll axis, pointing frontward, and z' is the yaw axis, which completes the dexterous frame. The robot is externally symmetrical with respect to the $x'z'$ and $x'y'$ planes, and also with respect to the $y'z'$ plane if the two Omni wheels are neglected. Consequently, the robot can't remain locked after a 180° overturn. Moreover, even if the robot remains on one flank after a fall, it can restore the locomotion position by rotating the leg in contact with the ground.

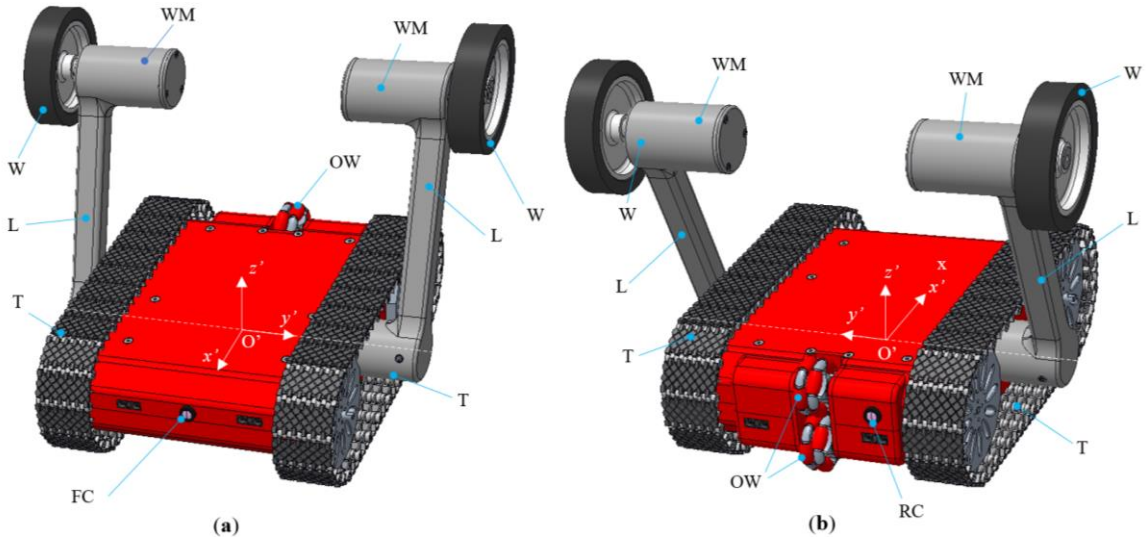

Figure 3-1 The WheTLHLoc robot: front view (a), rear view (b).

Figure 3-2 shows the three possible locomotion modes of the WheTLHLoc. On flat and compact grounds, the legs rotate to suspend the robot on the two wheels and on the lower Omni wheel. In this wheeled mode, speed is maximum and the field of view of the front camera is optimally exploited (Figure 3-2, a). Therefore, this mode is used whenever possible, in particular in all indoor flat-floor environments.

Tracked locomotion (Figure 3-2, b) is enabled on yielding and averagely irregular terrains by rotating the legs upwards. On sloping terrains, the position of the legs can be varied to improve the robot's stability.

In case of greater irregularities and climbing obstacles, steps, and stairs, it is possible to combine the motion of wheels, legs, and tracks. Legs and wheels can be moved independently to overcome asymmetric obstacles (Figure 3-2, c).

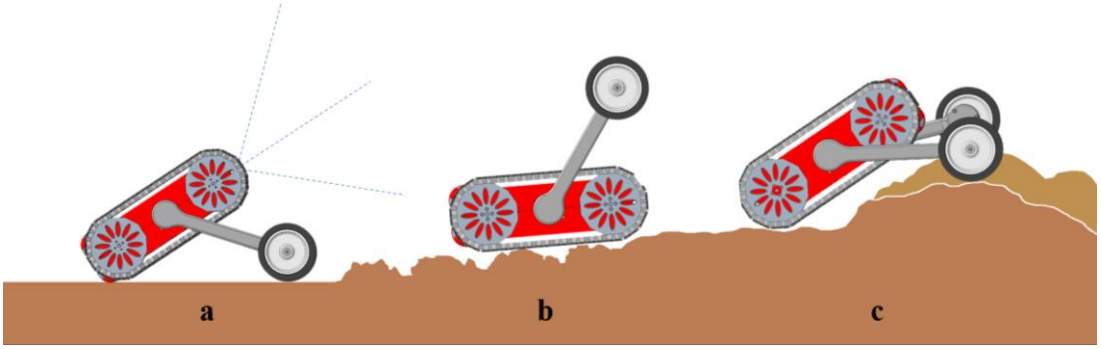

Figure 3-2 WheTLHLoc locomotion modes: wheeled locomotion (a), tracked locomotion (b), hybrid leg-wheel-track locomotion (c).

As already said, WheTLHLoc has some similarities with the solutions proposed in [144], [157], and [165], but also remarkable differences:

- differently from HELIOS-VI [144] and from the patented architecture [165], WheTLHLoc has two independently actuated legs, and can perform purely wheeled locomotion exploiting the Omni wheels; moreover, with respect to HELIOS-VI, the wheels at leg tips are actuated instead of idle;
- with respect to the Kylin robot [157], WheTLHLoc has a more compact and robust design, with two long legs purposely designed to climb steps and obstacles;
- differently from HELIOS-VI and Kylin, WheTLHLoc is fully symmetric and thus can operate after an overturn.

Square steps and stairs represent the most important class of obstacles to be considered in the design of small-scale ground mobile robots suitable for mobility in indoor environments structured for humans. Steps and stairs are not critical for medium-scale and large-scale robots, longer than 2÷3 treads, since they can touch more than one step edge [166], [167]. On the contrary, the design of a smaller robot capable of effectively climbing stairs is challenging, because the robot must be sufficiently small to stand on one tread, but also able to overcome the riser, and these requirements are conflicting. An example of a small-scale robot, capable of standing on one step but capable of climbing risers higher than itself is Mantis[168]. The WheTLHLoc robot has been initially conceived as a tracked alternative to Mantis since both robots use rotating legs to lift their body over the step edge. Nevertheless, besides the introduction of the tracks, WheTLHLoc and Mantis have two remarkable differences. The first is the symmetry of WheTLHLoc, with the already discussed functional benefits. The second is the architecture of the legs, with actuated wheels at their ends for WheTLHLoc, which improves the step and obstacle climbing capability.

In [97] the WheTLHLoc motion for climbing and descending stairs has been discussed and tested by multibody simulation. In the next section, the step climbing sequence is kinematically defined to evaluate analytically the stability and non-slipping conditions.

3.2 Step climbing analysis

3.2.1 Definition and kinematics of the step climbing phases

Starting from the experience acquired with the robot remotely controlled by a human, the kinematics of the step climbing represented in Figure 3-3 has been delineated. It is divided into nine phases: step approach (1), leg lowering (2), track raising (3), edge approach (4), leg retreat (5), lift completion (6), edge overcoming (7), leg raising (8), and step depart (9). The maneuver is kinematically defined by imposing two conditions: the vertical motion of the robot center O' in phase 3 (track raising, Figure 3-3), and the rotation around the step edge with motionless tracks in phase 6 (lift completion, Figure 3-3).

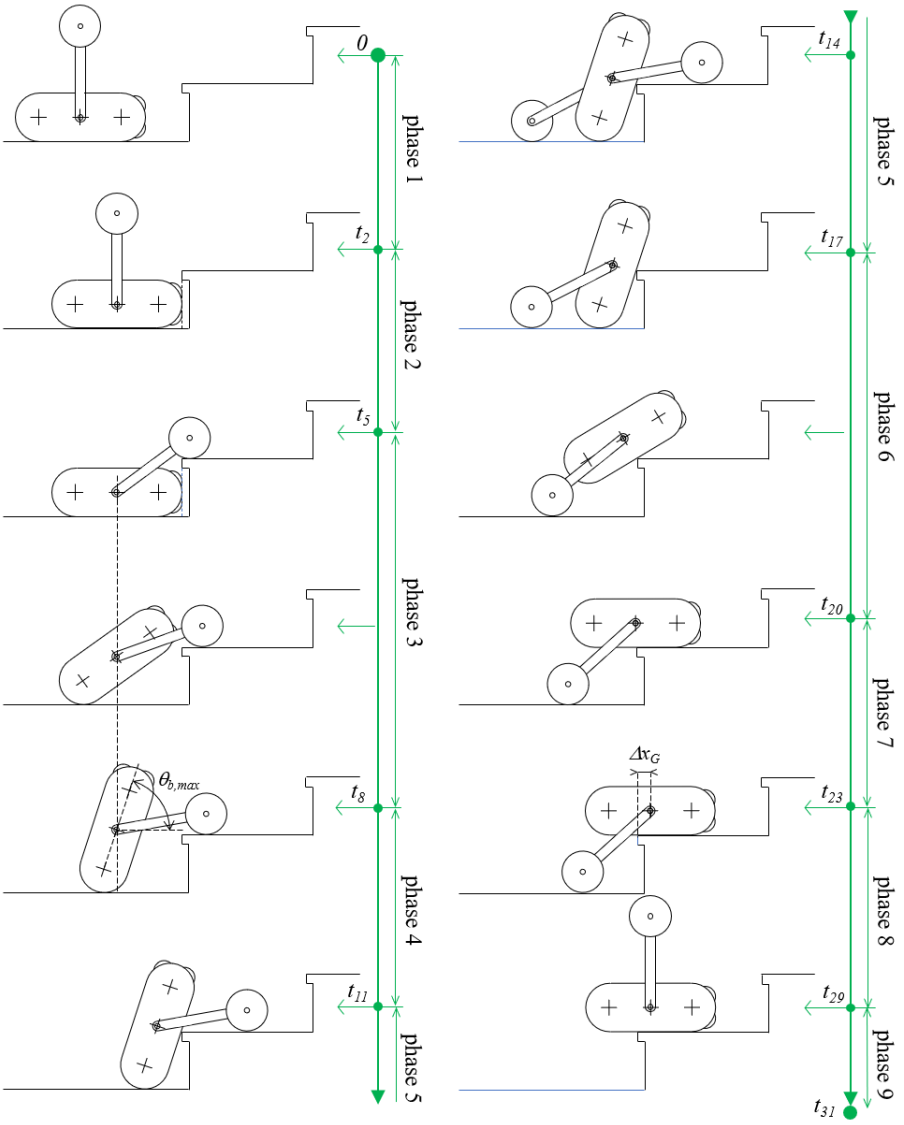

Figure 3-3 Step climbing sequence, divided in nine phases: step approach (1), leg lowering (2), track raising (3), edge approach (4), leg retreat (5), lift completion (6), edge overcoming (7), leg raising (8), and step depart (9).

Each phase ($t_i \leq t < t_i+3$) is divided into three sections: acceleration for $t_i \leq t < t_i+1$, constant speed for $t_i+1 \leq t < t_i+2$, and deceleration for $t_i+2 \leq t < t_i+3$. The only exceptions are phases 1 and 9, with only two sections: the first phase doesn't have the acceleration section, and the last doesn't have the deceleration section. In this way, the sequence starts and ends with the same velocity, and can be repeated cyclically for all the steps of a stair. Moreover, phases 5 and 8 (leg retreat and leg raising) are split into six sections, since the legs rotate one by one for better stability, as discussed later.

The step/stair descent can be executed by inverting the stair climbing sequence.

Let us note that, due to the versatility of the proposed mechanical architecture, many different motion plans for step climbing are conceivable, for

example keeping constant the x coordinate of the wheel center in phase 3, or moving forward slowly the tracks in phase 6. However, the proposed solution is effective and statically stable at each instant, as discussed in sections 3.2.2 and 3.2.3. Moreover, it has the advantage that the robot trajectory can be obtained from only one geometrical parameter, the step height, as discussed in section 3.3.

The kinematics and the stability of the step climbing maneuver can be analyzed by considering the geometrical parameters listed in Table 3-1 Main geometrical parameters and variables and corresponding dimensionless ratios. and shown in Figure 3-4. For the sake of generality, for each length parameter, the corresponding ratio with respect to the track radius is defined (Table 3-1 Main geometrical parameters and variables and corresponding dimensionless ratios. and Figure 3-4, blue).

Table 3-1 Main geometrical parameters and variables and corresponding dimensionless ratios.

Description	**Parameter/variable**	**Dimensionless parameter/variable** (divided by r_t)
Track radius	r_t	1
Wheel radius	r_w	ρ
Track wheelbase	w	ω
Leg length	l_l	λ
Leg width	w_l	ω_l
Step height	h	δ
Robot width measured at the tracks	b_t	β_t
Robot width measured at the wheels	b_w	β_w
Main body pitch angle	θ_b	-
Absolute main body coordinates	$x_{O'}, y_{O'}, z_{O'}$	$\psi_{xO}, \psi_{yO}, \psi_{zO}$
Left leg angle (relative reference frame)	θ'_l	-
Right leg angle (relative reference frame)	θ'_r	-
Distance between the leg C.O.G and O' in the xz plane	l_{lG}	ξ_l
Relative main body C.O.G. coordinates	$x'_{Gb}, y'_{Gb}, z'_{Gb}$	$\psi'_{xGb}, \psi'_{yGb}, \psi'_{zGb}$
Absolute main body C.O.G. coordinates	x_{Gb}, y_{Gb}, z_{Gb}	$\psi_{xGb}, \psi_{yGb}, \psi_{zGb}$
Relative coordinates of the left leg C.O.G.	$x'_{Gl}, y'_{Gl}, z'_{Gl}$	$\psi'_{xG1}, \psi'_{yG1}, \psi'_{zG1}$
Relative coordinates of the right leg C.O.G.	$x'_{Gr}, y'_{Gr}, z'_{Gr}$	$\psi'_{xGr}, \psi'_{yGr}, \psi'_{zGr}$
Relative coordinates of the overall C.O.G.	x'_G, y'_G, z'_G	$\psi'_{xG}, \psi'_{yG}, \psi'_{zG}$
Absolute coordinates of the overall C.O.G.	x_G, y_G, z_G	$\psi_{xG}, \psi_{yG}, \psi_{zG}$

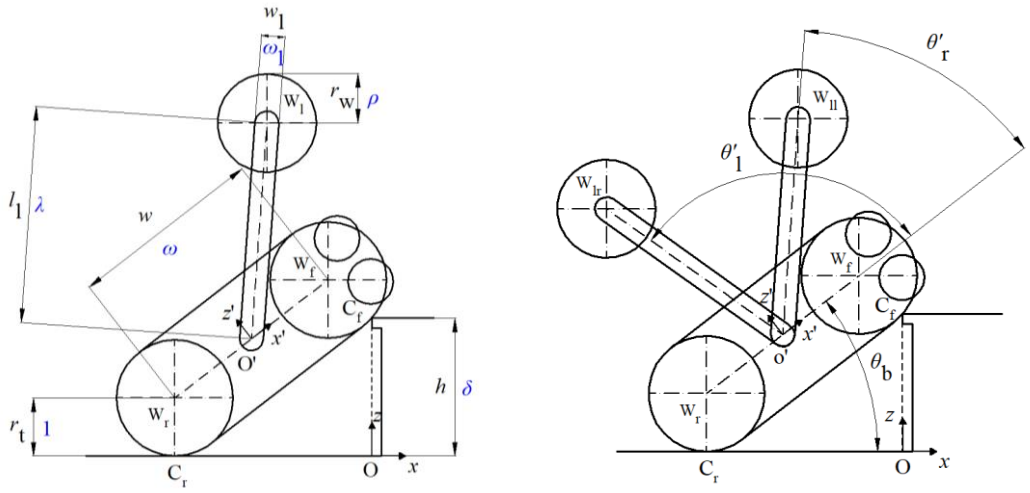

Figure 3-4 Main geometrical parameters of the WheTLHLoc robot.

Phase 1 (*step approach*), $0 \le t < t_2$

The robot approaches the step in a backward motion, with the Omni wheels close to the step, moving on the tracks, with vertical legs. Consequently, in all the phases $z_{O'} = r_t$, $\theta_b = 0$, $\theta'_l = \theta'_r = \pi/2$. At t_2 the robot stops with the front vertical tangent to the track vertically aligned with the step edge.

Phase 1 is divided into two sections: for $0 \le t < t_1$ the robot has constant speed v_1; for $t_1 \le t < t_2$ the robot has constant deceleration a_1; the robot velocity is null at $t = t_2$. The track velocity is proportional to the time derivative of $x_{O'}$.

Phase 2 (*leg lowering*), $t_2 \le t < t_5$

The robot legs rotate towards the next step surface until touching it with null speed, while tracks and wheels are at rest. Consequently $z_{O'} = r_t$, $\theta_b = 0$, and $x_{O'} = x_{O'}(t_2)$. The angles θ'_l and θ'_r varies from $\pi/2$ to θ'_5 with constant acceleration for $t_2 \le t < t_3$, constant velocity for $t_3 \le t < t_4$, and constant deceleration for $t_4 \le t < t_5$. The final leg angle θ'_5 can be derived from the geometrical scheme of Figure 3-5:

$$\theta'_5 = \arcsin\left(\frac{r_w + h - r_t}{l_l}\right) \qquad 26$$

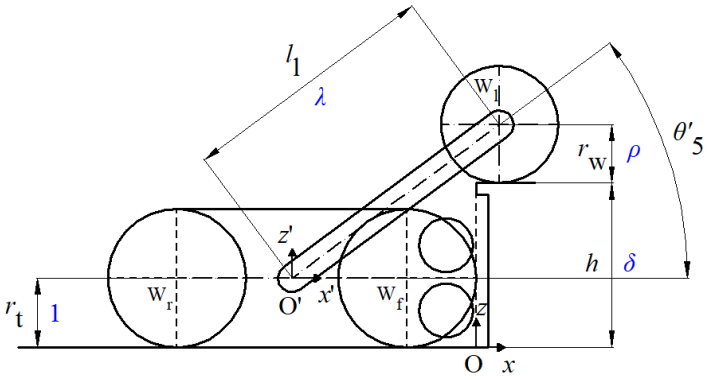

Figure 3-5 Final positions of phase 2, step approach ($t = t_5$).

Phase 3 (*track raising*), $t_5 \leq t < t_8$

After the instantaneous stop at t_5, the legs restart to rotate in the same direction, lifting up the robot body, while keeping constant the horizontal position of the origin of the main body reference frame O'(x',y',z'). To obtain this motion, tracks, wheels, and legs must rotate simultaneously. Therefore $x_{O'} = x_{O'}(t_2)$ for all the phases, while $z_{O'}$ varies from r_t to $z_{O',8}$ with constant acceleration for $t_5 \leq t < t_6$, constant velocity for $t_6 \leq t < t_7$, and constant deceleration for $t_7 \leq t < t_8$. At t_8 the velocity of O' is null, and the robot body reaches the maximum pitch angle $\theta_{b,max}$. The coordinate $z_{O',8}$ is obtained considering the geometry of Figure 3-6 and imposing the maximum pitch angle $\theta_{b,max}$:

$$z_{O',8} = r_t + \frac{w}{2}\sin\theta_{b,\max} \qquad 27$$

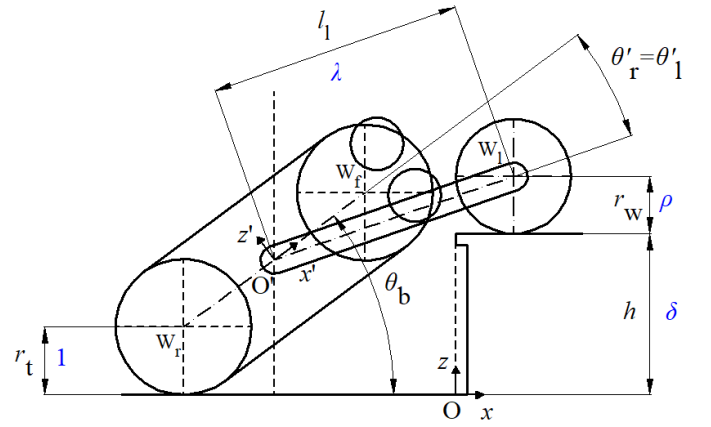

Figure 3-6 Generic position in phase 3, track raising ($t_5 \leq t \leq t_8$) [169].

In all phase 3, the following relations express the pitch angle and the relative leg angles as a function of $x_{O'}$ and $z_{O'}$:

$$\theta_b(t) = \arcsin\left(\frac{z_{O'}(t) - r_t}{w/2}\right) \quad 28$$

$$\theta_l'(t) = \theta_r'(t) = \arcsin\left(\frac{h + r_w - z_{O'}(t)}{l_l}\right) - \theta_b(t) \quad 29$$

Then the relative rotations of the track sprockets, with respect to the main body, and of the wheels, with respect to the legs, are obtained imposing non-slipping conditions:

$$\theta_T(t) = \theta_T(t_5) + \frac{x_{Wr}(t) - x_{Wr}(t_5)}{r_t} + \theta_b(t) \quad 30$$

$$\theta_W(t) = \frac{x_{Wf}(t) - x_{Wf}(t_5)}{r_w} + \theta_l'(t) + \theta_b(t) - \theta_l'(t_5) - \theta_b(t_5) \quad 31$$

In equations 30 and 31 the horizontal coordinates of the front and rear contact points W_l and W_r can be obtained by the geometry of Figure 3-6:

$$x_{Wl}(t) = x_{O'}(t) + l_l \cos\left(\theta_l'(t) + \theta_b(t)\right) \quad 32$$

$$x_{Wr}(t) = x_{O'}(t) - \frac{w}{2}\cos\left(\theta_b(t)\right) \quad 33$$

Phase 4 (*edge approach*), $t_8 \le t < t_{11}$

The robot advances horizontally with a constant pitch angle, moving only tracks and wheels. In this phase the legs are motionless and the robot advances horizontally with a constant pitch angle. The coordinate $x_{O'}$ varies from $x_{O'}(t_8) = x_{O'}(t_2)$ to $x_{O'}(t_{11})$ with constant acceleration for $t_8 \le t < t_9$, constant velocity for $t_9 \le t < t_{10}$, and constant deceleration for $t_{10} \le t < t_{11}$. At t_{11} the tracks touch the step edge with null speed. The stop position for $t = t_{11}$ is calculated considering the geometry of Figure 3-7 and imposing the contact between tracks and step edge:

$$x_{O'}(t_{11}) = \frac{w}{2}\cos\theta_{b,\max} - \frac{h - r_t}{\tan\theta_{b,\max}} - \frac{r_t}{\sin\theta_{b,\max}} \qquad 34$$

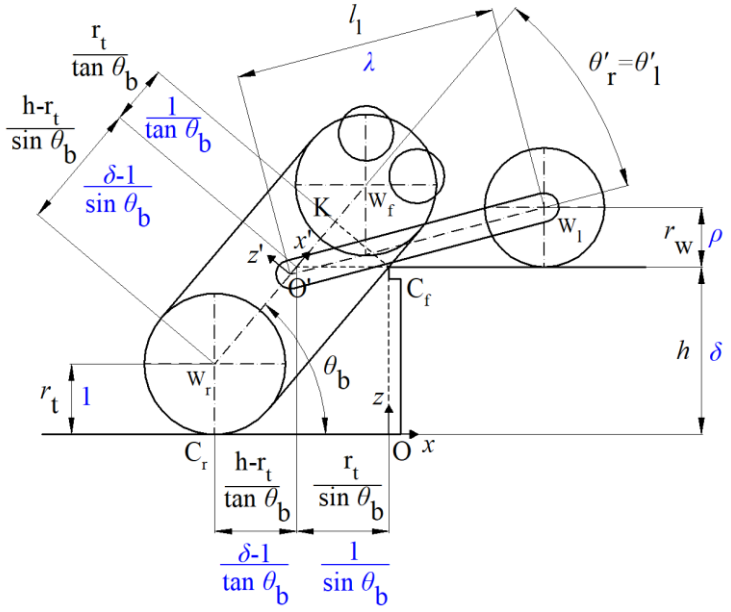

Figure 3-7 Final positions of phase 4, edge approach ($t = t_{11}$) [169].

Also in phase 4 the track and wheel relative angles can be obtained by imposing non-slipping conditions by equations 30 to 33.

Phase 5 (leg retreat), t11 ≤ t < t17

The legs rotate in an inverted direction, to touch the lower ground surface behind the robot body, while the tracks and wheels are at rest. The legs can move simultaneously or one by one. In the case of high steps, the robot stability is better guaranteed if the legs rotate one by one, as will be discussed in section 3.2.2 In this case, represented in Figure 3-3, the second leg starts to rotate when the first leg stops.

The final relative angle of the legs can be obtained considering the geometry represented in Figure 3-8:

$$\theta'_{l17} = \pi - \theta_{b,\max} + \arcsin\left(\frac{r_t + \frac{w}{2}\sin\theta_{b,\max} - r_w}{l_l}\right) \qquad 35$$

The left leg rotates from $\theta'_l(t_{11}) = \theta'_r(t_{11})$ to $\theta'_l(t_{17})$ with constant acceleration for $t_{11} \le t < t_{12}$, constant velocity for $t_{12} \le t < t_{13}$, and constant deceleration for $t_{13} \le t < t_{14}$. Then the right leg performs the same motion, with constant acceleration for $t_{14} \le t < t_{15}$, constant velocity for $t_{15} \le t < t_{16}$, and constant

deceleration for $t_{16} \leq t < t_{17}$. If the legs rotate simultaneously in the first three sections, $t_{14} = t_{15} = t_{16} = t_{17}$.

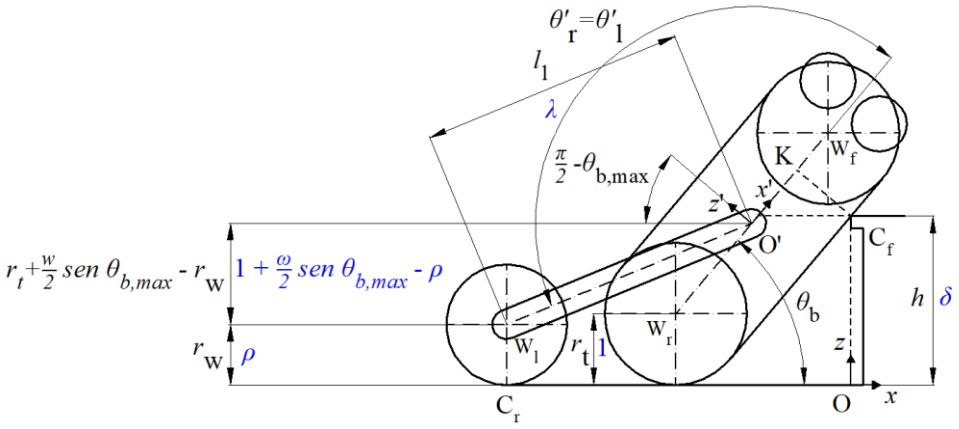

Figure 3-8 Final positions of phase 5, leg retreat ($t = t_{17}$) [169].

Phase 6 (*lift completion*), $t_{17} \leq t < t_{20}$

In this phase, the tracks are motionless, while the legs rotate backward to lift up the robot's body. The robot body rotates around the first contact point of tracks and the step edge, at $t = t_{17}$. Moreover, the wheels rotate to compensate for the horizontal displacement of the wheel-ground contact point.

The pitch angle θ_b decreases from $\theta_{b,max}$ to 0 with $d^2\theta_b/dt^2$ negative constant for $t_{17} \leq t < t_{18}$, with $d\theta_b/dt$ negative constant for $t_{18} \leq t < t_{19}$, and with $d^2\theta_b/dt^2$ positive constant for $t_{19} \leq t < t_{20}$. At t_{20} $d\theta_b/dt$ is null. The main body coordinates and the leg angle can be calculated considering the geometry of Figure 3-9:

$$x_{O'}(t) = -r_t \sin\theta_b(t) - x'_K(t_{11})\cos\theta_b(t) \qquad 36$$

$$z_{O'}(t) = h + r_t \cos\theta_b(t) - x'_K(t_{11})\sin\theta_b(t) \qquad 37$$

$$\theta'_l(t) = \theta'_r(t) = \pi - \theta_b(t) + \arcsin\left(\frac{z_{O'}(t) - r_w}{l_l}\right) \qquad 38$$

The x' coordinate of the point K at the end of phase 4 ($t = t_{11}$), which is used in equations 36 and 37, is (Figure 3-7):

$$x'_K(t_{11}) = \frac{r_t}{\tan\theta_{b,\max}} + \frac{h - r_t}{\sin\theta_{b,\max}} - \frac{w}{2} \qquad 39$$

Finally, the wheels' rotation can be obtained by imposing non-slipping conditions:

$$\theta_W(t) = \frac{x_{Wl}(t) - x_{Wl}(t_{17})}{r_w} + \theta'_l(t) + \theta_b(t) - \theta'_l(t_{17}) - \theta_b(t_{17}) + \theta_W(t_{17}) \qquad 40$$

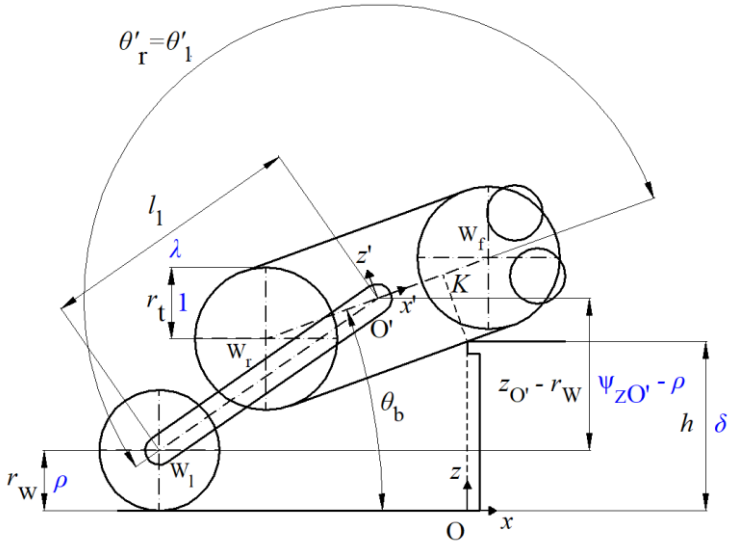

Figure 3-9 Generic position in phase 6, lift completion ($t_{17} \le t \le t_{20}$) [169].

Phase 7 (*edge overcoming*), $t_{20} \le t < t_{23}$

In this phase the legs are motionless, and the robot advances horizontally until the robot center O' is sufficiently forward with respect to the step edge to ensure stability in the following phase 8, of forward leg rotation. At the end of this phase, the horizontal advancement of O' with respect to the step edge is □xO' and the robot speed is null. Moreover, the pitch angle □b is null, zO' is equal to h + rt, and the legs angles are equal to □'l(t20). The coordinate xO' increases from xO'(t20) = -x'K(t11) to $\Delta x_{O'}$ with constant acceleration for $t_{20} \le t < t_{21}$, constant speed for $t_{21} \le t < t_{22}$, and constant deceleration for $t_{22} \le t < t_{23}$. Since both the wheels and the tracks are in contact with the ground, their velocities are proportional to the time derivative of $x_{O'}$.

Phase 8 (*leg raising*), $t_{23} \le t < t_{29}$

In this phase, the legs rotate forward to reach the vertical position at $t = t_{29}$. Tracks and wheels are motionless. The legs can move simultaneously or one by one, but the robot stability is better if the legs rotate one by one, as will be discussed in section 3.2.2.

In this phase the pitch angle θ_b is null, $z_{O'}$ is equal to $h + r_t$ and $x_{O'}$ is equal to $\Delta x_{O'}$. If the legs are rotated one by one, there are six sections: for the left leg, constant acceleration for $t_{23} \le t < t_{24}$, constant speed for $t_{24} \le t < t_{25}$, and constant deceleration for $t_{25} \le t < t_{26}$. At t_{26} the left leg arrives in the vertical position with null speed, and the same motion starts for the right leg (constant acceleration for $t_{26} \le t < t_{27}$, constant speed for $t_{27} \le t < t_{28}$, and constant deceleration for

$t_{28} \leq t < t_{29}$). If the legs are rotated simultaneously in the first three sections, $t_{26} = t_{27} = t_{28} = t_{29}$.

Phase 9 (*step depart*), $t_{29} \leq t < t_{31}$

The robot advances horizontally on the tracks, with motionless legs and wheels. This phase completes the cycle, which can be repeated n times for a stair with n steps.

This phase is divided into two sections: for $t_{29} \leq t < t_{30}$ the robot has constant acceleration, a_9, while for $t_{30} \leq t < t_{31}$ the robot speed is constant, $v_9 = v_1$, and the cycle can restart from phase 1 for the next step.

The outlined kinematic discussion and equations 26 to 40 are the basis of the motion planning scheme to be carried out as the robot approaches a step or a stair to be climbed. Obviously, environment features, geometrical tolerances, compliances and backlashes of the robot members, position control errors, and other dynamic effects introduce unavoidable uncertainties in the actual robot motion. To consider these issues, the static robustness of this motion sequence is carried out in section 3.2.2, where static stability margins are evaluated with respect to the proposed planning. Moreover, the proposed motion planning has been used in experimental tests on the prototype, during which the robot has demonstrated an excellent capacity for stair climbing and robustness of the maneuver with respect to uncertainties, as discussed in section 3.4.

3.2.2 Stability analysis

The static stability of a mobile robot during step climbing can be quantified by means of the tipping angle [170]. It is the rotation that must be imposed on the robot's main body with respect to its actual orientation to reach the limit of stability. This limit is reached when the vertical projection of the overall C.O.G. intersects the border of the polygon of the contact points. There is a tipping angle for any polygon edge. If the rotation around an edge exceeds the corresponding tipping angle due to external disturbances, the robot capsizes. Consequently, the minimum tipping angle is the most critical. Even if it is sufficient for static stability, in absence of disturbances, that all tipping angles are only strictly positive, in real conditions an adequate value of the minimum tipping angle is necessary to have a sufficient margin over uncontrolled overturning.

The quantification of the minimum value of the tipping angle to avoid overturning is very complex since it depends on several phenomena that are neglected in the static stability analysis:

- the dynamic effects, related not only to the trajectory of the climbing maneuver but also to the time history with which it is executed, in terms of linear and angular speed/acceleration of each link;
- the deformation of tracks and wheels;
- the uncertainty on geometrical and inertial parameters, and on the relative angles between the links due to the gearbox backlashes.

In the present work, a minimum value of 8° for the tipping angle has been imposed to have a sufficient margin over uncontrolled overturning. The validity of this choice has been confirmed by the successful experimental tests, discussed in section 3.4.

The position of the robot's overall center of gravity (C.O.G.) in the relative reference frame can be determined considering the main body mass m_b and the leg mass m_l. The overall mass is $m_{tot} = m_b + 2m_l$. For constructive reasons, the position of the leg C.O.G. in the xz plane is along the leg axis O'W$_1$ (Figure 3-4, left), and with distance l_{Gl} from the robot center O'. Let us note that the legs rotate along the y' axis, therefore y_G and y'_G are constant, and null if $y'_{Gb} = 0$. Consequently, in the following, only the x and z coordinates will be considered. The xz position of the overall C.O.G. in the relative reference frame is:

$$x'_G = \frac{m_b}{m_{tot}} x'_{Gb} + \frac{m_l l_{Gl}}{m_{tot}} \left(\cos\theta'_l + \cos\theta'_r \right) \quad 41$$

$$z'_G = \frac{m_b}{m_{tot}} z'_{Gb} + \frac{m_l l_{Gl}}{m_{tot}} \left(\sin\theta'_l + \sin\theta'_r \right) \quad 42$$

In dimensionless terms:

$$\psi'_{xG} = \frac{m_b}{m_{tot}} \psi'_{xGb} + \frac{m_l \xi_l}{m_{tot}} \left(\cos\theta'_l + \cos\theta'_r \right) \quad 43$$

$$\psi'_{zG} = \frac{m_b}{m_{tot}} \psi'_{zGb} + \frac{m_l \xi_l}{m_{tot}} \left(\sin\theta'_l + \sin\theta'_r \right) \quad 44$$

In the following, for sake of brevity, only the dimensionless expressions will be reported. Starting from equations 43 and 44, the xz position of the overall C.O.G. in the absolute reference frame can be obtained:

$$\psi_{xG} = \psi_{xO'} + \left(\frac{m_b}{m_{tot}} \psi'_{xGb} + \frac{m_l \xi_l}{m_{tot}} \left(\cos\theta'_l + \cos\theta'_r \right) \right) \cos\theta_b - \left(\frac{m_b}{m_{tot}} \psi'_{zGb} + \frac{m_l \xi_l}{m_{tot}} \left(\sin\theta'_l + \sin\theta'_r \right) \right) \sin\theta_b \quad 45$$

$$\psi_{zG} = \psi_{zO'} + \left(\frac{m_b}{m_{tot}} \psi'_{xGb} + \frac{m_l \xi_l}{m_{tot}} \left(\cos\theta'_l + \cos\theta'_r \right) \right) \sin\theta_b + \left(\frac{m_b}{m_{tot}} \psi'_{zGb} + \frac{m_l \xi_l}{m_{tot}} \left(\sin\theta'_l + \sin\theta'_r \right) \right) \cos\theta_b \quad 46$$

Performing the step climbing as discussed in section 3.2.1, the robot position is always symmetric with respect to the xz plane, except in phases 5 and 8, in which the legs rotate one by one. Consequently, in phases 1-4, 6, 7, and 9 the y coordinate of the C.O.G. is null. Therefore, in these phases, the polygon of the contact points is symmetric with respect to the xz plane, with the front and rear edges, which are the front and rear tipping lines, aligned with the y axis. Moreover, in these phases, the y coordinates of the track-ground and wheel-ground contact points are constant and can be easily determined from the robot's main dimensions (see Table 3-2). As a result, in these phases stability can be analyzed as a planar problem, evaluating the front and rear tipping angles γ_f and γ_r in the xz plane.

Lateral tipping angles are much higher than the front and rear ones due to the robot width and are not considered in the analysis.

On the contrary, in phases 5 and 8, the legs rotate one by one. Consequently, the polygon of the contact points is not symmetric with respect to the *xz* plane, and its front and rear edges are not parallel to the *y* axes. Therefore, in these phases the stability problem cannot be considered planar, and also the *y* coordinate must be taken into account. The tipping lines and angles can be calculated by means of equations (47) and (48), as will be discussed in the following.

Table 3-2 collects the coordinates of the four contact points with the ground in each phase, obtained from the geometric relationships discussed in section 3.2.13.

Table 3-2 Coordinates the contact points with the ground for the nine-step climbing phases.

Phase	$P_1 = C_{fl}$	$P_2 = C_{fr}$	$P_3 = C_{rr}$	$P_4 = C_{rl}$
1, 2	$x_{O'}(t)+\frac{w}{2};\frac{b_t}{2};0$	$x_{O'}(t)+\frac{w}{2};-\frac{b_t}{2};0$	$x_{O'}(t)-\frac{w}{2};-\frac{b_t}{2};0$	$x_{O'}(t)-\frac{w}{2};\frac{b_t}{2};0$
3, 4	$x_{O'}(t)+l_l\cos(\theta_b(t)+\theta_l'(t));\frac{b_w}{2};h$	$x_{O'}(t)+l_l\cos(\theta_b(t)+\theta_l'(t));-\frac{b_w}{2};h$	$x_{O'}(t)-\frac{w}{2}\cos\theta_b(t);-\frac{b_t}{2};0$	$x_{O'}(t)-\frac{w}{2}\cos\theta_b(t);\frac{b_t}{2};0$
5 ($t_{11} \le t < t_{14}$)	$0;\frac{b_t}{2};h$	$x_{O'}(t)+l_l\cos(\theta_b(t)+\theta_r'(t));-\frac{b_w}{2};h$	$x_{O'}(t)-\frac{w}{2}\cos\theta_b(t);-\frac{b_t}{2};0$	$x_{O'}(t)-\frac{w}{2}\cos\theta_b(t);\frac{b_t}{2};0$
5 ($t_{14} \le t < t_{17}$)	$0;\frac{b_t}{2};h$	$0;-\frac{b_t}{2};h$	$x_{O'}(t)-\frac{w}{2}\cos\theta_b(t);-\frac{b_t}{2};0$	$x_{O'}(t)+l_l\cos(\theta_b(t)+\theta_l'(t));\frac{b_w}{2};0$
6	$0;\frac{b_t}{2};h$	$0;-\frac{b_t}{2};h$	$x_{O'}(t)+l_l\cos(\theta_b(t)+\theta_r'(t));-\frac{b_w}{2};0$	$x_{O'}(t)+l_l\cos(\theta_b(t)+\theta_l'(t));\frac{b_w}{2};0$
7	$x_{O'}(t)+\frac{w}{2};\frac{b_t}{2};h$	$x_{O'}(t)+\frac{w}{2};-\frac{b_t}{2};h$	$x_{O'}(t)+l_l\cos\theta_r'(t);-\frac{b_w}{2};0$	$x_{O'}(t)+l_l\cos\theta_l'(t);\frac{b_w}{2};0$
8 ($t_{23} \le t < t_{26}$)	$x_{O'}(t)+\frac{w}{2};\frac{b_t}{2};h$	$x_{O'}(t)+\frac{w}{2};-\frac{b_t}{2};h$	$x_{O'}(t)+l_l\cos\theta_r'(t);-\frac{b_w}{2};0$	$0;\frac{b_t}{2};h$
8 ($t_{26} \le t < t_{29}$)	$x_{O'}(t)+\frac{w}{2};\frac{b_t}{2};h$	$x_{O'}(t)+\frac{w}{2};-\frac{b_t}{2};h$	$0;-\frac{b_t}{2};h$	$0;\frac{b_t}{2};h$
9	$x_{O'}(t)+\frac{w}{2};\frac{b_t}{2};h$	$x_{O'}(t)+\frac{w}{2};-\frac{b_t}{2};h$	$\max\left(0,x_{O'}(t)-\frac{w}{2}\right);-\frac{b_t}{2};h$	$\max\left(0,x_{O'}(t)-\frac{w}{2}\right);\frac{b_t}{2};h$

Phase 5 is the most critical for stability since the lowest values of the rear tipping angle are reached during it, as will be discussed extensively in section 3.2.2. Figure 3-10 shows the benefit of the sequential leg rotation over the simultaneous leg rotation in phase 5: if legs rotate one by one, in the worst stability position (Figure 3-10, *b*) the overall C.O.G. G is almost coincident with the robot geometric center O', while with simultaneous leg rotation (Figure 3-10, *a*) both the legs point backward reducing the rear tipping angle γ_r.

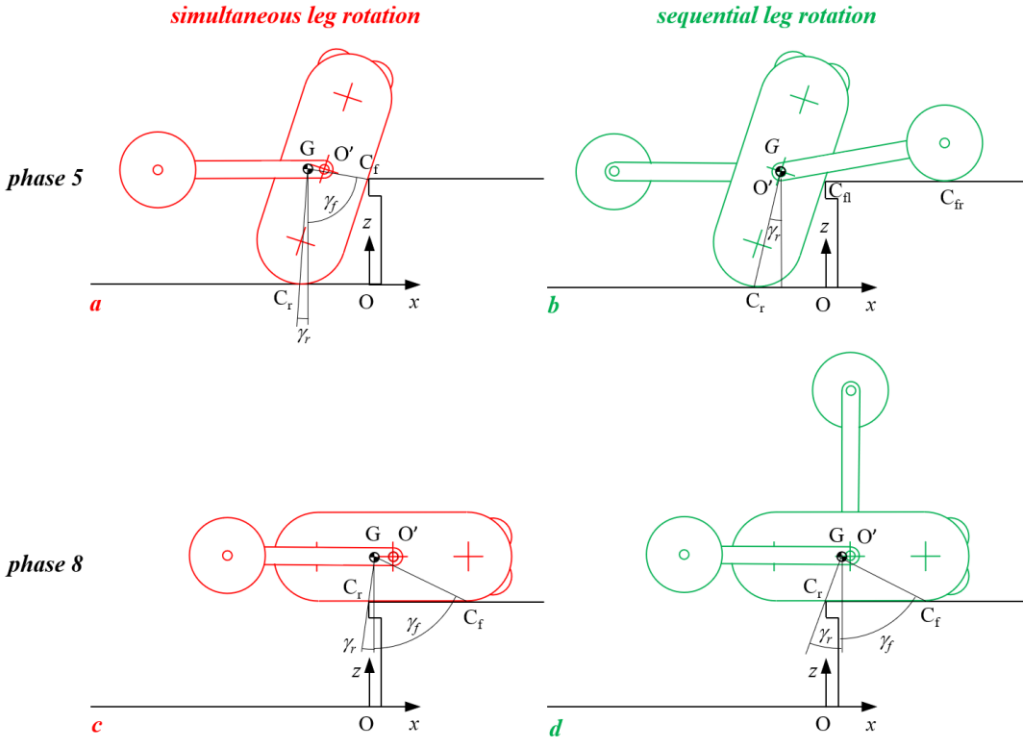

Figure 3-10 Front and rear tipping angles in the worst stability conditions in phase 5, leg retreat (a: simultaneous leg rotation, b: sequential leg rotation), and in phase 8, leg raising (c: simultaneous leg rotation, d: sequential leg rotation).

Similarly, in phase 8, in the worst stability position with simultaneous leg rotation (Figure 3-10, *c*) G is placed backward with respect to the worst stability position with sequential leg rotation (Figure 3-10, *d*), thus decreasing the rear tipping angle γ_r. Moreover, in the position of Figure 3-10, *d* the left leg can point forward instead of being vertical to increase even more stability, but it is in general not necessary.

Starting from a generic polygon of contact points P_i, numbered clockwise as in Table 3-2, the vector of the tipping line $\mathbf{l}_i$ of each edge (Figure 3-11) can be calculated by means of the following formula [170]:

$$\mathbf{l}_i = \left(\mathbf{I} - \hat{\mathbf{a}}_i \hat{\mathbf{a}}_i^T\right)\left(P_{i+1} - O\right),\ \hat{\mathbf{a}}_i = \mathbf{a}_i / \left\|\mathbf{a}_i\right\| \qquad 47$$

where $\mathbf{I}$ is the identity matrix and $\mathbf{a}_i$ is the vector from P_i to P_{i+1}; in equation (47) and in the following the circumflex accent indicates a unit vector with the same direction as the corresponding vector.

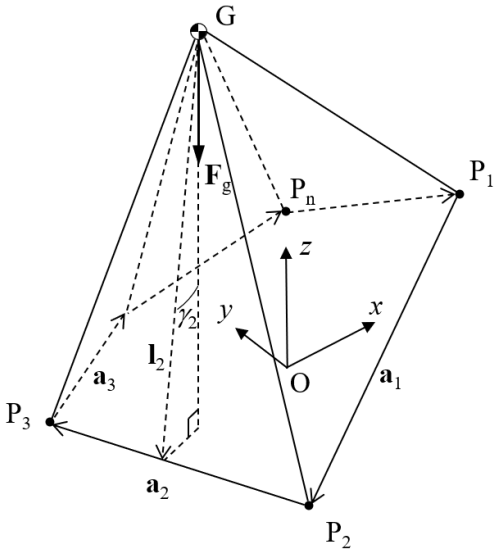

Figure 3-11 Schematic diagram of stability cone

The tipping angle γ_i of the i^{th} edge line is the angle between $\mathbf{l}_i$ and the vertical gravity force $\mathbf{F}_g$ applied in the overall C.O.G. The tipping angle γ_i can be calculated as follows [170]:

$$\gamma_i = \sigma_i \arccos\left(\hat{\mathbf{F}}_g \cdot \hat{\mathbf{l}}_i\right), \qquad \sigma_i = \begin{cases} +1, & \left(\hat{\mathbf{F}}_g \times \hat{\mathbf{l}}_i\right) \cdot \hat{\mathbf{a}}_i > 0 \\ -1 & \end{cases} \qquad 48$$

Adopting equation 48, a positive tipping angle indicates stability (the vertical straight line passing through the overall C.O.G. intersects the support polygon). Equations 47 and 48 and the contact points summarized in Table 3-2 are used to calculate the front and rear tipping angles in phases 5 and 8, in which the stability problem is not planar.

In Figure 3-12 to Figure 3-15 kinematic and stability results are presented considering the main geometrical and mass parameters of the first WheTLHLoc prototype: r_t = 59 mm, r_w = 50 mm, w = 196 mm, l_l = 220 mm, b_t = 271 mm, b_w = 405 mm, l_{Gl} = 182 mm, m_b = 4.05 kg, and m_l = 0.59 kg. Due to the internal robot layout [43], the main body C.O.G. is slightly shifted with respect to the relative reference frame: [x'_{Gb}, y'_{Gb}, z'_{Gb}] = [11, 0, -2] mm. The considered step has riser h = 160 mm and tread r = 300 mm. The robot motion is completely defined by the equations discussed in section 3.1 and by the parameters collected in Table 3-3.

Figure 3-12 represents the relative angular displacements imposed to track sprockets, wheels, and legs (robot internal coordinates). Figure 3-13 shows the corresponding absolute angles of the main body and legs. Figure 3-14 represents the absolute coordinates in the *xz* plane of the main body reference frame (O') and of the overall C.O.G. (G). Finally, Figure 3-15 shows the front and rear tipping angles γ_f and γ_r (lateral tipping angles are evidently higher and never critical). It is possible to see that the rear tipping angle γ_r is more critical, with 2 minimum

values of 12.7° in phase 5 and 12.9° in phase 8; however, these values indicate a sufficient margin of stability.

Table 3-3 Kinematic parameters considered in the simulations.

h			v_1		$x_O(0)$			$x_O(t_2)$			$x_O(t_{23}) = \Delta x_O$			$\theta_{b,max}$	
160 mm			0.02 m/s		-190 mm			-160 mm			30 mm			70°	
t_1	t_2	t_3	t_4	t_5	t_6	t_7	t_8	t_9	t_{10}	t_{11}	t_{12}	t_{13}	t_{14}	t_{15}	t_{16}
1.0 s	2.0 s	2.4 s	3.6 s	4.0 s	4.8 s	7.2 s	8.0 s	8.6 s	10.4 s	11.0 s	11.4 s	12.6 s	13.0 s	13.4 s	14.6 s
t_{17}	t_{18}	t_{19}	t_{20}	t_{21}	t_{22}	t_{23}	t_{24}	t_{25}	t_{26}	t_{27}	t_{28}	t_{29}	t_{30}	t_{31} (cycle)	
15.0 s	15.6 s	17.4 s	18.0 s	18.4 s	19.6 s	20.0 s	20.4 s	21.6 s	22.0 s	22.4 s	23.6 s	24.0 s	25.0 s	28.5 s	

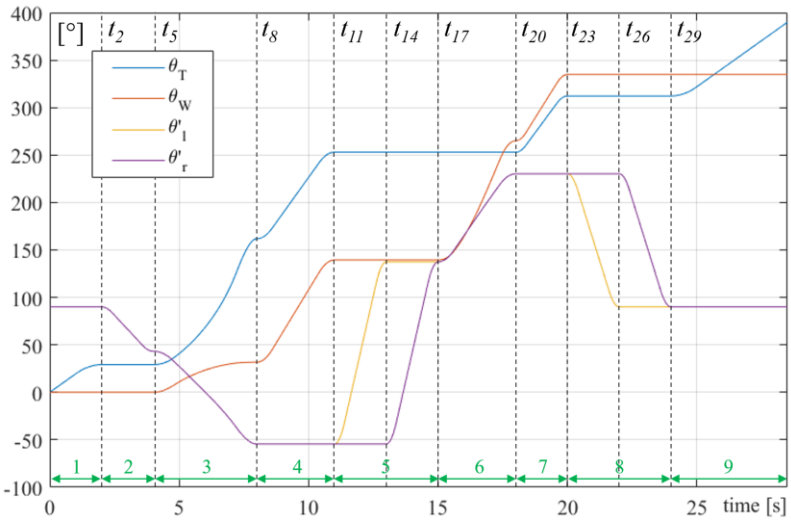

Figure 3-12 Rotation of the track sprockets relative to the main body (θ_T), of wheels relative to the legs (θ_W), of the left and right leg relative to the main body (θ'_l and θ'_r); phases are numbered in green.

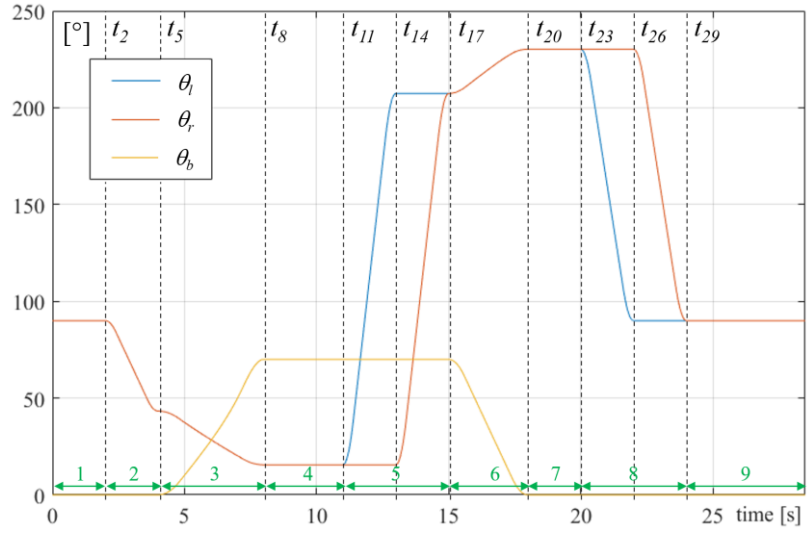

Figure 3-13 Angles of left and right leg (θ_l and θ_r) and main body pitch angle (θ_b) with respect to the fixed reference frame O(x,y,z); phases are numbered in green.

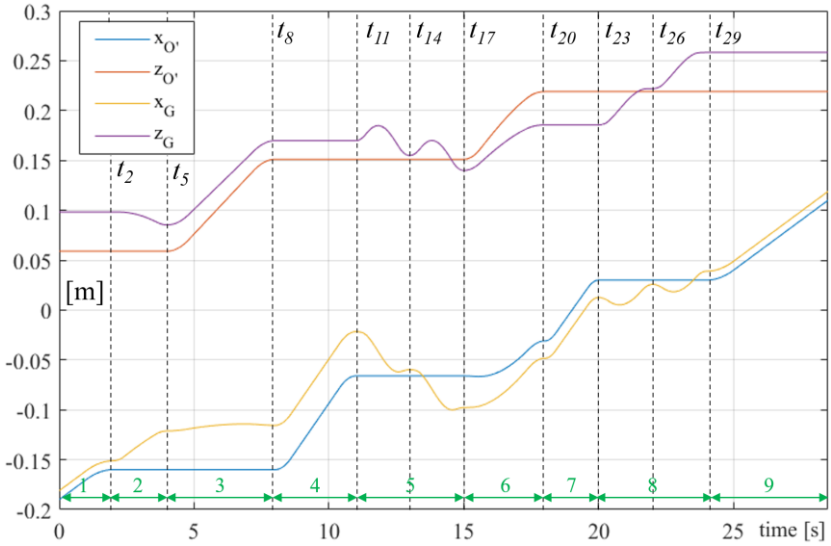

Figure 3-14 Absolute x and z coordinates of the main body reference frame (O') and of the overall C.O.G. (G); phases are numbered in green.

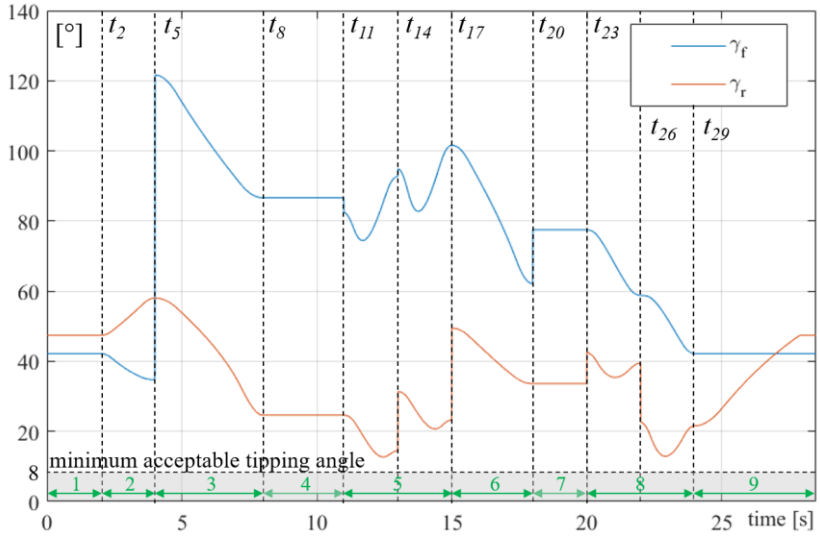

Figure 3-15 Front and rear tipping angles (γ_f and γ_r); phases are numbered in green. The grey zone indicates insufficient tipping angles.

Once the time histories of all robot members are known, they can be time-derived to obtain speeds, accelerations, and inertial forces. This allows for validating the static stability approach, comparing overturning moments, due to gravity, and stabilizing moments, due to inertial forces. Starting from the time histories of Figure 3-12 to Figure 3-14, the minimum stabilizing moment is 0.94 Nm, while the maximum overturning moment is 0.09 Nm (calculations are omitted for brevity). This confirms the validity of the static stability analysis.

3.2.3 Non-slipping conditions

Besides evaluating the robot's stability, it is necessary to verify if the friction forces of tracks and wheels are sufficient to overcome the gravity force, lifting up the robot body over the step edge. Reasoning on the step climbing sequence discussed in section 3.2.1, it is possible to understand that the most critical instant from this point of view is at $t = t_{17}$, at the beginning of phase 6, for the reasons explained below.

In phases, 1-4 and 7-9 tracks and legs are in contact with horizontal ground surfaces, so the vertical gravity force is balanced by vertical normal reactions, without tangential reaction components, and therefore without the possibility of slipping. On the contrary, in phases 5 and 6 the normal reactions in the contacts between tracks and the step edge are not vertical, so in general a tangential reaction can be necessary to balance the gravity force and slipping is possible.

In phase 5 there are always at least three contacts. For example, in Figure 3-10, *b* four contacts can be identified: two track-ground contacts in C_r (left and right), a wheel-ground contact in C_{fr}, and a track-step edge contact in C_{fl}. When the left leg finishes its rotation, the left wheel touches the ground behind the robot and the right wheel detaches from the horizontal step surface in C_{fr}. In general, in phase 5 the stability problem is three-dimensional and overconstrained and can't be solved without considering the system compliance. Nevertheless, the kinematic

analysis shows that the robot C.O.G is placed along the horizontal direction between the two track-ground contacts, whose vertical normal reactions can support most of the gravity force, avoiding slipping.

In phase 6 the robot position is symmetric with respect to the *xz* plane, and the problem is planar: there are two contacts, the rear between wheels and ground, and the front between tracks and step edge (Figure 3-9). In absence of friction in these contacts, due to the inclination of the normal reaction in the track-step edge contact, the robot slips, lowering its C.O.G.; therefore friction is necessary to maintain equilibrium, and the non-slipping condition must be analyzed. The most critical position is at the beginning of phase 6 ($t = t_{17}$, Fig. 16), since the inclination of the track-step edge normal reaction is maximum.

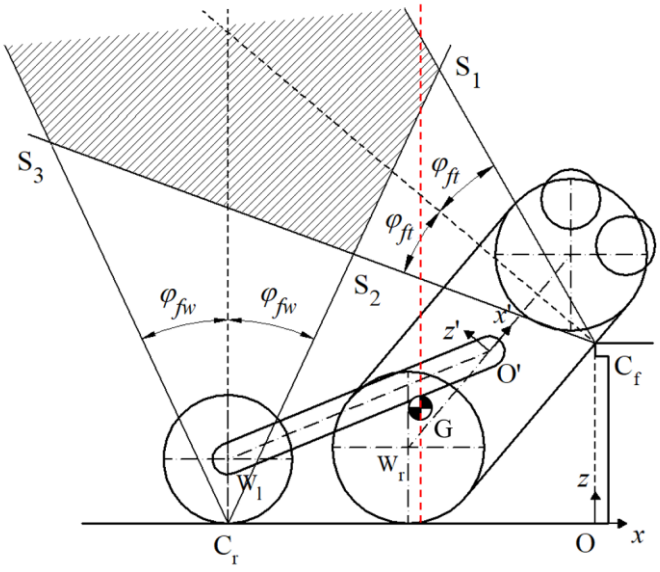

Figure 3-16 Static conditions at the beginning of phase 6, lift completion ($t = t_{17}$).

As the legs start to rotate backward, the tracks touch the ground only at the step edge (C_f); therefore the robot, in quasi-static conditions, with negligible inertial forces, is subject only to three forces: the two contact forces in C_r and C_f, and the gravity force applied in the robot C.O.G. If f_w and f_t are the wheel-terrain and track-terrain static friction coefficients, in non-slipping conditions the two contact forces must lie inside two friction cones with semi-angles $\varphi_{fw} = atan(f_w)$ and $\varphi_{ft} = atan(f_t)$. Moreover, a necessary condition for the static stability of a planar body subject to three forces is that the lines of action of the three forces intersect at the same point. Consequently, the robot is statically stable in the starting position of phase 6 only if the vertical line passing through the robot's overall C.O.G. (Figure 3-16, red dotted line) intersects the hatched area of Figure 3-16. Therefore, the non-slipping condition corresponds to $x_{S1} > x_G$, where S_1 is the area vertex with a higher x coordinate (Figure 3-16). Writing the equations of the two straight lines which limit the two stability cones and intersect in S_1 and

considering the robot geometry, the non-slipping condition can be expressed in the following dimensional and dimensionless forms:

$$x_{S1} - x_G = -\frac{x_{Wl}(t_{17})\tan\left(\frac{\pi}{2} - \varphi_{fw}\right) + h}{\tan\left(\frac{\pi}{2} + \theta_b(t_{17}) - \varphi_{ft}\right) - \tan\left(\frac{\pi}{2} - \varphi_{fw}\right)} - x_G > 0 \qquad 49$$

$$\psi_{xS1} - \psi_{xG} = -\frac{\psi_{xWl}(t_{17})\tan\left(\frac{\pi}{2} - \varphi_{fw}\right) + \delta}{\tan\left(\frac{\pi}{2} + \theta_b(t_{17}) - \varphi_{ft}\right) - \tan\left(\frac{\pi}{2} - \varphi_{fw}\right)} - \psi_{xG} > 0 \qquad 50$$

It is necessary to verify the non-slipping condition only at the beginning of phase 6, since as the pitch angle θ_b decreases the friction cone in C_f rotates forward and x_{S1} increases, thus making less critical the fulfillment of conditions (49) and (50).

Let us note that in the case of step descent, which is executed by inverting the step climbing motion, from phase 9 to phase 1, the non-slipping condition is less critical since it is not necessary to overcome the gravity force by means of the traction of wheels and tracks. A little slippage in phase 6, near the maximum pitch condition, can result only in a small uncontrolled motion, which ends when the tracks touch the lower step but doesn't imply the failure of the maneuver.

3.3 Selection of the step climbing kinematics as a function of the step height

In order to plan properly the step climbing kinematics for different values of the step height h, the stability, and non-slipping conditions discussed in sections 3.2.2 and 3.2.3 have been assessed as functions of the step height h and of the maximum pitch angle $\theta_{b,max}$, which characterizes the execution of the phases 3 to 6.

Regarding stability, Figure 3-17 shows the influence of h and $\theta_{b,max}$ on the minimum values of the front and rear tipping angles γ_f and γ_r for the climbing maneuver performed according to the kinematics discussed in section 3.2.1 and with the parameters of Table 3-3. The considered range of h is between 0.035 m and 0.165 m. It is useless to consider lower steps, since they can be climbed by tracked locomotion, without using the legs. The considered range of $\theta_{b,max}$ is between 10° and 80°.

Observing Figure 3-17, it is possible to note that the minimum front tipping angle $\gamma_{f,min}$ (red surface) is negative if high-pitch angles are used in combination with small steps, compromising stability, with the robot falling forward. However, high values of $\theta_{b,max}$ are necessary only to face high steps, since the maximum pitch angle must be sufficient to lift the track over the step edge in phase 3. Therefore, proper motion planning must impose an increasing function $\theta_{b,max}(h)$, as discussed in the following.

As regards the rear angle γ_r, observing Figure 3-15 it is possible to note that it has two local minima in phases 5 and 8, $\gamma_{r,min5}$ and $\gamma_{r,min8}$, which are represented respectively by the green and the blue surfaces in Figure 3-17. These minima are always positive in the considered ranges of $\theta_{b,max,}$ and h. Moreover, $\gamma_{f,min8}$ is constant, since it depends only on the horizontal advancement of the robot body center O' with respect to the step edge ($\Delta x_{O'}$ = 30 mm), but not on h and $\theta_{b,max}$.

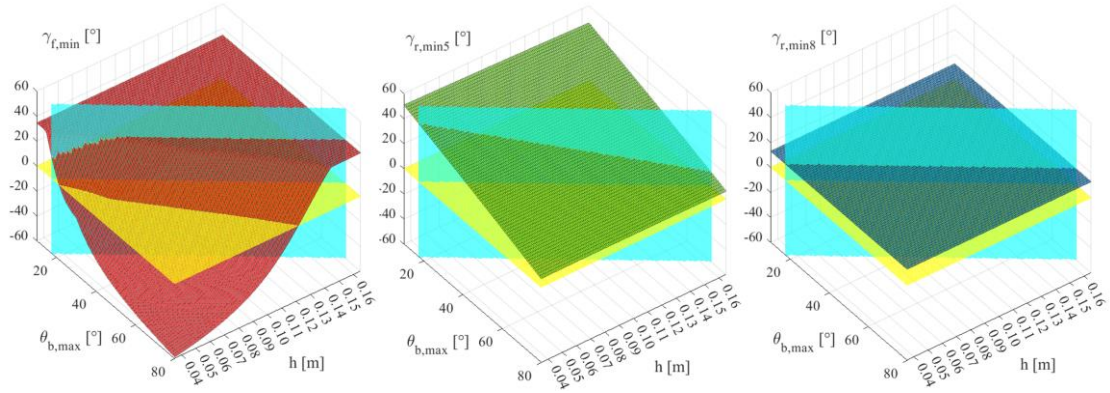

Figure 3-17 Influence of step height h and maximum pitch angle $\theta_{b,max}$ on the robot stability; $\gamma_{f,min}$: minimum front tipping angle; $\gamma_{r,min5}$: minimum rear tipping angle in phase 5; $\gamma_{r,min8}$: minimum rear tipping angle in phase 8. The yellow plane represents the null surface, and the cyan plane represents the motion planning relationship imposed by Eq. (51).

The non-slipping condition is represented in Figure 3-18, which shows the surfaces corresponding to $x_{S1} - x_G$ for different static friction coefficients: $f_w = f_t$ = 0.5, 0.7, 0.9, 1.1. The condition expressed by inequality (24) is satisfied for positive vertical values of these surfaces. As obvious, lower friction coefficients correspond to lower surfaces, with smaller regions in which the non-slipping condition is fulfilled. For the highest friction coefficient (1.1, almost technically infeasible) the condition is verified for any combination of h and $\theta_{b,max}$.

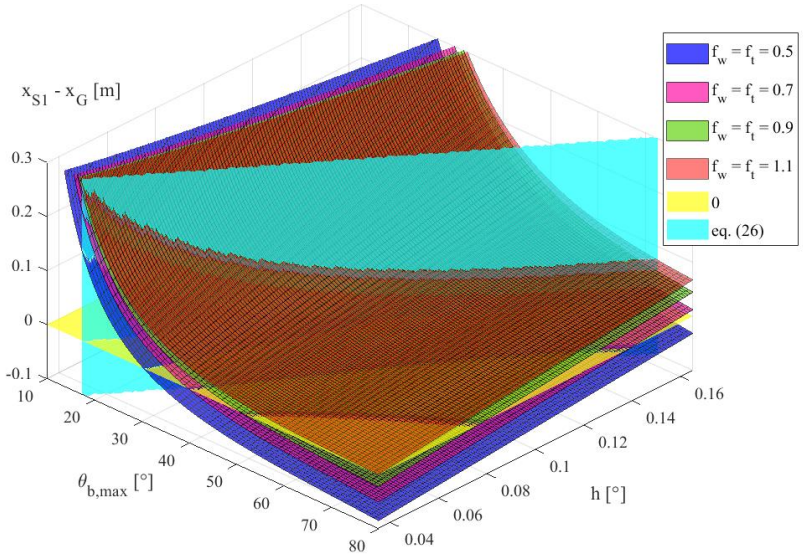

Figure 3-18 Influence of step height h and maximum pitch angle $\theta_{b,max}$ on the non-slipping condition ($x_{S1} - x_G > 0$), for different static friction coefficients: $f_w = f_t = 0.5$ (blue), 0.7 (violet), 0.9 (green), 1.1 (red); the stability condition is verified in the regions where the surfaces are higher than the null surface (yellow). The cyan plane represents the motion planning relationship imposed by Eq. (51).

The kinematics of the step climbing maneuver is completely defined by the parameters collected in Table 3-3. Neglecting $x_{O'}(0)$ and $x_{O'}(t_2)$, which are related to the approach phase, without stability or non-slipping issues, the remaining parameters are h, v_1, $\Delta x_{O'}$, $\theta_{b,max}$, and the time parameters t_1, …, t_{31}. The time and velocity parameters don't influence the robot's trajectory, but only the speed at which it is executed. Therefore, they don't influence static stability and non-slipping conditions. The remaining parameters are h, $\Delta x_{O'}$, and $\theta_{b,max}$. Since the step height is given, in order to automatize the step climbing maneuver it is necessary to measure h and then select $\Delta x_{O'}$ and $\theta_{b,max}$ as a function of h through a proper strategy.

The proposed strategy has been conceived by piloting the robot manually and observing that successful execution of the step climbing maneuver can be obtained for any step height in the considered range by keeping constant $\Delta x_{O'} = 30$ mm and increasing $\theta_{b,max}$ linearly as a function of h according to the following relationship:

$$\theta_{b,\max}(h) = 24° + \frac{h - 0.05}{0.11} 46° \qquad 51$$

Equation 51 is obtained linearly interpolating between two conditions: $\theta_{b,max} = 24°$ for $h = 0.05$ m and $\theta_{b,max} = 70°$ for $h = 0.16$ m. This empirical relationship has been validated by considering the previously discussed static stability and non-slipping conditions. As a matter of fact, imposing this linear relationship between $\theta_{b,max}$ and h correspond to intersecting the 3D surfaces of Figure 3-17 and Figure 3-18 with the vertical plane shown in cyan in Figure 3-17 and Figure 3-18. These intersections are represented in Figure 3-19: the continuous lines of the left graph represent the intersections with the tipping angle surfaces of Figure 3-17, while the continuous lines of the right graph represent the intersections with the $x_{S1} - x_G$ surfaces of Figure 3-18, with corresponding colors.

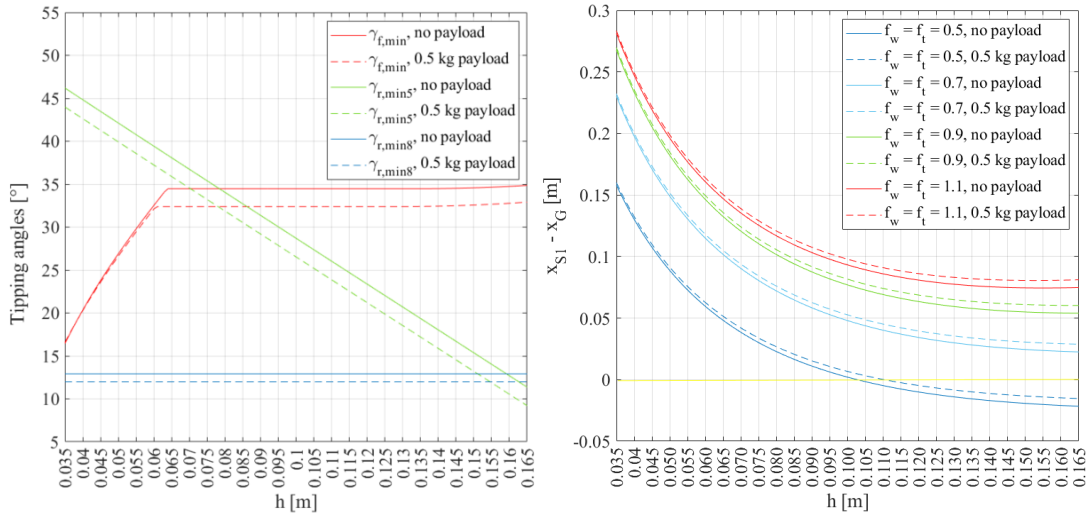

Figure 3-19 Stability and non-slipping conditions as a function of the step height h with the proposed maximum pitch angle law $\theta_{b,max}(h)$. Left: minimum front and rear tipping angles $\gamma_{f,min}$ (red), $\gamma_{r,min5}$ (green), and $\gamma_{r,min8}$ (blue) [°]. Right: $x_{S1} - x_G$ [m] for different static friction coefficients: $f_w = f_t = 0.5$ (blue), 0.7 (cyan), 0.9 (green), 1.1 (red). Continuous lines refer to the absence of payload and dashed lines to the maximum payload (0.5 kg).

Moreover, in order to show the influence of a possible external payload, the dashed lines in Figure 3-19 represent the same surface intersections in case of a 0.5 kg payload, the maximum considered in the design specifications, placed on the upper main body surface with C.O.G at [0, 0, 75 mm] in the O'(x',y',z') reference frame. It is possible to see that the influence of the payload is not relevant. There is a limited decrease of the minimum front and rear tipping angles (up to -1.9°, -2.2°, -0.9° respectively for $\gamma_{f,min}$, $\gamma_{r,min5}$ and $\gamma_{r,min8}$), since the payload shifts upward the main body C.O.G., slightly worsening stability. On the other hand, the shift of the main body C.O.G. decreases x_G in phase 5, slightly facilitating the fulfillment of the non-slipping condition, since $x_{S1} - x_G$ increases up to 6 mm for h = 165 mm.

From the analysis of Figure 3-19, it is possible to note that the proposed law (51) assures that all the tipping angles remain higher than 11.3° for any step height (9.2° with the payload). These values assure a sufficient margin of stability during the step climbing maneuver since they represent the additional rotation that must be caused by external disturbances to make the robot capsize. As regards the non-slipping condition, for the three higher values of friction coefficients (0.7, 0.9, 1.1, cyan, green, and red continuous lines of Figure 3-19), the condition (24) is verified for any step height in the considered range. On the contrary, for $f_w = f_t = 0.5$ (blue continuous line of Figure 3-19) there is slipping for $h > 0.103$ m (0.110 m with the payload). This represents a physical limitation: it is impossible to climb high steps with the proposed maneuver without a sufficient friction coefficient. This limitation is analyzed in Figure 3-20, left, where the blue surface represents $x_{S1} - x_G$ calculated applying the law (26) with a friction coefficient $f_w = f_t$ which varies from 0.1 to 1.1, without payload. The non-slipping condition is verified in the regions where $x_{S1} - x_G$ (the blue surface) is higher than zero (yellow plane). For the minimum considered step (h = 0.035 m), the minimum friction coefficient to perform step climbing is 0.24; for the maximum considered step height (h = 0.165 m), the minimum friction coefficient to perform step

climbing is 0.59; for intermediate values, the minimum friction coefficient varies nonlinearly along the intersection between the blue and yellow surfaces of Figure 3-20, left.

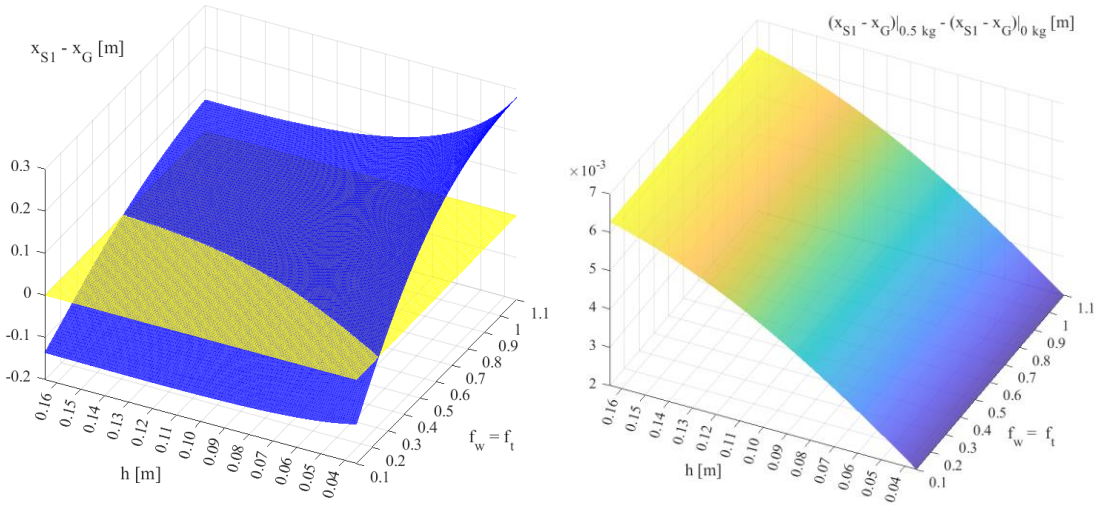

Figure 3-20 Non-slipping condition as a function of step height h and of the static friction coefficient $f_w = f_t$. Left: $x_{S1} - x_G$ without payload; the condition is verified in the region where $x_{S1} - x_G$ (blue surface) is higher than 0 (yellow plane). Right: the difference between $(x_{S1} - x_G)$ with 0.5 kg payload and $(x_{S1} - x_G)$ without payload.

As already said, the payload slightly increases $x_{S1} - x_G$; however, even in the case of maximum payload, the $x_{S1} - x_G$ surface of Figure 3-20, left, varies unnoticeably. The variation of $x_{S1} - x_G$ in the case of a payload is represented in Figure 3-20, right: the increase is independent of the friction coefficient and has a maximum value of 6.3 mm for h = 165 mm.

3.4 Experimental tests on the prototype

A prototype of the WheTLHLoc robot has been realized. Figure 3-21 shows its internal layout, with the components disposed of in two layers. The lower layer (Figure 3-21, a) hosts the two gearmotors of the tracks (TM) and the two of the legs (LM), connected to the shafts of tracks and legs by gears (TG and LG). In the lower layer, there are also the motor drivers of wheels, legs, and tracks (WD, LD, TD) and the voltage regulator (VR). The leg shafts (LS) are hollow and equipped with slip rings (SR) to connect the power supply and encoder signals of the wheel gearmotors (WM) even if the legs perform continuous rotation. In the upper layer (Figure 3-21, b), two 14.8 V LiPo batteries (B) and the National Instruments MyRio-1900 controller (C) are placed on 3D-printed supports. All the structural parts, except shafts, sprockets, tracks, wheels, and Omni wheels, are 3D printed in ABS, PLA, and Onyx.

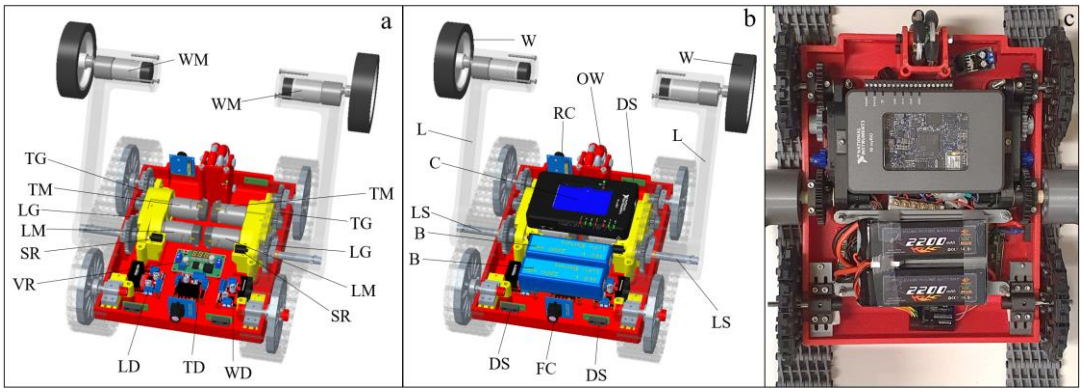

Figure 3-21 Internal layout of the robot: upper layer (a), lower layer (b), internal view of the prototype (c).

The prototype has been used for experimental validation of the proposed step-climbing maneuver capability of the robot. In these tests, the six axes (of tracks, legs, and wheels) are position controlled by the MyRio-1900, which is programmed in LabView. The position loop sampling time is 5 ms. The six set-point time histories are precomputed offline on a PC by MATLAB, implementing the kinematic relationships discussed in section 3.2.1. In these tests, the step height is known a priori, but in the future, it will be measured by the camera vision through image recognition or exploiting other sensors, and the set-point time histories will be calculated onboard. Figure 3-22 shows the robot climbing a step with h =165 mm. According to equation 51, the maximum pitch angle is $\theta_{b,max}$ = 72°.

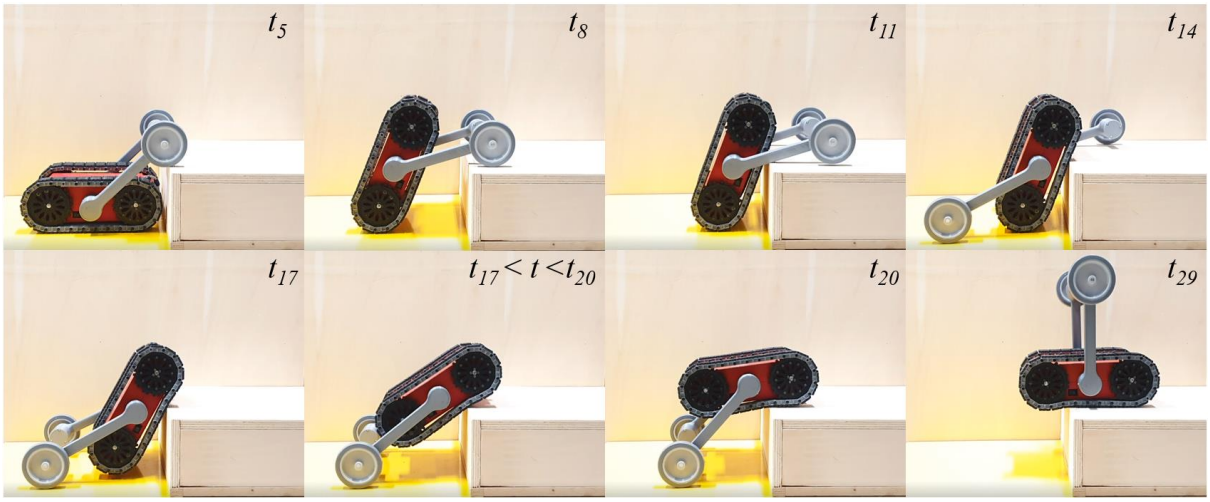

Figure 3-22 Step climbing sequence (h = 165 mm).

Although the kinematics analyzed in section 3.2.1 is not perfectly executed due to the unavoidable compliance of the tracks, which is visible in the last four frames of Figure 3-22, the experimental tests confirm the feasibility of the proposed maneuver. As a matter of fact, the track compliance is favorable for the non-slipping condition, since the normal to the track in the contact point rotates slightly forward (clockwise in Figure 3-16) thus advancing the horizontal position of point S_1.

Figure 3-23 compares simulations based on the kinematic relationships discussed in section 3.2.1 and the experimental results in terms of x-z coordinates of the main body reference frame O' and pitch angle θ_b, for two different step heights (142 mm and 165 mm). The experimental results have been obtained by analyzing the videos of the step-climbing maneuver by means of the Tracker software, built on the Open Source Physics (OSP) Java framework [171]. The comparison shows a good agreement, with maximum differences between simulations and experiments of 5 mm, 3 mm, and 1.3° respectively for $x_{O'}$, $z_{O'}$, and θ_b. These small differences are both due to real physical phenomena (compliance of the tracks, backlashes in gearheads, errors of the six position controllers) and measurement errors.

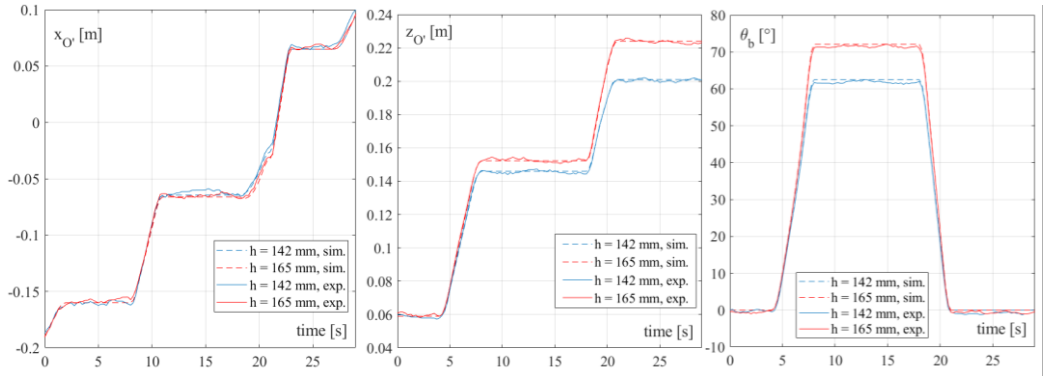

Figure 3-23 Comparison of simulation and experimental results: $x_{O'}$ (left), $z_{O'}$ (center), θ_b (right). Continuous lines: experimental tests; dashed lines: simulation. Blue lines: h = 142 mm; red lines: h = 165 mm.

Several tests of the step climbing maneuver have been carried out in real operative environments, for example with marble stairs (Figure 3-24, a) and with stairs with steel edges (Figure 3-24, b).

Besides the step climbing tests performed with position control, tests with remote control by a human have been carried out to assess the motion performance and maneuverability in various conditions: wheeled locomotion on flat and compact grounds (Figure 3-24, c), hybrid leg-wheel-track locomotion to overcome irregular obstacles (Figure 3-24, d), tracked locomotion on soft and yielding terrains (Figure 3-24, e) and on irregular terrains (Figure 3-24,f). The two 2200 mAh LiPo batteries provide autonomy of 2.5 hours in wheeled locomotion or 2 hours in tracked locomotion. A supporting video of the experimental tests is available at [172].

Figure 3-24 Experimental tests in various operative conditions: climbing of a marble stair (a) and of a stair with steel edge (b), locomotion on wheels and Omni wheels on flat and even terrain (c), mixed leg-wheel-track locomotion to climb irregular obstacles (d), tracked locomotion on soft and yielding terrain (e) and on irregular terrain (f).

3.4.1 Control Architecture

The MyRio-1900 controller has been selected for its capability of controlling in position of six motors and managing a Wi-Fi connection to a remote PC, with the possibility of video transmission. Moreover, it is equipped with a three-axial accelerometer, suitable to monitor the robot dynamics in step and obstacle climbing. It is programmed in the block-scheme-based LabView language.

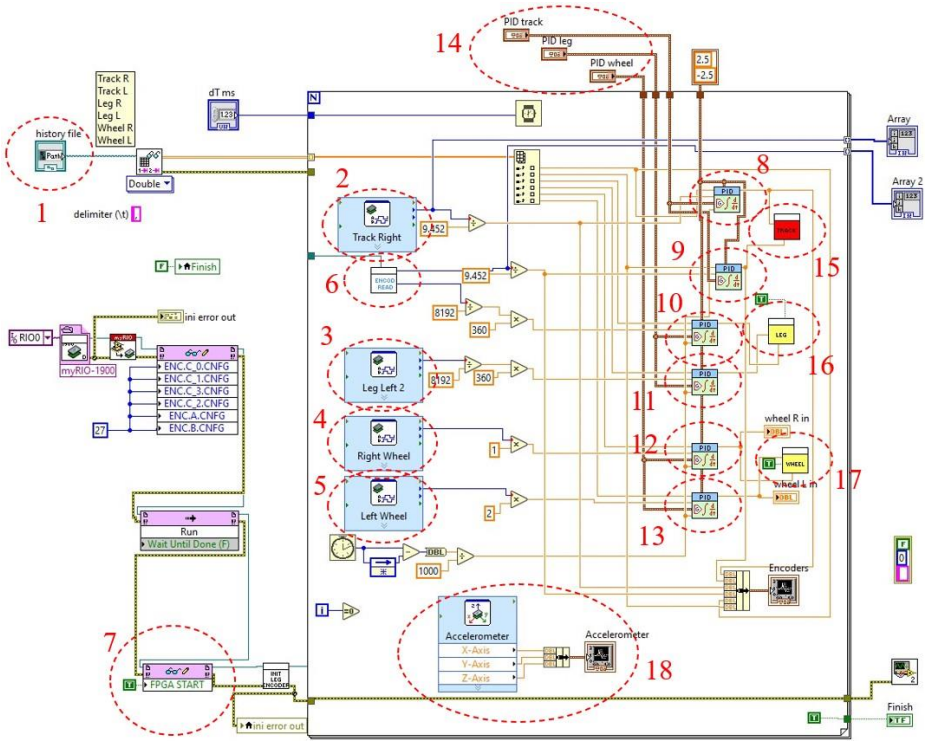

Figure 3-25 LabView main virtual instrument for motion control

The main LabView virtual instrument for motion control is represented in Figure 3-25. The motion profiles of the six motors are provided by an external planning block, which defines them on the basis of the task to be performed, and sent to block 1. The MyRio-1900 is equipped with four native encoder inputs (blocks 2-5); the other two encoders are read by means of other general-purpose digital inputs managed by the FPGA board (blocks 6, 7).

The reference and measured positions of the actuators are sent to six PID controllers (blocks 8-13) for closed-loop control. The PID gains are set independently for wheels legs and tracks by block 14. The PID outputs are sent to the three motor drivers (each driver manages the left and right actuator) through blocks 15-17. Block 18 provides the accelerometer measurement.

3.5 Conclusion

In this chapter, the step climbing capability of the WheTLHLoc hybrid robot has been discussed, defining the phases and the kinematics of the proposed maneuver and analyzing the stability and non-slipping conditions. Then, starting from this analysis, a method to plan the step/stair climbing motion as a function of the step height has been discussed and experimentally validated on the first robot prototype. In general, the experimental campaign has confirmed that the proposed hybrid locomotion architecture can face a wide variety of operative conditions. As a matter of fact, it can alternate wheeled locomotion with higher speed and maneuverability on flat and compact grounds, slower tracked locomotion on irregular, yielding, rocky or grassy terrains, and combined use of legs, wheels, and tracks to climb steps, stairs or other irregular obstacles.

For these reasons, the WheTLHLoc robot can be considered an interesting and flexible platform for indoor and outdoor surveillance and inspection tasks. In the continuation of the work, to increase the technology readiness level and to pursue possible industrialization, two main research directions will be followed. The first is a general refinement of the robot design, to improve its structural resistance and motion performance. The second is the development of a navigation system with a higher level of autonomy. In particular, an interesting research issue is the development of automatic motion planning in presence of obstacles with different shapes, which can be faced by exploiting Reinforcement Learning techniques [173]. Moreover, another possible future investigation direction is the improvement of the step climbing motion planning through optimization methods, also adopting dynamic gait.

4 SnakeTrack

SnakeTrack, a bio-inspired, single-track mobile robot with a compliant vertebral column for surveillance and inspection

In the present technological era, rescue robots are one of the fastest-expanding research areas [33]. In particular, ground mobile robots can substitute human beings in a wide variety of hazardous and unsafe applications, comprising: surveillance, an inspection of sites with chemical or radioactive contamination, intervention in extreme environments, rescue operations, as well as, homeland security.

Independently of the payload, which depends on the specific task, a ground mobile robot is primarily characterized by its locomotion system. Ground mobile robots are often required to move in unstructured environments, and the selection of the locomotion architecture is based on the expected operative conditions.

There are many different kinds of calamities that stem from natural and man-made causes: earthquakes, floods, hurricanes, fires, etc. It is crucial to reach the victims and casualties within the first 48 hours after the disaster. For the purpose of conquering these difficulties, technological studies are concentrated on the development of search and rescue robots. The biggest contribution of these robots will be keeping the search and rescue personnel out of the disaster region and gathering and processing more information from the sites via several sensors and accordingly, preventing further casualties and losses of lives. In such circumstances, rescue robots must act and take decisions quickly for the detection of victims and casualties. All of these duties which used to be performed by humans and/or trained dogs, in unsafe and unpredictable conditions are more and more undertaken by search and rescue robots. Until now, search and rescue robots have been used with various locomotion systems [13].

4.1 Single track robot

In recent years, numerous types of single-tracked robots have been developed to complete search, rescue, pipe inspection, industrial maintenance, defense, and many more [32].

The SnakeTrack mobile robot was not designed to overcome large obstacles, but rather to move in tight spaces. In order to understand what are the advantages of this mobile robot, two other examples of mobile robots characterized by a mechanical structure similar to the SnakeTrack, with different characteristics as regards the locomotion system, are discussed below.

4.1.1 FMT (Flexible Mono-tread mobile Track) robot

The mechanical structure of the SnakeTrack robot is similar to that of the FMT (Flexible Mono-tread mobile Track) robot [101], which is also equipped with a single track that wraps around the entire body of the robot during operation. The difference lies in the locomotion system, in fact, the FMT robot is characterized by active retroflection, that is the ability to actively lift its front part. The SnakeTrack robot, on the other hand, is equipped with passive retroflection, this makes the robot's locomotion system more geared to facing slight irregularities in the ground and small obstacles, and not to the active lifting of the front part.

This choice is motivated by the fact that the SnakeTrack robot was not designed to climb over large obstacles, but rather to move in small spaces. The choice of having passive conformity to retroflection was considered a useful aspect to increase traction instead, respecting the need to have a rigid plane on which to be able to move.

In the FMT robot, the retraction is independent of the movement of the track. As you can see in Figure 4-1, the vertebrae of the FMT robot are connected through intervertebral disks made by means of rubber cylinders that allow rotations around the roll, pitch, and yaw axes. Also for the SnakeTrack the vertebrae are connected via joints, but these have been molded in TPU material and are not compliant with rotation around the roll and pitch axes.

The FTM robot, like the SnakeTrack, has been made completely symmetrical from a functional point of view, for this reason, it can continue to move after reversing the motion by reversing the direction of rotation of the track.

Finally, unlike the FTM robot, a solution was found that allows visibility of the room, greatly improving the possibilities of using the robot.

Figure 4-1 Robot FTM [101].

Figure 4-2 Flexible track of the FTM robot [101].

4.1.2 The RCTR (Reconfigurable Continous Track Robot) robot

The second example of a mobile single-track robot is represented by the RCTR (Reconfigurable Continous Track Robot) robot. Its geometry is such to allows it to adapt the external shape to different terrains or to the presence of obstacles; furthermore, this is facilitated by retroflection which is also active for the RCTR robot. This characteristic of the locomotion system is obtained through a complex active locking system located in the front part of the robot. This system is operated using a servomotor that allows the movement of a button in three different positions, establishing for each of them a particular shape of the geometry. of the robot.

Error! Reference source not found. shows the locking button in the three p ossible positions, center right, and left; it is noted that when the button is positioned to the left the track is locked at 0° and the robot moves linearly. By moving the red button to the right position, the track assumes an inclination of the front of 20°. By moving the button to the left instead, the track is no longer fixed in one position, but the system is unlocked, so the relative angle can change and the robot is free to adapt to the different shapes of the terrain or to the presence of obstacles. different sizes.

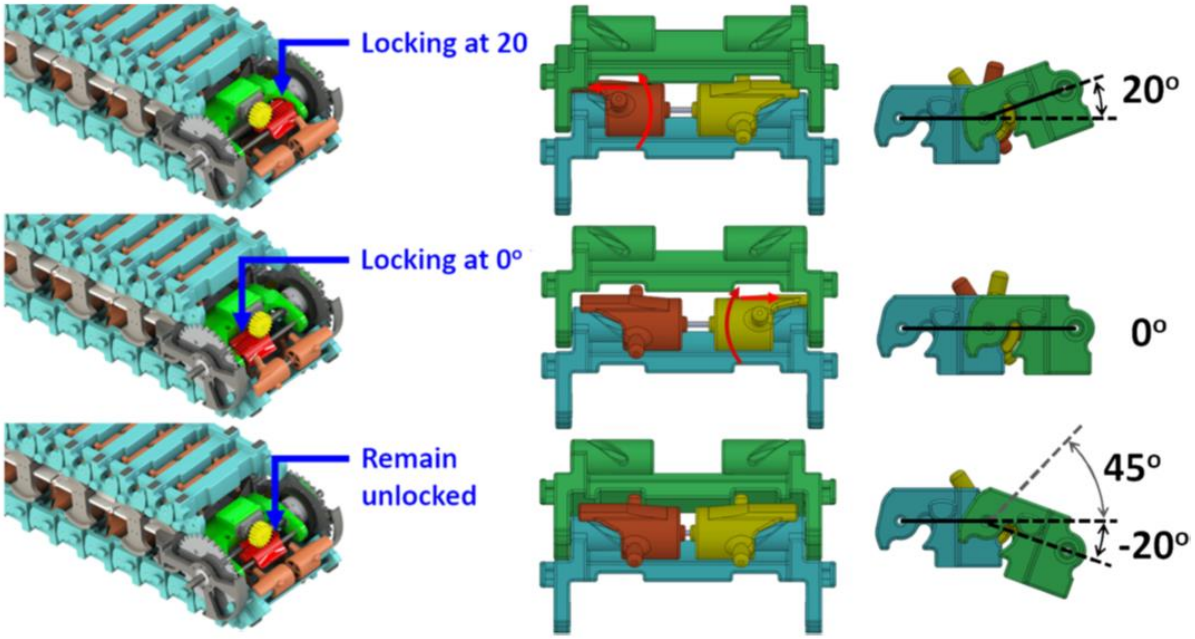

Figure 4-3 RCTR robot track locking system [174]

The unlocking mechanism, on the other hand, is attached to the rear wheel, and passively unlocks the track modules as they rotate on the rear wheel, pushing the locking pins into the central position. Figure 4-4 shows how the pivot passes from the lateral to the central positions.

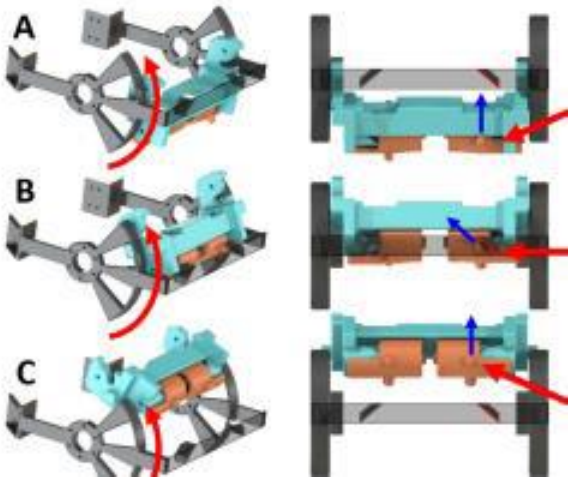

Figure 4-4 RCTR robot track release system [174]

The system has many functional limitations: the direction of the track cannot be reversed, and it is not possible to change the retroflection at zero speed, or to release the joints until it reaches the rear sprocket. For these reasons, the movement of the robot must be planned in advance based on the shape of the obstacle it must overcome.

The intervertebral joints of the RCTR robot are revolute joints, also called hinge joints, which do not allow lateral flexion or steering. Another limitation is the inability to reverse the direction of travel, or advance in the same direction after a 180° rotation; this is due to the non-symmetrical locking / unlocking mechanism that characterizes these joints.

Furthermore, if the RCTR robot were to fall on one side, it would be stuck on the ground without being able to get up again; in contrast, the FTM and SnakeTrack robots would be able to simultaneously use lateral flex to lift up on the track end modules, and the traction motion to drop to the track surface and resume motion.

Table 4-1 Comparison of the main characteristics that have been identified in the three types of robots taken as an example.

Features	FMT	RCTR	Snake Track
Possibility to steer	Yes	No	Yes
Active retroflection (possibility to climb over obstacles)	Yes	Yes	No
Vertebral joints	Cylindrical in shape made of rubber	Revolute joint	TPU, rigid contact profiles
Possibility of reversing the motion	Yes	No	Yes
Possibility of movement in the same direction after reversing the direction of travel	Yes	No	Yes
Rise up from side fall	Yes	No	Yes
video camera	No	No	Yes

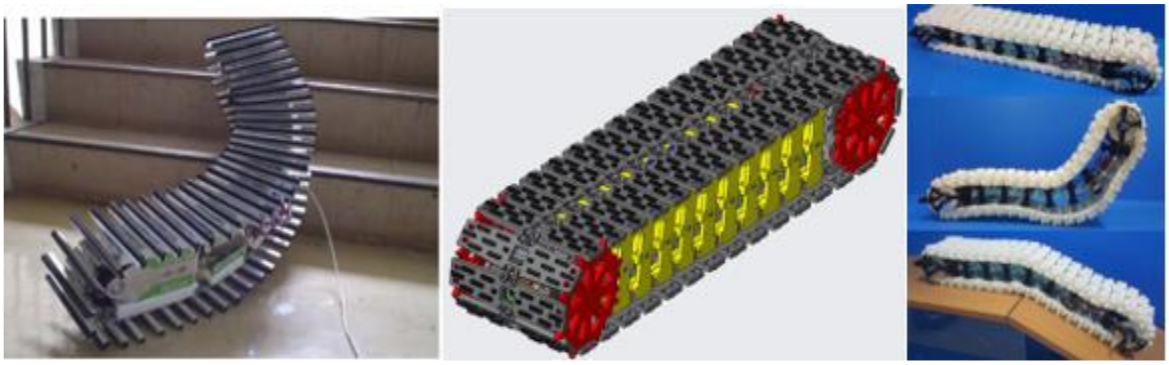

Figure 4-5 The three examples shown of mobile robots compared: from left to right the FTM robot, the Snake Track and the RCTR robot [3,4]

4.2 The SnakeTrack mobile robot

4.2.1 Functional designing of the SnakeTrack robot

SnakeTrack is a bio-inspired single-track ground mobile robot, designed for surveillance and inspection tasks in unstructured and uneven environments with narrow spaces and specially designed for pipelines. [175]

The SnakeTrack mobile robot is equipped with a modular structure, which can be modified by adding or subtracting modules according to the task assigned to the robot. It consists of a single track that surrounds the entire structure, which in turn consists of the central vertebral system and two motorized modules placed at the ends. The individual vertebrae are connected to each other by joints made of TPU material, specially designed to allow lateral flexion of the vertebral system and allow the robot to steer. The intervertebral joints were also used to connect the adjacent vertebrae with the ends of the robot.

Its overall length is 640 mm while the approximate weight is 3.5 kg referring to a configuration with ten vertebrae.

During the design phase of various components, the geometry chosen was designed to be compatible with the molding rules imposed by 3D printing, the material chosen for the construction of the robot is PLA+, with the exception of the intervertebral joints to which the TPU material.

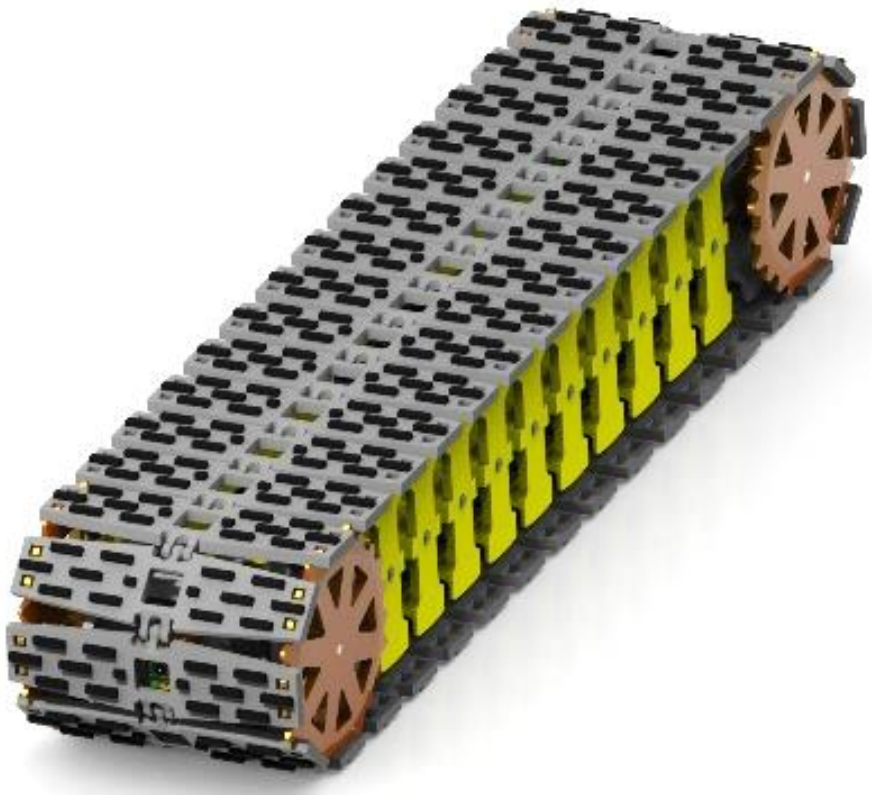

Figure 4-6 3D model of the SnakeTrack robot

The movement of the robot is allowed by four motors placed at both ends, which are electronically controlled by means of a device connected to the power supply battery and to the voltage regulator. The four motors are two-gear motors that allow the traction of the robot, and two-gear motors that allow steering.

As for the electronic part dedicated to robot control, at present, the robot is radio-controlled by means of a radio control that communicates with a signal receiver placed on the robot. This device in turn sends the signal to the Motor Driver, whose outputs are connected to the four-gear motors. By means of a voltage regulator, the output signal is established at a fixed 12V as the power supply voltage value for the motors. These components are powered with a 4s LiPo battery.

After performing the various tests on the motor and having ascertained the perfect functioning of the mechanical components, the robot will host a Raspberry controller on board which will be programmed from a PC using the LabVIEW programming environment.

Table 4-2 summarizes the main features of the SnakeTrack robot and the details regarding the pieces ready for use. Remember that these dimensional characteristics refer to the configuration of the robot by adopting a number of vertebrae equal to ten.

Table 4-2 Main characteristics of SnakeTrack

Dimensions (l × l × s)	640 × 150 × 120 mm
Weight	3,5 kg
Approximate track radius (for a 90 ° bend)	255 mm
Maximum achievable speed	0,14 m/s
Battery	LiPo 12v-43-12-2S
Video camera	Raspberry Pi camera module V2
Controller	Raspberry Pi 4B 8Gb
Micro SD Card	32 GB
Traction Gearmotor	RH 158 2S 12V 200
Gearmotor for steering	L149 2S 12V 90

The 3D model of the robot sees the assembly of different components, defined in turn in two main sub-assemblies:

- the vertebral column, composed of an internal vertebral structure and two motorized modules placed at the ends
- the external track, consisting of 34 modules in succession

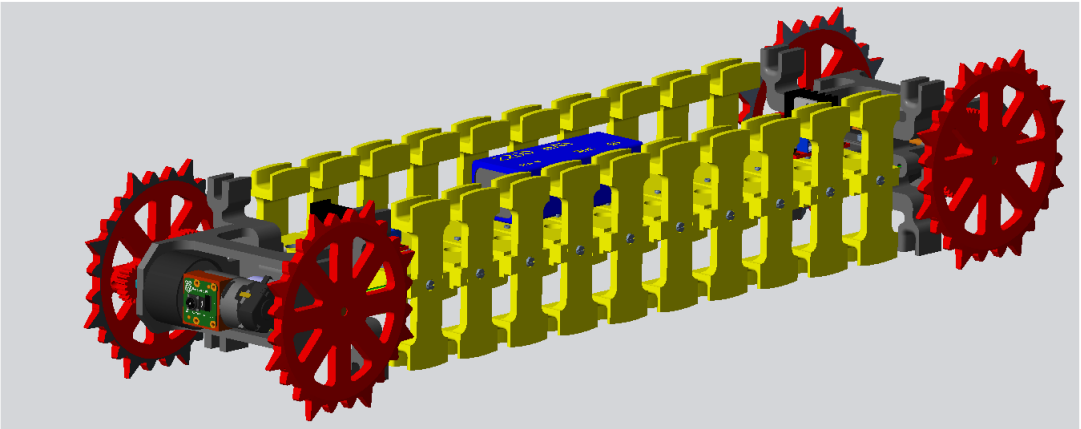

Figure 4-7 3D view of the vertebral column

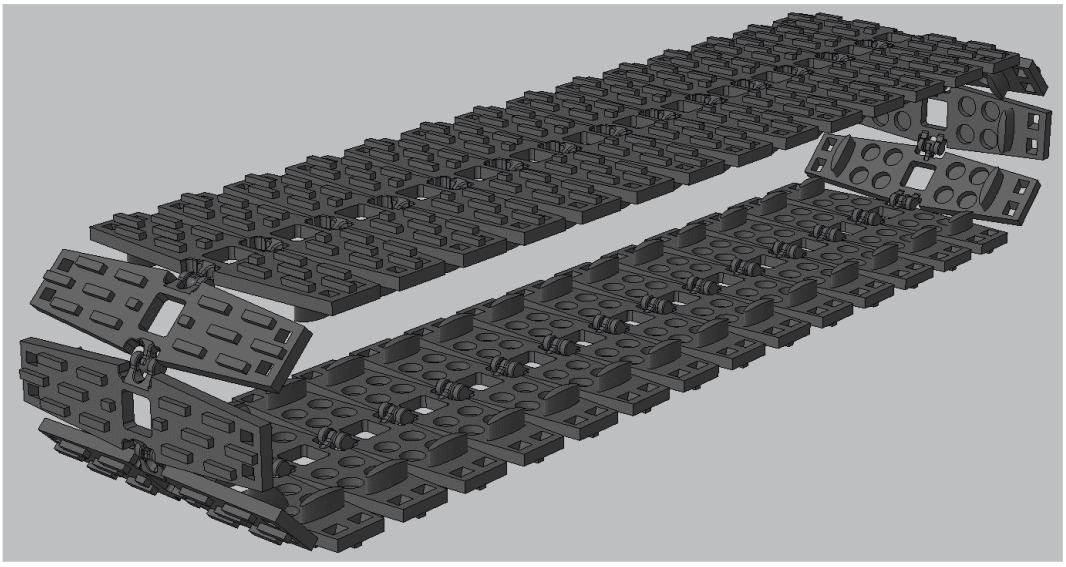

Figure 4-8 3D view of the external track

4.2.2 3D printing process and materials

The term 3D printing refers to the creation of three-dimensional objects by additive manufacturing, starting from a digital 3D model. The digital model is produced with dedicated software and subsequently processed to be then created with different technologies, including the one that builds prototypes layer by layer, through a 3D printer.

Rapid prototyping, which was created in the 1980s for making models and prototype components, was the first method of building a three-dimensional object layer by layer using computer-aided design (CAD). Engineers developed this technology to aid in the execution of their ideas. One of the first additive manufacturing (AM) techniques is rapid prototyping. Not just models but also printed items may be made with it. Time and cost savings, more human connection, and a shorter product development cycle are some of the significant advancements this approach brought to product development [176]. Furthermore the ability to make essentially any form, including those that can be incredibly challenging to manufacture is another improvement of this method. Scientists, medical professionals, students and lecturers, market researchers, and artists utilize it, but the industrial sector has not yet completely accepted it. Scientists and students may quickly construct and evaluate models for theoretical understanding and research thanks to rapid prototyping.

Market researchers can find out what consumers think of a certain new product, doctors can create a model of a wounded body to examine it and better plan the surgery, and artists can more easily express their creativity thanks to fast prototyping.

A particular and very important feature of 3D printing is the infill, that is the filling, a reticulate that is printed inside the object layer by layer. The 3D printed objects are much lighter than what they appear to the eye, this effect is due to the slicer, the program that realizes the printing commands. In fact, to save material,

which in any case would not be visible, it builds a structure internally which, even if it is not full, gives the creation exceptional resistance [177]. The most important feature of the infill is its percentage. A high percentage of infill is associated with a greater strength of the piece, but also with a longer printing time; a low percentage saves a considerable amount of material and printing time. Figure 2.4 shows how the appearance of the material varies as the filling percentage varies.

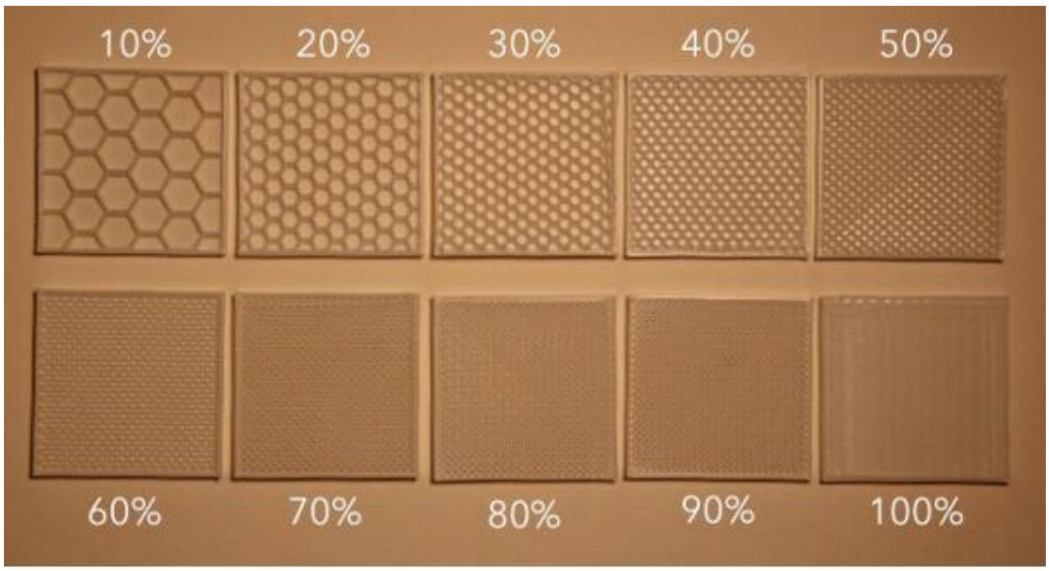

Figure 4-9 How the appearance of the material varies with the percentage of infill [177]

After having designed, by the Creo Parametric 3D modeling program, the components necessary for the realization of the Snake Track robot, we moved on to the molding phase.

The material used for their realization was PLA + with the exception of the intervertebral joints, which were molded in TPU. This choice was dictated by the fact that the joints must allow lateral flexion but at the same time ensure a good seal with the profiles of the vertebrae that contain them, this effect was not found with the PLA material. In general, when printing with a high percentage of infill, as in the case of the SnakeTrack which has been assigned a percentage of 70%, printing in TPU makes the pieces more easily flexible. This first version of the robot was made in PLA + as the TPU filaments currently present in the university were not sufficient to print all the components; for the realization of the final product of SnakeTrack, the material will be replaced with TPU.

4.2.2.1 The PLA plus material

The PLA + material is a variant of PLA (polylactic acid). PLA is a thermoplastic polymer obtained from renewable resources, this makes it a more ecological material than other filaments. In production, there are no substantial differences between the two materials, even the print settings, such as speed, temperature, and shrinkage are very similar, with the difference that PLA + tends to have slightly better surface qualities, color, or mechanical properties. The main

difference is in the mixture of plastics, additives, and pigments that help improve the weaknesses recognized in the standard PLA; in fact, PLA plus, unlike the latter, has added more material to make the filament less brittle, have a smoother surface finish and less likely to absorb moisture. It resists higher temperatures and more applied forces, reducing the risk of breakage and thus causing the material to flex rather. It gives the piece a high aesthetic quality, extreme ease of printing, and negligible deformation values. [178], [179] In Table 4-3 some mechanical properties of PLA are reported.

Table 4-3 mechanical properties of PLA

Density	1,24 $g/cm3$
Tensile modulus	2346,5 MPa
Flexural strength	103,0 MPa
Stress to break	45,6 MPa
Stress at yield	49,5 MPa
Flexion modulus	3150,0 MPa
Poisson's ratio	0,33

4.2.2.2 The TPU material

Due to its superior physical properties (such as high tensile strength, abrasion and tear resistance, oil and solvent resistance, low-temperature flexibility, paintability, etc.) and high versatility in chemical structures, thermoplastic polyurethane (TPU), which has properties ranging from a high-performance elastomer to tough thermoplastic, has been widely used. TPU is a linear segmented block copolymer made up of alternating hard and soft segments made of polyester, polyether, hydrocarbon, silicone, and other soft materials like polyester. Physical crosslinks made of interchain hydrogen bonds bind the hard segments together. Hydrogen bonds are broken and linear main chains are liberated at melt temperatures. Meanwhile, the hard segments' urethane connections (carbamate, -NHCOO-) become unstable and irreversibly break down into free isocyanate and alcohol [180].

TPU is composed of a part of polyurethane, one of the most resistant plastic materials, and rubber, which gives it elasticity. It is not made of toxic materials, so it is not toxic once printed. It has a shrinkage rate of between 0.8 and 1.6%, which is perfectly manageable through a slight increase in flow. It does not absorb water, so it does not deteriorate. It is ideal to be used for objects subjected to mechanical stress, it is a soft, extremely resistant, and flexible material. It has an excellent coefficient of adhesion with road surfaces, and its high elasticity is the most interesting feature, which allows the creation of rubbery objects. It is extremely resistant to the actions of chemicals, acids, fats, and oils. Like most elastomers, it is commonly used to make seals, gaskets, and hoses. It can also be

present in over-molded plastic pieces due to its ability to provide superior grip or dampen vibrations. In Table 4-4 some mechanical properties of the TPU are reported.

Table 4-4 TPU Features [180]

Relative density	1,22 MPa
Tensile modulus	26,0 MPa
Stress to break	39,0 MPa
Stress at yield	8,6 MPa
Poisson's ratio	0,4
Flexion modulus	78,7 MPa
Flexural strength	4,3 MPa

4.2.3 The spinal column of the robot

The first sub-assembly (Figure 4-10) is represented by the spine of the SnakeTrack. Since the robot is completely modular, the number of vertebrae can be varied according to the required task, resulting in a further variation of the space available for the payload.

The vertebral system constitutes the internal structure of the robot; the adjacent vertebrae are suitably connected by intervertebral joints which are characterized by low resistance to rotation, which allows minimizing the energy consumption necessary to allow the lateral flexion of the robot.

The structure of the individual vertebrae was designed so that it could house electronic components in the appropriate spaces between the side supports, such as the motor, the control unit, the battery, and sensors. The sensors have not been inserted at the moment; if necessary the robot can be equipped with two additional environmental sensors and carry out various tasks.

Table 4-5 shows, in the form of a list, the components indicated in the figure below.

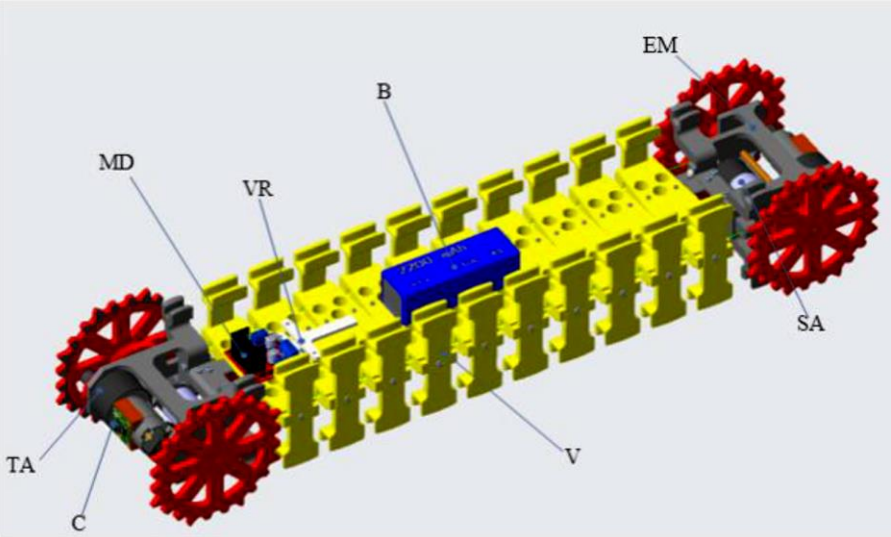

Figure 4-10 3D view of the vertebral column.

Table 4-5 components indicated in Figure 4-10

Components	Symbol shown
End modules	EM
Vertebrae (vertebras)	V
Track actuator	TA
Steering actuator	SA
Battery	B
Voltage regulator	VR
camera	CA

Figure 4-11 shows the 3D model of the configuration assumed by the robot while turning 90 °. The angle taken is the maximum allowed by the intervertebral joints, i.e. +/- 9 °; with this curvature, the track reaches the minimum allowed radius equal to about 255 mm, calculated from the center of rotation with respect to which the robot is turning. The lateral flexion of each joint equal to +/- 9 ° causes flexion of the entire robot by 90 ° being, in this case, ten vertebrae.

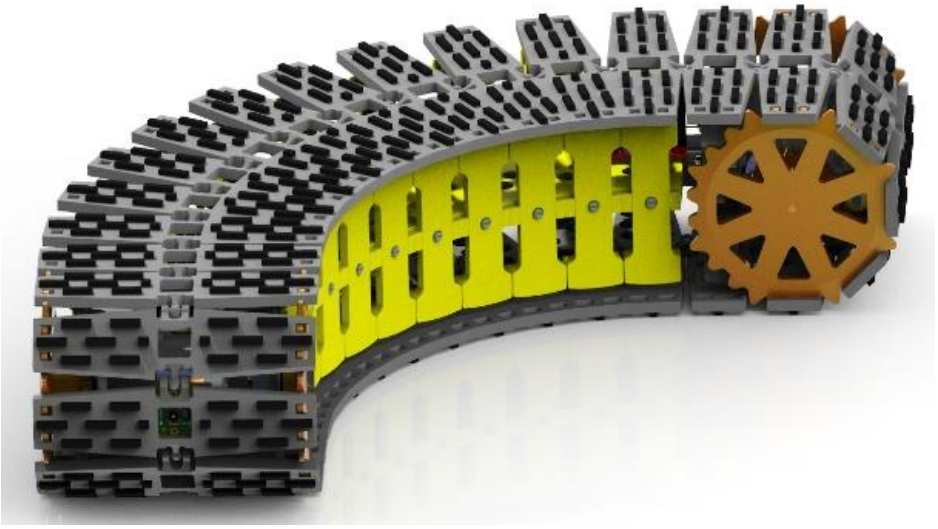

Figure 4-11 3D models when turning to the right with a minimum radius

The figure below (Figure 4-12) shows the 2D CAD of the track in the maximum steering condition, in this case for a left bend of the robot. The angle that is formed between the adjacent modules is 18°, unlike the 9° assumed during linear movement; in addition, the value of the turning radius is reported for a 90 ° bend of the track.

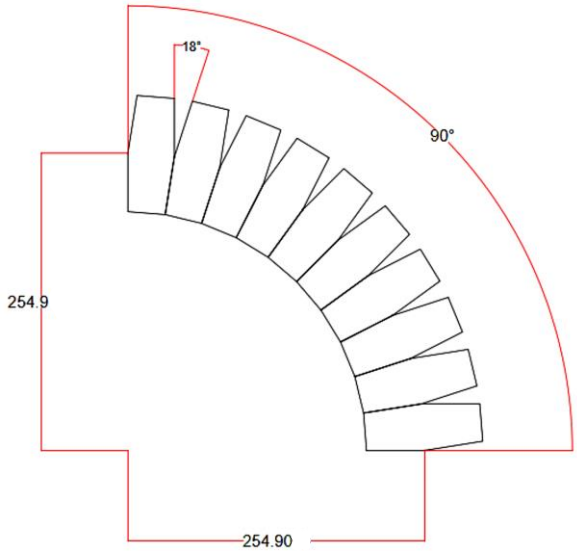

Figure 4-12 Geometric diagram with the minimum turning radius

4.2.4 The motorized end modules

As previously stated, the vertebral column is made up of ten central vertebrae and two motorized modules placed at the ends. Figure 4-13 shows the top view of the final modules of the SnakeTrack robot and the side ropes that cross the entire vertebral system. As can be seen from the figure, the ropes end at one end wound on the pulleys, which are connected to the motors that allow the robot to steer. Driven by the motors, the pulleys, rotating in the opposite direction, pull and

loosen the ropes in order to allow the curvature of the vertebral system according to the needs of the robot.

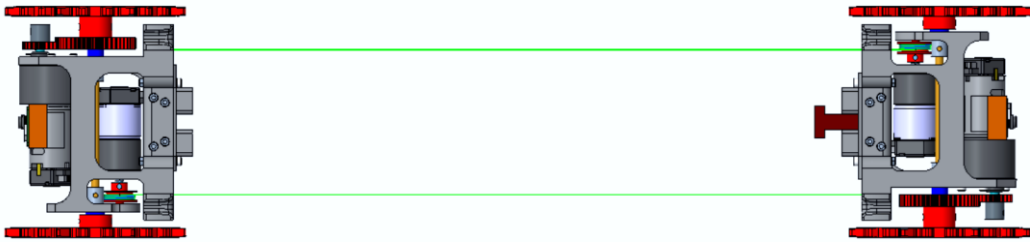

Figure 4-13 Top views of the end modules

In order to maintain the symmetry of the robot, the modules placed at the ends have been made identical to each other; they house several important elements for functioning. Among these, we have two actuators, two toothed wheels, two pinions, and a pulley. The two actuators have different functions, the traction actuator (Figure 4-14, TA) allows the linear movement of the robot and is connected to a toothed wheel, which by transmitting the motion to a second wheel allows the further reduction of speed, at the expense of an increase in the torque delivered. In this way, the motion is transmitted from the traction gearmotor to the output shaft on which the pinions are mounted, according to the transmission ratio imposed by the two toothed wheels.

The second actuator allows the steering of the robot (Figure 4-14, SA); it is directly connected to the pulley on which the rope is wound which allows the entire vertebral system to follow the imposed trend. The torque delivered by the gearmotor is transmitted directly to the pulley without the presence of interposed external gears.

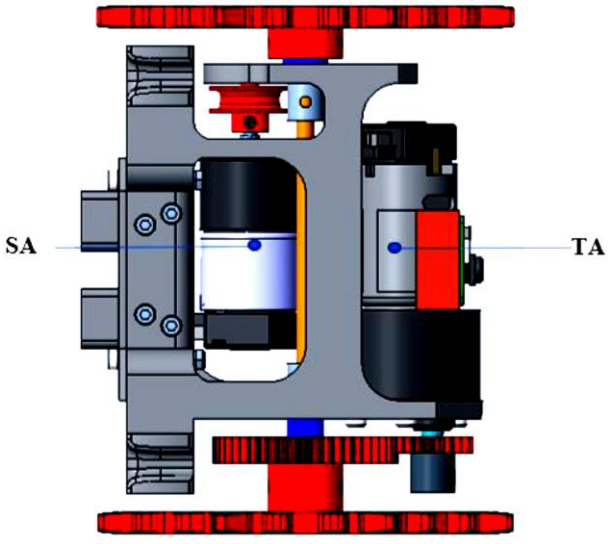

Figure 4-14 End modules of SnakeTrack

The side ropes cross the side holes present in each vertebra and have the purpose of making the robot bend in one or in the other direction; therefore, the robot can steer only by pulling the rope which is on the side of the center of rotation with respect to which you want to bend. The gearmotors are mounted to rotate in the opposite direction; their movement causes the consequent rotation of the pulley and therefore also of the rope that is wound on it; one rope will be stretched more while the other is loosened.

For this reason, the movements of the pairs of actuators are not independent. The two traction actuators, connected to the toothed wheels, must necessarily rotate at the same speed to allow linear movement of the robot; likewise, to carry out the bending of the robot, the gearmotors present at the two ends rotate in the opposite direction to allow the lateral ropes to follow the direction of bending imposed.

As can be seen from Figure 4-15, bending to the right, the gear motor at the head of the robot loosens the rope wound on the pulley to which it is connected, at the opposite end the other gearmotor operates producing the opposite effect on the rope on the right.

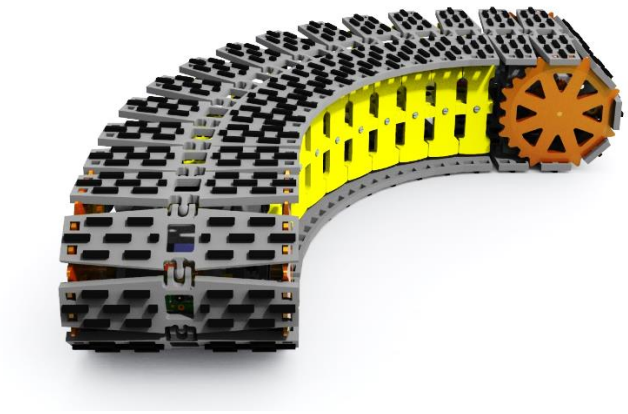

Figure 4-15 Front view of the SnakeTrack in full steering configuration

4.2.5 The geometry of the track

4.2.5.1 Summary of track geometry

The robot track is made up of a succession of modules, specially made to be able to connect to each other. The connection of the lateral ends takes place by means of joints whose geometry has been designed to allow the variation of the relative angle between the connected ends and allow the robot to turn.

Figure 4-16 shows the 3D model of the external track of the SnakeTrack, hiding the vertebral structure and the motorized parts. It is noted how the creation of the single track that wraps the entire body of the robot was allowed by the connection between the ends of each module.

Referring to a vertebral system consisting of ten vertebrae, 34 modules were needed to build the entire track; remember that since the track is completely modular, the number of modules can be varied to respond to the different tasks required for the robot.

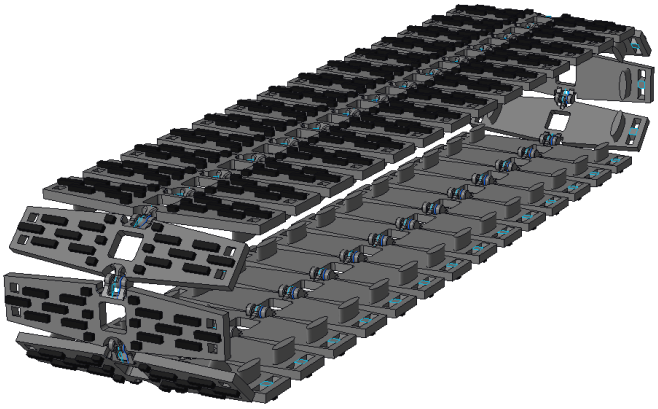

Figure 4-16 3D model of the track

The initial geometry of the modules was different from how it was finally made; Figure 4-17 shows the 2D CAD from which we started to design the module design. The quotas indicated were pre-established, and our design was based on modifying the design while maintaining the initial sizes. The modules were made entirely with the PTC Creo 3D drawing software, while the CAD shown in the figure was created with the Solid Edge drawing software.

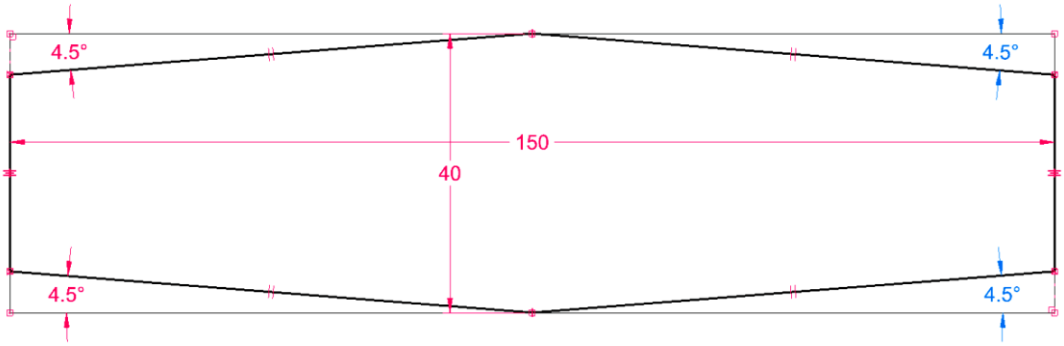

Figure 4-17 Initial geometry of the module

Particular attention was paid to the creation of the connecting joints between the track modules; these joints have been designed so that they can allow the modules to follow the motion of the robot even when it is bending.

In this regard, it was decided to make the joints as shown in Figure 4-18. The female end is represented by an 8 mm diameter sphere coupled with the male end

of the joint represented by a fork, specially made to accommodate the sphere. The connection between the two ends was obtained by making the centers of the joints coincide. In order to maintain the preset values for the geometry of the module, the joints were made so that the intersection points of the respective central axes were 40 mm from each other.

The details regarding sizing and construction of the joints will be discussed in chapter 4.3.

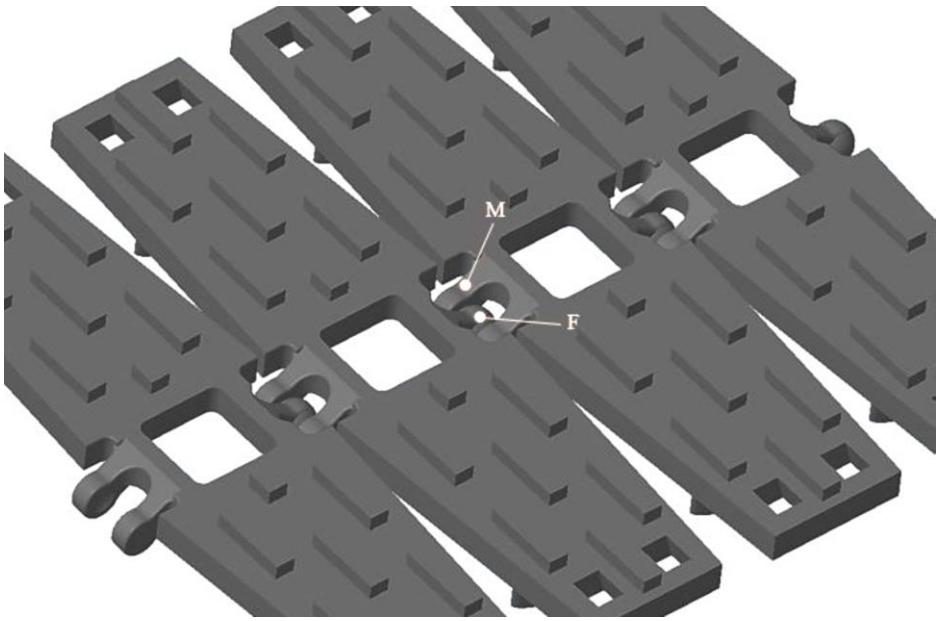

Figure 4-18 Top views of track-connected modules

Each module has a central opening that allows the cameras mounted on the final modules to monitor the progress of the robot. Visibility is intermittent, as it is achieved when the module window is aligned with the camera.

The vision of the video camera is active during the movement of the robot only when the camera is in front of the central opening. Considering a speed of 0.1 m/s, with a field equal to 40 mm, the view of the camera can be updated 2.5 times per second; this frequency is sufficient to drive the robot at this speed even if there is no continuous view.

If continuous monitoring is required, the robot can stop with the central opening of the track module aligned with the chamber and ensure the view.

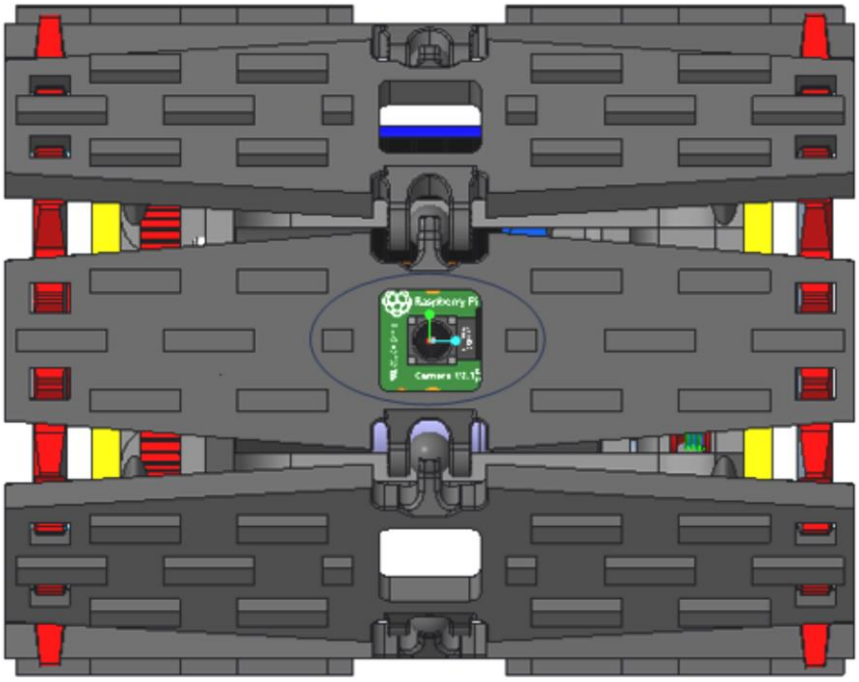

Figure 4-19 Rear views of SnakeTrack

Figure 4-20 shows a section of the robot in order to better understand how its internal structure was made. At the base of each module of the track, two elliptical pegs have been made that slide through the lateral profiles of the vertebrae. The side profiles have been designed with the aim of providing support and creating a sliding guide for the track pegs when the robot is in motion. In this way the track follows the course of the vertebral system even when it is bended.

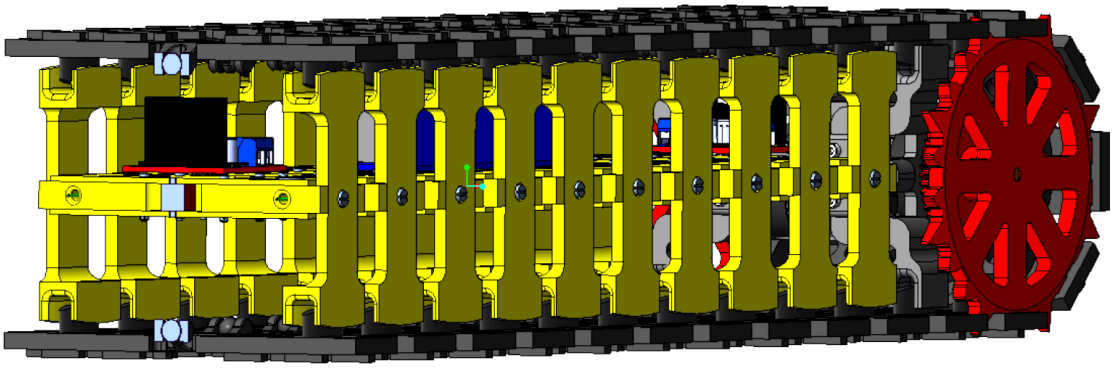

Figure 4-20 Sectioned view of SnakeTrack

At the base of each module, 8 non-through holes have been made (Figure 4-21), with a diameter of 12 mm and a height of 4 mm, in order to lighten the piece and save material used in the printing phase. The module is perfectly symmetrical with respect to the central vertical plane.

Figure 4-22 shows the 3D model of a single module, as you can see, parallelepiped-shaped elements with a height of 4 mm have been created, to avoid

direct contact of the track with the ground and therefore wear. These are all equally spaced and symmetrical with respect to the central plane.

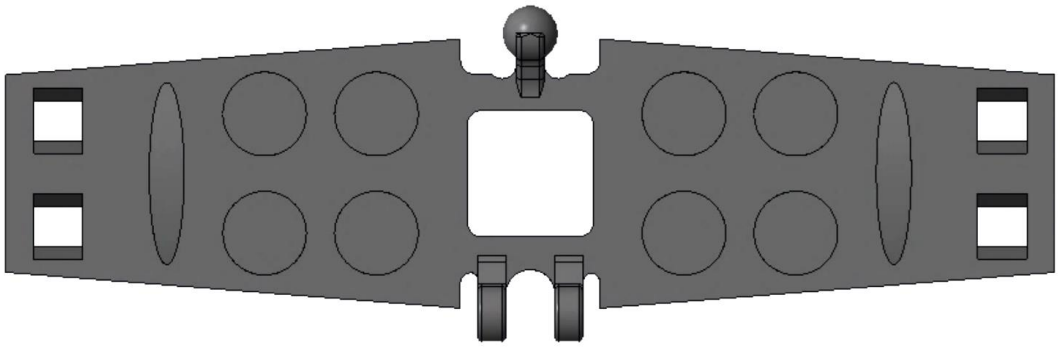

Figure 4-21 Bottom views of a single module of track

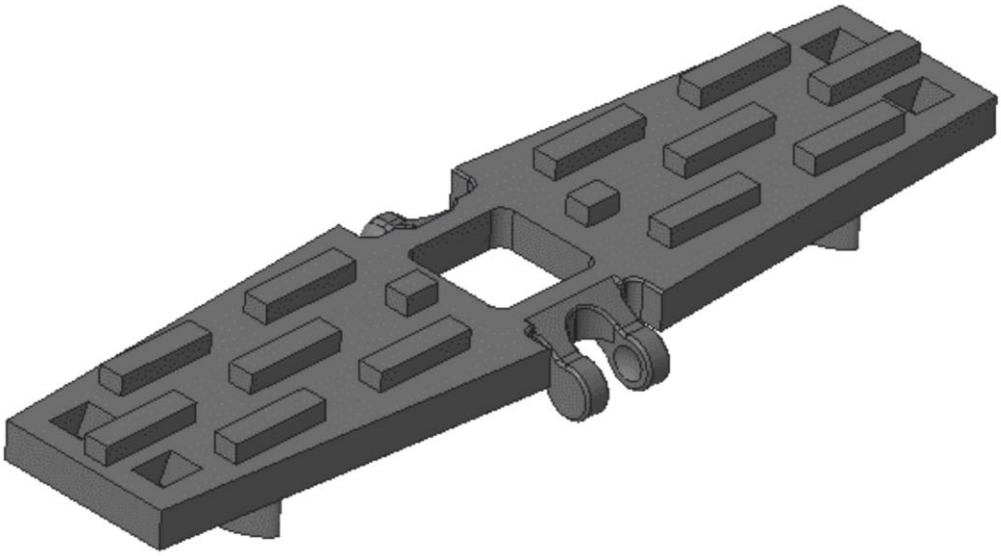

Figure 4-22 3D model of a single track module

4.2.5.2 The positioning of the centers of the joints

Figure 4-23 shows the front view of three track modules connected to each other. The coupling between the two male and female ends of the joint is achieved by making their central axes coincide. A focal point in the construction of the track was the centering of the joints, as previously mentioned the centers of the two ends are 40 mm apart, and are lowered with respect to the base of the module of 1.72 mm.

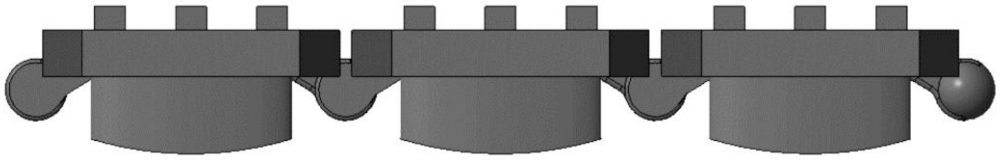

Figure 4-23 Side view of three connected modules

4.2.6 Static analysis of the thrust exerted by the actuators when it moves on a 60 ° inclined plane

The SnakeTrack robot has been designed to move on preferably rigid terrains, this does not exclude the possibility of advancing on terrains with different inclinations. In order to study the thrust exerted by the robot when it is moving on land with different slopes, the example studied in the case where the ground has an inclination of 60 ° is shown below. As explained in the previous pages, the material with which the robot was printed is PLA+, this material does not guarantee a sufficient coefficient of friction between the track and the ground to allow the advancement with such a slope. For this reason, the study reported refers to a Snake Track prototype, the values of the quantities used are typical of the real model. In this first phase of design, the fundamental aspect on which we based was to guarantee the movement of the robot and the possibility of steering, while more sophisticated aspects, such as guaranteeing the holding of the robot on the inclined ground, have been neglected for the moment.

Once these aspects of primary importance have been perfected, further improvements will be made, including choosing a material that can allow the robot to advance on land with greater slopes.

Figure 4-24 shows the robot advancing on the inclined ground. The external force components have been applied, these are basically the weight force, broken down into the two components x and y, respectively parallel and normal to the surface of the track, and the component of friction that is established between the robot track and the ground.

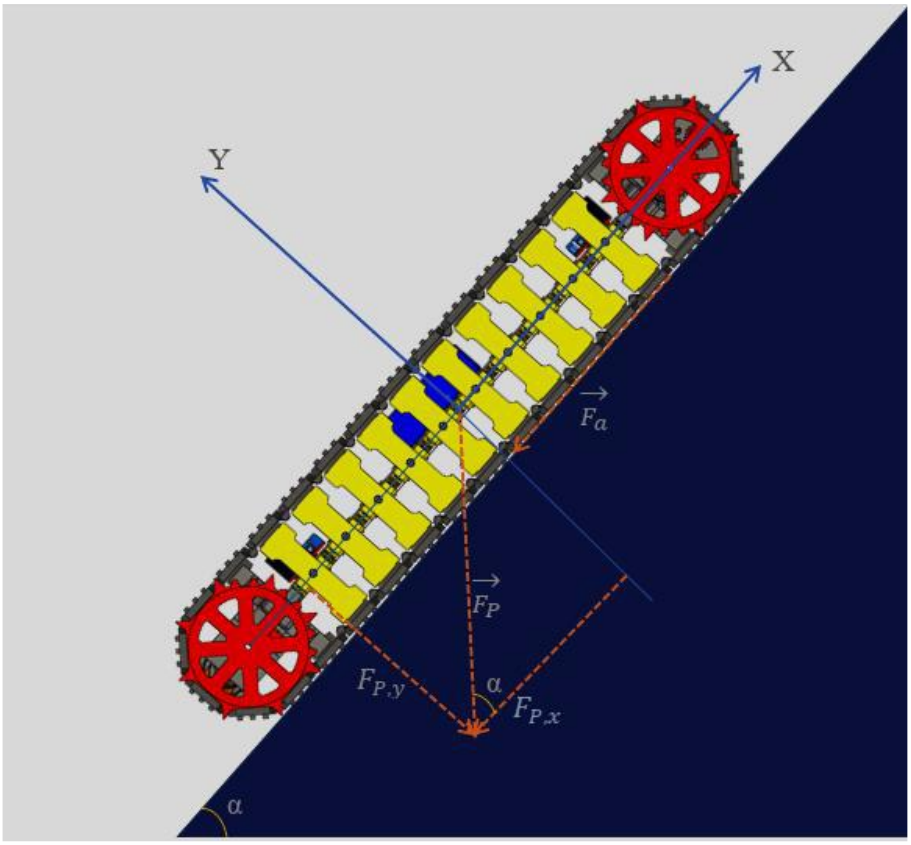

Figure 4-24 SnakeTrack prototype reaching a ramp

Recalling that the robot has a total mass of 3.5 kg, the components of the weight force have been calculated according to the x and y axes:

$$F_{P.y} = m \cdot g \cdot \sin(\alpha) \quad 52$$

$$F_{P.x} = m \cdot g \cdot \cos(\alpha) \quad 53$$

where is it,

m = mass of the robot,

g = gravitational acceleration,

α = inclination of the plane.

Furthermore, the friction component, which is established between the ground and the track, is calculated:

$$F_a = f_v \cdot F_{py} \quad 54$$

where,

f_v = coefficient of viscous friction

By substituting the value of the force components obtained, the resisting force that would oppose the advancement of the robot on the plane is obtained:

$$F_r = F_{Px} + F_a \quad (55)$$

By substituting the value obtained from (55) it is possible to obtain the moment that each of the two pairs of pinions exerts, which is why there is a factor of 2 in the denominator:

$$C_p = (F_r \cdot r_c)\ /2 \quad (56)$$

where is it,

C_p = moment generated by the pair of pinions,

r_c = track radius.

To evaluate the torque that is delivered by the traction gearmotor during the advancement on the inclined plane, the value obtained from (56) has been reported to the gearmotor according to the following transmission ratio:

$$\tau_t = \frac{\omega_p}{\omega_{mr}} = \frac{C_{mr}}{C_p} = \frac{z_1}{z_2} \quad (57)$$

where is it,

z_1 = number of teeth of the drive wheel,

z_2 = number of teeth of the driven wheel,

ω_{mr} = rotation speed of the traction gearmotor,

ω_p = speed of rotation of the pinions,

C_{mr} = torque delivered by the traction gearmotor,

C_p = torque generated by the pinions.

Using equations (56) and (57), it is possible to calculate the torque delivered by the traction gearmotor:

$$C_{mt} = C_p \cdot \tau_t \quad (58)$$

From equation (57) it is also possible to obtain the value of the rotation speed of the pinions, known from the catalog the value of the rotation speed of the gearmotor. The traction speed of the robot is thus calculated:

$$v = \omega_p \cdot r_c \quad (59)$$

Table 4-6 shows the values obtained from the quantities examined.

Table 4-6 Values obtained, and quantities used to carry out the calculations

F_{px}	Component of the weight force according to the x-axis	29,735	N
F_{py}	Component of the weight force according to the y-axis	17,168	N
F_r	Resistant force	31,451	N
f_v	Viscous coefficient of friction	0,1	-
F_a	Frictional force	1,717	N
r_c	Track radius	0,055	m
z_1	Number of driven wheel teeth	48	-
z_2	Drive wheel teeth number	20	-
d_1	The pitch diameter of the driven wheel	48	mm
d_2	Drive wheel pitch diameter	20	mm
τ_t	Transmission report	0,417	-
C_p	The torque generated by the pinions	0,865	Nm
C_{mt}	The torque generated by the traction gearmotor	0,360	Nm
ω_p	Rotation speed of each pinion	1	rad/s
ω_{mr}	Rotation speed of the traction gearmotor	2,41	rad/s
v	Traction speed of the robot	0,055	m/s

4.3 Detailed design

4.3.1 Design of the joints

4.3.1.1 The connection joints for the vertebral elements

The intervertebral joints have been made of TPU material to allow greater lateral flexion. They are used to connect the adjacent vertebrae together and to create a connection between the end modules and the vertebrae placed at the ends. The choice of TPU material was made to give the piece lateral flexion but also sufficient stiffness.

When the robot advances linearly, the intervertebral joints assume the configuration shown in Figure 4-25. This figure shows the upper view of the vertebral column hiding the upper profiles of the vertebrae that normally isolate the joints from the external environment.

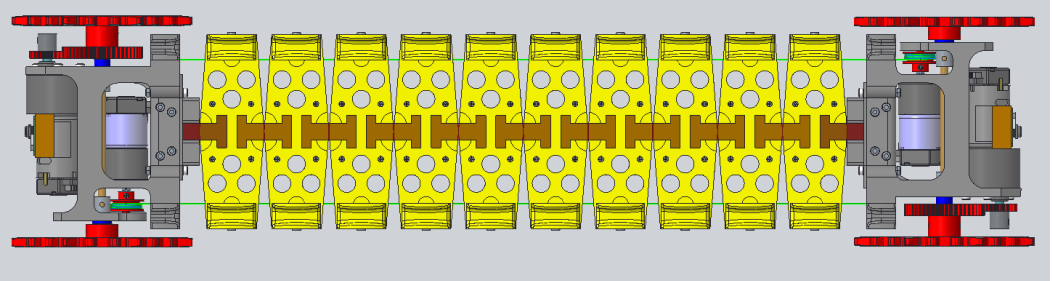

Figure 4-25 Top views of the robot spine, showing the internal structure of the vertebral elements

Figure 4-26 instead shows the same representation of the robot hiding the profiles that cover the central elements. The configuration shown is assumed by the robot when it performs the maximum lateral flexion of curvature of the robot is +/- 90°.

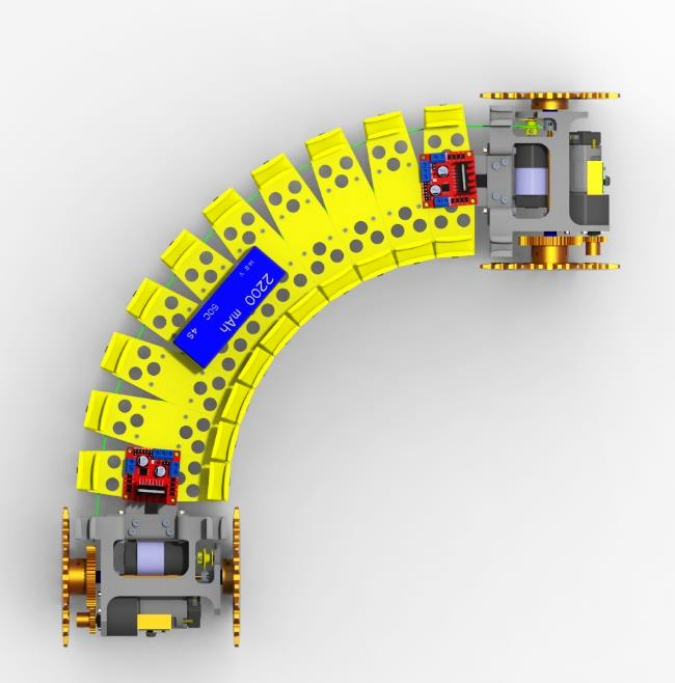

Figure 4-26 Top view of the spinal column when the robot turns 90°

4.1.2 The connection joints for the track modules

The robot track is made up of a succession of modules, connected to each other by joints. As announced, the connection joints were made at the lateral ends of each module. The connection between the two ends, male and female, of the joint, is made as discussed in the following.

The female end consists of a sphere with a diameter of 8 mm (Figure 4-27); the axes of the sphere intersect at a distance of 20 mm with respect to the central plane of the module; this, to maintain the 40mm dimension as the distance between the center of the two lateral ends.

This sphere was not made aligned with the rest of the module, but its center was lowered by 1.72 mm with respect to the base of the module; as we will see, these values have been respected to allow the coupling between the track and the sprockets. To make the connection between the sphere and the module, a connection element was therefore made; this is 6 mm high, equal to the height of the module, and is inclined so that its central axis intersects the center of the sphere. This element also has the function of incorporating the sphere and making the connection more stable. The figure shows the 3D model of the module, the elements just described are indicated.

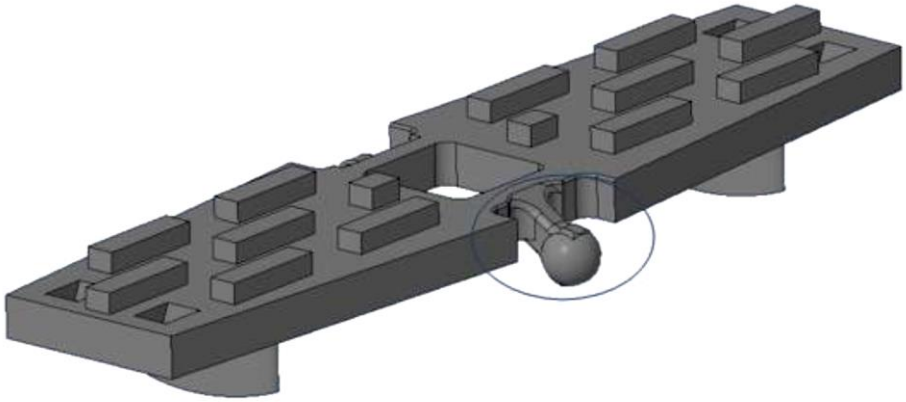

Figure 4-27 Male ends of the connection joints between the track modules

The female end of the joint consists of two identical elements. Figure 4-28 shows the 3D model of the module again, referring to the opposite end of the joint. As can be seen, this element is represented by a single piece, made with a compatible geometry to make the connection with the sphere. To make this possible, a sphere of 8.6 mm diameter was created by material removal, with the center aligned with the opposite end; in this way, the two elements have been suitably shaped to allow the connection with the sphere, with a tolerance of 0.6 mm.

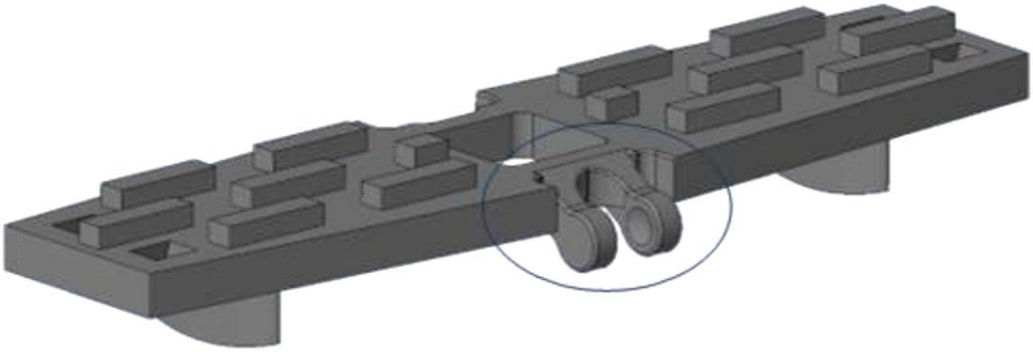

Figure 4-28 Female ends of the connection joints between the track modules

4.3.2 The modules of the tracks

The track is made up of 34 modules, designed to be connected to each other through the joints. Being the robot is completely modular, even the number of modules, as for the vertebrae, can be varied according to the required tasks. By adopting a number of vertebrae equal to ten, the track is made up as follows:

- ten modules in correspondence with the vertebrae
- seven modules covering the final elements

The particular geometry of the modules was thus designed to allow the robot to steer without the adjacent modules being worn during contact. This contact is obtained only when the condition of maximum lateral flexion occurs, for a 90° curvature of the robot.

For the initial design of the modules, the values of the quantities assumed in the first design phase of the track geometry and were maintained. The respective length is 150 mm, while the width is 40 mm, calculated with respect to the points placed at a maximum distance, while the four sides of the module are inclined by 4.5° with respect to the horizontal. The length of the vertical sides was calculated by difference.

Figure 4-29 shows a 1:1 scale reproduction of the top view of two track modules connected to each other, omitting the true geometry of the joints for simplicity. Furthermore, it can be noted that the angle created between the sides of the module when the robot advances linearly are equal to 9°.

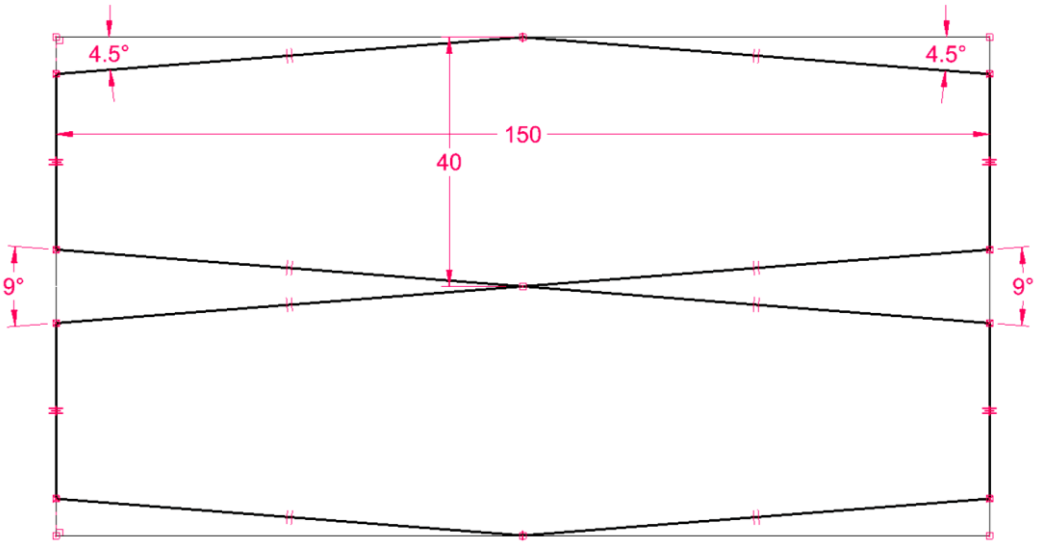

Figure 4-29 Scale drawing of the top view of two connected modules

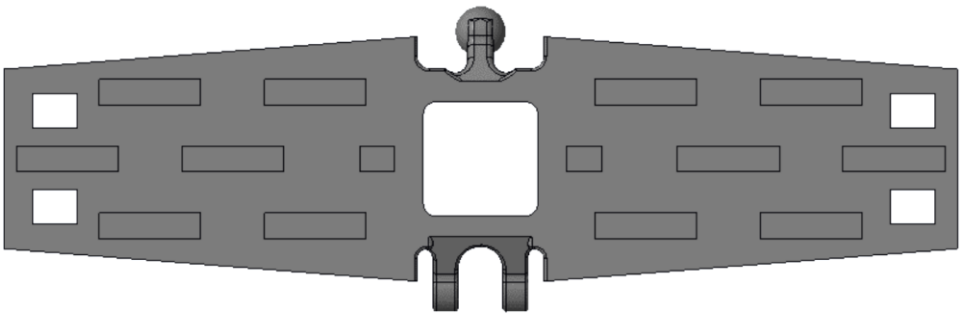

Figure 4-30 top views of the module; the four holes at the lateral ends allow the coupling of the track with the sprocket teeth

As can be seen from Figure 4-31 the four side holes have a trapezoidal shape, this choice was made to allow coupling with the teeth of the four sprockets made with the same geometry. The major base of the hole measures 9.10 mm, while the

height is 6 mm, the value of the minor base was calculated by difference since the oblique sides are inclined by 107 °.

Each hole has a tolerance of 0.5 mm with respect to the greater base of the pinion teeth; moreover, the holes are 7mm wide, while the sprockets are 6mm. The trapezoidal shape was chosen to facilitate insertion between the track and pinion when the robot is in motion.

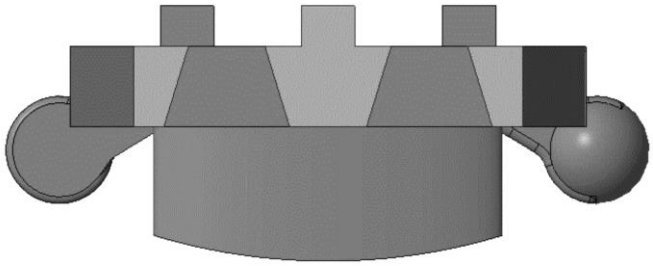

Figure 4-31 Side section view of the track module

4.3.3 FEM analysis of stresses and displacements that occur at the connection end of the module

The track of the SnakeTrack robot, as has already been explained in the previous chapter, is made from a succession of modules connected to each other through joints specially designed to allow them to be connected. The ends of the module have been made to make this connection possible and to allow the spheres not to come out of the caps inside which they are positioned during the robot's advancement.

In order to better understand what happens during the movement of the robot inside the caps where the spheres are housed, a simulation was created with the Creo Simulate tool to analyze the displacements and Von Mises stresses that are established in the piece.

Figure 4-32 shows the detail of the mesh made at a connection end of a track module. Figure 4-32 shows the FEM analysis of a track module; before carrying out the analysis loads and constraints were applied and a more accurate mesh was created in the areas that were considered most interesting to analyze. The module was constrained to the base, in correspondence with the rungs, constraining the translations in the three directions; while the forces were applied to the spherical caps with an inclination of 45°. To apply the forces, two portions of spherical caps, 1.5 mm wide, were cut out, since during the traction of the robot the contact between the sphere and the cap occurs mostly at the ends. The applied components derive from the breakdown of the maximum traction force exerted by the pair of pinions. These force components were identified by tracing the normal to the tangent planes identified with respect to the outer edges of the two caps.

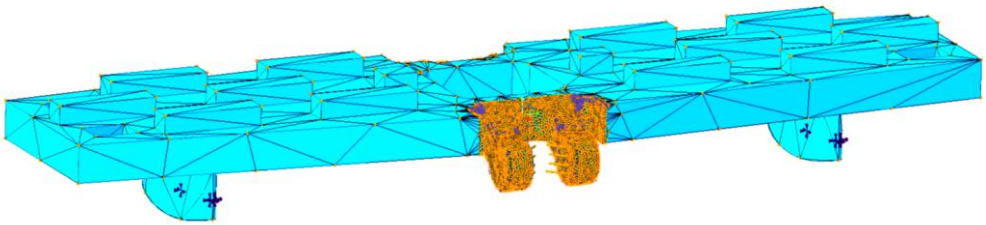

Figure 4-32 FEM analysis of single module

Figure 4-33 shows the detail of the mesh made at a connection end of a track module. The mesh was made for the areas indicated in the figure; each area was divided into tetrahedral elements whose sides measure 0.5 mm.

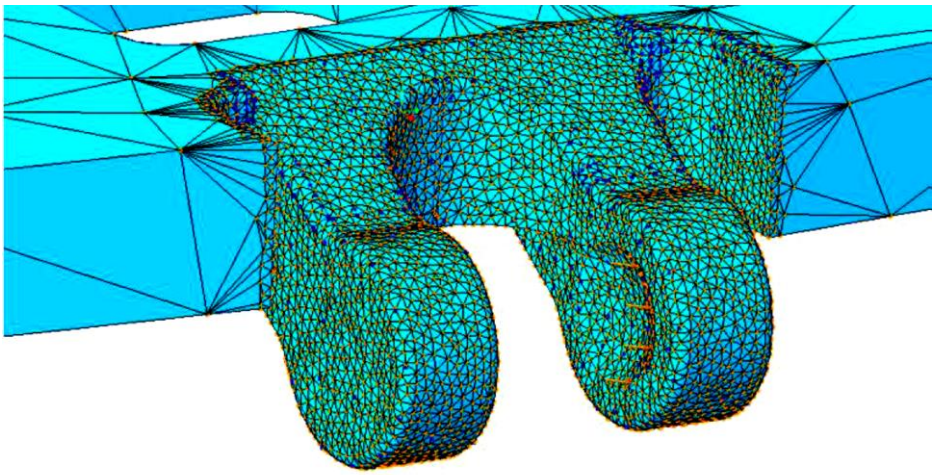

Figure 4-33 Detail of the FEM mesh made at the connection end of the track module

The following are the calculations performed to obtain the value of the force components applied to the caps.

The value of the traction force was obtained as follows:

$$F_{max} = \frac{C_{max}}{r_c} \qquad 60$$

where is it,

F_{max} = traction force exerted by the sprockets on the output shaft,

C_{max} = nominal torque generated by the sprockets,

r_c = track radius.

The torque generated by the pinions is obtained by reporting to the output shaft the value of the torque delivered by the gearmotor according to the transmission ratio expressed by equation (57):

$$C_p = \frac{C_{mr}}{\tau_t} \quad 61$$

The value of the transmission ratio τt is known, as it is calculated as the ratio between the number of teeth, z_1 and z_2, of the toothed wheels that make the gear between the axis of the gearmotor and the output shaft where the sprocket. Obtaining the value of the traction force from (60), the decomposition of the force into the two components at 45 ° is immediate from the rule of the triangle of forces. The table (Table 4-7) shows the results of the calculations performed and the data that were necessary for their performance.

Table 4-7 Results obtained from the calculations carried out

Cp	1,224 Nm
τt	0,4167
rc	0,055 mm
Cn	1 Nm
Ft	22,255 N
$F45°$	11,127 N

Once the values of the applied force components were obtained, the analysis was performed with applied loads and constraints. Figure 4-34 shows how the Von Mises stresses are distributed in the track module. The piece is represented divided into elements, it can be seen that the most stressed areas are at the end of the module; in this area, the size of the elements that make up the component is very small, 0.5 mm, since the mesh, as it has been said initially, has been thickened in the areas of greatest interest.

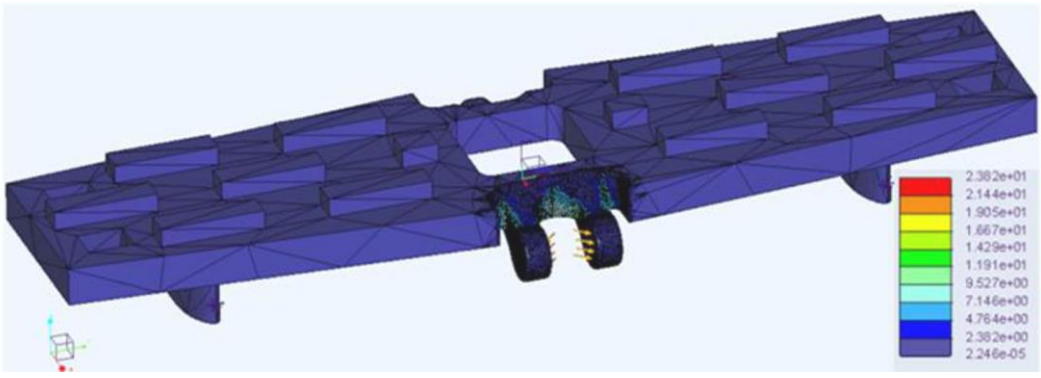

Figure 4-34 Von Mises stresses (track traction)

In order to better understand what happens in the most stressed areas, a detailed zoom is shown in Figure 4-35 alongside the voltage values recorded following the analysis carried out. As can be seen from the comparison with the data reported, the maximum voltage values recorded in the piece are close to 24

Mpa. This value was not considered worrying for the purposes of the material resistance, as the average value of the breakdown voltage for PLA is equal to 39 Mpa, while the reference value is 60 Mpa.

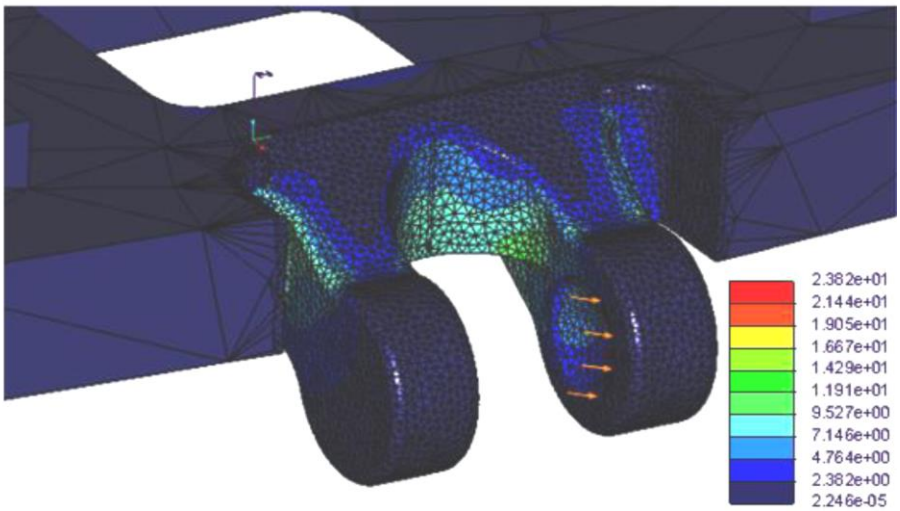

Figure 4-35 Detail zoom of the Von Mises tension

After carrying out the simulation, the displacements recorded in the module as a result of the forces applied due to the traction of the robot were also analyzed. Figure 4-36 shows again a 3D view of the module, this time analyzing the reported displacements. As the figure shows, the most stressed areas are naturally near the connection ends as they are affected by the force components applied.

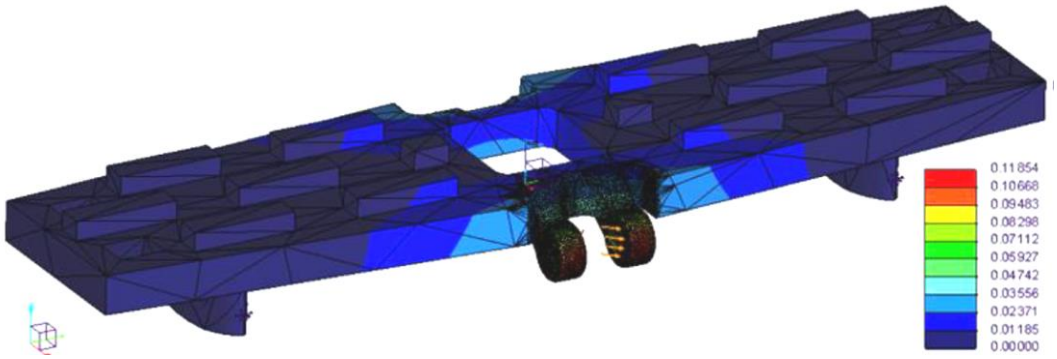

Figure 4-36 Displacements recorded for the track module

A detailed zoom of the areas of greatest interest was also reported for the analysis of the movements. We can see from Figure 4-37 below, that the displacements gradually increase from the center of the module to the end of the joint. By comparing the different colors that characterize the stressed areas with the data shown on the side, we can find that the greatest displacement is just over a tenth of a millimeter; considering that the areas of the spherical caps, where the spheres made at the opposite end of the module will be housed, have a depth of 0.6

mm, the recorded movements are not such as to cause the possible spheres to escape during the advancement of the robot.

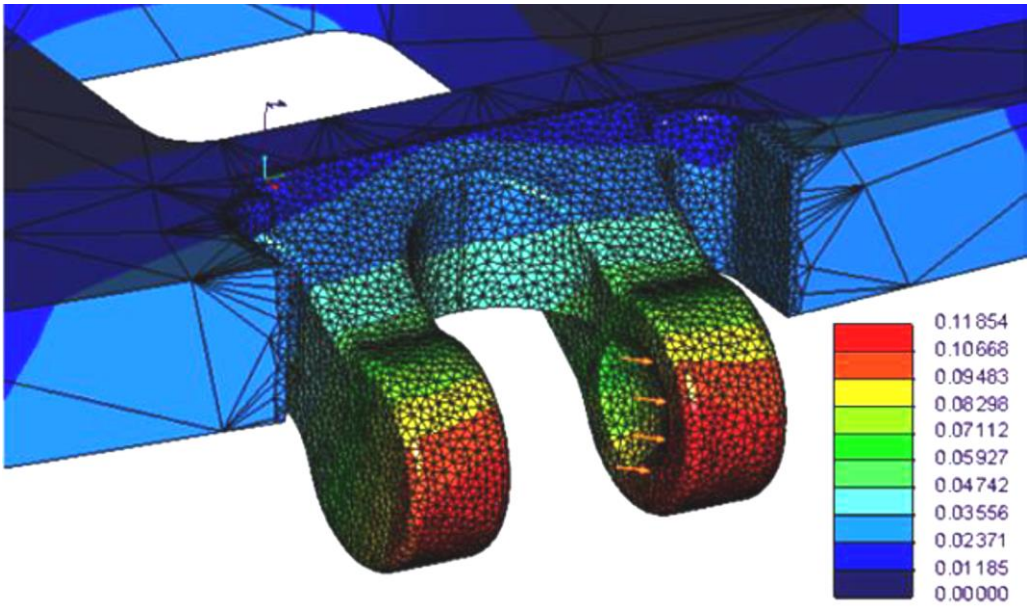

Figure 4-37 Detail zoom of the areas most subject to movement

4.3.4 Constructive design of the vertebral joints

For the realization of the vertebral joints, several alternatives have been considered, starting from the functional requirements of limited stiffness in the yaw direction (for actuated lateral flexion with low energy consumption) and higher stiffness in the pitch direction (for passive retroflection) and in the roll direction (for passive torsion). Passive retroflection and torsion of the vertebral column are needed to obtain a flexible structure that adapts to terrain unevenness, improving traction.

The most widespread approach for realizing compliant joints in robotics is to realize lumped elastic elements in which compliance is concentrated. For universal joints, several possible designs are considered in [181]. In Figure 4-38, two possible solutions are represented: the two-axis flexure joint (Figure 4-38a) and the compliant Cardan U joint (Figure 4-38b). Such compliant realizations of universal joints also allow compliance along x (roll torsion), therefore they can be used as vertebral joints for SnakeTrack.

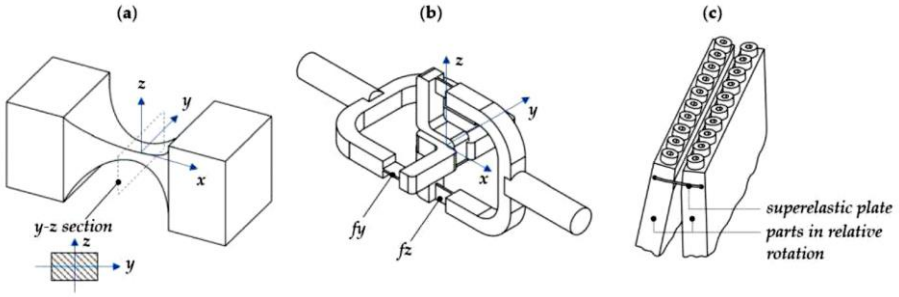

Figure 4-38 Possible realizations of compliant universal joints: two-axis flexure joint (a) and compliant cardan U joint (b); revolute joint with superelastic insert (c).

The two-axis flexure joint is the extension to two axes of the revolute flexure hinge, and has the same main drawback: the stress is highly concentrated in the central section, and this lowers its mechanical resistance. Different stiffness along y and z can be obtained by adopting a rectangular central section (Figure 4-38a). The compliant Cardan U-joint of Figure 4-38b reduces the stress concentration issue, since strains and stresses are evenly distributed along the flexure plates fy and fz, which usually have constant thicknesses. Different stiffnesses along y and z can be obtained by adopting different thicknesses and lengths for the fy and fx flexure plates. The mechanical resistance of this joint can be further improved by replacing the flexure plates with inserts in super-elastic materials (Figure 4-38c), as proposed in [182], [183], but this greatly increases the joint size and weight because it can't be realized in a single part. On the other hand, the practical realization of a flexible cardan U joint is rather complex even with additive manufacturing techniques. An alternative approach to design a 3-DoF compliant joint is represented by beam-based compliant mechanisms [184], but they not very compact, are not suited for the present application.

An alternative solution, which greatly simplifies the design of the vertebral joints, is to use the soft robotic paradigm, adopting a compliant joint without shrinkages, exploiting the hyperelasticity of materials such as thermoplastic polyurethane (TPU).

Figure 4-39 represents the design of the proposed compliant joints. Each vertebra is composed of a central core (C) and two external plates (P), fixed by bolts. A central TPU elastic element (EE) connects two adjacent vertebrae; the two external plates P lock the elastic element EE. Moreover, the contact of the profiles of the plates P of two adjacent vertebrae, with a limited gap when EE is undeformed (0.13 mm), limits the relative pitch and roll motion and consequently the passive retroflection and torsion, while lateral flexion and is almost not affected by the plates P.

This design has the following advantages: low cost, resilience to shocks much higher than conventional compliant joints, and the possibility of easily tuning the range of retroflection by changing the shape of the plates P and consequently the gap between the plates of two adjacent vertebrae.

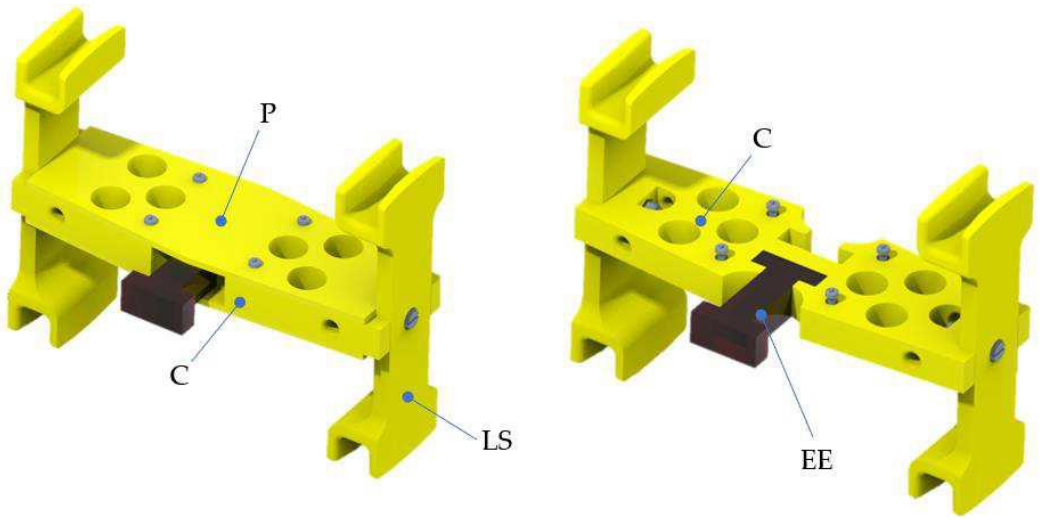

Figure 4-39 Design of the compliant vertebral joints: core (C), external plates (P), lateral supports (LS) TPU elastic element (EE).

The vertebral element consists of the assembly of the following components:

- two side profiles
- the central profile, designed to accommodate the intervertebral joints
- two profiles to cover the central element

The side profiles have been made with a geometry that allows the passage of the track pegs when the robot is in motion. Figure 4-40 shows three vertebral elements connected in succession, we can glimpse the connection joints positioned within the two adjacent vertebrae, and the figure shows the configuration assumed in the case of linear robot movement.

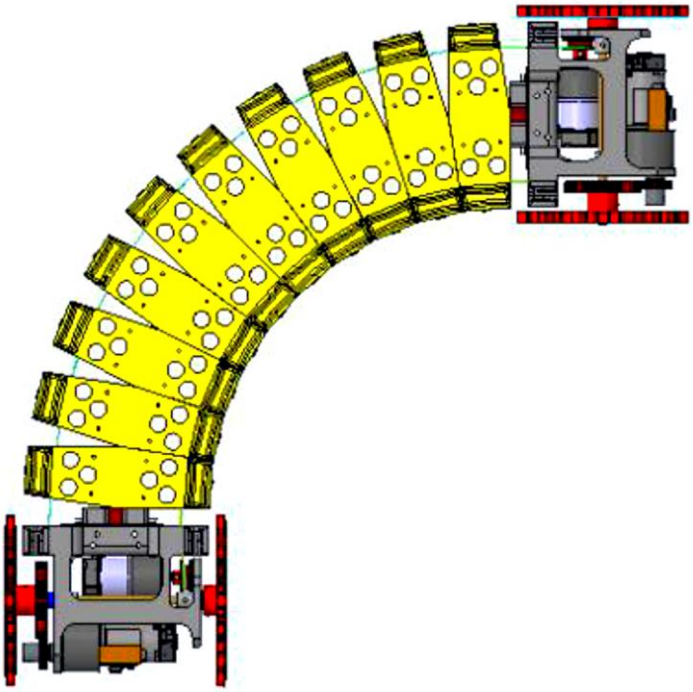

Figure 4-40 Top view of the spinal column of the robot

4.3.5 The motorized end modules

The ends of the robot consist of two motorized modules, also made perfectly symmetrical in order to maintain the prerogative established for the Snake Track robot. These modules, as shown in Figure 4-41, are obtained by assembling different components, some of these are indicated in the figure and explained in Table 4-8.

Among the components present in the end modules, there are two of the four motors with which the robot is equipped. The traction actuator (Figure 4-41, TA) is represented by a gearmotor, controlled by the Motor Driver component (located in the spaces between the vertebrae).

This gearmotor is connected to a toothed wheel whose pitch diameter is 20 mm (Figure 4-41, G), which produces a gear with a second toothed wheel with a diameter of 48 mm, made integral with one of the two pinions. The gear just described has the task of further reducing the speed in order to increase the transmissible torque to the output shaft where both pinions are mounted.

The actuator that allows the robot to turn (Figure 4-41, SA) consists of a gearmotor connected to a pulley (Figure 4-41, P) on which the rope that crosses the lateral holes present in all the vertebral elements are wound and allows the robot to steer.

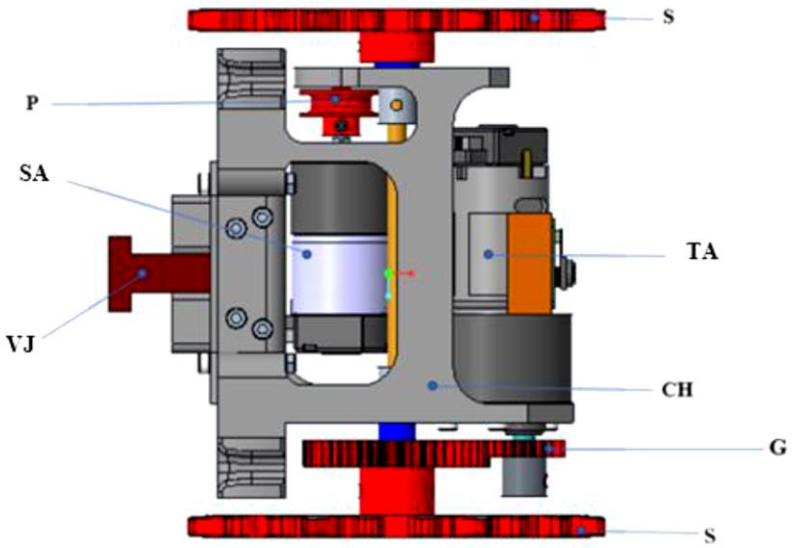

Figure 4-41 Top views of one of the two motorized modules placed at the ends of the robot

Table 4-8 shows the components used necessary for the realization of the module; pins and bolts used to fasten some components to the frame have been excluded from the list.

Table 4-8 components present in the robot end modules

Components	Symbol shown
sprocket	S
Chassis (head chassis)	CH
Track actuator	TA
Steering actuator	SA
Rod	RD
Pulley	PU
Hub	HB
Vertebral joint	VJ
joint cap	JC
spacer	SP
camera support	CS
camera	C
gear	G
washer	W

4.3.6 The robot Sprockets

Figure 4-42 shows the front view of one of the four pinions; the 2D drawing of the pinions was made starting from an octagon, tangent to an internal circumference with a diameter of 100 mm.

The pinion teeth were made taking the sides of the octagon as a basis. Each tooth has its own axis translated by 7.55 mm with respect to the central axis; the eight pairs of teeth are rotated 45 ° with respect to the adjacent pairs.

To facilitate the insertion of the sprockets inside the track modules during the movement of the robot, at the eight edges, spikes of a height equal to the track itself have been created.

A 5 mm diameter hole was made in the center of the pinion to allow coupling with the output shaft; in addition, eight triangular-shaped cavities were made positioned at 22.5 ° from each other.

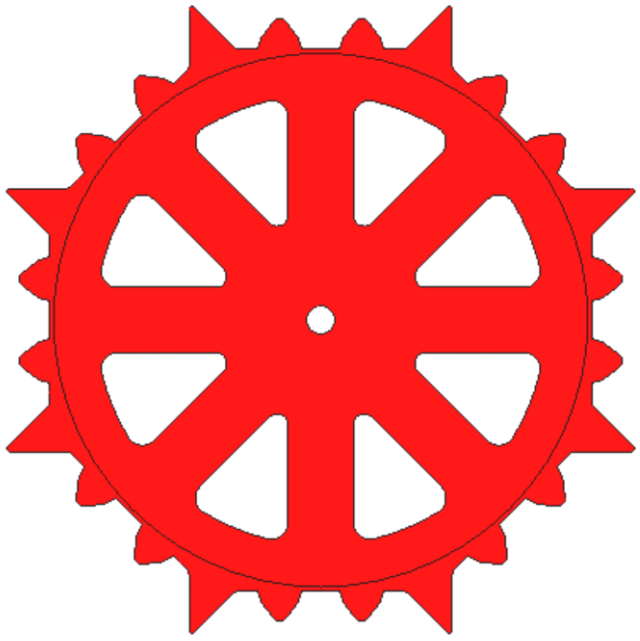

Figure 4-42 Front views of one of the four sprockets in the robot

To make known the dimensions used in the realization of the four pinions, the 2D CAD model of one of the eight sides of the polygon is shown in Figure 4-43. As can be seen from the figure, the teeth have a trapezoidal shape and their symmetry axes are at a distance of 7.55 mm from the central reference, while the height is 5.5 mm. This dimension has been designed so that the teeth of the sprockets are not at the same height as the track, but rather have 0.5 mm of tolerance; this value was again imposed between the pinion teeth and the holes made at the base of each module, to facilitate the sliding of the track.

The oblique sides of the teeth have an inclination equal to 107 °, the same as for the holes in the modules; over 2 mm in height, the pinion teeth have a more

pronounced inclination to facilitate their insertion into the track; the value relating to the inclination was calculated by the difference after establishing the minor base of the teeth equal to 1.5 mm.

A perfect match was made between the eight sides of the sprocket and the length of the straight sides of the track modules; as shown in the figure, the dotted line is lowered by 1.72 mm with respect to the track support base; this value, which was discussed when discussing the positioning of the connection joints, represents how much their centers are translated with respect to the base of the modules. The intersections between the dotted line and the oblique sides of the pinion represent the points where the centers of the joints are located. We can note that these intersections are located 40 mm from each other, that is, the distance between the centers of the connection joints. This value, which had already been found by treating the initial geometry of the track, was maintained in the construction of the sprockets to allow the correspondence between the track modules and the four sprockets during the movement of the robot.

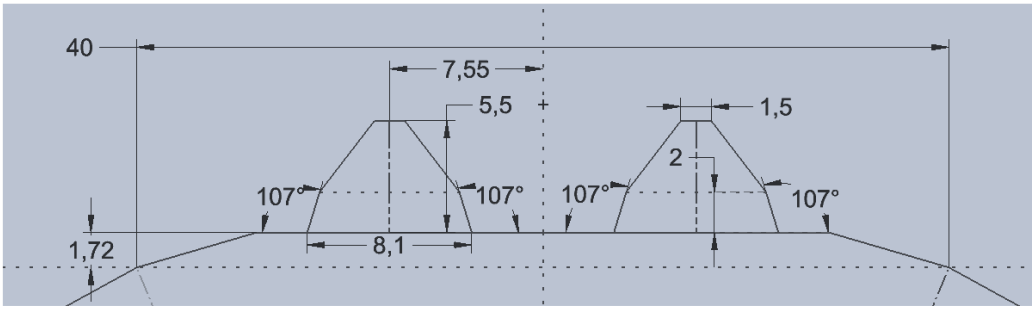

Figure 4-43 2D CAD of one side of the polygon

The geometry of the sprockets is the same for all four, the only difference between the two pairs of sprockets lies in the way they are mounted on the central rod. Figure 4-43 shows the rear view of the 3D model of one of the four pinions; we can see the presence of a toothed wheel made concentric to the pinion.

The toothed wheel has a pitch diameter of 48 mm and makes the gear with a second toothed wheel with a diameter of 20 mm keyed onto the motor shaft. This gear is characterized by the following transmission ratio τ_t:

$$\tau_t = \frac{z_1}{z_2} = \frac{d_1}{d_2} \qquad 62$$

where:

z_1 = number of driven wheel teeth,

z_2 = number of drive wheel teeth,

d_1 = driven wheel pitch diameter,

d_2 = driving wheel pitch diameter.

Figure 4-44 shows a 3D view of the gear made in the two end modules between the toothed wheel connected to the traction gearmotor and the second toothed wheel connected to the pinion. This gear has the purpose of further reducing the output speed in order to obtain an increase in the transmitted torque.

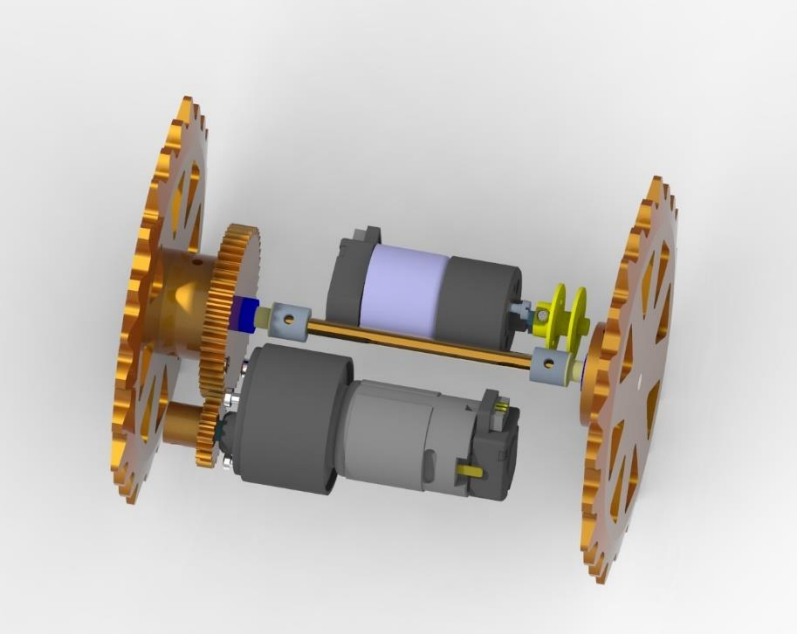

Figure 4-44 3D view of the gear interposed between the gearmotor shaft and sprockets axis

4.3.7 Sizing of the actuators

4.3.7.1 The gearmotors

The SnakeTrack robot is equipped with four gearmotors located in the two modules placed at the ends of the robot. These modules each house two gearmotors that allow traction and steering. The traction motor is mounted on the input shaft, which is connected via a gear, integrated with one of the two pinions, to the output shaft. This gear was used to transmit motion, with a given speed reduction, to the output shaft in order to produce an increase in the torque to be transmitted to the pinions. The curvature of the robot is achieved thanks to a second gearmotor; which is directly connected to a pulley on which the rope is wound, which allows the vertebral system to steer with respect to the direction you want the robot to follow. By controlling the gearmotor, you decide how much to make the robot bend and in what direction, pulling the relative rope.

The two traction gearmotors were selected from the RobotItaly catalog, while the steering gearmotors were chosen from the Micromotors catalog.

The main characteristics of the two gearmotors are shown below; the calculations performed for their sizing are also reported.

4.3.7.2 Steering Actuators (SA)

The characteristics of the gearmotor chosen to allow the robot to turn are shown in Table 4-9; the values refer to room temperature (20 °) and have a tolerance of +/- 10%.

Table 4-9 Gearmotor technical data

Typology			Nominal tension	length	Reduction ratio	Nominal torque	The speed at rated torque	Electric Power
			V	mm		Nm	rpm	w
L149	12	90	12	41	90,3:1	0.08	18	0.5

As previously explained, the lateral ropes that allow the curvature of the vertebral system are wound on two pulleys placed at the two ends of the robot, connected to the steering gearmotor. In order to know the speed with which the rope relative to the internal radius of curvature of the robot is stretched, the following is the calculation of the robot's steering speed:

$$v_s = \omega_{mr} \cdot r_c \qquad 63$$

Where is it:

v_s = robot steering speed,

ω_{mr} = rotation speed of the gearmotor

r_c = radius of the pulley on which the rope is wound (0.008 m).

The calculation of the steering force provided by the gearmotor in nominal conditions, which can be used to overcome the resistance, given by the intervertebral joints, to lateral flexion is reported:

$$S_s = \frac{C_n}{r_c} \quad 64$$

where:

S_s = force exerted by the robot to steer,

C_n = nominal torque delivered by the gearmotor.

Table 4-10 shows the values obtained from the gearmotor sizing and the quantities that were necessary to perform the calculations.

Table 4-10 Characteristic quantities of the gearmotor and useful data for sizing

Pulley radius	r_c	0,008	m
Number of gearmotors	N	1	-
Nominal torque	C_n	0.08	Nm
Output speed from the gearmotor	ω_{mr}	1.884	Rad/s
Track steering speed	v_s	0.015	m/s
Track steering force	S_s	10	N
Length	l	41	mm
Approximate weight	m	55	g

4.3.7.3 Track Actuator (TA)

The gearmotor chosen for the traction of the robot is equipped with a VDR noise suppressor on the manifold, the gears inside it are made of metal, and the rear axis of the motor protrudes for the application of the encoder. This gearmotor is equipped with a Hall effect encoder, and three pulses are generated for each revolution of the motor.

This gearbox and metal case allow for very high torque and maximum reliability. The values shown in Table 4-11 refer to the ambient temperature condition (20°) and have a tolerance of +/- 10%.

Table 4-11 Technical characteristics of the traction gearmotor

Typology	Nominal tension	length	Reduction ratio	Nominal torque	The speed at rated torque	Electric power

			V	mm		Nm	rpm	w
Rh158	12	75	12	66.5	76,84:1	0.5	55	8.2

To know the speed assumed by the robot during traction, the value of the nominal rotation speed of the gearmotor at the output shaft is reported, according to the transmission ratio expressed by (3.6). Once the radius of the track is known, equal to 0.055 m, the traction speed of the robot is calculated as follows:

$$v_t = \omega_n \cdot r_c \qquad 65$$

where,

v_t = robot traction speed,

ω_n = speed of rotation of the pinions,

r_c = track radius.

The calculation relating to the thrust that the robot exerts during traction is shown below, assuming an efficiency value of 0.8, and again reporting the nominal torque delivered by the motor, to the output shaft on which the pinions are mounted, according to (3.6), we obtain:

$$S_t = \frac{N \cdot C_n \cdot \mu}{r_c} \qquad 66$$

where is it:

S_t = traction force exerted by the robot,

N = number of traction motors,

C_n = torque generated by the pinions.

Again, Table 4-12 shows the values, relating to the traction gearmotor, obtained from the sizing and the quantities necessary for carrying out the calculations.

The values obtained, compared with the results of Table 4-6 concerning the study of the robot advancing on a ground inclined by 60 °, prove that the chosen motors can support the given slope. The resisting force component is lower than the traction component exerted by the robot, furthermore, the required torque is lower than the nominal torque delivered by the RH158-12-75 traction gearmotor.

Table 4-12 Characteristic quantities of the gearmotor and useful data for sizing

Track radius	rc	0.055	m
Number of traction motors	N	2	-

Track performance	μ	0.8	-
Transmission report	τt	0.4166	-
Nominal torque delivered by the gearmotor	Cmr	0.5	Nm
The torque generated by the pinions	Cp	1.224	Nm
Nominal rotation speed of the gearmotor	ωmr	5.757	Rad/s
Speed of rotation of the pinions	ωp	2.399	Rad/s
Traction speed of the robot	vt	0.322	m/s
The traction force of the robot	Ft	34.909	N
Length	l	66.5	mm
Approximate weight	m	190	g

4.4 KINEMATICS OF THE UNDERACTUATED STEERING

The steering system of Porcospino is highly underactuated; as a matter of fact, the lateral flexion of the whole vertebral column is driven by the tension of a single rope, but the vertebral column is characterized by several compliant joints.

Consequently, the definition of the time-varying profile of the column, even with the hypothesis of the robot lying on a flat surface, is a complex problem, which involves the friction conditions between each track module and the ground. In the case of uneven terrain, the problem is even more complex, not planar, and not only the yaw rotations of the compliant joints but also their pitch and roll rotations, have to be considered.

Nevertheless, some useful kinematic relationships can be obtained considering the following assumptions (Figure 4-45):

- the robot stands on a flat horizontal surface (planar problem);
- the gap between the plates (**Error! Reference source not found.**) is n eglected, and the compliant joint is considered as a pure revolute joint placed in the geometric center of the undeformed elastic element EE;
- the yaw rotation is equal (σ) for all the joints.

The third assumption is a reasonable approximation on flat and uniform surfaces since the elastic return forces of the compliant joints tend to distribute uniformly the curvature along the vertebral column; this fact is confirmed by the experimental results (section 4.4.1 and section 5.3).

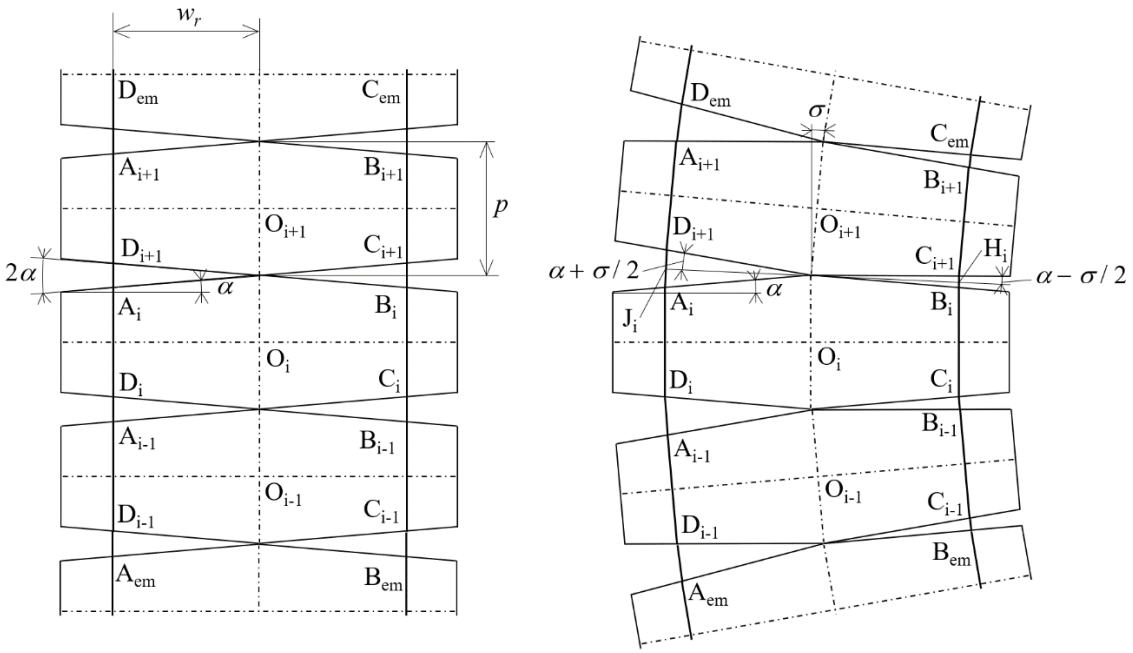

Figure 4-45 Relative orientations of adjacent vertebrae in a straight position (left) and steered position (right) of the vertebral column.

Figure 4-45 represents the geometry of the vertebral column in undeformed (left) and steered position (right). In the figure, three vertebrae are represented, but in general, n is the number of vertebrae.

In the steered position the length of the rope on the external side of the curve (l_{ext}) is represented by the broken line from A_{em} to D_{em}, plus a constant cr which depends on the geometry of the end modules and the attachment of the rope on the winch. The length of the rope on the internal side of the curve (l_{int}) is represented by the broken line from B_{em} to C_{em}, plus c_r.

Considering the geometry of Figure 4-45, it is possible to obtain the following relationships:

$$\overline{A_i D_{i+1}} = 2\overline{J_i D_{i+1}} = 2\frac{w_r}{\cos\alpha}\sin\left(\alpha+\frac{\sigma}{2}\right) \qquad 67$$

$$\overline{B_i C_{i+1}} = 2\overline{H_i C_{i+1}} = 2\frac{w_r}{\cos\alpha}\sin\left(\alpha-\frac{\sigma}{2}\right) \qquad 68$$

$$\overline{A_i D_i} = p - 2w_r \tan\alpha \qquad 69$$

$$\begin{aligned} l_{ext} &= n\overline{A_i D_i} + (n+1)\overline{A_i D_{i+1}} + c_r = \\ &= n(p - 2w_r \tan\alpha) + 2(n+1)\frac{w_r}{\cos\alpha}\sin\left(\alpha+\frac{\sigma}{2}\right) + c_r \end{aligned} \qquad 70$$

$$\begin{aligned} l_{int} &= n\overline{A_i D_i} + (n+1)\overline{B_i C_{i+1}} + c_r = \\ &= n(p - 2w_r \tan\alpha) + 2(n+1)\frac{w_r}{\cos\alpha}\sin\left(\alpha-\frac{\sigma}{2}\right) + c_r \end{aligned} \qquad 71$$

In equations (67) to (71) the constant geometrical parameters p (the vertebral pitch), w_r and α characterize the geometry of the vertebrae, while the variable angle σ is the angular displacement of each vertebral joint; the angle σ is limited by the geometry of the plates between 0 and 2 α.

When the vertebral column is rectilinear, σ is null and:

$$l_{ext} = l_{int} = np + 2w_r \tan\alpha + c_r = l_{med} \qquad 72$$

Consequently, the variations of the lengths of the external rope (positive) and the internal rope (negative) are respectively:

$$\Delta l_{ext} = l_{ext} - l_{med} = 2(n+1)w_r\left(\frac{\sin(\alpha+\sigma/2)}{\cos\alpha} - \tan\alpha\right) \quad 73$$

$$\Delta l_{\text{int}} = l_{int} - l_{med} = 2(n+1)w_r\left(\frac{\sin(\alpha-\sigma/2)}{\cos\alpha} - \tan\alpha\right) \quad 74$$

For the Porcospino prototype, n = 10, p = 40 mm, w_r = 43.5 mm, and α = 4.5°. Figure 4-46 shows the graphs of Δl_{ext} and Δl_{int} as functions of σ with these parameters.

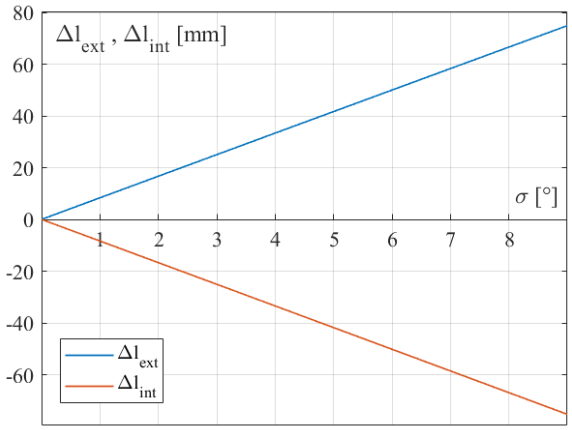

Figure 4-46 Variations of the rope lengths as functions of the yaw angle of the vertebral joints.

It is possible to notice that:

the maximum magnitudes are similar but not perfectly equal: $\Delta l_{ext,max}$ = 74.8 mm, $\Delta l_{int,min}$ = -75.3 mm;

the relationships are almost linear.

In order to evaluate the linearity of the equations (73) and (74), Figure 4-47 shows the differences e$\Delta l_{ext}(\sigma)$ and e$\Delta l_{int}(\sigma)$ between $\Delta l_{ext}(\sigma)$ and $\Delta l_{int}(\sigma)$ and their linear approximations passing through the endpoints at $\sigma = 0$ and $\sigma = 2\alpha$.

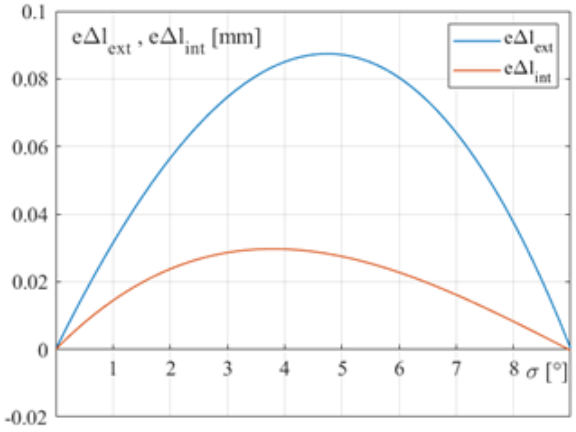

Figure 4-47 Differences between the variations of the rope lengths and their linear approximations as functions of the yaw angle of the vertebral joints.

It is possible to note that these differences are negligible (the maximum values are respectively 0.09 mm for $e\Delta l_{ext}$ and 0.03 mm for $e\Delta l_{int}$); consequently, it is evident that for real-time control purposes, it is convenient to use the linear approximations.

Considering the geometry of Figure 4-45 (right), it is possible to observe that the center of the circular trajectory of the vertebral column is the intersection of the transversal axes of the vertebrae (dash-dotted in Figure 4-45); this allows us to calculate the turning radius r_t of the vertebral column as a function of σ:

$$r_t = \frac{p}{2\tan\left(\frac{\sigma}{2}\right)} \qquad 75$$

Figure 4-48 shows the turning radius r_t as a function of σ: for $\sigma = 0$ the column is rectilinear and r_t tends to be infinite; for $\sigma = 2\alpha$ the turning radius is minimum (254 mm).

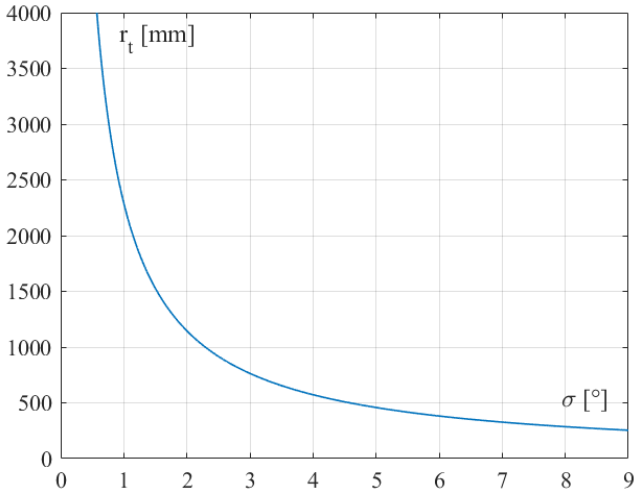

Figure 4-48 Turning radius as a function of the yaw angle of the vertebral joints.

4.4.1 Prototyping

4.4.1.1 The preliminary prototype of the SnakeTrack robot

After 3D-printing the components designed for the robot, they were properly assembled, adding other components. The commercial components were bought and also mounted on the robot.

Figure 4-49 shows the overall view of the SnakeTrack robot, on its right, there is the remote control used in this first phase of experimentation to control the movement of the robot.

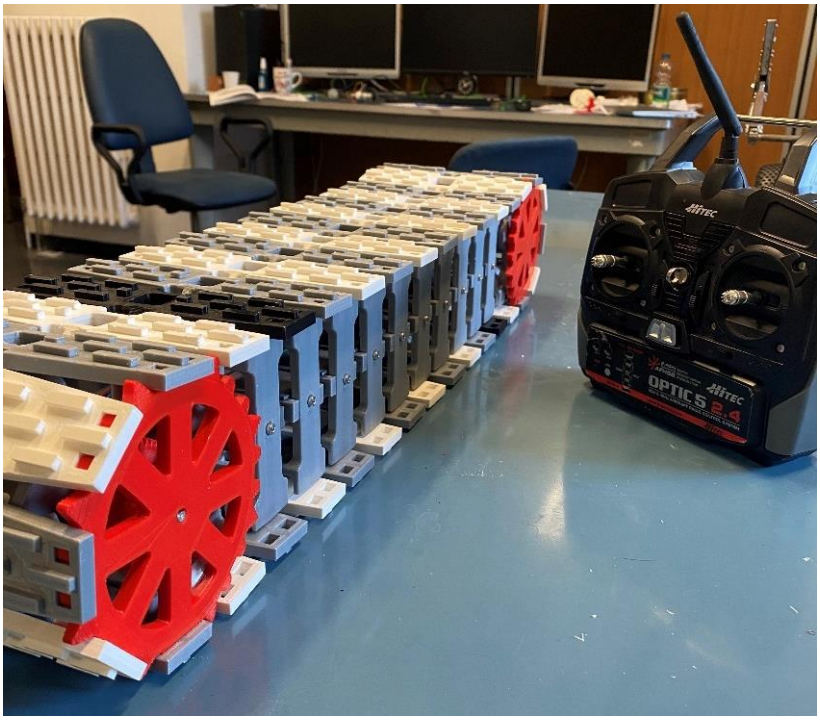

Figure 4-49 The SnakeTrack robot and its remote control

Figure 4-50 shows, with a top view, the system of vertebrae that makes up the spinal column of the robot. It is possible to see the electronic components placed in the appropriate spaces between the profiles of the vertebrae, and next to the robot we find the radio control. The figure on the right shows the top view referring only to the electronic components, in order to better understand where they are located and how they are connected to each other. We can see the presence of the radio receiver, characterized by a blue LED, which receives the signal from the radio control and is connected in turn to the Motor Driver Controller. It allows to control up to four DC motors and communicates with the voltage regulators PWM, which control the supply voltage for the four 12V motors. Power is supplied by a 4s Li-Po battery capable of delivering 14.8 V, higher than the 12V necessary for the motors, to ensure the required voltage even in the event of an incomplete charge.

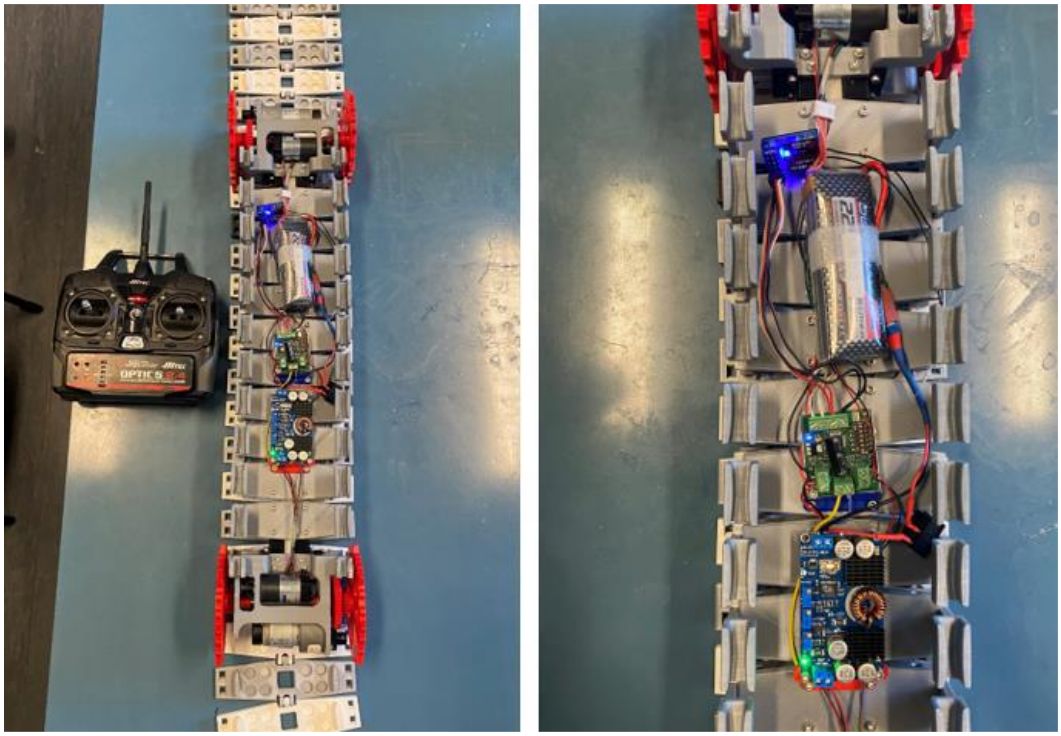

Figure 4-50 Left: the top view of the spinal column of the robot with the radio control, Right: electronic components positioned in the spaces between the robot's vertebrae.

The first image on the left of Figure 4-51 shows the lateral structure of the vertebral column. It is possible to see how the lateral profiles of the vertebrae have been specially designed with the aim of creating a sliding guide for the pegs made at the base of the track modules. These modules are clearly visible in the right image of Figure 4-51, where the lightening made at the base of the modules is highlighted. The central opening of tracks which allow the camera to view, is not visible in the figure, but will be mounted at the ends of the robot and subsequently connected to the Raspberry Pi controller.

Figure 4-51 Left: view of the lateral profiles of the vertebral elements; Right: robot track modules

The vertebral profiles were made by assembling several components; the side profiles, as can be seen from the figure, are fixed by a pin and the relative bolt to the central element of the vertebra. The connection between the vertebrae is established through joints, positioned at the ends of the central elements to realize connection. Figure 4-52 shows how the elements are connected to each other and where the intervertebral joints are inserted. It can be seen that the elements were made with two different materials; in fact, the vertebra element was printed in PLA, while the joints, to allow greater flexion to the vertebral system, were 3D printed in TPU.

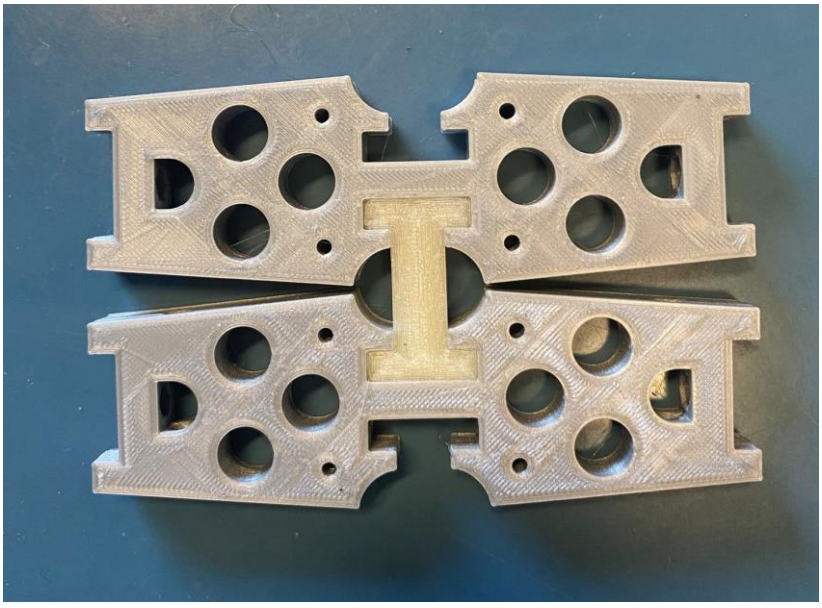

Figure 4-52 Top view of two central elements of the vertebrae connected by TPU joints

In Figure 4-53 there are two views of the SnakeTrack robot, depicting it in the steered configuration.

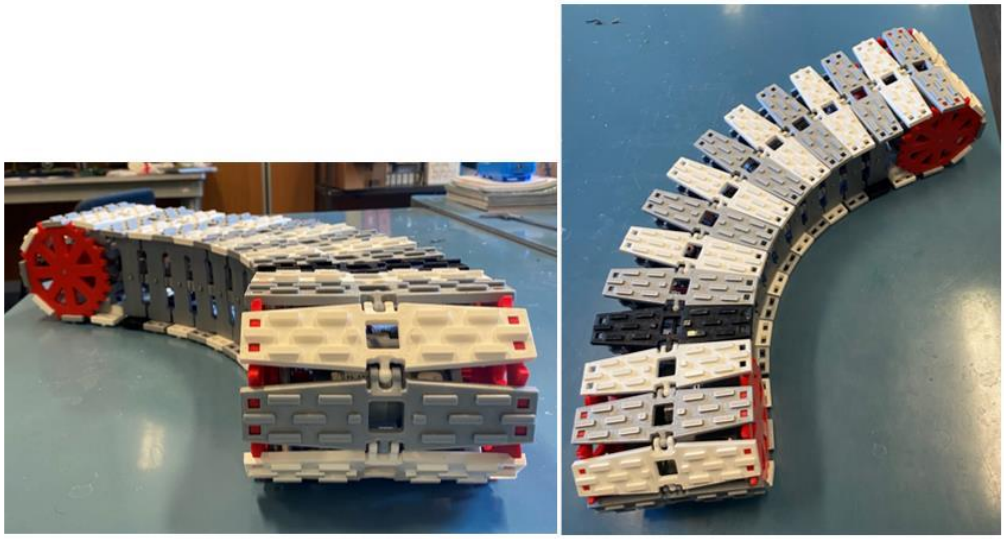

Figure 4-53 Views of the SnakeTrack robot when it assumes the steering configuration

The first prototype of the SnakeTrack has been realized. The first tests have confirmed the overall functionality of the proposed mechanical design and in particular the capability to steer using lateral flexion (Figure 4-54, left) and to move by adapting to terrain unevenness by means of the passive retroflection and torsion of the vertebral joints (Figure 4-54, right). A supporting video of the experimental tests is available at [175].

Figure 4-54 Preliminary experimental tests on the SnakeTrack prototype: steering (left) and locomotion on uneven grounds (right).

4.4.2 Conclusion

The functional design of a small size tracked robot for surveillance and inspection of unstructured and narrow spaces has been presented. It is characterized by a modular structure composed of a vertebral column and a single peripherical track revolving around it. The vertebral column can perform actuated lateral flexion for steering, while passive retroflection and torsion are allowed by the compliant vertebral joints to adapt to terrain unevenness. Thanks to the modular architecture, the length of the robot can be adapted to the payload necessary for the specific task.

The robot is fully symmetric and can continue operating after a capsize; moreover, if it falls on its flank, it can restore the correct position by combining lateral flexion, to lift on the track ends, and track motion. The conceptual design of the robot has been presented and the embodiment design of the vertebral joints has been discussed. The experimental results have confirmed the robot's capability to walk and steer while adapting to uneven grounds and suggested possible refinements in the detailed design of the tracks and of the steering system. In the next steps of the research, these modifications will be implemented in order to obtain further prototypes with higher technology readiness levels.

5 Porcospino

SPINED SINGLE-TRACK MOBILE ROBOT FOR INSPECTION OF NARROW SPACES AND PIPELINES

5.1 Summary

This chapter discusses the design and the experimental tests on Porcospino, a bio-inspired single-track ground mobile robot for surveillance and inspection in unstructured environments characterized by narrow spaces. It is an evolution of the SnakeTrack, a single-track robot with steering capabilities; differently from SnakeTrack, the track modules of Porcospino are characterized by elastic spines, which improve traction on unevenness and irregular terrains. The main body is a vertebral column, comprising a series of vertebrae and two end modules, connected by compliant joints. Each end module carries two actuated sprockets, sharing a common axis, which drives the single peripherical track. Moreover, each end module hosts two actuators, one for the track rotation and one for pilot steering. The remaining mobilities of the vertebral column allow it to cope passively with the terrain profile, to enhance traction. The control unit, batteries, drivers, and environmental sensors are placed along the vertebral column. Both the end modules are equipped with a camera for intermittent vision, which is possible thanks to openings realized on the track modules. In this section, the experimental campaign on the first Porcospino prototype is discussed, highlighting the differences with its early version.

5.2 FUNCTIONAL DESIGN OF PORCOSPINO

Although Porcospino has certain similar functionalities with SnakeTrack but in terms of guiding pegs in track modules (Figure 5-3, GP) the design improved and locked the track inside the latteral support (Figure 5-3, LS). This improvement prevent the track from moving out of its path when crossing obstcles and improve the stability in steering. Additionally, each tracks has 12 spines which has 60 degree inclined with respect to the horizental plane of tracks. These spines 3D printed with TPU which is soft material and could be used instead of supension and help the robot to btter crossing obstcles. Furthermore this spines could help the stability of robot in rocky and sandy terrains and slops by craping the rocks.

Figure 5-1 represents the external view of the Porcospino robot, with an overall size of 670 mm (length) × 165 mm (width) × 145 mm (height). Its main structural parts are the vertebral column and the track. The robot is a bit bigger than SnakeTrack but with higher maneuverability and satbility.

A detail of the track modules is shown in Figure 5-3. They are characterized by central openings (Figure 5-3, O) that allow, during the track motion, an intermittent view using the two cameras mounted on the end modules (Figure 5-2 and Figure 5-3, CA). The guidance of the tracks along the vertebral column is assured by lateral supports attached to each vertebra (Figure 5-3, LS), and by the guiding pegs (Figure 5-3, GP) attached to the track modules (Figure 5-3, TM). The track modules are connected by spherical joints (Figure 5-3, SJ), composed of a male spherical part (Figure 5-3, SJM) and a female part (Figure 5-3, SJF), printed directly on the tracked module; the two parts of the spherical joint can be assembled thanks to the elasticity of the female part. On the contrary, the track spines (Figure 5-3, S) and the guiding pegs of the track modules (Figure 5-3, GP) are printed separately and then assembled by interference fit.

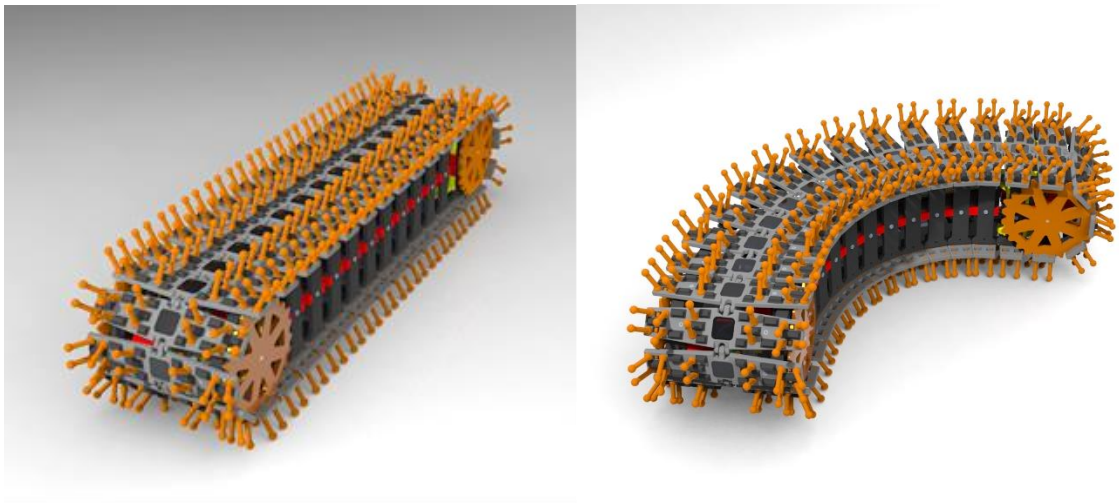

Figure 5-1 External view of Porcospino: straight position (left) and steering position with minimum turning radius (right).

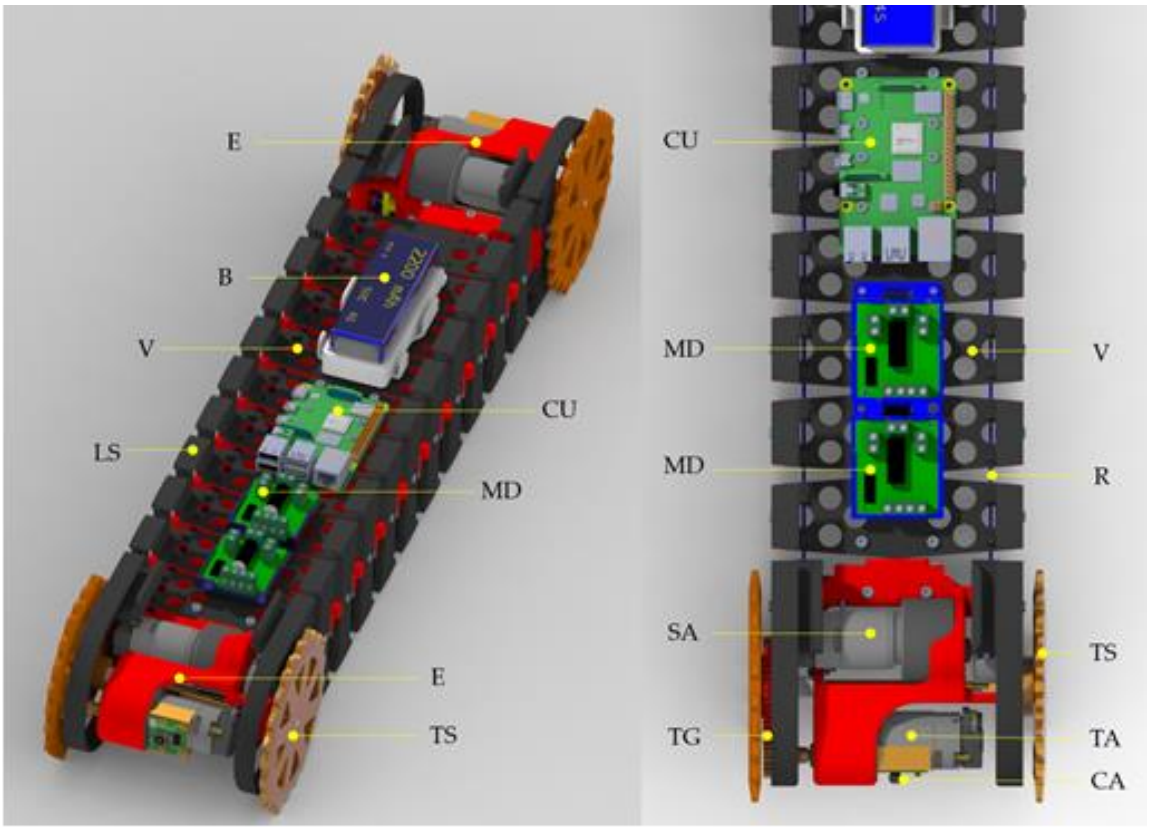

Figure 5-2 Vertebral column of Porcospino.

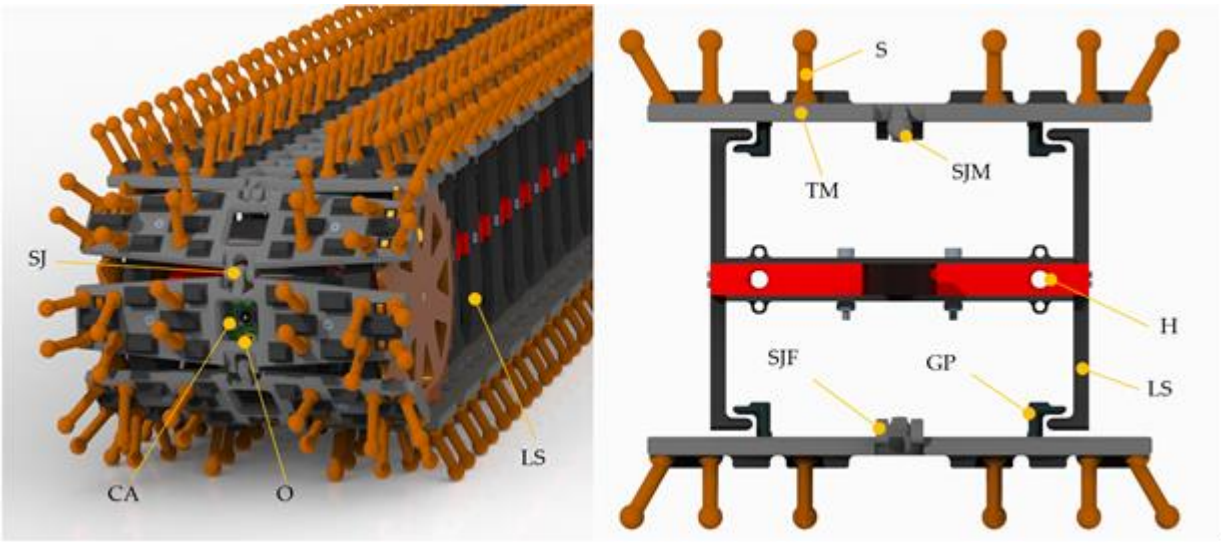

Figure 5-3 Detail of the track modules with a central opening (O) for camera vision (left); transversal section of the track guidance system (right).

5.3 PROTOTYPING AND EXPERIMENTAL TESTS

The experimental tests on the Porcospino prototype are in progress, by now with the robot radio-controlled by an operator. The tests have confirmed the overall functionality of the proposed mechanical design, and the capability to steer using lateral flexion while adapting to terrain unevenness thanks to the passive retroflection and torsion of the vertebral column. Figure 5-4 shows Porcospino moving on uneven and grassy terrain during the inspection of a pipe with a 300 mm diameter.

The first frame sequence of Figure 5-5 (1a – 4a) shows the capability of quickly changing curvature direction even on irregular terrain. Frame 2a shows an intermediate position while switching curvature direction: it is possible to see in frame 2a that the vertebral column is not perfectly aligned, since it is underactuated, as discussed in section 4.4, and its dynamic behavior is influenced by the interactions with the ground irregularities. The second frame sequence of Figure 5-5 shows the Porcospino climbing on an obstacle exploiting the passive compliance of its vertebral column.

An important issue for mobile robots moving in unstructured environments is tip-over. Some researchers try to prevent tip-over through proper motion planning [185]; a different approach is to design robots that can recover operativity after a tip-over [14]. Porcospino follows this second approach. The frame sequence of Figure 5-6 shows the capability of recovering a correct locomotion position after a 90° capsize on a flank. The maneuver is performed by curving the vertebral column through the steering actuators, until the robot reaches an unstable position, suspended on its ends (frame 3); then, a small motion of the tracks causes the fall on the correct locomotion position (frame 4).

Figure 5-4 Experimental tests: locomotion on uneven grassy terrain (left) and inspection of a pipe with diameter of 300 mm (right).

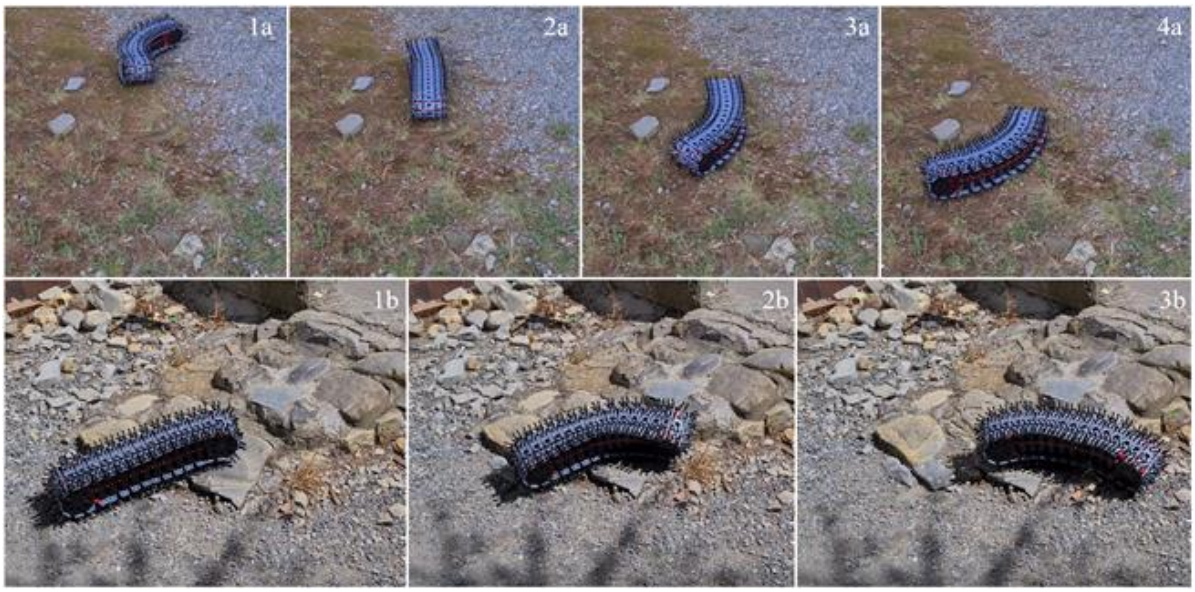

Figure 5-5 Experimental tests: quick change of direction on uneven terrain (frame sequence 1); passive adaptability of the vertebral column on terrain irregularities (right).

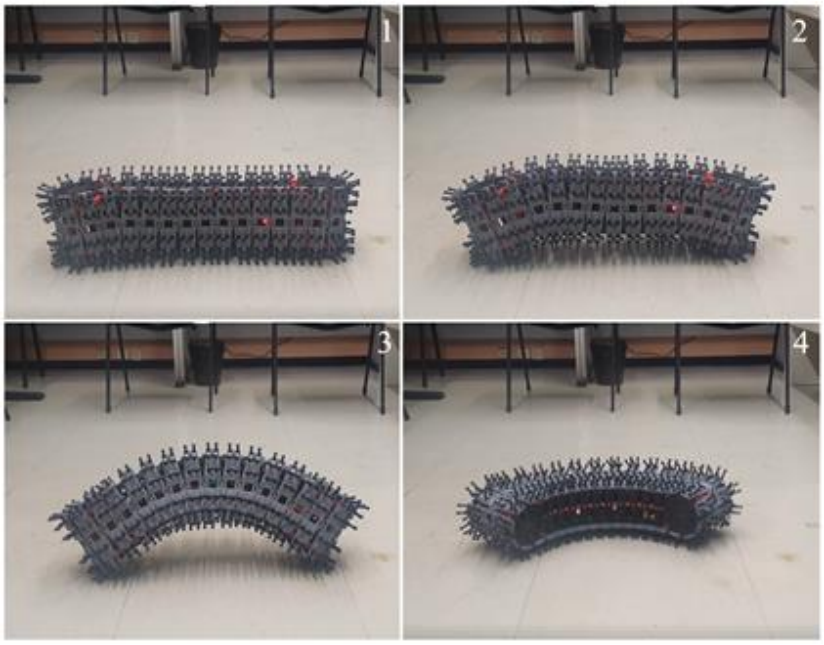

Figure 5-6 Experimental tests: recovery maneuver after a capsize on a flank.

These tests have shown the overall functionality of the Porcospino design, even if refinements of the detailed design are necessary to improve the reliability of the track guiding systems. With respect to the prototype, the SnakeTrack, without spines on the tracks [13], the experimental campaign has shown the effectiveness of the spines to improve traction on irregularities in presence of firm ground, and a certain degree of shock absorption. Nevertheless, spines are counterproductive on soft and yielding terrains, since they reduce the contact surface with the ground. However, the robot concept is fully modular, and not only the robot length can be varied based on the specific task, but also the track type. A supporting video of the experimental tests is available at [186].

5.4 CONCLUSIONS AND FUTURE DEVELOPMENTS

The overall design of Porcospino, a small-size tracked robot for surveillance and inspection of unstructured and narrow spaces has been presented. The functional design of the robot, the embodiment design of the vertebral joints, and the kinematics of the steering system have been discussed.

The Porcospino structure is fully modular, composed of a vertebral column and a single peripherical track revolving around it. The vertebral column can perform actuated lateral flexion for steering, while passive retroflection and torsion are allowed by the compliant vertebral joints to adapt to terrain unevenness.

Exploiting its modularity, the length of the robot can be adapted to the payload necessary for the specific task.

Thanks to its small turning radius (254 mm), its maneuverability in narrow spaces is good. It can't pivot around a vertical axis, but this is not a remarkable limitation, due to the full bi-directionality.

The symmetry of Porcospino brings another useful functional feature: it can continue operating after a 180° capsize; moreover, if it falls on its flank (90° capsize), it can restore the correct position by combining lateral flexion, to lift on the track ends, and track motion.

The first experimental results confirmed the robot's capability to walk and steer while adapting to uneven grounds and suggested possible mechanical refinements in the detailed design of the tracks and the steering system.

Porcospino is the evolution of SnakeTrack; the main difference with respect to SnakeTrack is the presence of flexible spines on the track modules, which are particularly effective to improve traction on uneven but firm terrains, and introduces a certain degree of shock absorption which increases the overall structural resistance of the robot. Other improvements are refinements of the shape of the track guidance system (lateral supports, LS, **Error! Reference s ource not found.**, and guiding pegs, GP, Figure 5-3). As a matter of fact, the track guidance system is the main weak point of the concept, and further work must be done to reach a degree of reliability sufficient for real applications.

Provided that these issues are solved and a proper technology readiness level is obtained, the proposed design seems to be interesting for inspection of narrow unstructured environments, such as pipelines or collapsed buildings, thanks to its small front section and adaptability to unevenness.

In the future of work, another important topic to be addressed is the development of an active retroflection system to increase the obstacle climbing capability.

6 Conclusion

In the next decade, the global market for mobile robots is anticipated to grow significantly, exceeding the market for industrial robotics in terms of sales and units. These robots gained a lot of attention in recent decades, mainly due to their vast usage in uneven, multi-structured environments. Homeland security, surveillance, demining, reconnaissance in risky situations, and agriculture are significant application areas. In general, designing mobile robot locomotion systems for unstructured environments is difficult, especially when the robots must navigate rough or soft terrain or overcome obstacles [32].

In the fast-growing and quickly evolving scenario of mobile robotics, tracked ground mobile robots are attracting the attention of many researchers in the industrial and academic worlds. Tracked locomotion is particularly suited in presence of soft and yielding terrains, but by adopting hybrid solutions the range of profitable applicability of crawlers greatly extends.

In section 3 the design and prototyping of the WheTLHLoc robot are presented. This robot is a small-scale hybrid locomotion robot for surveillance and inspection, capable of combining tracked locomotion on soft terrains, wheeled locomotion on flat and compact grounds, and high obstacle crossing capability (ratio between the maximum climbable step and the robot height higher than one). The limits on the robot size (track length of 300 mm and width of 350 mm) have been selected as a compromise between two conflicting requirements: sufficient compactness to explore narrow spaces and to stand on the tread of a standard indoor stair, and the capability to climb a standard stair using tracks, legs, and wheels. The step climbing capability and motion planning are discussed analytically and then verified by experimental tests.

Section 4 presents the functional design of a small-size mono-track robot, “SnakeTrack”, for surveillance and inspection of unstructured and narrow spaces. It is characterized by a modular structure composed of a vertebral column and a single peripherical track revolving around it. The vertebral column can perform actuated lateral flexion for steering, while passive retroflection and torsion are allowed by the compliant vertebral joints to adapt to terrain unevenness. Thanks to the modular architecture, the length of the robot can be adapted to the payload necessary for the specific task.

The robot is fully symmetric and can continue operating after a capsize; moreover, if it falls on its flank, it can restore the correct position by combining lateral flexion, to lift on the track ends, and track motion. The conceptual design of the robot has been presented and the embodiment design of the vertebral joints has been discussed. The experimental results have confirmed the robot's capability to walk and steer while adapting to uneven grounds and suggested possible refinements in the detailed design of the tracks and of the steering system. In the next steps of the research, these modifications will be implemented in order to obtain further prototypes with higher technology readiness levels.

Ultimately, Section 5 discusses the overall design of Porcospino, an evolution of SnakeTrack. Like SnakeTrack, Porcospino is fully modular, composed of a vertebral column and a single peripherical track revolving around it. The main difference with respect to SnakeTrack is the presence of flexible spines on the track modules, which are particularly effective to improve traction on uneven but firm terrains, and introduces a certain degree of shock absorption which increases the overall structural resistance of the robot. Other improvements are refinements of the shape of the track guidance system. As a matter of fact, the track guidance system is the main weak point of the concept, and further work must be done to reach a degree of reliability sufficient for real applications. Provided that these issues are solved and a proper technology readiness level is obtained, the proposed design seems to be interesting for inspection of narrow unstructured environments, such as pipelines or collapsed buildings, thanks to its small front section and adaptability to unevenness.

Another development for Porcospino is to design an active retroflection system to increase the obstacle climbing capability and unify the main body of the robot using a compliant mechanism and sustainable design to improve the retroflection and reduce mechanical complexity. These aspects are under development right now, exploiting a collaboration with the Nottingham Trent University.

6.1 List of Publications:

1- Bruzzone L., **Nodehi S.E.**, Domenico D. De, Fanghella P.. " WheTLHLoc: hybrid locomotion robot for surveillance and inspection with stair climbing capability". ASME, Journal of Mechanisms and Robotics, January 2023; https://doi.org/10.1115/1.4056770.

2- Bruzzone L., **Nodehi S.E.,** Application of half-derivative damping to Cartesian space position control of a SCARA-like manipulator, Robotics 2022, 11(6), 152; https://doi.org/10.3390/robotics1106015.

3- **Nodehi S.E.,** Bruzzone L., Fanghella P "Porcospino, spined single track mobile robot for inspection of narrow spaces", International Journal of Mechanics and Control, November 2022 (Submitted)

4- Bruzzone L., **Nodehi S.E.**, Fanghella P "Tracked Locomotion Systems for Ground Mobile Robots: A Review". *Machines* 2022, *10*, 648. https://doi.org/10.3390/machines10080648

5- **Nodehi S.E.**, Bruzzone L., Fanghella P. "SnakeTrack, a bio-inspired, single track mobile robot with compliant vertebral column for surveillance and inspection", 31st International Conference on Robotics in Alpe-Adria-Danube Region (RAAD2022), Jun 2022, Austria. https://doi.org/10.1007/978-3-031-04870-8_60

6- Bruzzone L., **Nodehi S.E.**, "Fractional-Order $PII^{1/2}DD^{1/2}$ control of a mechatronic axis: influence of the discrete-time approximation of the half-order derivative and integral", 31st International Conference on Robotics in Alpe-Adria-Danube Region (RAAD2022), Jun 2022, Austria. https://doi.org/10.1007/978-3-031-04870-8_25

7- Bruzzone L., Baggetta M., **Nodehi S.E.**, Bilancia P., Fanghella P. "Functional Design of a Hybrid Leg-Wheel-Track Ground Mobile Robot". Machines 2021, 9, 10. https://doi.org/10.3390/machines9010010
Selected as the cover of Machines magazine (January 2021). Best cover paper award 2021

8- Bruzzone L., **Nodehi S.E.**, V. Belotti, P. Fanghella " Actuation and control layout of the hybrid locomotion ground mobile robot WheTLHLoc" Fourth international conferences of IFToMM Italy, Sep. 2022, Mechanisms and Machine Science, vol 122. Springer, Cham. https://doi.org/10.1007/978-3-031-10776-4_78

9- Bruzzone L., **Nodehi S.E.** Sustainability-oriented applications of the half-derivative and of the half-integral in control system design, 11th International Conference on Mathematical Modeling in Physical Sciences, 5-8 Sep. 2022.

7 References

[1] L. Bruzzone and G. Quaglia, "Review article: Locomotion systems for ground mobile robots in unstructured environments," *Mechanical Sciences*, vol. 3, no. 2. Copernicus GmbH, pp. 49–62, 2012, doi: 10.5194/ms-3-49-2012.

[2] International Federation of Robotics (IFR), "A Mobile Revolution - How mobility is reshaping robotics," no. June, 2021.

[3] "Mobile Robots Market Size, Growth, Trend and Forecast to 2023 | MarketsandMarkets." https://www.marketsandmarkets.com/Market-Reports/mobile-robots-market-43703276.html (accessed Jun. 21, 2022).

[4] G. Quaglia, C. Visconte, L. S. Scimmi, M. Melchiorre, P. Cavallone, and S. Pastorelli, "Design of a UGV powered by solar energy for precision agriculture," *Robotics*, vol. 9, no. 1, 2020, doi: 10.3390/robotics9010013.

[5] T. Wang, B. Chen, Z. Zhang, H. Li, and M. Zhang, "Applications of machine vision in agricultural robot navigation: A review," *Comput. Electron. Agric.*, vol. 198, p. 107085, Jul. 2022, doi: 10.1016/j.compag.2022.107085.

[6] T. de J. Mateo Sanguino, "50 years of rovers for planetary exploration: A retrospective review for future directions," *Rob. Auton. Syst.*, vol. 94, pp. 172–185, Aug. 2017, doi: 10.1016/j.robot.2017.04.020.

[7] A. Thoesen and H. Marvi, "Planetary Surface Mobility and Exploration: A Review," *Curr. Robot. Reports*, vol. 2, no. 3, pp. 239–249, 2021, doi: 10.1007/s43154-021-00056-3.

[8] K. Nagatani *et al.*, "Emergency response to the nuclear accident at the Fukushima Daiichi Nuclear Power Plants using mobile rescue robots," *J. F. Robot.*, vol. 30, no. 1, pp. 44–63, Jan. 2013, doi: 10.1002/rob.21439.

[9] J. L. M. Philip J. Mattson, *Homeland Security and Public Safety: Research, Applications and Standards*. San Diego, California: ASTM International, 2019.

[10] P. Gonzalez de Santos, J. A. Cobano, E. Garcia, J. Estremera, and M. A. Armada, "A six-legged robot-based system for humanitarian demining missions," *Mechatronics*, vol. 17, no. 8, pp. 417–430, Oct. 2007, doi: 10.1016/j.mechatronics.2007.04.014.

[11] R. P. Saputra *et al.*, "Resqbot 2.0: An improved design of a mobile rescue robot with an inflatable neck securing device for safe casualty extraction," *Appl. Sci.*, vol. 11, no. 12, Jun. 2021, doi: 10.3390/app11125414.

[12] W. H. Chun and N. Papanikolopoulos, "Robot Surveillance and Security," in *Springer Handbook of Robotics*, B. Siciliano and O. Khatib, Eds. Cham:

Springer International Publishing, 2016, pp. 1605–1626.

[13] S. E. Nodehi, L. Bruzzone, and P. Fanghella, *SnakeTrack, A Bio-inspired, Single Track Mobile Robot with Compliant Vertebral Column for Surveillance and Inspection*, vol. 120 MMS. 2022.

[14] E. M. Coates and T. I. Fossen, "Geometric Reduced-Attitude Control of Fixed-Wing UAVs," *Appl. Sci.*, vol. 11, no. 7, p. 3147, Apr. 2021, doi: 10.3390/app11073147.

[15] J. Yuh and M. West, "Underwater robotics," *Adv. Robot.*, vol. 15, no. 5, pp. 609–639, Jan. 2001, doi: 10.1163/156855301317033595.

[16] F. Ruggiero, V. Lippiello, and A. Ollero, "Aerial Manipulation: A Literature Review," *IEEE Robot. Autom. Lett.*, vol. 3, no. 3, pp. 1957–1964, Jul. 2018, doi: 10.1109/LRA.2018.2808541.

[17] The White House, "FACT SHEET: New Commitments to Accelerate the Safe Integration of Unmanned Aircraft Systems," 2016. https://obamawhitehouse.archives.gov/the-press-office/2016/08/02/fact-sheet-new-commitments-accelerate-safe-integration-unmanned-aircraft.

[18] Il Mattino, "Esperimento nel Sannio, primo volo del drone sulla Cerreto medievale," 2015. https://www.ilmattino.it/benevento/benevento_drone_cerreto_sannita-807586.html.

[19] D. Schneider, "Flying selfie bots," *IEEE Spectr.*, vol. 52, no. 1, pp. 49–51, Jan. 2015, doi: 10.1109/MSPEC.2015.6995634.

[20] B. Siciliano *et al.*, "EuRoC - The challenge initiative for european robotics," *Proc. Jt. Conf. ISR 2014 - 45th Int. Symp. Robot. Robot. 2014 - 8th Ger. Conf. Robot. ISR/ROBOTIK 2014*, pp. 292–298, 2014.

[21] G. Antonelli, T. I. Fossen, and D. R. Yoerger, "Underwater Robotics," in *Springer Handbook of Robotics*, vol. 1, Berlin, Heidelberg: Springer Berlin Heidelberg, 2008, pp. 987–1008.

[22] Y. Wang, *Space Robotics*, vol. 65, no. 3. Singapore: Springer Singapore, 2021.

[23] E. Feron and E. N. Johnson, "Aerial Robotics," in *Springer Handbook of Robotics*, B. Siciliano and O. Khatib, Eds. Berlin, Heidelberg: Springer Berlin Heidelberg, 2008, pp. 1009–1029.

[24] B. Siciliano and O. Khatib, "Robotics and the Handbook," in *Springer Handbook of Robotics*, Cham: Springer International Publishing, 2016, pp. 1–6.

[25] D. Invernizzi, M. Giurato, P. Gattazzo, and M. Lovera, "Full Pose Tracking for a Tilt-Arm Quadrotor UAV," *2018 IEEE Conf. Control Technol. Appl. CCTA 2018*, no. November 2019, pp. 159–164, 2018, doi:

10.1109/CCTA.2018.8511566.

[26] O. Vaughan, "RoboBee breaks free," *Nat. Electron.*, vol. 2, no. 7, pp. 265–265, Jul. 2019, doi: 10.1038/s41928-019-0280-8.

[27] A. S. Marton, J. R. Azinheira, A. R. Fioravanti, E. C. De Paiva, J. R. H. Carvalho, and R. R. Costa, "Filtering and Estimation of State and Wind Disturbances Aiming Airship Control and Guidance," *Aerospace*, vol. 9, no. 9, p. 470, Aug. 2022, doi: 10.3390/aerospace9090470.

[28] J. Yuh *et al.*, "Design of a semi-autonomous underwater vehicle for intervention missions (SAUVIM)," in *Proceedings of 1998 International Symposium on Underwater Technology*, 1998, vol. 1, pp. 63–68, doi: 10.1109/UT.1998.670059.

[29] P. Marty, "ALIVE: An Autonomous Light Intervention Vehicle," *Scand. Oil-Gas Mag.*, vol. 32, no. 5/6, p. 10,11, 2004, [Online]. Available: https://www.osti.gov/etdeweb/biblio/20501074.

[30] T. I. Fossen, *Marine Control Systems – Guidance. Navigation, and Control of Ships, Rigs and Underwater Vehicles*. Trondheim, Norway: Marine Cybernetics, 2002.

[31] S. Bennett, "A brief history of automatic control," *IEEE Control Syst.*, vol. 16, no. 3, pp. 17–25, Jun. 1996, doi: 10.1109/37.506394.

[32] L. Bruzzone and G. Quaglia, "Review article: locomotion systems for ground mobile robots in unstructured environments," *Mech. Sci.*, vol. 3, no. 2, pp. 49–62, Jul. 2012, doi: 10.5194/ms-3-49-2012.

[33] L. Bruzzone, S. E. Nodehi, and P. Fanghella, "Tracked Locomotion Systems for Ground Mobile Robots: A Review," *Machines*, vol. 10, no. 8, p. 648, Aug. 2022, doi: 10.3390/machines10080648.

[34] L. Bruzzone and G. Quaglia, "Review article: Locomotion systems for ground mobile robots in unstructured environments," *Mech. Sci.*, vol. 3, no. 2, pp. 49–62, 2012, doi: 10.5194/ms-3-49-2012.

[35] R. Altendorfer *et al.*, "RHex: A biologically inspired hexapod runner," *Auton. Robots*, vol. 11, no. 3, pp. 207–213, 2001, doi: 10.1023/A:1012426720699.

[36] A. Seeni, B. Schäfer, B. Rebele, and N. Tolyarenko, "Robot mobility concepts for extraterrestrial surface exploration," *IEEE Aerosp. Conf. Proc.*, 2008, doi: 10.1109/AERO.2008.4526237.

[37] L. Bruzzone and G. Quaglia, "Review article: Locomotion systems for ground mobile robots in unstructured environments," *Mech. Sci.*, vol. 3, no. 2, pp. 49–62, Jul. 2012, doi: 10.5194/ms-3-49-2012.

[38] B. Siciliano and O. Khatib, *Springer handbook of robotics*. 2016.

[39] D. Mechanism and L. Suspension, "Development of an Omni-Directional with 3 DoF Decoupling Drive Mobile Robot Mechanism Koichi Ozaki * 1 , Akihiro Matsumoto * 2 and Isao Endo * 1," pp. 95–100, 1996.

[40] L. Ferrière, G. Campion, and B. Raucent, "ROLLMOBS, a new drive system for omnimobile robots," *Robotica*, vol. 19, no. 1, pp. 1–9, Jan. 2001, doi: 10.1017/S0263574700002873.

[41] Woojin Chung, *Nonholonomic Manipulators*, 1st ed. Springer Berlin, Heidelberg, 2004.

[42] J. E. Colgate, M. A. Peshkin, and W. Wannasuphoprasit, "Nonholonomic haptic display," *Proc. - IEEE Int. Conf. Robot. Autom.*, vol. 1, no. April, pp. 539–544, 1996, doi: 10.1109/robot.1996.503831.

[43] R. Nakajima, T. Tsubouchi, S. Yuta, and E. Koyanagi, "A development of a new mechanism of an autonomous unicycle," in *Proceedings of the 1997 IEEE/RSJ International Conference on Intelligent Robot and Systems. Innovative Robotics for Real-World Applications. IROS '97*, vol. 2, pp. 906–912, doi: 10.1109/IROS.1997.655117.

[44] G. C. Nandy and Yangsheng Xu, "Dynamic model of a gyroscopic wheel," in *Proceedings. 1998 IEEE International Conference on Robotics and Automation (Cat. No.98CH36146)*, 1998, vol. 3, pp. 2683–2688, doi: 10.1109/ROBOT.1998.680751.

[45] Y. S. Ha and S. Yuta, "Trajectory tracking control for navigation of the inverse pendulum type self-contained mobile robot," *Rob. Auton. Syst.*, vol. 17, no. 1-2 SPEC. ISS., pp. 65–80, 1996, doi: 10.1016/0921-8890(95)00062-3.

[46] Y. Takahashi, T. Takagaki, J. Kishi, and Y. Ishii, "Back and forward moving scheme of front wheel raising for inverse pendulum control wheel chair robot," *Proc. - IEEE Int. Conf. Robot. Autom.*, vol. 4, pp. 3189–3194, 2001, doi: 10.1109/robot.2001.933109.

[47] K.-S. Byun and J.-B. Song, "Design and construction of continuous alternate wheels for an omnidirectional mobile robot," *J. Robot. Syst.*, vol. 20, no. 9, pp. 569–579, Sep. 2003, doi: 10.1002/rob.10107.

[48] M. West and H. Asada, "Design and control of ball wheel omnidirectional vehicles," in *Proceedings of 1995 IEEE International Conference on Robotics and Automation*, 1995, vol. 2, pp. 1931–1938, doi: 10.1109/ROBOT.1995.525547.

[49] G. Poole and G. Bush, "Omni-Directional Robots," in *Embedded Robotics*, vol. 125, no. 1698, Berlin, Heidelberg: Springer Berlin Heidelberg, 2008, pp. 147–156.

[50] M. Wada and S. Mori, "Holonomic and omnidirectional vehicle with conventional tires," *Proc. - IEEE Int. Conf. Robot. Autom.*, vol. 4, no. April,

pp. 3671–3676, 1996, doi: 10.1109/robot.1996.509272.

[51] D. B. Reister and M. A. Unseren, "Position and constraint force control of a vehicle with two or more steerable drive wheels," *IEEE Trans. Robot. Autom.*, vol. 9, no. 6, pp. 723–731, 1993, doi: 10.1109/70.265916.

[52] Y. Nakamura, H. Ezaki, Yuegang Tan, and Woojin Chung, "Design of steering mechanism and control of nonholonomic trailer systems," *IEEE Trans. Robot. Autom.*, vol. 17, no. 3, pp. 367–374, Jun. 2001, doi: 10.1109/70.938393.

[53] G. Campion and W. Chung, "Wheeled Robots," *Robotics*, pp. 391–410, 2016.

[54] D. Messuri and C. Klein, "Automatic body regulation for maintaining stability of a legged vehicle during rough-terrain locomotion," *IEEE J. Robot. Autom.*, vol. 1, no. 3, pp. 132–141, 1985, doi: 10.1109/JRA.1985.1087012.

[55] M. H. Raibert and E. R. Tello, "Legged Robots That Balance," *IEEE Expert*, vol. 1, no. 4, pp. 89–89, Nov. 1986, doi: 10.1109/MEX.1986.4307016.

[56] M. VUKOBRATOVIĆ and B. BOROVAC, "ZERO-MOMENT POINT — THIRTY FIVE YEARS OF ITS LIFE," *Int. J. Humanoid Robot.*, vol. 01, no. 01, pp. 157–173, Mar. 2004, doi: 10.1142/S0219843604000083.

[57] M. Wisse and R. Q. van der Linde, "Passive Dynamic Walking," in *Springer Tracts in Advanced Robotics*, vol. 34, 2007, pp. 7–24.

[58] I. R. Manchester, U. Mettin, F. Iida, and R. Tedrake, "Stable dynamic walking over uneven terrain," *Int. J. Rob. Res.*, vol. 30, no. 3, pp. 265–279, Mar. 2011, doi: 10.1177/0278364910395339.

[59] H. Hirukawa, S. Kajita, F. Kanehiro, K. Kaneko, and T. Isozumi, "The Human-size Humanoid Robot That Can Walk, Lie Down and Get Up," *Int. J. Rob. Res.*, vol. 24, no. 9, pp. 755–769, Sep. 2005, doi: 10.1177/0278364905057217.

[60] J.-J. Aucouturier, "Cheek to Chip: Dancing Robots and AI's Future," *IEEE Intell. Syst.*, vol. 23, no. 2, pp. 74–84, Mar. 2008, doi: 10.1109/MIS.2008.22.

[61] "aldebaran-robotics," [Online]. Available: https://www.aldebaran.com/en.

[62] "ROBONOVA-I." http://www.theoldrobots.com/SmallRobot9.html.

[63] R. Playter, M. Buehler, and M. Raibert, "BigDog," in *Unmanned Systems Technology VIII*, May 2006, vol. 6230, p. 62302O, doi: 10.1117/12.684087.

[64] R. D. Quinn *et al.*, "Parallel Complementary Strategies for Implementing Biological Principles into Mobile Robots," *Int. J. Rob. Res.*, vol. 22, no. 3–4, pp. 169–186, Mar. 2003, doi: 10.1177/0278364903022003003.

[65] R. Hodoshima, T. Doi, Y. Fukuda, S. Hirose, T. Okamoto, and J. Mori, "Development of a Quadruped Walking Robot TITAN XI for Steep Slope

Operation - Step Over Gait to Avoid Concrete Frames on Steep Slopes -," *J. Robot. Mechatronics*, vol. 19, no. 1, pp. 13–26, Feb. 2007, doi: 10.20965/jrm.2007.p0013.

[66] M. McKenna and D. Zeltzer, "Dynamic simulation of autonomous legged locomotion," *ACM SIGGRAPH Comput. Graph.*, vol. 24, no. 4, pp. 29–38, Sep. 1990, doi: 10.1145/97880.97882.

[67] A. Spröwitz, A. Tuleu, M. Vespignani, M. Ajallooeian, E. Badri, and A. J. Ijspeert, "Towards dynamic trot gait locomotion: Design, control, and experiments with Cheetah-cub, a compliant quadruped robot," *Int. J. Rob. Res.*, vol. 32, no. 8, pp. 932–950, Jul. 2013, doi: 10.1177/0278364913489205.

[68] M. Khoramshahi, A. Sprowitz, A. Tuleu, M. N. Ahmadabadi, and A. J. Ijspeert, "Benefits of an active spine supported bounding locomotion with a small compliant quadruped robot," in *2013 IEEE International Conference on Robotics and Automation*, May 2013, pp. 3329–3334, doi: 10.1109/ICRA.2013.6631041.

[69] E. P. Zehr and J. Duysens, "Regulation of Arm and Leg Movement during Human Locomotion," *Neurosci.*, vol. 10, no. 4, pp. 347–361, Aug. 2004, doi: 10.1177/1073858404264680.

[70] G. Parker and G. Rawlins, "Cyclic genetic algorithms for the locomotion of hexapod robots," *Proc. World Autom. Congr. (* …, 1996, [Online]. Available: http://citeseerx.ist.psu.edu/viewdoc/download?doi=10.1.1.219.4567&rep=rep1&type=pdf.

[71] J. Mills, "Stiquito II and Tensipede: Two Easy-to-Build Nitinol-Propelled Robots," Indiana, USA, 1994. [Online]. Available: https://legacy.cs.indiana.edu/.

[72] I. R. N. and D. S. Roland Siegwart, *Introduction to Autonomous Mobile Robots*, Second Edi. MIT press, 2011.

[73] Z. Xu, T. Lü, and F. Ling, "Trajectory planning of jumping over obstacles for hopping robot," *J. Brazilian Soc. Mech. Sci. Eng.*, vol. 30, no. 4, pp. 327–334, Dec. 2008, doi: 10.1590/S1678-58782008000400009.

[74] M. Hirose and K. Ogawa, "Honda humanoid robots development," *Philos. Trans. R. Soc. A Math. Phys. Eng. Sci.*, vol. 365, no. 1850, pp. 11–19, Jan. 2007, doi: 10.1098/rsta.2006.1917.

[75] B. Jakimovski, *Biologically Inspired Approaches for Locomotion, Anomaly Detection and Reconfiguration for Walking Robots*, vol. 14, no. 3. Berlin, Heidelberg: Springer Berlin Heidelberg, 2011.

[76] D. Gouaillier *et al.*, "Mechatronic design of NAO humanoid," in *2009 IEEE International Conference on Robotics and Automation*, May 2009, pp. 769–774, doi: 10.1109/ROBOT.2009.5152516.

[77] T. Uchiyama, T. Morita, and N. Sawasaki, “Development of Personal Robot,” in *Springer Tracts in Advanced Robotics*, vol. 66, no. STAR, 2010, pp. 319–336.

[78] F. Plestan, J. W. Grizzle, E. R. Westervelt, and G. Abba, “Stable walking of a 7-dof biped robot,” *IEEE Trans. Robot. Autom.*, vol. 19, no. 4, pp. 653–668, Aug. 2003, doi: 10.1109/TRA.2003.814514.

[79] K. Mitobe, G. Capi, and Y. Nasu, “Control of walking robots based on manipulation of the zero moment point,” *Robotica*, vol. 18, no. 6, pp. 651–657, Nov. 2000, doi: 10.1017/S0263574700002708.

[80] S. Kajita *et al.*, “Biped walking pattern generation by using preview control of zero-moment point,” in *2003 IEEE International Conference on Robotics and Automation (Cat. No.03CH37422)*, 2003, vol. 2, pp. 1620–1626, doi: 10.1109/ROBOT.2003.1241826.

[81] D. L. Hu, B. Chan, and J. W. M. Bush, “The hydrodynamics of water strider locomotion,” *Nature*, vol. 424, no. 6949, pp. 663–666, Aug. 2003, doi: 10.1038/nature01793.

[82] C. Kertész and M. Turunen, “Exploratory analysis of Sony AIBO users,” *AI Soc.*, vol. 34, no. 3, pp. 625–638, Sep. 2019, doi: 10.1007/s00146-018-0818-8.

[83] “Spot.” https://www.bostondynamics.com/products/spot?utm_term=&utm_campaign=LMG_NonBranded_Robotics&utm_source=adwords&utm_medium=ppc&hsa_acc=2933450915&hsa_cam=14547854154&hsa_grp=131897108630&hsa_ad=550072315623&hsa_src=g&hsa_tgt=dsa-1433406777573&hsa_kw=&hsa_m (accessed Jan. 23, 2023).

[84] K. Arikawa and S. Hirose, “Development of quadruped walking robot TITAN-VIII,” in *Proceedings of IEEE/RSJ International Conference on Intelligent Robots and Systems. IROS ’96*, 1996, vol. 1, pp. 208–214, doi: 10.1109/IROS.1996.570670.

[85] N. G. and P. M. Carlos Queiroz, “A STUDY ON STATIC GAITS FOR A FOUR LEG ROBOT,” *Proc. Control. ACC Int. Conf. Control*, vol. 0, pp. 1–6, 1999, [Online]. Available: https://www.academia.edu/download/53062584/A_Study_on_Static_Gaits_for_a_Four_Legge20170509-17113-1ia9sso.pdf.

[86] A. Saunders, D. I. Goldman, R. J. Full, and M. Buehler, “The RiSE climbing robot: body and leg design,” in *Unmanned Systems Technology VIII*, May 2006, vol. 6230, p. 623017, doi: 10.1117/12.666150.

[87] S. Cordes, K. Berns, M. Eberl, W. Ilg, and P. Buhrle, “On the design of a four-legged walking machine,” in *1997 8th International Conference on Advanced Robotics. Proceedings. ICAR’97*, 1997, pp. 65–70, doi: 10.1109/ICAR.1997.620163.

[88] R. Brooks, M. I. of T. D. of E. Engineering, C. Science, M. I. of T. D. of E. Engineering, and C. Science, "Genghis, a six legged autonomous walking robot," Doctoral dissertation, Massachusetts Institute of Technology, 1989.

[89] H. Kimura GEN, F. Toru Yamashita YAMA, and F. J. TITECHAC Shigenobu Kobayashi, "Reinforcement Learning of Walking Behavior for a Four-Legged Robot," *Proc. IEEE Conf. Decis. Control*, no. December, pp. 411–416, 2001, [Online]. Available: http://sysplan.nams.kyushu-u.ac.jp/gen/papers/CDC2001/CDC2001_080.pdf.

[90] "Surveillance Security Robots Robotic Platform Inspectorbots sells rugged, low cost, multi-purpose robotic platforms. Pre-made and custom robots with live video feeds. These teleoperated robots are great for wireless video camera surveillance and use as a robotics development platform." https://www.inspectorbots.com/Home.html (accessed Jun. 21, 2022).

[91] P. Ben-Tzvi and W. Saab, "A hybrid tracked-wheeled multi-directional mobile robot," *J. Mech. Robot.*, vol. 11, no. 4, pp. 1–10, 2019, doi: 10.1115/1.4043599.

[92] S. Hirose, T. Shirasu, and E. F. Fukushima, "Proposal for cooperative robot 'Gunryu' composed of autonomous segments," *Rob. Auton. Syst.*, vol. 17, no. 1-2 SPEC. ISS., pp. 107–118, 1996, doi: 10.1016/0921-8890(95)00066-6.

[93] X. Han, M. Lin, X. Wu, and J. Yang, "Design of An Articulated-tracked Mobile Robot with Two Swing Arms," in *2019 IEEE 4th International Conference on Advanced Robotics and Mechatronics (ICARM)*, Jul. 2019, pp. 684–689, doi: 10.1109/ICARM.2019.8833638.

[94] Z. Sun *et al.*, "BIT-DMR: A Humanoid Dual-Arm Mobile Robot for Complex Rescue Operations," *IEEE Robot. Autom. Lett.*, vol. 7, no. 2, pp. 802–809, 2022, doi: 10.1109/LRA.2021.3131379.

[95] T. Sasaki and T. Fujita, "Gap traversing motion via a hexapod tracked mobile robot based on gap width detection," *J. Robot. Mechatronics*, vol. 33, no. 3, pp. 665–675, 2021, doi: 10.20965/JRM.2021.P0665.

[96] S. Hong, M. Wu, J. Xiao, X. Xu, and H. Lu, "Kylin: A transformable track-wheel hybrid robot," in *2017 International Conference on Advanced Mechatronic Systems (ICAMechS)*, Dec. 2017, vol. 2017-Decem, pp. 7–12, doi: 10.1109/ICAMechS.2017.8316541.

[97] L. Bruzzone, M. Baggetta, S. E. Nodehi, P. Bilancia, and P. Fanghella, "Functional design of a hybrid leg-wheel-track ground mobile robot," *Machines*, vol. 9, no. 1, 2021, doi: 10.3390/machines9010010.

[98] Z. Gong, F. Xie, X. J. Liu, and S. Shentu, "Obstacle-crossing Strategy and Formation Parameters Optimization of a Multi-tracked-mobile-robot System with a Parallel Manipulator," *Mech. Mach. Theory*, vol. 152, p. 103919, 2020, doi: 10.1016/j.mechmachtheory.2020.103919.

[99] Y. Fukuoka, K. Oshino, and A. N. Ibrahim, “Negotiating Uneven Terrain by a Simple Teleoperated Tracked Vehicle with Internally Movable Center of Gravity,” *Appl. Sci.*, vol. 12, no. 1, 2022, doi: 10.3390/app12010525.

[100] J. Kim, J. Kim, and D. Lee, “Mobile robot with passively articulated driving tracks for high terrainability and maneuverability on unstructured rough terrain: Design, analysis, and performance evaluation,” *J. Mech. Sci. Technol.*, vol. 32, no. 11, pp. 5389–5400, 2018, doi: 10.1007/s12206-018-1037-4.

[101] T. Haji, T. Kinugasa, K. Yoshida, H. Amano, and K. Osuka, “Experiment of maneuverability of flexible mono-tread mobile track and differential-type tracked vehicle,” *Ind. Robot An Int. J.*, vol. 37, no. 3, pp. 263–272, May 2010, doi: 10.1108/01439911011037668.

[102] M. Neumann, T. Predki, L. Heckes, and P. Labenda, “Snake-like, tracked, mobile robot with active flippers for urban search-and-rescue tasks,” *Ind. Robot An Int. J.*, vol. 40, no. 3, pp. 246–250, Apr. 2013, doi: 10.1108/01439911311309942.

[103] K. Nagatani *et al.*, “Redesign of rescue mobile robot Quince - Toward emergency response to the nuclear accident at Fukushima Daiichi Nuclear Power Station on March 2011,” in *9th IEEE International Symposium on Safety, Security, and Rescue Robotics, SSRR 2011*, 2011, pp. 13–18, doi: 10.1109/SSRR.2011.6106794.

[104] W. Guo, J. Qiu, X. Xu, and J. Wu, “TALBOT: A Track-Leg Transformable Robot,” *Sensors*, vol. 22, no. 4, pp. 1–21, 2022, doi: 10.3390/s22041470.

[105] T. Robots, “Reinforcement Learning Based, Staircase Negotiation Learning,” no. December, 2021.

[106] Y. Yuan, Q. Xu, and S. Schwertfeger, “Configuration-Space Flipper Planning on 3D Terrain,” *2020 IEEE Int. Symp. Safety, Secur. Rescue Robot. SSRR 2020*, pp. 318–325, 2020, doi: 10.1109/SSRR50563.2020.9292598.

[107] C. Zong, Z. Ji, and H. Yu, “Dynamic stability analysis of a tracked mobile robot based on human–robot interaction,” *Assem. Autom.*, vol. 40, no. 1, pp. 143–154, 2020, doi: 10.1108/AA-10-2018-0156.

[108] P. Ben-Tzvi, A. A. Goldenberg, and J. W. Zu, “Design, simulations and optimization of a tracked mobile robot manipulator with hybrid locomotion and manipulation capabilities,” *Proc. - IEEE Int. Conf. Robot. Autom.*, pp. 2307–2312, 2008, doi: 10.1109/ROBOT.2008.4543558.

[109] Z. Li, X. Jing, B. Sun, and J. Yu, “Autonomous Navigation of a Tracked Mobile Robot With Novel Passive Bio-Inspired Suspension,” *IEEE/ASME Trans. Mechatronics*, vol. 25, no. 6, pp. 2633–2644, Dec. 2020, doi: 10.1109/TMECH.2020.2987004.

[110] Y. Li *et al.*, "Development and applications of rescue robots for explosion accidents in coal mines," *J. F. Robot.*, vol. 37, no. 3, pp. 466–489, 2020, doi: 10.1002/rob.21920.

[111] X. Gao, D. Cui, W. Guo, Y. Mu, and B. Li, "Dynamics and stability analysis on stairs climbing of wheel-track mobile robot," *Int. J. Adv. Robot. Syst.*, vol. 14, no. 4, pp. 1–13, 2017, doi: 10.1177/1729881417720783.

[112] S. M. Malik, L. Jun, and A. A. Goldenberg, "Virtual prototyping for conceptual design of a tracked mobile robot," in *Canadian Conference on Electrical and Computer Engineering*, 2006, pp. 2349–2352, doi: 10.1109/CCECE.2006.277740.

[113] J. Kim, Y. G. Kim, J. H. Kwak, D. H. Hong, and J. An, "Wheel & Track hybrid robot platform for optimal navigation in an urban environment," *Proc. SICE Annu. Conf.*, pp. 881–884, 2010.

[114] "Surveillance Security Robots Robotic Platform." https://www.inspectorbots.com/Home.html (accessed Jan. 04, 2023).

[115] R. Galati and G. Reina, "Terrain awareness using a tracked skid-steering vehicle with passive independent suspensions," *Front. Robot. AI*, vol. 6, no. JUN, pp. 1–11, 2019, doi: 10.3389/frobt.2019.00046.

[116] Y. Liu, S. Liu, L. Wang, X. Wu, Y. Li, and T. Mei, *A Novel Tracked Wall-Climbing Robot with Bio-inspired Spine Feet*, vol. 11741 LNAI. Springer International Publishing, 2019.

[117] M. Fiedeń and J. Bałchanowski, "A Mobile Robot with Omnidirectional Tracks—Design and Experimental Research," *Appl. Sci.*, vol. 11, no. 24, p. 11778, Dec. 2021, doi: 10.3390/app112411778.

[118] K. Tadakuma, R. Tadakuma, K. Nagatani, K. Yoshida, and K. Iagnemma, "Crawler Mechanism with Circular Section to Realize a Sideling Motion," *IEEE/RSJ Int. Conf. Intell. Robot. Syst.*, 2008.

[119] R. Galati, G. Mantriota, and G. Reina, "Design and Development of a Tracked Robot to Increase Bulk Density of Flax Fibers," *J. Mech. Robot.*, vol. 13, no. 5, pp. 1–10, 2021, doi: 10.1115/1.4051017.

[120] P. A. Bogdan, J. Wheadon, F. B. Klein, and M. Gianni, "Magnetic tracked robot for internal pipe inspection," *2021 10th Eur. Conf. Mob. Robot. ECMR 2021 - Proc.*, 2021, doi: 10.1109/ECMR50962.2021.9568790.

[121] J. Shi *et al.*, "Design, simulation and experimentation of a biomimetic wall-climbing robot with tracked spines," *Proc. 2020 IEEE Int. Conf. Power, Intell. Comput. Syst. ICPICS 2020*, pp. 744–750, 2020, doi: 10.1109/ICPICS50287.2020.9202054.

[122] V. Kumar, S. Agarwal, R. Vadapalli, N. Govindan, and K. M. Krishna, "Design and analysis of modular pipe climber-III with a multi-output

differential mechanism," *IEEE/ASME Int. Conf. Adv. Intell. Mechatronics, AIM*, vol. 2021-July, pp. 1021–1026, 2021, doi: 10.1109/AIM46487.2021.9517351.

[123] H. Taheri and C. X. Zhao, "Omnidirectional mobile robots, mechanisms and navigation approaches," *Mech. Mach. Theory*, vol. 153, 2020, doi: 10.1016/j.mechmachtheory.2020.103958.

[124] W. Steeds, "Tracked vehicles," *Automob. Eng. 40*, vol. no. 4, 1950.

[125] K. . Weiss, "Skid-steering," *Automob. Eng. 61, no. 4*, vol. 61, no. 22–25, 1971.

[126] J. E. Crosheck, "Skid Steering of Crawlers," 1975.

[127] M. Kitano and H. Jyozaki, "A theoretical analysis of steerability of tracked vehicles," *J. Terramechanics*, vol. 13, no. 4, pp. 241–258, Dec. 1976, doi: 10.1016/0022-4898(76)90045-8.

[128] W. Ehlert, B. Hug, and I. C. Schmid, "Field measurements and analytical models as a basis of test stand simulation of the turning resistance of tracked vehicles," *J. Terramechanics*, vol. 29, no. 1, pp. 57–69, Jan. 1992, doi: 10.1016/0022-4898(92)90014-B.

[129] J. Y. Wong and C. F. Chiang, "A general theory for skid steering of tracked vehicles on firm ground," *Proc. Inst. Mech. Eng. Part D J. Automob. Eng.*, vol. 215, no. 3, pp. 343–355, Mar. 2001, doi: 10.1243/0954407011525683.

[130] T. D. Thai and T. Muro, "Numerical analysis to predict turning characteristics of rigid suspension tracked vehicle," *J. Terramechanics*, vol. 36, no. 4, pp. 183–196, 1999, doi: 10.1016/S0022-4898(99)00016-6.

[131] G. Y. W. D. etc. Wu Ziyue, "Unified Dynamic Simulation Analysis of Tracked Mobile Robot Based on RecurDyn," *Mach. Des. Res.*, vol. 05, no. 35–39, 2016.

[132] S. Tang, Z. Guo, G. Wang, and X. Wang, "Comparative Performance Analysis of Different Travelling Mechanisms Based on RecurDyn," *IOP Conf. Ser. Mater. Sci. Eng.*, vol. 782, no. 4, 2020, doi: 10.1088/1757-899X/782/4/042059.

[133] I. Moskvin, R. Lavrenov, E. Magid, and M. Svinin, "Modelling a Crawler Robot Using Wheels as Pseudo-Tracks: Model Complexity vs Performance," *2020 IEEE 7th Int. Conf. Ind. Eng. Appl. ICIEA 2020*, pp. 1–5, 2020, doi: 10.1109/ICIEA49774.2020.9102110.

[134] M. G. Bekker, *Theory of Land Locomotion*. Ann Arbor, MI: University of Michigan Press, 1962.

[135] J. Y. (Jo Y. Wong, *Theory of ground vehicles*. John Wiley, 2001.

[136] M. G. Bekker, *Off-the-road locomotion: Research and development in terramechanics*. 1960.

[137] K. Tadakuma *et al.*, "Mechanical design of the wheel-leg hybrid mobile robot

to realize a large wheel diameter," *IEEE/RSJ 2010 Int. Conf. Intell. Robot. Syst. IROS 2010 - Conf. Proc.*, vol. 1, pp. 3358–3365, 2010, doi: 10.1109/IROS.2010.5651912.

[138] and R. S. Lauria, M., Y. Piguet, "Octopus - An Autonomous Wheeled Climbing Robot," 2002, pp. 315–322, doi: 10.3929/ethz-a-010098355.

[139] M. van Siegwart, Roland; Lauria, Michel; Mäusli, Pierre-Alain; Winnendael, "Design and Implementation of an Innovative Micro-Rover," 1998, pp. 181–187, doi: 10.3929/ethz-a-010111043.

[140] G. Quaglia, P. Torino, L. Bruzzone, G. Bozzini, R. Oderio, and P. Torino, "Epi . q-TG : mobile robot for surveillance," *Ind. Rob.*, vol. 38, no. 3, pp. 282–291, 2011, doi: https://doi.org/10.1108/01439911111122789.

[141] E. Caffrey, "iRobot SUGV." http://www.irobot.com/gi/ground/SUGV.

[142] S. Hirose *et al.*, "Quadruped walking robots at Tokyo Institute of Technology," *IEEE Robot. Autom. Mag.*, vol. 16, no. 2, pp. 104–114, Jun. 2009, doi: 10.1109/MRA.2009.932524.

[143] S. Yokota, K. Kawabata, P. Blazevic, and H. Kobayashi, "Control Law for Rough Terrain Robot with Leg-type Crawler," in *2006 International Conference on Mechatronics and Automation*, Jun. 2006, vol. 2006, pp. 417–422, doi: 10.1109/ICMA.2006.257570.

[144] S. Hirose, E. F. Fukushima, R. Damoto, and H. Nakamoto, "Design of terrain adaptive versatile crawler vehicle HELIOS-VI," in *Proceedings 2001 IEEE/RSJ International Conference on Intelligent Robots and Systems. Expanding the Societal Role of Robotics in the the Next Millennium (Cat. No.01CH37180)*, 2001, vol. 3, pp. 1540–1545, doi: 10.1109/IROS.2001.977198.

[145] "Galileo wheel." http://www.galileomobility.com.

[146] F. Michaud *et al.*, "Multi-Modal Locomotion Robotic Platform Using Leg-Track-Wheel Articulations," *Auton. Robots*, vol. 18, no. 2, pp. 137–156, Mar. 2005, doi: 10.1007/s10514-005-0722-1.

[147] J. Y. (Jo Y. Wong, *Theory of ground vehicles*. John Wiley & Sons, Inc., Hoboken, NJ, 2022.

[148] A. Angelova, L. Matthies, D. Helmick, and P. Perona, "Learning and prediction of slip from visual information," *J. F. Robot.*, vol. 24, no. 3, pp. 205–231, Mar. 2007, doi: 10.1002/rob.20179.

[149] R. Gonzalez, M. Fiacchini, T. Alamo, J. L. Guzman, and F. Rodriguez, "Adaptive Control for a Mobile Robot Under Slip Conditions Using an LMI-Based Approach," *Eur. J. Control*, vol. 16, no. 2, pp. 144–155, Jan. 2010, doi: 10.3166/ejc.16.144-155.

[150] G. Dudek and M. Jenkin, *Computational Principles of Mobile Robotics*. Cambridge University Press, 2010.

[151] "SuperDroid Robots," 2022. https://www.superdroidrobots.com/ (accessed Sep. 12, 2022).

[152] G. Lee, H. Kim, K. Seo, J. Kim, M. Sitti, and T. Seo, "Series of Multilinked Caterpillar Track-type Climbing Robots," *J. F. Robot.*, vol. 33, no. 6, pp. 737–750, Sep. 2016, doi: 10.1002/rob.21550.

[153] "Wheel-tracked Combined Robot Adaptable to Complicated Unstructured Environments such as Nuclear Power Plant," CN203806022U.

[154] "Self-climbing control method of tracked mobile robot with double-rod arm," CN104875800A., 2015.

[155] T. Fujita and T. Sasaki, "Development of hexapod tracked mobile robot and its hybrid locomotion with object-carrying," *Proc. - 2017 IEEE 5th Int. Symp. Robot. Intell. Sensors, IRIS 2017*, vol. 2018-Janua, pp. 69–73, 2018, doi: 10.1109/IRIS.2017.8250100.

[156] P. Rea and E. Ottaviano, "Design and development of an Inspection Robotic System for indoor applications," *Robot. Comput. Integr. Manuf.*, vol. 49, no. May 2017, pp. 143–151, Feb. 2018, doi: 10.1016/j.rcim.2017.06.005.

[157] C. Han, Y. Xu, X. Xu, Z. Zeng, H. Lu, and Z. Zhou, "Remote Control and Autonomous Driving: The System-wide Design of a Wheel-track Transformable Robot — Kylin Blaster," in *2018 Chinese Automation Congress (CAC)*, Nov. 2018, vol. 44, no. 8, pp. 3446–3451, doi: 10.1109/CAC.2018.8623389.

[158] Andrew A. GoldenbergJun Lin, "Mobile robot," US8360178B2, 2011.

[159] P. M. Pinhas Ben-Tzvi. ; Moubarak, "Mobile robot with hybrid traction and mobility mechanism," US9004200B2, 2015.

[160] Z. Luo, J. Shang, G. Wei, and L. Ren, "A reconfigurable hybrid wheel-track mobile robot based on Watt II six-bar linkage," *Mech. Mach. Theory*, vol. 128, pp. 16–32, 2018, doi: 10.1016/j.mechmachtheory.2018.04.020.

[161] F. Zhou, X. Xu, H. Xu, and X. Zhang, "A multimodal hybrid robot with transformable wheels," in *2017 IEEE International Conference on Real-time Computing and Robotics (RCAR)*, Jul. 2017, vol. 2017-July, pp. 139–144, doi: 10.1109/RCAR.2017.8311849.

[162] G. Quaglia, W. Franco, and R. Oderio, "Wheelchair.q, a motorized wheelchair with stair climbing ability," *Mech. Mach. Theory*, vol. 46, no. 11, pp. 1601–1609, Nov. 2011, doi: 10.1016/j.mechmachtheory.2011.07.005.

[163] Scewo Bro, "Power Wheelchair, the new generation." https://www.scewo.com/ (accessed Jan. 04, 2023).

[164] Carla R. Gillett, “Modular robotic service vehicle,” US20210283783A1, 2021.

[165] “Robot for stairs climbing,” KR101304107B1, 2012.

[166] Z. Song, Z. Luo, G. Wei, and J. Shang, “A Portable Six-Wheeled Mobile Robot With Reconfigurable Body and Self-Adaptable Obstacle-Climbing Mechanisms,” *J. Mech. Robot.*, vol. 14, no. 5, pp. 1–21, Oct. 2022, doi: 10.1115/1.4053529.

[167] Y. Kim, J. Kim, H. S. Kim, and T. Seo, “Curved-Spoke Tri-Wheel Mechanism for Fast Stair-Climbing,” *IEEE Access*, vol. 7, pp. 173766–173773, 2019, doi: 10.1109/ACCESS.2019.2956163.

[168] L. Bruzzone and P. Fanghella, “Mantis hybrid leg-wheel robot: Stability analysis and motion law synthesis for step climbing,” *MESA 2014 - 10th IEEE/ASME Int. Conf. Mechatron. Embed. Syst. Appl. Conf. Proc.*, pp. 0–5, 2014, doi: 10.1109/MESA.2014.6935540.

[169] L. Bruzzone, S. E. Nodehi, D. De Domenico, and P. Fanghella, “WheTLHLoc: small-scale hybrid locomotion robot with stair climbing capability,” *J. Mech. Robot.*, pp. 1–37, Jan. 2023, doi: 10.1115/1.4056770.

[170] Y. Zhu, Y. Fei, and H. Xu, “Stability Analysis of a Wheel-Track-Leg Hybrid Mobile Robot,” *J. Intell. Robot. Syst. Theory Appl.*, vol. 91, no. 3–4, pp. 515–528, 2018, doi: 10.1007/s10846-017-0724-1.

[171] “Tracker, Video Analysis and Modeling Tool.” https://physlets.org/tracker/.

[172] Shahab E. Nodehi, “WheTLHLoc,” 2022. https://www.youtube.com/watch?v=-cp3JdUlZpU&t=4s (accessed Jan. 04, 2023).

[173] I. Vincent and Q. Sun, “A combined reactive and reinforcement learning controller for an autonomous tracked vehicle,” *Rob. Auton. Syst.*, vol. 60, no. 4, pp. 599–608, 2012, doi: 10.1016/j.robot.2011.12.003.

[174] T. Kislassi and D. Zarrouk, “A Minimally Actuated Reconfigurable Continuous Track Robot,” *IEEE Robot. Autom. Lett.*, vol. 5, no. 2, pp. 1–1, 2019, doi: 10.1109/LRA.2019.2959237.

[175] Shahab E. Nodehi, “Snake Track,” 2022. https://www.youtube.com/watch?v=TVJFplnYO2o&t=3s (accessed Jan. 16, 2023).

[176] K. V. Wong and A. Hernandez, “A Review of Additive Manufacturing,” *ISRN Mech. Eng.*, vol. 2012, pp. 1–10, Aug. 2012, doi: 10.5402/2012/208760.

[177] JESIMON0801, “Intro to 3D Printing,” 2014. https://enablingthefuture.org/2014/11/13/tech-talk-thursday-intro-to-3d-printing/ (accessed Jan. 08, 2023).

[178] S. Inkinen, M. Hakkarainen, A.-C. Albertsson, and A. Södergård, “From Lactic Acid to Poly(lactic acid) (PLA): Characterization and Analysis of PLA and Its Precursors,” *Biomacromolecules*, vol. 12, no. 3, pp. 523–532, Mar. 2011, doi: 10.1021/bm101302t.

[179] B. Ghiban *et al.*, “Surface Characterization of Fracture in Polylactic Acid vs. PLA + Particle (Cu, Al, Graphene) Insertions by 3D Fused Deposition Modeling Technology,” *Coatings*, vol. 11, no. 6, p. 633, May 2021, doi: 10.3390/coatings11060633.

[180] Q.-W. Lu and C. W. Macosko, “Comparing the compatibility of various functionalized polypropylenes with thermoplastic polyurethane (TPU),” *Polymer (Guildf).*, vol. 45, no. 6, pp. 1981–1991, Mar. 2004, doi: 10.1016/j.polymer.2003.12.077.

[181] D. F. Machekposhti, N. Tolou, and J. L. Herder, “A Review on Compliant Joints and Rigid-Body Constant Velocity Universal Joints Toward the Design of Compliant Homokinetic Couplings,” vol. 137, no. March, pp. 1–12, 2015, doi: https://doi.org/10.1115/1.4029318.

[182] L. Bruzzone and R. M. Molfino, “A novel parallel robot for current microassembly applications,” vol. 4, pp. 299–306, 2006, doi: 10.1108/01445150610705218.

[183] L. Bruzzone and G. Bozzini, “A flexible joints microassembly robot with metamorphic gripper,” 2004, doi: 10.1108/01445151011061136.

[184] P. Bilancia and G. Berselli, “Computer-Aided Design An Overview of Procedures and Tools for Designing Nonstandard Beam-Based Compliant Mechanisms ☆,” *Comput. Des.*, vol. 134, p. 103001, 2021, doi: https://doi.org/10.1016/j.cad.2021.103001.

[185] M. Oehler, S. Kohlbrecher, and O. von Stryk, “Optimization-based planning for autonomous traversal of obstacles with mobile ground robots,” *Int. J. Mech. Control*, vol. 21, no. 1, pp. 33–40, 2020.

[186] Shahab E. Nodehi, “Porcospino,” 2022. https://www.youtube.com/watch?v=ngbYS4rAJA8 (accessed Jan. 16, 2023).